

University of Nevada, Reno

**Reversible Metal Electrodeposition and Ion Intercalation for
Dynamic Windows**

A dissertation submitted in partial fulfillment of the
requirements for the degree of Doctor of Philosophy in
Chemistry

by

Molla Shakirul Islam

Dr. Christopher J. Barile/Dissertation Advisor

December, 2021



THE GRADUATE SCHOOL

We recommend that the dissertation
prepared under our supervision by

Molla Shakirul Islam

entitled

**Reversible Metal Electrodeposition and Ion Intercalation for
Dynamic Windows**

be accepted in partial fulfillment of the
requirements for the degree of

Doctor of Philosophy

Christopher J. Barile, Ph.D.
Advisor

Samuel Odoh, Ph.D.
Committee Member

Mario A. Alpuche, Ph.D.
Committee Member

Dev Chidambaram, Ph.D.
Committee Member

Mohammed Ben-Idris, Ph.D.
Graduate School Representative

David W. Zeh, Ph.D., Dean
Graduate School

December, 2021

Abstract:

Buildings are responsible for ~40% of total U.S. energy demand, and lighting, heating, and cooling are responsible for ~53% of total building energy consumption. Dynamic windows, which electronically control opacity and heat flow, can save up to 10-15% of the total energy consumption of a building by reducing lighting, heating, and cooling demand compared with static windows that use low-E glass. However, due to their high cost, slow switching speed, and inadequate opacity, traditional electrochromic dynamic windows are not yet widely commercialized for building applications.

In this dissertation, I have developed a new class of dynamic windows based on reversible metal electrodeposition (RME) coupled with ion storage layer-based counter electrodes. I have studied the stability and electrochromic properties of metal oxides and hexacyanoferrate-based compounds for their application as a counter electrode in dynamic windows. In addition to the improved scalability of these devices, the ion storage layer-based counter electrode also improves device switching speed.

I also studied pH-neutral electrolytes for reversible Zn electrodeposition on a transparent conductive electrode for application in dynamic windows. A reaction mechanism for the reversible Zn electrodeposition was proposed during the deposition and dissolution process. As a result of compact Zn electrodeposition on a transparent conductive electrode, the dynamic windows showed fast switching speeds, <0.01% opacity in the opaque state, and excellent resting stability. The high opacity of these windows, in particular, opens a new direction for using dynamic windows in residential settings, where privacy is required.

Acknowledgment:

This dissertation results from four years of work at the Barile Research Group in the Department of Chemistry at the University of Nevada, Reno (UNR). It would not be possible without love, support, and kindness of the people around me.

I want to start by thanking my mentor and advisor, Prof. Christopher Barile. When I first joined his group, I didn't have much research experience and vision. Chris taught me everything from scratch and helped me in every perspective of my life. His philosophy on academic and personal life inspires me a lot. Whatever I am now and achieved was not possible without his great help and support.

The Chemistry department, and the Barile Research Group, was like my second family. I want to mention Barile Research Lab's first cohort of graduate students: Rajendra Gautam and Jason Manel. Jason helped me understand the new culture in the US, and Raj helped me and my family adjust and settle down in Reno. We always shared our joys and challenging times. Additionally, I want to acknowledge my lab mates both in the windows and catalysis teams: Darren Miller, Joe Jeanetta, Judy Li, Desmond Madu, Profulla Mondol, Tania Akter, Hanqing Pan, Alexis Palma, Jose Juarez-Rolon, Lorenzo Arvisu, and Meagan LeBerth, and Christine Fini always helped me accelerate my research progress.

I want to acknowledge our collaborators Prof. Mike McGehee, Prof. Wesley Chalifoux, Tyler Hernandez, and Ryan Malone.

I want to thank my friend Amir Mirzanejad for helping me both in academic and non-academic affairs. My life as an international student would not be easier without his kind and significant support. Moreover, his helpful, honesty, and hard-working ethics inspired me vastly.

I want to thank the Department of Chemistry for giving me a Teaching Assistantship for four years. My Ph.D. would not be possible without this support. Also, I want to thank Dr. Munro, who was my teaching mentor for all my teaching courses and taught me how to become a good course instructor.

I want to acknowledge my personal friends: Mahmud Rabby Nahid, Yeasin Prodhan, Mostafa Kamal, Qazi Abdur Rahman, Sayed Zawad, Musa Aman, Shafiqul Islam, Anisur Rahman who always believed in me and helped me travel to the USA to become a successful Ph.D. candidate. In addition, I want to thank my fellow Bangladeshi students at the UNR chemistry department: Chowdhury Raihan Bikash, and Md. Azizul Islam, for their kind support.

My PhD journey would not be possible without the support of my previous teachers and advisors, Md. Hasanuzzam, Bikash Chondro Mondol, Dr. Anamul Hoque, Dr. Abdus Sabur, and Dr. Shahed Rana.

This research was partially supported by Research and Innovation at the University of Nevada, Reno (UNR). SEM-EDS analysis was performed in the Mackay Microbeam Laboratory at UNR, we acknowledge J. Desormeau for his kind assistance. We acknowledge the National Science Foundation for financial support through a CAREER Award (CHE-2046105) for support of the battery work. We also acknowledge the Shared

Instrumentation Laboratory in the Department of Chemistry at the University of Nevada, Reno (UNR). The support of the National Science Foundation (CHE-1429768) for the purchase of the powder X-ray diffractometer is gratefully acknowledged. Dynamic window research was supported in part by the National Science Foundation grant EPMD-2127308 and by the Department of Energy's Office of Energy Efficiency and Renewable Energy and its Buildings Energy Efficiency Frontiers & Innovation Technologies program under award number DE-EE0009701.

My Mom, and Dad for giving me your support and love for everything and believing in me all time. My only younger brother Barkat, for his immense love and support.

I want to thank my lovely wife, Naima, who sacrificed almost everything for me. My Ph.D. would not be possible without her love, and support. In addition, my eighteen-month-old daughter Sierra gives me immense pleasure of my life. I forgot all my stress after seeing her smiling face end of the day.

Table of Contents

<i>Chapter 1: Introduction</i>	1
<i>Chapter 2: Hybrid Dynamic Windows using Reversible Metal Electrodeposition and Ion Insertion</i>	10
2.1. Introduction:	10
2.2. Results and Discussion:	13
2.2.1. Selecting a Compatible Metal Oxide Counter Electrode.....	13
2.2.2. 25 cm ² Hybrid Dynamic Windows using Reversible Metal Electrodeposition and NiO.....	14
2.2.3. Large-Scale Hybrid Dynamic Windows.....	21
2.2.4. Outlook and Comparison to other Dynamic Window Technologies	22
2.3. Experimental:	24
2.3.1. Electrochemical Methods	24
2.3.2. Dynamic Window Assembly.....	25
2.3.3. Thin Film Synthesis.....	25
2.3.4. Materials Characterization.....	27
2.4. Conclusion	27
<i>Chapter 3: Cuprous Oxide Electrodeposited with Nickel for the Oxygen Evolution Reaction in 1 M NaOH</i>	29
3.1. Introduction	29
3.2. Experimental	30
3.2.1. Chronoamperometric Electrodeposition of Cuprous Oxide	30
3.2.2. Chronopotentiometric Electrodeposition of Nickel.....	31
3.2.3. Electrochemical Measurements	31
3.3. Results and Discussion	32
3.3.1. Electrodeposition of Ni-Cu ₂ O Thin Films.....	32
3.3.2. OER Activity of Ni-Cu ₂ O Thin Films.....	33
3.3.3. Surface Characterization of Ni-Cu ₂ O Thin Films	36
3.4. Conclusion	41
<i>Chapter 4: Dynamic Windows based on Reversible Metal Electrodeposition with Enhanced Functionality</i>	42
4.1. Introduction	42
4.2. Experimental	43
4.3. Results and Discussion	46
4.3.1. Dynamic Windows with One and Two Working Electrodes	46
4.3.2. Modeling the Switching Speed of a Two Working Electrode Window	49

4.3.3. Effect of Voltage on Metal Electrodeposition	50
4.4. Conclusion.....	60
<i>Chapter 5: Dual Tinting Dynamic Windows using Reversible Metal Electrodeposition and Prussian Blue.....</i>	<i>61</i>
5. 1. Introduction	61
5. 2. Result and Discussion.....	64
5. 2. 1. Dual Tinting Device Architecture	64
5. 2. 2. Thin Film Characterization.....	66
5. 2. 3. Electrolyte Design	67
5. 2. 4. Cycling Durability	72
5. 3. Experimental.....	73
5.3.1. General Procedures.....	73
5. 3. 2. Electrodeposition of Prussian Blue Thin Films.....	74
5. 3. 3. Electrodeposition of Bi Thin Films	75
5. 3. 4. Construction of 25 cm ² Two-Electrode Dynamic Windows.....	75
5. 3. 5. Materials Characterization.....	75
5. 4. Conclusion.....	76
<i>Chapter 6: Optically Switchable Thin Films based on Reversible Cu and Au Electrodeposition.....</i>	<i>77</i>
6. 1. Introduction	77
6.2. Experimental.....	80
6.3. Results and Discussion	81
6.3.1. Two-Electrode Studies of the Cu-Au Electrolyte.....	81
6.3.2. Three-Electrode Studies of the Cu-Au Electrolyte.....	85
6. 4. Conclusion.....	96
<i>Chapter 7: Hybrid Dynamic Windows with Color Neutral and Fast Switching using Reversible Metal Electrodeposition and Cobalt Hexacyanoferrate Electrochromism..</i>	<i>97</i>
7.1. Introduction	97
7.2. Results and Discussion	101
7. 2. 1. Hybrid Dynamic Window Architecture	101
7. 2. 2. Color Neutrality of CoHCF Hybrid Dynamic Windows.....	104
7. 2. 3. Thin Film Characterization.....	106
7.2.4. Ion Intercalation and Electrolyte Design	108
7.2.5. Cycling Durability	113
7.4. Experimental.....	114
7.4.1. General Procedures.....	114

7. 4.2. Synthesis and Deposition of CoHCF Thin Films	115
7. 4.3. Electrodeposition of Bi Thin Films	116
7.4.4. Construction of 25 cm ² Two-electrode Hybrid Dynamic Windows	117
7.4.5. Materials Characterization.....	117
<i>Chapter 8: Aqueous Alkaline Electrolytes for Dynamic Windows based on Reversible Metal Electrodeposition with Improved Durability</i>	118
8.1. Introduction	118
8.2. Experimental.....	121
8.3. Results and Discussion	122
8.4. Conclusion.....	136
<i>Chapter 9: Dynamic Windows using Reversible Zn Electrodeposition in Neutral Electrolytes with High Opacity and Excellent Resting Stability</i>	137
9. 1. Introduction	137
9.2. Results and Discussion	140
9.2.1. Dynamic Window Architecture and Reaction Mechanism	140
9.2.2. Cycle Life and Durability	142
9.2.3. 100 cm ² Dynamic Window.....	147
9.2.4. Study of Electrolytes	149
9.3. Conclusion.....	154
9.4. Experimental.....	154
9.4.1. General Procedure	154
9.4.2. Material Characterization	155
9.4.3. Dynamic Window Assembly.....	155
<i>Chapter 10: Electrolytes for Reversible Zinc Electrodeposition for Dynamic Windows</i>	157
10.1. Introduction	157
10.2. Experimental.....	160
10. 3. Results and Discussion	161
10.3.1. Zn Haloacetate Electrolytes.....	161
10. 3. 2. Effects of Ligand Chain Length on Zn Electrolytes.....	166
10.3.3. Effect of Halides on Zn Electrolytes	168
10. 3. 4. Surface Characterization of Zn Electrodeposits	173
10. 3. 5. The Electrochemical Window of ITO in Zn Electrodeposition Electrolytes	176
10. 3. 6. Practical Two-Electrode Devices using Reversible Zn Electrodeposition	179
10. 4. Conclusion.....	183

<i>Chapter 11: Nanographene Cathode Materials for Nonaqueous Zn-ion Batteries....</i>	<i>184</i>
11.1. Introduction	184
11.2. Experimental.....	186
11.3. Results and discussion.....	187
11.4. Conclusion.....	197
<i>Chapter 12: Appendices. Supporting Figures.....</i>	<i>198</i>
12.1. Supporting Figures for Chapter 2: Hybrid Dynamic Windows using Reversible Metal Electrodeposition and Ion Insertion	198
12.2. Supporting Figures for Chapter 3: Cuprous Oxide Electrodeposited with Nickel for the Oxygen Evolution Reaction in 1 M NaOH	208
12.3. Supporting Information for Chapter 4: Dynamic Windows based on Reversible Metal Electrodeposition with Enhanced Functionality	213
12.4. Supporting information for chapter 5: Dual Tinting Dynamic Windows using Reversible Metal Electrodeposition and Prussian Blue.....	219
12. 5. Supporting Information for Chapter 7: Hybrid Dynamic Windows with Color Neutral and Fast Switching using Reversible Metal Electrodeposition and Cobalt Hexacyanoferrate Electrochromism	225
12.6: Supporting Information for chapter 8: Aqueous Alkaline Electrolytes for Dynamic Windows based on Reversible Metal Electrodeposition with Improved Durability	231
12.7. Supporting Information for Chapter 9: Dynamic Windows using Reversible Zn Electrodeposition in Neutral Electrolytes with High Opacity and Excellent Resting Stability	235
12.8. Supporting Information for Chapter 10: Electrolytes for Reversible Zinc Electrodeposition for Dynamic Windows	240
12.9. Supplementary Information for Chapter 11: Nanographene Cathode Materials for Nonaqueous Zn-ion Batteries	245
<i>Chapter 13. References:.....</i>	<i>248</i>

List of Tables

Table 3.1: Calculated thicknesses of Ni obtained during electrodeposition for various plating times and calculated Cu ₂ O: Ni mass proportions of the samples.	33
Table 7.1: RGB color profiles and La*b*C* values for 25 cm ² hybrid dynamic windows based on reversible metal electrodeposition and a counter electrode containing Prussian Blue (top, calculated from data in reference 20) and CoHCF (bottom).	105
Table 8. 1: Composition of some of the various EDTA electrolytes studied.	125
Supporting Table 12.2.1: Summary of performance of various OER electrocatalysts reported in the literature arranged by catalyst family.	213

Table of Figures

Figure 1.1: Per capita energy consumption in the U.S. from 1650 to 2000 (a) [2], Energy consumption sources in the U.S. (b). [3]	1
Figure 1.2: Pie chart of greenhouse gases (GHGs) emissions in the U.S. [4]	2
Figure 1.3: Change of global CO ₂ level over last 800,000 years. [6]	3
Figure 1.4: Global CO ₂ gas emissions[7].....	4
Figure 1.5: Diagram for electrochemical reduction of CO ₂ . [12]	5
Figure 1.6: Pie chart showing energy consumption in the U.S.A. [33]	7
Figure 2.1: Metal-based Dynamic Window Architectures. Schematic of reversible metal electrodeposition device architectures (expanded view at the top and side view at the bottom) with (a) a metal frame around the device perimeter, which requires lateral metal ion diffusion to the center of the window, and (b) a plane-parallel counter electrode, which maintains constant transverse ion diffusion regardless of scale.	12
Figure 2.2. Transmission Profile of 25 cm² Hybrid Dynamic Window. a, Transmission of a 25 cm ² dynamic window with a Pt-modified ITO on glass working electrode, a LiNiO _x on ITO on glass counter electrode formed using electrodeposition, and a Cu-Bi gel electrolyte as a function of wavelength after 0 s (black), 15 s (red), 30 s (blue), and 60 s (teal) of window tinting at -2.5 V. b, Transmission of the same window at 600 nm during 60 s of metal electrodeposition at -2.5 V and 120 s of metal stripping at 0 V.....	16
Figure 2.3. A Metal Inhibitor on LiNiO_x Improves Device Durability. a, Schematic of LiNiO _x counter electrode in a metal-based dynamic window after extensive cycling. Cu ²⁺ and Bi ³⁺ metallic ions (blue and green, respectively) are reduced to Cu ⁰ and Bi ⁰ solid metal (brown and grey, respectively) on the surface of the unmodified LiNiO _x (top panels). When the LiNiO _x counter electrode is modified with BTD, a triazole-based metal inhibitor, metal deposition does not occur on the LiNiO _x , which improves device durability. b, Cyclic voltammograms of LiNiO _x (black) and BTD-coated LiNiO _x (red) on ITO on glass in a three-electrode cell with a Cu-Bi liquid electrolyte at a scan rate of 50 mV/s. c, Contrast ratio of dynamic window with a Pt-modified ITO on glass working electrode and a BTD-coated LiNiO _x on ITO on glass counter electrode over the course of 4,000 cycles.....	17
Figure 2.4. Transmission of LiNiO_x during Lithiation and Delithiation. Transmission of a 200-nm-thick NiO film on an ITO on glass working electrode in a three-electrode cell using a 1 M LiBr electrolyte. A voltage of -0.01 V was applied for 180 s to lithiate the electrode and 0.67 V was applied for 60 s to delithiate the electrode.....	20
Figure 2.5. Flexible Hybrid Dynamic Windows. Photographs of a 25 cm ² flexible dynamic window after 0 s (a) and 120 s (b) of metal electrodeposition using a Pt-modified ITO on PET working electrode and a LiNiO _x on ITO on PET counter electrode formed using a chemical bath deposition technique. c, Transmission at 600 nm of the window during 120 s of metal electrodeposition at -2.5 V and 180 s of metal stripping at 0 V.....	21

Figure 2.6. 100 cm² Hybrid Dynamic Windows. Photographs of a 100 cm ² dynamic window after 0 s (a) and 120 s (b) of metal electrodeposition using a Pt-modified ITO on glass working electrode and a LiNiO _x on ITO on glass counter electrode. c, Transmission at 600 nm through the edge (black) and the center (red) of the window during switching at -2.5 V for 60 s followed by 0 V for 120 s.	22
Figure 3.1: Linear sweep voltammograms of the oxygen evolution reaction in 1 M NaOH using Cu ₂ O on ITO working electrodes that have been electrodeposited with Ni for 0 s (red line), 100 s (orange line), and 500 s (blue line) at a scan rate of 10 mV/s. Panel B is an inset of panel A.	34
Figure 3.2: Linear sweep voltammograms of the oxygen evolution reaction in 1 M NaOH using Cu ₂ O on ITO working electrodes that have been electrodeposited with Ni for 20 s (A, green line), 160 s (A, red line), and 200 s (A, purple line) at a scan rate of 10 mV/s. Analogous experiments were also performed with Cu (B, black line) and Ni (B, red line) foils.	35
Figure 3.3: Plot of overpotentials for the onset of the oxygen evolution reaction using various working electrodes in 1 M NaOH.	36
Figure 3.4: XRD spectrum of a Cu ₂ O on ITO electrode with a Ni overlayer formed using 100 s of Ni electrodeposition.	37
Figure 3.5: SEM images of Cu ₂ O on ITO electrodes with a Ni overlayer formed via 0 s (A), 20 s (B), 100 s (C), 160 s (D), 200 s (E), and 500 s (F) of Ni electrodeposition.	38
Figure 3.6: SEM image (A), EDS spectrum (B), and corresponding elemental distribution maps (C-F) as determined by EDS of a Cu ₂ O on ITO electrode with a Ni overlayer formed using 100 s of Ni electrodeposition. Brighter colors in the EDS maps represent higher relative elemental concentrations.	40
Figure 4.1: Schematic of the architecture of a dynamic window based on reversible metal electrodeposition that contains one Pt-modified ITO on glass working electrode and a glass back pane. Metal electrodeposition only occurs on the ITO during window tinting.	46
Figure 4.2: Schematic of the architecture of a dynamic window based on reversible metal electrodeposition that contains two Pt-modified ITO on glass working electrodes. Metal electrodeposition occurs on both ITO electrodes during window tinting.	47
Figure 4.3: Transmission of 25 cm ² metal-based dynamic windows with two (blue) and one (red) working electrodes during switching at -0.6 V for 30 s and +0.8 V for 30 s.	48
Figure 4.4: Chronoamperometry of 25 cm ² metal-based dynamic windows with two (blue) and one (red) working electrodes during switching at -0.6 V for 30 s and +0.8 V for 30 s.	48
Figure 4.5: Transmission at 600 nm of a 25 cm ² metal-based dynamic window with two working electrodes during switching at -0.6 V for 30 s (black). The dashed lines represent the predicted transmission curves with two different models.	50
Figure 4.6: Transmission of 25 cm ² metal-based dynamic windows with two (blue) and one (red) working electrodes during switching at -1.2 V for 30 s and +0.8 V for 60 s.	51

- Figure 4.7:** Transmission of a 25 cm² metal-based dynamic window with two working electrodes as a function wavelength after 0 s (black), 10 s (red), 20 s (blue), and 30 s (green) of window darkening at -1.2 V..... 52
- Figure 4.8:** Photographs of a 25 cm² metal-based dynamic window during switching at -1.2 V for 0 s (a), 15 s (b), and 30 s (c). 53
- Figure 4.9:** More than 1,000 cycles of a 4 cm² dynamic window based on reversible metal electrodeposition with two working electrodes. Each switching cycle consisted of applying -1 V for 3 s and +0.8 V for 7 s. 53
- Figure 4.10:** Electrochemical impedance spectroscopy of 25 cm² metal-based dynamic windows with one working electrode and one counter electrode (black), and two working electrodes and one counter electrode (red). The resistances of the counter electrode anode were calculated to be 29 Ω, and 53 Ω for these three devices, respectively. 55
- Figure 4.11:** Cyclic voltammograms in a Ag-Cu electrolyte using a Pt-modified ITO on glass (black) and unmodified ITO on glass (red) working electrode at 20 mV/s. 56
- Figure 4.12:** Photographs of a 25 cm² dynamic window in its clear state (left) and after 60 s of metal electrodeposition at -0.6 V using ITO on glass working electrodes with two different patterns of SAMs of Pt nanoparticles (right). 57
- Figure 4.13:** Schematic showing the fabrication of micro-patterned metal electrodeposition with a SAM of Pt nanoparticles templated by polystyrene beads. 58
- Figure 4.14:** Optical microscopy of 1 μm polystyrene spheres spin-coated on ITO on glass (a). False-color SEM image of Ag-Cu electrodeposits (B, purple) on ITO with a Pt SAM patterned with 1 μm polystyrene spheres. The Pt SAM does not deposit where the polystyrene spheres once were (indicated by black circles), leaving bare ITO (B, green). For the most part, the Ag-Cu electrodeposits grow selectively on the Pt SAM. 59
- Figure 5.1.** Schematic of dual tinting dynamic windows that facilitate reversible Bi metal electrodeposition on an ITO on glass working electrode modified with a SAM of Pt nanoparticles and a Prussian blue on ITO on glass counter electrode. 63
- Figure 5.2.** Transmission of a 25 cm² dynamic window with a Pt-modified ITO on glass working electrode, a PB on ITO on glass counter electrode formed using 6 minutes of electrodeposition, and a Bi gel electrolyte as a function of wavelength after 0 s (black), 1 s (red), 2 s (blue), and 3 s (pink) of window tinting at -2 V (a). Transmission of the same window at 700 nm during 3 s of window tinting at -2 V followed by 15 s of window lightening at +1.5 V (b). 64
- Figure 5.3.** Photographs of a 25 cm² metal-based hybrid dynamic window with a Prussian blue counter electrode during switching at -2 V for 0 s (a), 1 s (b), and 3 s (c). 66
- Figure 5.4.** Scanning electron microscopy images of the working (a) and counter (b) electrodes of a hybrid dynamic window in its tinted state. 67
- Figure 5.5.** Cyclic voltammograms (a, c) and transmission at 700 nm (b, d) of a Prussian blue on ITO on glass working electrode in a three-electrode cell in a liquid electrolyte containing 0.2 M LiBr (a, b) or KBr (c, d) with 100 mM HCl at a scan rate of 5 mV/s. . 69

Figure 5.6. Cyclic voltammograms of Prussian blue on ITO on glass working electrode in the Bi-Cu (black), Bi only (blue), and Cu only (red) electrolytes in a three-electrode cell at a scan rate of 5 mV/s.	72
Figure 5.7. Maximum (red line) and minimum (cyan line) transmission of a 25 cm ² dynamic window with a Pt-modified ITO on glass working electrode and a Prussian blue on ITO on glass counter electrode over the course of 1,500 cycles.	73
Figure 6.1: Transmission at 600 nm (a) and current density (b) during the first switching cycle of a Pt-modified ITO on glass working electrode in the Cu-Au electrolyte in a two-electrode cell with a Au wire counter electrode. The potential was held at -1.65 V for 60 s to induce metal electrodeposition followed by +1.2 V for 60 s to elicit metal stripping..	82
Figure 6.2: Transmission as a function of wavelength during metal electrodeposition on a Pt-modified ITO on glass working electrode in the Cu-Au electrolyte in a two-electrode cell with a Au wire counter electrode (a). The potential was held at -1.65 V for 60 s to induce metal electrodeposition. Calculated transmission values (b) of 20 nm thick films of Au (black) and Cu (red) as compared to the Cu-Au film obtained after 60 s of electrodeposition (blue).	83
Figure 6.3: Maximum (black line) and minimum (red line) transmission values at 600 nm of the Pt-modified ITO on glass working electrode in the Cu-Au electrolyte in a two-electrode cell with a Au wire counter electrode over 100 switching cycles. For each cycle, the potential was held at -1.65 V for 60 s to induce metal electrodeposition followed by +1.2 V for 60 s to elicit metal stripping. The blue line plots the optical contrast or difference between the maximum and minimum transmissions during the 100 switching cycles.....	84
Figure 6.4: Cyclic voltammetry at a scan rate of 10 mV/s (a) and corresponding transmission at 600 nm (b) of a Pt-modified ITO on glass working electrode in a Cu-Au electrolyte in a three-electrode cell.	87
Figure 6.5: Cyclic voltammetry at scan rate of 10 mV/s of a Pt-modified ITO on glass working electrode in an electrolyte containing 3 M NaCl, 400 mM NaBr, and 1 mM NaI adjusted to pH 3.4 with HCl.	88
Figure 6.6: Cyclic voltammetry at a scan rate of 10 mV/s of a Pt-modified ITO on glass working electrode in the Cu-Au electrolyte (black line) and electrolytes containing only Cu (red line) and only Au (blue line) as the redox active metals.	89
Figure 6.7: Transmission at 600 nm during seven cycles of cyclic voltammetry at a scan rate of 10 mV/s of a Pt-modified ITO on glass working electrode in electrolytes containing only Cu (red line) and only Au (blue line) as the redox active metals.	90
Figure 6.8: Cyclic voltammetry at a scan rate of 10 mV/s of a Pt-modified ITO on glass working electrode in electrolytes without halides containing Cu-Au (black line), only Cu (red line), and only Au (blue line) as the redox active metals.	92
Figure 6.9: Transmission at 600 nm during seven cycles of cyclic voltammetry at a scan rate of 10 mV/s of a Pt-modified ITO on glass working electrode in the Cu-Au electrolyte without halides.	93

- Figure 6.10:** Onset potential for Cu-Au electrodeposition as determined by cyclic voltammetry at a scan rate of 10 mV/s of a Pt-modified ITO on glass working electrode in the Cu-Au electrolyte with various concentrations of NaBr..... 94
- Figure 6.11:** Cyclic voltammetry at a scan rate of 10 mV/s of a Pt-modified ITO on glass working electrode in the Cu-Au electrolyte with (black line) and without (red line) NaBr. 95
- Figure 6.12:** Tafel slopes extracted from cyclic voltammetry of the Cu-Au electrolyte with (black lines) and without (red lines) NaBr for Au electrodeposition at c.a. +0.55 V (a) and Cu/Au electrodeposition at c.a. -0.3 V (b) The solid lines represent the linear fits used to calculate the Tafel slopes..... 95
- Figure 7.1:** Schematic of a hybrid dynamic window that facilitates reversible Bi and Cu metal electrodeposition on an ITO on glass working electrode modified with a SAM of Pt nanoparticles and migration of Na⁺ on a CoHCF on ITO on glass counter electrode.... 101
- Figure 7.2:** Transmission of a 25 cm² hybrid dynamic window with a Pt-modified ITO on glass working electrode, a CoHCF on ITO on glass counter electrode, and a Bi-Cu-NaBr gel electrolyte as a function of wavelength after 0 s (black), 5 s (red), 10 s (blue), 15 s (magenta), and 20 s (green) of window tinting at -2.5 V (a). Transmission of the same window at 650 nm during 20 s of window tinting at -2.5 V followed by 20 s of window lightening at 0.75 V (b). 102
- Figure 7.3:** Photographs of a 25 cm² metal-based hybrid dynamic window with a CoHCF counter electrode during switching at -2.5 V for 0 s (a), 10 s (b), and 40 s (c). 104
- Figure 7.4:** Scanning electron microscopy images of the working (a) and counter (b) electrodes of a CoHCF hybrid dynamic window in its tinted state. 107
- Figure 7.5:** Cyclic voltammograms (a, c, e) and transmission at 500 nm (b, d, f) of a CoHCF on ITO on glass working electrode in a three-electrode cell in an electrolyte containing 1M LiBr (a, b), NaBr (c, d), or KBr (e, f) at a scan rate 10 mV/s..... 111
- Figure 7.6:** Cyclic voltammogram (a) and transmission at 650 nm (b) of a CoHCF on ITO on glass working electrode in a three-electrode cell in a liquid electrolyte containing Bi-Cu-NaBr at a scan rate of 10 mV/s. 113
- Figure 7.7:** Contrast ratio of a hybrid dynamic window with CoHCF over the course of 1000 cycles..... 114
- Figure 8.1:** Cyclic voltammetry (A) and corresponding transmission at 500 nm (B) of a Pt-modified ITO on glass working electrode in an electrolyte containing 202 mM Bi(NO₃)₃, 308 mM EDTA, 550 mM 5-sulfosalicylic acid, 266 mM potassium sodium tartrate, and 107 mM KCl adjusted to pH 8.5 with NaOH. 123
- Figure 8.2:** Cyclic voltammetry (A) and corresponding transmission at 500 nm (B) of a Pt-modified ITO on glass working electrode in an electrolyte containing 120 mM Bi(NO₃)₃, 5 mM CuCl₂, 1.5 M EDTA, and 2.0 M NaI adjusted to pH 8.5 with HCl.... 126
- Figure 8.3:** Cyclic voltammetry (A) and corresponding transmission at 500 nm (B) of a Pt-modified ITO on glass working electrode in an electrolyte containing 120 mM Bi(NO₃)₂, 5 mM CuCl₂, and 1.5 M EDTA adjusted to pH 8.5 with HCl. 127

- Figure 8.4:** Cyclic voltammetry of a Pt-modified ITO on glass working electrode in an electrolyte containing 1.5 M EDTA and 2.0 M NaI adjusted to pH 8.5 with HCl. 128
- Figure 8.5:** Cyclic voltammetry (A) and corresponding transmission at 500 nm (B) of a Pt-modified ITO on glass working electrode in an electrolyte containing 5 mM CuCl₂, 1.5 M EDTA, and 2.0 M NaI adjusted to pH 8.5 with HCl. 129
- Figure 8.6:** Cyclic voltammetry (A) and corresponding transmission at 500 nm (B) of a Pt-modified ITO on glass working electrode in an electrolyte containing 120 mM Bi(NO₃)₂, 1.5 M EDTA, and 2.0 M NaI adjusted to pH 8.5 with HCl. 130
- Figure 8.7:** Scanning electron microscope images of metal electrodeposits on Pt-modified ITO on glass working electrodes electrodeposited from an electrolyte containing 120 mM Bi(NO₃)₂, 1.5 M EDTA, and 2.0 M NaI adjusted to pH 8.5 with HCl without (A, B, Solution I) and with 5 mM CuCl₂ (C, D, Solution F). Electrodeposition was performed at -0.9 V for 30 s (A, C) or 60 s (B, D). 131
- Figure 8.8:** Sheet resistances of ITO on glass substrates over time measured using a four-point probe when immersed in an electrolyte containing 5 mM BiCl₃, 15 mM CuCl₂, 10 mM HCl, and 1.0 M LiBr (red line, acidic electrolyte) and an electrolyte containing 120 mM Bi(NO₃)₂, 5 mM CuCl₂, 1.5 M EDTA, and 2.0 M NaI adjusted to pH 8.5 with HCl (black line, EDTA electrolyte, Solution F). 133
- Figure 8.9:** Photographs of a 25 cm² window containing the Bi-Cu EDTA electrolyte (Solution F) after 0 s (A), 30 s (B), and 60 s (C) of metal electrodeposition at -0.9 V. . 134
- Figure 8.10:** Contrast ratio of Pt-modified window with electrolyte solution containing 5 mM BiCl₃, 15 mM CuCl₂, 10 mM HCl, and 1.0 M LiBr (red dot, acidic electrolyte) and an electrolyte containing 120 mM Bi(NO₃)₂, 5 mM CuCl₂, 1.5 M EDTA, and 2.0 M NaI adjusted to pH 8.5 with HCl (black dot, EDTA electrolyte, Solution F). 135
- Figure 9.1:** Schematic of a dynamic window that facilitates reversible Zn electrodeposition on an ITO on glass working electrode and a Zn mesh counter electrode. 142
- Figure 9.2:** (a) Transmission of a 25 cm² dynamic window with an ITO on glass working electrode, a Zn mesh counter electrode, and a Zn acetate gel electrolyte as a function of wavelength after 0 s (black), 10 s (red), 15 s (blue), and 30 s (teal) of window tinting at -1 V. (b) Transmission of the same window at 600 nm during 30 s of metal electrodeposition at -1 V and 60 s of metal stripping at 1 V. 144
- Figure 9.3:** (a) Transmission of a 25 cm² dynamic window with an ITO on glass working electrode, a Zn counter electrode, and a Zn acetate gel electrolyte during switching. The device was switched once a week for four consecutive weeks. The window was darkened at -0.5 V for 60 s and lightened at 1 V for 120 s. (b) Contrast ratio at 600 nm of an analogous dynamic window with a Zn-Cu electrolyte over the course of 2,500 cycles. 145
- Figure 9.4:** Photographs of a 100 cm² dynamic window after (a) 0 s, (b) 10 s, and (c) 30 s of metal electrodeposition using an ITO on glass working electrode and a Zn grid counter electrode. (d) Transmission at 600 nm through the edge (green) and the center (red) of the window during switching at -1 V for 30 s followed by 1 V for 60 s. 148

- Figure 9.5. (a, b)** Transmission at 600 nm during cyclic voltammetry scanning from 2 V to -1 V to 2 V of a 25 cm² dynamic window with an ITO on glass working electrode and a Zn metal frame as the counter and reference electrodes with a 0.5 M Zn acetate gel electrolyte. The scan rate was **(a)** 5 mV/s or **(b)** 50 mV/s. The corresponding CVs are shown in Supporting Figure 12.7.5. **(c)** Schematic of the working electrode during the deposition (left) and dissolution (right) portions of the CV at the two scan rates. 151
- Figure 9.6. (a)** Cyclic voltammogram at a scan rate of 5 mV/s of a 25 cm² dynamic window with an ITO on glass working electrode and a Zn metal frame as the counter and reference electrodes with a 0.5 M Zn acetate gel electrolyte. **(b)** Percentage of ZnO (black), Zn (red), and Zn(OH)₂ (blue) on the working electrode as determined by XRD analysis after performing voltammetry at 5 mV/s from **(I)** 2 V to -0.46 V, **(II)** 2 V to -1 V, **(III)** 2 V to -1 V to 0.5 V, and **(IV)** 2 V to -1 V to 1.45 V. 152
- Figure 10.1:** Cyclic voltammograms at a scan rate of 25 mV s⁻¹ of Pt-modified ITO working electrodes in electrolytes containing 0.5 M ZnCl₂ and 0.5 M NaCH₃COO (sodium acetate, panel A, black line), NaCClH₂COO (sodium chloroacetate, ClAc, panel A, red line), NaCCl₃COO (sodium trichloroacetate, Cl₃Ac, panel a, blue line), NaFCH₂COO (sodium fluoroacetate, panel B, black line), or NaClF₂COO (sodium chlorodifluoroacetate, panel B, red line). 162
- Figure 10.2:** Coulombic efficiency and optical reversibility for Zn electrolytes containing different acetates (A) along with the transmission at 600 nm of the working electrode during the second cycle of CVs in these electrolytes (B). The corresponding CVs are displayed in Figure 1. 165
- Figure 10.3:** Cyclic voltammograms at a scan rate of 25 mV s⁻¹ of Pt-modified ITO working electrodes in electrolytes containing 0.5 M ZnCl₂ and 0.5 M sodium formate (black line), sodium propionate (red line), or sodium butyrate (blue line). 167
- Figure 10.4:** Coulombic efficiency and optical reversibility for Zn electrolytes containing different chain lengths of carboxylates (A) along with the transmission at 600 nm of the working electrode during the second cycle of CVs in these electrolytes (B). The corresponding CVs are displayed in Figure 3. 168
- Figure 10.5:** Cyclic voltammograms (A) at a scan rate of 25 mV s⁻¹ of Pt-modified ITO working electrodes in electrolytes containing 0.5 M sodium formate and 0.5 M ZnCl₂ (black line), 0.5 M ZnBr₂ (red line), or 0.25 M ZnCl₂ and 0.25 M ZnBr₂ (blue line). Coulombic efficiencies (B) of the CVs of formate and acetate electrolytes with various halide compositions. 170
- Figure 10.6:** Transmission at 600 nm of the working electrode during Zn electrodeposition (A) and stripping (B) in electrolytes containing 0.5 M sodium acetate and 0.5 M ZnCl₂ (black line), or 0.5 M sodium formate and 0.5 M ZnCl₂ (red line), 0.5 M ZnBr₂ (blue line), or 0.25 M ZnCl₂ and 0.25 M ZnBr₂ (green line). To elicit Zn electrodeposition, chronoamperometry was conducted at -1.0 V until the transmission at 600 nm reached 1%. Next, Zn stripping was conducted at +2.5 V for 30 s. 171
- Figure 10.7:** Scanning electron microscopy images of Zn electrodeposits obtained after a linear sweep voltammogram from 0 V to -1 V at 5 mV s⁻¹ in an electrolyte containing 0.5

- M sodium formate and 0.5 M ZnCl₂ (A, B), 0.5 M ZnBr₂ (C, D), or 0.25 M ZnCl₂ and 0.25 M ZnBr₂ (E, F)..... 174
- Figure 10.8:** Relative compositions of Zn and ZnO as determined by X-ray diffraction of Zn electrodeposits obtained using the conditions described in Figure 7. 175
- Figure 10.9:** Cyclic voltammogram obtained using the ZnCl₂-ZnBr₂-formate electrolyte containing 0.5 M sodium formate, 0.25 M ZnCl₂, and 0.25 M ZnBr₂ (A, black line). The experiment was halted at -0.1 V (E_{final}) during the negative sweep of the second cycle. After obtaining this voltammogram, the same working electrode was used in an electrolyte containing only 0.5 M sodium formate (A, red line). Lastly, the same working electrode was used a second time in the ZnCl₂-ZnBr₂-formate electrolyte (A, blue line). For panel B, a fresh working electrode was also first cycled in the ZnCl₂-ZnBr₂-formate electrolyte. The experiment was halted at an $E_{\text{final}} = 0$ V during the negative sweep of the second cycle. After obtaining this voltammogram, the same working electrode was used in an electrolyte containing only 0.5 M sodium formate (B, red line). Lastly, the same working electrode was used a second time in the ZnCl₂-ZnBr₂-formate electrolyte (B, blue line). 178
- Figure 10.10:** Transmission as a function of wavelength of a 25 cm² dynamic window based on reversible Zn electrodeposition after 0 s (black line), 7 s (red line), 15 s (blue line), 21 s (green line), and 30 s (purple line) of device darkening (A). Metal electrodeposition on the working electrode was elicited by applying -0.8 V for 30 s before +2.3 V was applied to induce metal stripping. The transmission at 600 nm during one cycle of switching is shown in panel B. The aqueous-based gel electrolyte used contained 0.5 M sodium formate, 0.25 M ZnCl₂, and 0.25 M ZnBr₂. 180
- Figure 10.11:** Minimum and maximum transmission values at 600 nm during cycling of a 3 cm² dynamic window based on Zn electrodeposition. The device was switched at -1 V for 5 s to induce metal electrodeposition and 1.5 V for 30 s to elicit metal stripping.... 181
- Figure 10.12:** X-ray diffraction spectrum of ITO working electrode obtained after 250 switching cycles in a dynamic window. 182
- Figure 11.1.** Schematic of a Zn²⁺ battery consisting of a peropyrene cathode and a Zn metal anode showing their nominal discharged and charged states. 188
- Figure 11.2.** Cyclic voltammetry evaluating Zn²⁺ intercalation in the peropyrene (black), a control without any nanographene (red), coronene (purple), and perylene (green) cast with Vulcan XC-72 carbon and PVDF. For panel a, the electrolyte used was 100 mM Zn(CF₃SO₃)₂ in acetonitrile, the cathode was cast on a Cu substrate, and the scan rate was 0.1 mV s⁻¹. For panel b, the electrolyte used was 100 mM Zn(ClO₄)₂ in acetonitrile, the cathode was cast on a graphite-coated stainless steel substrate, and the scan rate was 50 mV s⁻¹. The blue lines indicate voltammetry with the peropyrene using an electrolyte containing 100 mM TBACF₃SO₃ or TBAClO₄ in acetonitrile. 190
- Figure 11.3.** Energy-dispersive X-ray spectra of the peropyrene cathode cast on Cu foil in its intercalated (a) and deintercalated (b) states using an electrolyte containing Zn(CF₃SO₃)₂ in acetonitrile at a scan rate of 0.1 mV s⁻¹. 193

- Figure 11.4.** SEM images of electrodes with Vulcan XC-72 carbon, PVDF, and with (a) and without (b) the peropyrene. The yellow arrows in image a point to examples of the rod-like structures in the SEM, which are not present in image b and therefore are assigned to the peropyrene..... 193
- Figure 11.5.** Discharge (a) and charge (b) curves of a Zn-ion battery with the peropyrene cathode, a Zn metal anode, and an electrolyte containing $\text{Zn}(\text{ClO}_4)_2$ in acetonitrile. Discharge and charge rates were 100 mA g^{-1} and 500 mA g^{-1} , respectively..... 195
- Figure 11. 6.** Capacity as a function of cycle number of Zn-ion batteries with a cathode cast using Vulcan XC-72 carbon and PVDF with (black) and without (red) the peropyrene..... 195
- Figure 11.7.** Cycle voltammetry of Zn^{2+} intercalation in the peropyrene cast with Vulcan XC-72 carbon and PVDF. The electrolyte used contained $100 \text{ mM Zn}(\text{ClO}_4)_2$ in acetonitrile, and the scan rate was 50 mV s^{-1} 197
- Supporting Figure 12.1.1:** Cyclic voltammograms of ITO on glass electrodes coated with CeO_2 (A), V_2O_5 (B), and NiO (C) in the aqueous Cu-Bi electrolyte..... 199
- Supporting Figure 12.1.2:** SEM image of LiNiO_x (A) and the corresponding EDX spectrum (B), which confirms the presence of NiO and also exhibits In and Sn peaks from ITO and Si peaks from the glass. 200
- Supporting Figure 12.1.3:** Transmission of a 60-nm-thick (A) and 1- μm -thick (B) NiO film on an ITO on glass working electrode in a three-electrode cell using a 1 M LiBr electrolyte. A voltage of -0.01 V was applied for 180 s to lithiate the electrode and 0.67 V was applied for 60 s to delithiate the electrode. 200
- Supporting Figure 12.1.4:** Chronoamperometry of a 25 cm^2 dynamic window with a Pt-modified ITO on glass working electrode, a LiNiO_x on ITO on glass counter electrode formed using electrodeposition, and a Cu-Bi gel electrolyte during 60 s of metal electrodeposition at -2.5 V and 120 s of metal stripping at 0 V 201
- Supporting Figure 12.1.5:** Transmission at 600 nm of a 25 cm^2 hybrid dynamic window that was darkened to an intermediate transmission state using 15 s (black), 30 s (red), 45 s (blue), or 60 s (pink) of metal electrodeposition at -2.5 V followed by 300 s at -0.55 V to keep the window in its intermediate state (A). Representative chronoamperometry at -0.55 V (B). By calculating the average current density from the chronoamperometry, the average power density is calculated to be 2.7 W m^{-2} to keep the window in any dark state. 201
- Supporting Figure 12.1.6:** Transmission (A, B), reflection (C, D), and absorption (E, F) of a 25 cm^2 dynamic window with a Pt-modified ITO on glass working electrode, a LiNiO_x on ITO on glass counter electrode, and a Cu-Bi gel electrolyte as a function of wavelength after 0 s (black) and 60 s (red) of window tinting at -2.5 V 202
- Supporting Figure 12.1.7:** Transmission of a 25 cm^2 dynamic window with a Pt-modified ITO on glass working electrode, a LiNiO_x on ITO on glass counter electrode formed using electrodeposition, and a Cu-Bi liquid electrolyte as a function of wavelength after 0 s (black), 15 s (red), 30 s (blue), and 60 s (teal) of window tinting at -2.5 V (A). Transmission of the same window at 600 nm during 60 s of metal

electrodeposition at -2.5 V and 120 s of metal stripping at 0 V (B). Chronoamperometry of the window during switching (C).	203
Supporting Figure 12.1.8: Contrast ratio of dynamic window with a Pt-modified ITO on glass working electrode and a LiNiO _x on ITO on glass counter electrode over the course of 100 cycles.	204
Supporting Figure 12.1.9: EDX spectrum of a NiO on ITO on glass counter electrode after device cycling. The presence of Bi and Cu in the spectrum indicates that metal deposits on the counter electrode, giving rise to the visible greying of the electrode that lowers the maximum transmission of the device during cycling. Br is also present due to LiBr in the electrolyte.	204
Supporting Figure 12.1.10: SEM images of BTD on NiO on ITO on glass.	205
Supporting Figure 12.1.11: Photograph of a 25 cm ² dynamic window utilizing an unmodified ITO counter electrode. Following 10 complete cycles of -2.5V for 30 s and 0V for 60 s, the device turns yellow due to the formation of Br ₃ ⁻ in the electrolyte.	205
Supporting Figure 12.1.12: Transmission of a ITO on glass working electrode in a three-electrode cell using a 1 M LiBr electrolyte. A voltage of -0.01 V was applied for 180 s to lithiate the electrode and 0.67 V was applied for 60 s to delithiate the electrode.	206
Supporting Figure 12.1.13: Cyclic voltammograms of ITO on glass electrodes coated with NiO in the aqueous Cu-Bi electrolyte at 50 mV/s.	206
Supporting Figure 12.1.14: Transmission of a BTD-coated NiO film on an ITO on glass working electrode in a three-electrode cell using a 1 M LiBr electrolyte (A). A voltage of -0.01 V was applied for 180 s to lithiate the electrode and 0.67 V was applied for 60 s to delithiate the electrode. Cyclic voltammograms of the same electrode in the aqueous Cu-Bi electrolyte at 50 mV/s (B).	207
Supporting Figure 12.1.15: Transmission of a 25 cm ² dynamic window with a Pt-modified ITO on PET working electrode, a LiNiO _x on ITO on PET counter electrode formed using chemical bath deposition, and a Cu-Bi liquid electrolyte as a function of wavelength after 0 s (black), 60 s (red), and 120 s (blue) of window tinting at -2.5 V (A). Chronoamperometry (B) of the same window during 120 s of metal electrodeposition at -2.5 V and 180 s of metal stripping at 0 V.	207
Supporting Figure 12.1.16: Chronoamperometry of a 100 cm ² dynamic window using a voltage of -2.5 V for 60 s and 0 V for 120 s.	208
Supporting Figure 12.2.1: SEM images of a Cu ₂ O on ITO working electrode that has been soaked in 0.4 M boric acid for 100 s (A) and a linear sweep voltammogram of the same electrode in 1 M NaOH at a scan rate of 10 mV/s (B).	208
Supporting Figure 12.2.2: SEM image (A) of a Cu ₂ O on ITO electrode with a Ni overlayer formed using 100 s of Ni electrodeposition and EDS spectra taken at points B and C of the SEM image (B, C).	209
Supporting Figure 12.2.3: EDX spectrum of a Cu ₂ O on ITO electrode with a Ni overlayer formed using 500 s of Ni electrodeposition. The corresponding SEM image is shown in Figure 5F	210

Supporting Figure 12.2.4: AFM images of a Cu ₂ O on ITO electrode with a Ni overlayer formed using 100 s of Ni electrodeposition.	210
Supporting Figure 12.3.1: Transmission at 600 nm of 25 cm ² metal-based dynamic windows with two (blue) and one (red) working electrodes during switching at -0.6 V for 60 s and +0.8 V for 40 s.	213
Supporting Figure 12.3.2: Transmission at 600 nm of the center (black) and edge (red) of a 25 cm ² metal-based dynamic window with two working electrodes during switching at -1.2 V for 30 s and +0.8 V for 60 s.	214
Supporting Figure 12.3.3: Photographs of 25 cm ² metal-based dynamic windows with one (a, b) and two (c, d) working electrodes. The initially constructed windows (a, c) were cycled 10 times using -1.2 V for 30 s for metal electrodeposition and +0.8 V for 60 s for metal stripping.	215
Supporting Figure 13.3.4: Transmission at 600 nm of 25 cm ² metal-based dynamic windows with two (blue) and one (red) working electrodes during switching at -0.8 V for 60 s and +0.8 V for 60 s.	216
Supporting Figure 13.3.5: Transmission at 600 nm of 25 cm ² metal-based dynamic windows with two (blue) and one (red) working electrodes during switching at -1 V for 60 s and +0.8 V for 60 s.	216
Supporting Figure 12.3.6: Transmission at 600 nm of 25 cm ² metal-based dynamic windows with two (blue) and one (red) working electrodes during switching at -1.5 V for 60 s and +0.8 V for metal stripping.	217
Supporting Figure 12.3.7: Transmission at 600 nm of a 25 cm ² metal-based dynamic window as a function of wavelength after 0 s (black) and 30 s (red) of window darkening.	217
Supporting Figure 12.3.8: Near-infrared transmission of a 3 mm thick sample of the Bi-Cu electrolyte.	218
Supporting Figure 12.3.9: Reflection as a function of wavelength of a 25 cm ² metal-based dynamic window with one working electrode before switching (black line) and after switching at -0.6 V for 60 s (red line).	218
Supporting Figure 12.4.1. Chronoamperometry (a) and reflection (b) of a 25 cm ² dynamic window with a Pt-modified ITO on glass working electrode, a Prussian blue on ITO on glass counter electrode formed using 6 minutes of electrodeposition, and a Bi gel electrolyte during 3 s of window tinting at -2 V and 15 s of window lightening at 1.5 V.	219
Supporting Figure 12.4.2a. Energy-dispersive X-ray spectrum of Bi electrodeposition on ITO on glass. The In and Sn peaks are from ITO, and the Si peaks from the glass. .	220
Supporting 12.4.2b. Energy-dispersive X-ray spectrum of the Prussian blue electrodeposited on ITO on glass for 6 minutes. The Fe, K, N, and C peaks are from the Prussian blue. The In and Sn peaks are from ITO, and the Si peaks from the glass.	220
Supporting Figure 12.4.3. X-ray diffraction spectrum of the Prussian blue electrodeposited on ITO on glass for 6 minutes (red line) and of unmodified ITO (black line). The two peaks at 2θ values of 17.3° and 24.6° are not present in the unmodified	

ITO and are due to the (200) and (220) planes of Prussian blue, respectively, and match previous literature reports for Prussian blue thin films.[239]	221
Supporting Figure 12.4.4. Atomic force microscopy images of unmodified ITO on glass (a), Prussian blue electrodeposited for 6 minutes on ITO on glass electrodeposited (b), and the interface of Prussian blue and unmodified ITO (c). Panel d displays the height profile across the line drawn across the Prussian blue-ITO interface in panel c. The height profile indicates that Prussian blue thin film is ~150 nm thick.	222
Supporting Figure 12.4.5. Chronoamperometry (a) and transmission at 700 nm (b) of a 25 cm ² dynamic window with a Pt-modified ITO on glass working electrode, a Prussian blue on ITO on glass counter electrode formed using 1 minute of electrodeposition, and a Bi gel electrolyte during 3 s of window tinting at -2 V and 3 s of window lightening at 1.5 V.....	223
Supporting Figure 12.4.6. Chronoamperometry (a) and transmission at 700 nm (b) of a 25 cm ² dynamic window with a Pt-modified ITO on glass working electrode, a Prussian blue on ITO on glass counter electrode formed using 10 minutes of electrodeposition, and a Bi gel electrolyte during 3 s of window tinting at -2 V and 9 s of window lightening at 1.5 V.....	223
Supporting Figure 12.4.7. Photographs of a 2 cm ² with a Pt-modified ITO on glass working electrode, a Prussian blue on ITO on glass counter electrode formed using 6 minutes of electrodeposition switching at -2 V for 0 s (a) and 3 s (b) in a liquid Bi electrolyte.....	224
Supporting Figure 12.4.8. Cyclic voltammograms (a) and corresponding transmission at 700 nm (b) of Prussian blue on ITO on glass working electrode in the Bi-Cu electrolyte in a three-electrode cell at a scan rate of 5 mV/s.	224
Supporting Figure 12.5.1: Energy-dispersive X-ray spectrum of a CoHCF on ITO on glass. The In peaks are from ITO, and the Si peaks are from the glass.....	225
Supporting Figure 12.5.2. X-ray diffraction spectrum of the CoHCF on ITO on glass. The four peaks at 2 θ values of 17.4°, 24.6°, 35.1°, and 39.3° are due to the (200), (022), (004), and (042) planes of CoHCF respectively, which match previous literature reports for CoHCF thin films. [110]	225
Supporting Figure 12.5.3: Atomic force microscopy images of unmodified ITO on glass (a), CoHCF on ITO spin-coated at 1500 rpm (b), and the interface of CoHCF and unmodified ITO (c). Panel (d) displays the height profile across the line drawn on the CoHCF-ITO interface in panel (c). The height profile indicates that CoHCF film is ~3.5 μ m thick.	226
Supporting Figure 12.5.4: Transmission at 500 nm (a) and chronoamperometry (b) of 3 cm ² dynamic windows with Pt-modified ITO on glass working electrode, a CoHCF on ITO on glass counter electrode formed using Bi-Cu-NaBr liquid electrolytes during 60 s of window clearing at 0 V and 60 s of window tinting at 1.0 V.....	227
Supporting Figure 12.5.5: Transmission of 3 cm ² dynamic windows with Pt-modified ITO on glass working electrode, a CoHCF on ITO on glass counter electrode at 1200 rpm	

(a), 1500 rpm (b), and 1800 rpm (c) formed using Bi-Cu-NaBr liquid electrolytes during 50 s of window clearing at 0 V and 50 s of window tinting at 1.0 V.	228
Supporting Figure 12.5.6: Photographs of a 3 cm ² CoHCF on ITO on glass working electrode, Pt-wire counter electrode, and a Ag/AgCl reference electrode switching at -0.75 V for 0 s (a) and 30 s (b) in a liquid 1M NaBr electrolyte.....	229
Supporting Figure 12.5.7: Photographs of a 3 cm ² dynamic window with a Pt-modified ITO on glass working electrode, a Na-ion intercalated CoHCF on ITO on glass counter electrode switching at -2.5 V for 0 s (a) and 10 s (b) in a liquid Bi-Cu-NaBr electrolyte.	229
Supporting Figure 12.5.8: Transmission at 500 nm (a) and chronoamperometry (b) of 3 cm ² dynamic windows with Pt-modified ITO on glass working electrode, a CoHCF on ITO on glass counter electrode formed using Bi-Cu-NaBr liquid electrolytes during 70 s of window clearing at 0 V and 70 s of window tinting at 1.0 V.....	230
Figure 12.6.1: Energy-dispersive X-ray spectra of metal electrodeposits on Pt-modified ITO on glass working electrodes electrodeposited from an electrolyte containing 120 mM Bi(NO ₃) ₂ , 1.5 M EDTA, and 2.0 M NaI adjusted to pH 8.5 with HCl without (A, B, Solution I) and with 5 mM CuCl ₂ (C, D, Solution F). Electrodeposition was performed at -0.9 V for 30 s (A, C) or 60 s (B, D). The corresponding scanning electron microscopy images are displayed in Figure 7 in the main text.	231
Figure 12.6.2: Transmission at 500 nm of a 25 cm ² dynamic window using the EDTA Bi-Cu electrolyte (Solution F) during six cycles of chronoamperometry at -0.9 V for 40 s followed by +0.8 V for 120 s after resting at open circuit potential for 0 (A), 1 (B), 2 (C), 3 (D), 4 (E), 5 (F), 6 (G), and 7 (H) days. The data points in Figure 10 in the main text are derived by taking the average contrast ratios across each six cycles for each day.	232
Figure 12.6.3: Transmission at 500 nm of a 25 cm ² dynamic window using the acidic Bi-Cu electrolyte during six cycles of chronoamperometry at -0.6 V for 60 s followed by +0.8 V for 120 s after resting at open circuit potential for 0 (A), 1 (B), 2 (C), 3 (D), 4 (E), 5 (F), 6 (G), and 7 (H) days. The data points in Figure 10 in the main text are derived by taking the average contrast ratios across each six cycles after 0-5 days of rest. Because the transmission of the window on after six days of rest was irreversible after the first cycle, the contrast ratio plotted in Figure 10 (red point) for the sixth day is equal to the contrast during the first cycle.....	234
Figure 12.7.1: La*b*C* values along with the best RGB color representations of the transmission of a 25 cm ² dynamic window with an ITO on glass working electrode, a Zn mesh counter electrode, and a Zn acetate gel electrode during window darkening.	235
Figure 12.7.2: SEM image (a) and corresponding EDX spectrum (b) of an ITO working electrode after the application of -1V in a dynamic window. Peaks for In are due to the presence of ITO.....	236
Figure 12.7.3: Transmission of a 25 cm ² dynamic window with an ITO on glass working electrode, a Cu counter electrode, and an acidic Bi-Cu gel electrolyte during switching. The device was switched at week 0 and week 1. The window was darkened at -0.6 V for 60 s and lightened at +0.8 V for 120 s.	236

- Figure 12.7.4:** (a) Contrast ratio at 600 nm of a 25 cm² dynamic window with an ITO on glass working electrode, a Zn counter electrode, and a Zn acetate gel electrolyte during cycling over the course of 250 cycles. (b) XRD spectrum of the ITO working electrode after 250 cycles showing the accumulation of ZnO and Zn(OH)₂..... 237
- Figure 12.7.5:** Cyclic voltammograms at a scan rate of 5 mV/s (black) and 50 mV/s (red) of a 25 cm² dynamic window with an ITO on glass working electrode and a Zn metal frame as the counter and reference electrodes with a 0.5 M Zn acetate gel electrolyte. 237
- Figure 12.7.6:** Compositional analysis obtained from XRD measurements of dynamic windows with an ITO on glass working electrode and a Zn frame as the counter and reference electrodes with a 0.5 M Zn acetate gel electrolyte. XRD data were obtained after performing LSVs at 5 mV/s or 50 mV/s from 2 V to -1 V..... 238
- Figure 12.7.7:** XRD spectrum of the working electrode of a dynamic window with an ITO on glass working electrode, a Zn metal counter/reference electrode, and 0.5 M Zn acetate gel electrolyte after linear sweep voltammetry at 25 mV/s from 2 V to -1 V (a). The electrolytes were bubbled with O₂ (red line) or Ar (green line) for 1 hr before performing the voltammetry. Compositional analysis from the XRD spectra (b). 238
- Figure 12.7.8:** XRD spectra of a dynamic window with an ITO on glass working electrode, a Zn metal counter/reference electrode, and a 0.5 M Zn acetate gel electrolyte after voltammetry at 5 mV/s from (a) 2 V to -0.46 V (b) 2 V to -1 V (c) 2 V to -1 V to 0.5 V (d) 2 V to -1 V to 1.45 V..... 239
- Figure 12.7.9:** (a) XRD spectrum of the working electrode of a dynamic window with an ITO on glass working electrode, a Zn metal counter/reference electrode, and a 0.5 M Zn acetate gel electrolyte after chronoamperometry at -1 V for 15 s. (b) Percentage of Zn, ZnO, and Zn(OH)₂ during of the electrodeposits as determined from the XRD spectrum. 240
- Figure 12.8.1:** Cyclic voltammogram at a scan rate of 25 mV s⁻¹ of Pt-modified ITO working electrodes in electrolytes containing 0.5 M sodium acetate and 0.5 M ZnBr₂ (black line) or 0.25 M ZnCl₂ and 0.25 M ZnBr₂..... 240
- Figure 12.8.2:** Cyclic voltammogram at a scan rate of 25 mV s⁻¹ of a Pt-modified ITO working electrode in an electrolyte containing 0.5 M ZnI₂ and 0.5 M sodium acetate. . 241
- Figure 12.8.3:** Transmission at 600 nm of the working electrode during the second cycle of CVs in an electrolyte containing 0.5 M sodium acetate and 0.5 M ZnI₂ (black line) or ZnBr₂ (red line). The corresponding CVs are displayed in Supporting Figure 12.8.1 and 12.8.2..... 241
- Figure 12.8.4:** Chronoamperometry during Zn electrodeposition and stripping in electrolytes containing 0.5 M sodium acetate and 0.5 M ZnCl₂ (black line), or 0.5 M sodium formate and 0.5 M ZnCl₂ (red line), 0.5 M ZnBr₂ (blue line), or 0.25 M ZnCl₂ and 0.25 M ZnBr₂ (green line). To elicit Zn electrodeposition, chronoamperometry was conducted at -1.0 V until the transmission at 600 nm reached 1%. Next, Zn stripping was conducted at +2.5 V. 242
- Figure 12.8.5:** Representative X-ray diffraction spectra of Zn electrodeposits obtained after a linear sweep voltammogram from 0 V to -1 V at 5 mV s⁻¹ in an electrolyte

containing 0.5 M sodium formate and 0.5 M ZnCl_2 (A), 0.5 M ZnBr_2 (B), or 0.25 M ZnCl_2 and 0.25 M ZnBr_2 (C)..... 243

Figure 12.8.6: Chronoamperometry during switching of 25 cm^2 dynamic window based on reversible Zn electrodeposition. Metal electrodeposition on the working electrode was elicited by applying -0.8 V for 30 s before $+2.3 \text{ V}$ was applied to induce metal stripping. 244

Figure 12.9.1: Cyclic voltammetry at 50 mV s^{-1} of the peropyrene cathode cast on Cu foil in an electrolyte containing 100 mM $\text{Zn}(\text{ClO}_4)_2$ in acetonitrile. The large anodic peaks for all of the electrodes tested is due to the oxidation of the Cu substrate in this electrolyte. On a bare Cu electrode, this same oxidative current is not seen with 100 mM $\text{Zn}(\text{CF}_3\text{SO}_3)_2$ under a wide range of scan rates. The reason why Cu stripping occurs in $\text{Zn}(\text{ClO}_4)_2$, but not $\text{Zn}(\text{CF}_3\text{SO}_3)_2$ is not entirely clear, but it could be due to the differing solvation properties of Zn^{2+} in these two electrolytes. As described in the main text, Zn^{2+} in $\text{Zn}(\text{CF}_3\text{SO}_3)_2$ in acetonitrile is known to be highly solvated compared to $\text{Zn}(\text{ClO}_4)_2$. We hypothesize that it is the Lewis acidity of Zn^{2+} , when less solvated in the form of $\text{Zn}(\text{ClO}_4)_2$, that catalyzes the anodic dissolution of Cu. Regardless of the origin of these differences, it is clear from Figure 2b that stainless steel is a more suitable substrate for the preparation of cathode materials to be evaluated in the $\text{Zn}(\text{ClO}_4)_2$ in acetonitrile electrolyte..... 245

Figure 12.9.2: Discharge (a) and charge (b) curves of a Zn-ion battery with the peropyrene cathode, a Zn metal anode, and an electrolyte containing $\text{Zn}(\text{ClO}_4)_2$ in acetonitrile. Discharge and charge rates were 100 mA g^{-1} and 500 mA g^{-1} , respectively. 246

Figure 12.9.3: Coulombic efficiency, defined as the capacity during discharge divided by the capacity during charge, of a Zn-ion battery with the peropyrene cathode, a Zn metal anode, and an electrolyte containing $\text{Zn}(\text{ClO}_4)_2$ in acetonitrile during cycling..... 246

Figure 12.9.4: Discharge (a) and charge (b) curves of a Zn-ion battery using a cathode with Vulcan XC-72 and peropyrene without peropyrene, a Zn metal anode, and an electrolyte containing $\text{Zn}(\text{ClO}_4)_2$ in acetonitrile. Discharge and charge rates were 100 mA g^{-1} and 500 mA g^{-1} , respectively. 247

Chapter 1: Introduction

As a result of rapid population growth on Earth, global energy demand has increased substantially. Because of industrial and technological advances in the 21st century, the per capita energy consumption dramatically grew from 1990-2000 in the U.S. and developed countries (Figure 1A). [1, 2] Most of the countries in the world are still using fossil fuel as their main sources of energy supply. A study from the U.S. Energy Information Administration (EIA) in 2019 showed that 88% of the total U.S. energy supply comes from nonrenewable energy sources such as petroleum, natural gas, coal, and nuclear, and only 11% of energy comes from renewable sources such as solar, wind, geothermal, and biofuel (Figure 1B). The vast use of nonrenewable energy sources is mostly responsible for the emission of greenhouse gases (GHGs). [3]

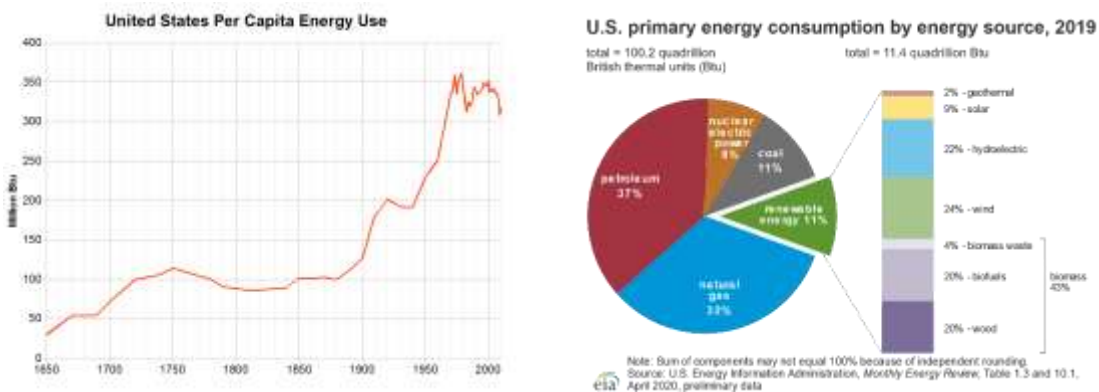


Figure 1.1: Per capita energy consumption in the U.S. from 1650 to 2000 (a) [2], Energy consumption sources in the U.S. (b). [3]

In the U.S., burning of fossil fuels is responsible for 74% of total CO₂ emissions and 92% of total anthropogenic GHGs emission (Figure 2A). There are other

important GHGs such as methane (10% of total GHG), which originates from landfills, coal mining, and agriculture and nitrous oxide (7% of total GHG), mainly coming from nitrogen-based fertilizer (Figure 2). [4]

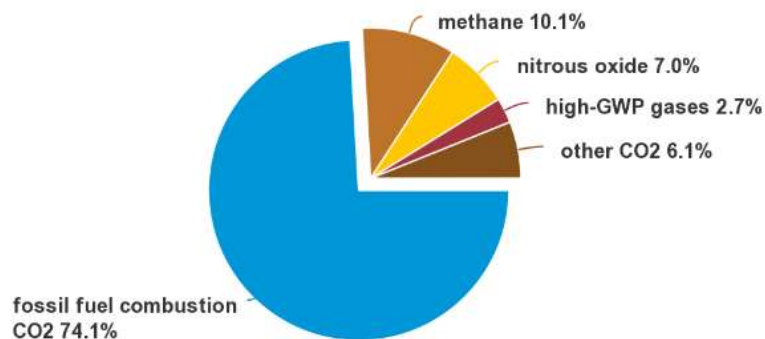


Figure 1.2: Pie chart of greenhouse gases (GHGs) emissions in the U.S. [4]

According to the National Aeronautics and Space Administration (NASA), the current level of CO₂ in Earth's atmosphere is higher than it was in the last 800,000 years (Figure 3). The CO₂ level in the atmosphere is ~416 ppm, and the trend is still sharply increasing (Figure 1). If fossil fuels continue to be burned at this rate, the level of CO₂ will reach ~1500 ppm over the next few centuries. This increase in CO₂ will cause further increases in the global temperature, melting of polar ice caps, and a considerable part of the Earth will go below sea level. [5, 6]

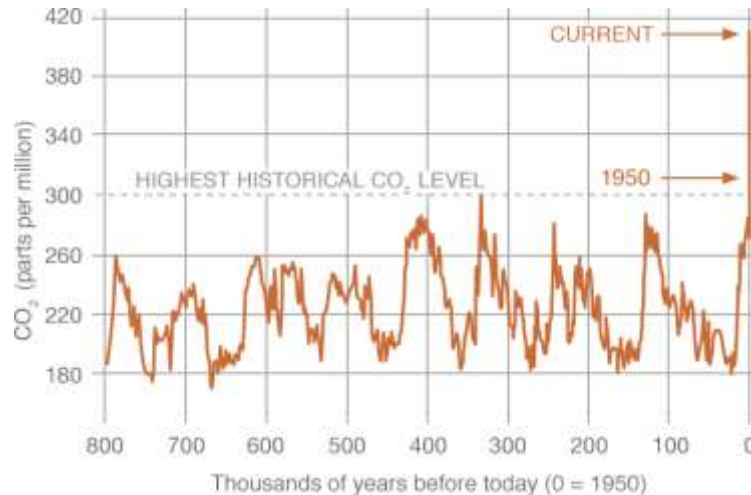


Figure 1.3: Change of global CO₂ level over last 800,000 years. [6]

Scientists and researchers are exploring different ways to mitigate climate change caused by GHGs such as:

- i) Renewable energy production
- ii) Negative CO₂ emissions
- iii) Electrochemical synthesis of fuels and other products
- iv) Energy storage
- v) Energy efficiency

According to Climate Watch U.S., China, and EU countries (including UK) are responsible for half of the global GHGs emissions (Figure 4). The majority of these GHGs emissions are the result of burning fossil fuels for energy supply. China has announced its plan to become a carbon-neutral country by 2060. The U.S., UK, and EU countries are also pushing goals for achieving carbon neutrality. Renewable energy production at a large scale is critical to avoid burning fossil fuels. As a result of modern

scientific and technological advances, the prices of solar and wind energy have reached the lowest in history and are expected to further decrease in the future. [7, 8]

Additionally, the electrification of vehicles is gaining popularity and becoming cheaper because of advanced battery research. The EU aims to ban new gasoline cars in 2035 and completely shift to electric vehicles. As a result, many countries are moving toward the goal of total renewable energy production. [9, 10]

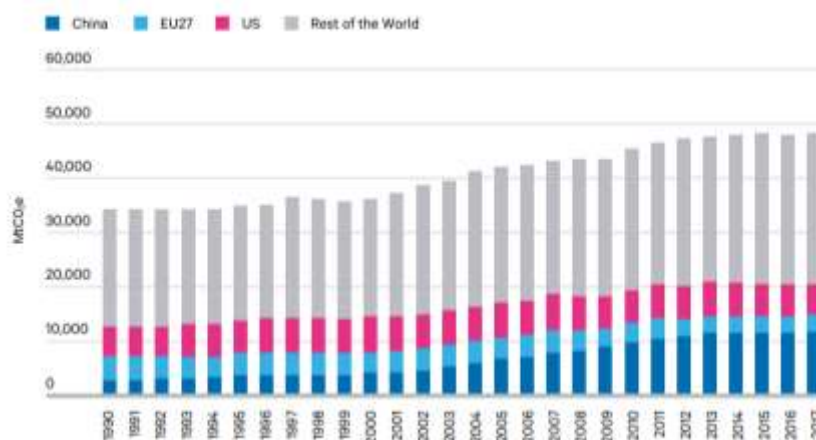


Figure 1.4: Global CO₂ gas emissions[7]

Actively removing GHGs from the air through what has been termed “negative carbon emissions” is another strategy to mitigate climate change. GHGs can be removed through the electrochemical reduction of CO₂ or through capture and storage of industrial waste gases. Electrochemical reduction of CO₂ into a valuable product is a long-standing goal for scientific society to complete the anthropogenic carbon cycle. [11, 12] CO₂ is a fully oxidized molecule and electrochemically stable, which makes it hard to activate. It

requires a significant energy barrier to overcome (-1.9 V vs. SHE), and multi-electron and proton exchange during the reduction process makes it extremely complicated. [13] Specific adsorption of CO₂ gas on the electrode surface and controlling electron and proton exchange is key to designing an efficient CO₂ reduction catalyst. As a result of the lower price of renewable electricity, electrochemical reduction of CO₂ is becoming promising and commercially viable besides CO₂ capture and storage (Figure 5). [11-14]

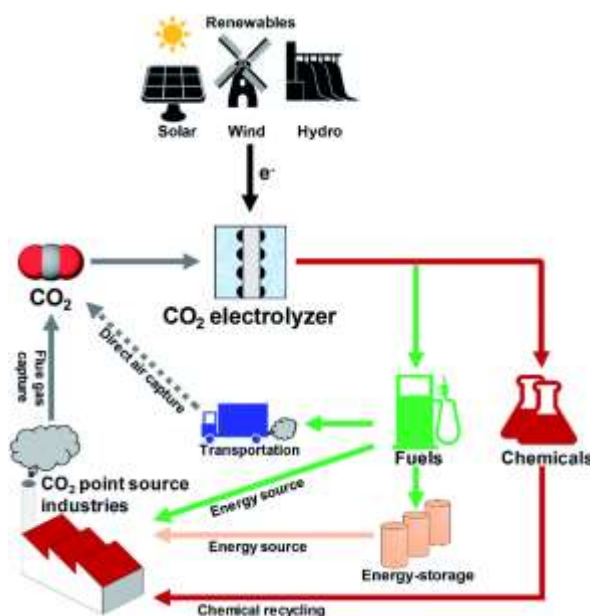


Figure 1.5: Diagram for electrochemical reduction of CO₂. [12]

Traditionally, most chemical syntheses use high temperature and pressure in chemical industries as a driving force for reactions. For example, synthesis of ammonia from N₂ and H₂ requires high temperatures (~500 °C) and pressures (300 bar). These inefficient and high energy-consuming chemical reactions are responsible for a large amount of GHGs emissions. As a result of cheap and reliable renewable energy supply,

electrochemical-driven chemical synthesis is promising to mitigate climate change. For example, if a chemical reaction is endothermic and needs higher pressure as a driving force, considering a voltage-driven process can be promising. Manthiram et al. showed that instead of using higher temperature and pressure one can produce ammonia from electrochemical reaction of H_2O and N_2 at room temperature and ambient pressure. [15-17]

For the transformation of fossil fuel to carbon free energy sources, renewable energy is integrated into the grid. This transition can only be achieved by developing cheap, reliable, and higher energy density grid-scale rechargeable batteries. For example, solar energy can only be obtained at daytime and does not alone fulfill the continuous demand for energy. [18-20] Li-ion batteries (LIBs) dominate the rechargeable battery market and have contributed to the revolution of personal electronic materials and electric cars. LIBs sales increased by an average of 16% per year from 1996 to 2016. In 2016, the market values of LIBs were more than \$20 billion, and it is predicted to reach \$40 billion in 2025. This sharp increase in demand of LIBs is mainly caused by EVs that use LIBs. [21] Although Li-ion battery price has declined ~8 % annually in the last decade, it is near its fundamental limit in terms of energy density. Moreover, some critical supply of Li-ion battery materials come from certain countries that put the supply chain at risk. For example, ~60 % of the global Co supply comes from the Republic of Congo, which is not a politically stable country and is accused of human rights' violations associated with mining. [22-24] To solve this problem, researchers are developing next-generation energy storage technologies such as multivalent batteries. Multivalent batteries such as Mg, Zn, or Al possess five to ten times higher energy density than Li-ion batteries. [25-29]

Increasing energy efficiency is another great way to mitigate CO₂ emissions. The cleanest energy is the energy which is not used in the first place. [30, 31] In the modern era, everything from light bulbs to cars are becoming more energy efficient. Buildings are responsible for huge sources of energy consumption, and the most energy inefficient part of buildings is windows. [32] In the U.S., buildings are responsible for 41% of total energy demand. Residential and commercial buildings are responsible for almost an equal share of energy consumption. In many modern buildings, particularly skyscrapers, the exterior surfaces of the buildings are almost completely covered by glass to access more natural light and view. Although the use of large amounts of glass is aesthetically beautiful, it is not energy efficient. For example, during summer time, a huge amount of heat is trapped inside the building that requires more air conditioning. In contrast, heat escaping through the glass during winter time requires heating energy costs.

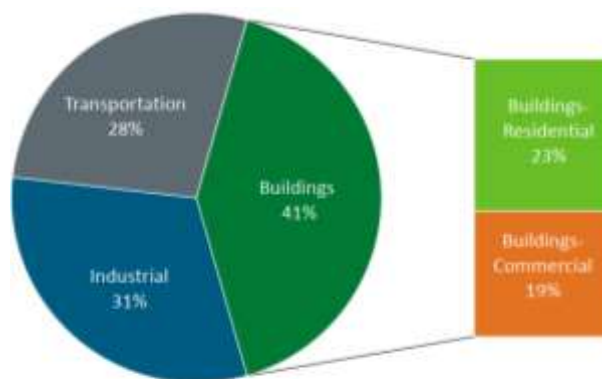


Figure 1.6: Pie chart showing energy consumption in the U.S.A. [33]

Moreover, when the sun shines directly through the building, users must block the outside view using blinds, which hinders view and increases lighting costs. [33] A dynamic window which can control opacity and heat flow of the building electronically can increase building energy efficiency by decreasing its lighting, heating, and cooling costs. A study conducted by the EIA showed that incorporating dynamic windows in a building can save about 10-15% of energy compared with low-emissivity static windows. [34] Most of dynamic window technologies in the market are electrochromic materials, the most common of which are based on transition metal oxides. As a result of their high cost, electrochromic-based dynamic windows are not commercially successful yet. According to the DOE, the cost per foot² of dynamic windows should be around ~8 USD before they will be widely adopted in buildings. The actual cost of the dynamic windows is currently around 50-100 USD per foot². [33, 35]

Reversible metal electrodeposition (RME) is a promising and underexplored technology for the application of dynamic windows, which can decrease the cost of dynamic windows and improve their performance. In RME, relatively cheap and stable metals like Cu, Bi, and Zn are electrodeposited on a transparent conductive electrode (TCE) from metal ions by the application of a negative potential. Uniform metal electrodeposition on the TCE causes the windows to become dark. By switching the polarity of the potential, the deposited metal dissolves back to its ionic form and makes the window dark to clear. To counter the reaction occurring on the TCE, a metal frame or grid, or an ion storage layer-based counter electrode undergoes a reversible reaction to balance the charge transfer. [36-38] RME-based dynamic windows have several important advantages over traditional electrochromic based dynamic windows. Firstly,

metals have superior light modulation properties than metal oxides. To block all visible and near-IR radiation, metals only need to be 20-30 nm thick, compared with electrochromic metal oxides, which require 100-1000 nm of material to block the same amount of light. [39, 40] Secondly, RME-based dynamic windows use aqueous electrolyte. Water is the cheapest and cleanest solvent source. In contrast, electrochromic-based dynamic windows use non-aqueous electrolytes, which further increases the cost of the device. [36, 41] Thirdly, RME-based dynamic windows do not need to any pre-deposited thin film (except those used to form the TCE) and use inexpensive electrodeposition techniques while switching the device. On the other hand, electrochromic-based dynamic windows often use expensive physical vapor deposition techniques for electrochromic metal oxide deposition, which further increases the cost of the device. [36, 37, 40]

This dissertation discusses intercalation-based counter electrodes and the design strategy of pH-neutral aqueous electrolytes for dynamic windows based on reversible metal electrodeposition.

Chapter 2: Hybrid Dynamic Windows using Reversible Metal Electrodeposition and Ion Insertion

2.1. Introduction:

Dynamic windows, which possess electronically controlled tinting, increase both the energy efficiency and aesthetics of interior spaces in buildings and automobiles. In buildings, dynamic windows enable lighting, heating, ventilation, and air conditioning (HVAC) energy savings that lead to an average reduction of 10% in energy consumption compared to static low-emissivity windows. [32] In automobiles, dynamic windows also lead to significant HVAC savings, which is particularly important in extending the driving range of battery-powered electric vehicles. [42]

Over the past several decades, researchers have explored numerous dynamic window technologies. The majority of this research has focused on electrochromic materials such as transition metal oxides, polymers, and small organic molecules, which change color upon application of a voltage. [43-46] It is difficult using these approaches, however, to simultaneously exhibit the fast switching times, color-neutral tinting, long-term durability, and low cost needed to achieve widespread commercialization. [47]

Recently, we started to explore reversible metal electrodeposition as a promising alternative to traditional electrochromic materials for dynamic windows. These windows possess minute-long switching times, a color-neutral opaque state, cycle thousands of times without significant degradation, and represent a substantial improvement upon previous metal-based dynamic windows. [40] Dynamic windows using reversible metal electrodeposition function via the reversible electrochemical movement of metal between two electrodes. The electrolyte of these windows contains a colorless salt containing

metal cations. Upon switching the device to the opaque state, electrochemical reduction of the metal cations to a solid thin film of elemental metal occurs at a transparent conducting cathode such as tin-doped indium oxide (ITO) on glass. Pt nanoparticles appended to the ITO substrate via a self-assembled monolayer (SAM) serve as metal nucleation sites that allow metals to electrodeposit uniformly across 25 cm^2 electrodes. [48] Oxidation of a metal anode hidden behind the frame of the window balances the cathodic reaction.

A number of properties of metals make them excellent materials for use in dynamic windows. First, the high extinction coefficient of metals causes them to almost completely block visible and infrared light at thicknesses of 20-30 nm. [39] By comparison, thin films of electrochromic materials are usually 100-1000 nm thick, which increases materials and deposition costs. [45, 49] Furthermore, many metals are color neutral in their opaque state as opposed to WO_3 , the most common electrochromic material, which is blue when dark. [50] In addition, most metals are chemically inert, photostable, and can be electrodeposited from inexpensive and nontoxic aqueous electrolytes. [51, 52]

Despite these numerous promising attributes, the main challenge hindering the progress of metal-based dynamic windows is that it is difficult to electrodeposit metals uniformly over the meter-long dimensions required for practical windows. This difficulty arises in part from the fact that metal ions must diffuse laterally across great distances from the counter electrode frame to the center of the window during electrodeposition (Figure 1a). With this diffusion requirement, metal will preferentially electrodeposit on

the edges of large-scale windows, or the switching speed of the window will have to be significantly decreased to achieve uniform tinting.

One strategy to reduce the ion diffusion lengths in metal-based dynamic windows is to incorporate a metal mesh counter electrode. [37] In this architecture, metal ions are removed from the metal mesh and electroplated onto the transparent conducting working electrode during window tinting. To ensure adequate transparency and minimize haze and diffraction patterns, the mesh lines must have a thickness of $\sim 10\ \mu\text{m}$ and a pitch of several hundred microns. [53] As the windows cycle, the mesh lines must grow and contract uniformly during device lightening and darkening, respectively. Furthermore, the dimensions of the initial mesh lines fabricated may limit the minimum achievable transmission of the devices.

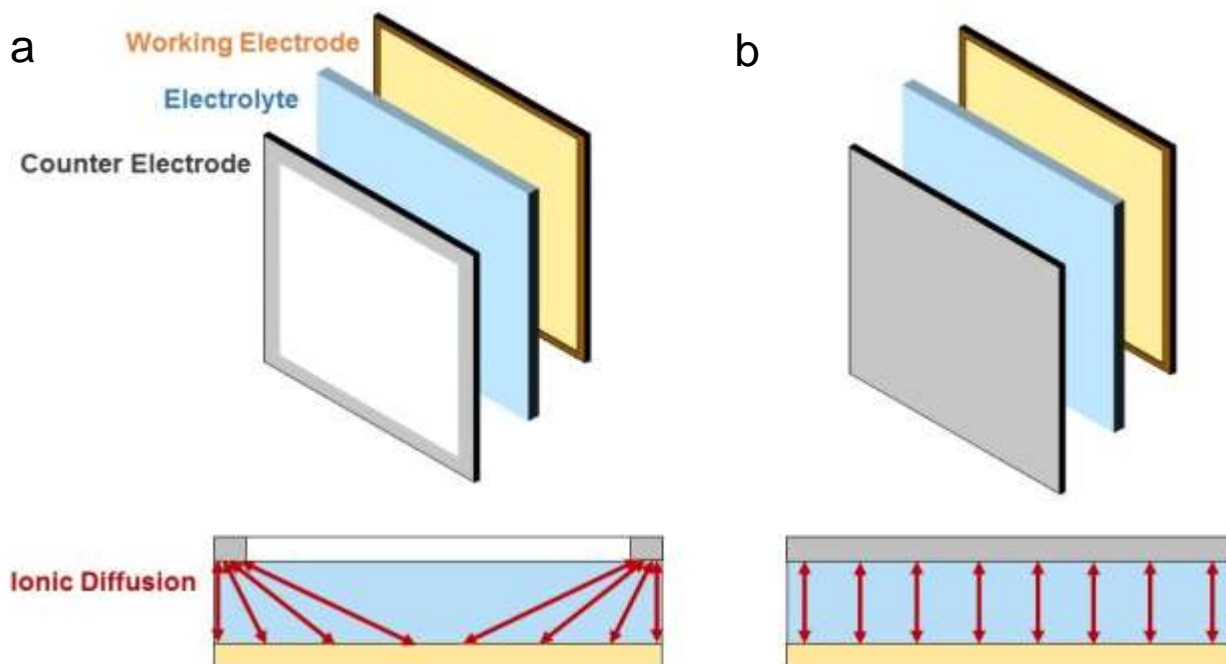


Figure 2.1: Metal-based Dynamic Window Architectures. Schematic of reversible metal electrodeposition device architectures (expanded view at the top and side view at the bottom) with (a) a metal frame around the device perimeter, which requires lateral metal ion diffusion to the center of the window, and (b) a plane-parallel counter electrode, which maintains constant transverse ion diffusion regardless of scale.

To circumvent the complications arising from a metal mesh counter electrode, here we develop metal-based dynamic windows that harness a plane-parallel NiO counter electrode that facilitates transverse ion diffusion (Figure 1b) via the insertion of Li ions. We demonstrate that both the metal-based working electrode and the NiO counter electrode in these second-generation hybrid windows switch rapidly and uniformly between colorless and color-neutral opaque states. Additionally, these hybrid windows are compatible with flexible substrates, cycle at least 4,000 times without degradation, and switch uniformly on the 100 cm² scale with an optical contrast of ~65% in one minute.

2.2. Results and Discussion:

2.2.1. Selecting a Compatible Metal Oxide Counter Electrode

Previously, we developed an aqueous electrolyte containing Cu and Bi that supports rapid and reversible electrodeposition and enables devices to switch between transparent and color-neutral opaque states. [36] To construct a dynamic window that combines this metal-based electrolyte with a traditional insertion-based counter electrode found in electrochromic devices, we first needed to select a counter electrode material that is compatible with the Cu-Bi electrolyte. We evaluated three different metal oxides for use in the counter electrode that are known to intercalate Li⁺ in conventional electrochromic windows. [45, 54] Using cyclic voltammetry, we assessed the durability of NiO, V₂O₅, and CeO₂ in the Cu-Bi electrolyte, which also contains a high concentration of LiBr that allows for Li⁺ insertion. The voltammograms show that a thin film of CeO₂ degrades significantly within a few cycles of lithiation and delithiation

(Supporting Figure 12.1a). A thin film of V_2O_5 is more stable, but still degrades substantially after 30 cycles (Supporting Figure 12.1.1b). In contrast, we find that thin films of NiO are stable with respect to lithiation and delithiation in the acidic (pH \sim 2) Cu-Bi electrolyte for at least 1,000 cycles (Supporting Figure 12.1.1c). It is known that oxides with less electronegative elements are more basic, which renders them less stable in the presence of acid.[55] The electronegativity of Ni, V, and Ce follows the trend Ni > V > Ce, which directly correlates to the order of the durability of the oxides in the Cu-Bi electrolyte.

2.2.2. 25 cm² Hybrid Dynamic Windows using Reversible Metal Electrodeposition and NiO

Having determined that NiO thin films are compatible with the Cu-Bi electrolyte, we constructed 25 cm² dynamic windows using ITO on glass modified with a SAM of Pt nanoparticles as the working electrode and an ITO on glass counter electrode coated with LiNiO_x formed via electrodeposition. The \sim 200 nm-thick LiNiO_x films are porous (see SEM-EDX data in Supporting Figure 12.1.2), allowing for rapid and sufficient Li⁺ insertion. Thinner or thicker films produced less than optimal optical properties (Supporting Figure 12.1.3). These windows possess initial transparencies of about 65-75% across the visible spectrum (Figure 12.1.2A, black line). This initial visible transparency is comparable to standard low-emissivity glass windows and higher than currently commercialized dynamic windows. [56] Upon applying -2.5 V to a device, the transmission of the window decreases to about 6% within 60 s and returns to its original transparency within 90 s when the voltage is switched to 0 V (Figure 12.1.2b and

Supporting Figure 12.1.4). The differences in cell potentials between the working and counter electrodes when the window is in its dark state establish a nonzero open circuit potential, which allows for switching the device to clear to occur at 0 V. Importantly, after tinting the device using -2.5 V, the device can be held at any desired intermediate transparency by applying a voltage of -0.55 V, and the average amount of power required to keep the device at any tinted state is very low (2.7 W m^{-2} , Supporting Figure 12.1.5). Moreover, the transmission profile during switching is relatively flat over the visible part of the spectrum, which gives rise to an aesthetically-pleasing clear-to-grey-to-black transition. Furthermore, the transmission spectra demonstrate that the windows also effectively modulate infrared light (Supporting Figure 12.1.6), which makes them useful for controlling the flow of heat in and out of spaces such as buildings and automobiles. Although smooth metal films have a mirror appearance, the windows appear black in their opaque state due to the morphology of the metal electrodeposits. [36] The electrodeposits consist of rough features on the nanometer scale, which by broadening plasmon absorption and promoting light trapping enhance absorption relative to reflection and result in a black opaque state. The performance of the windows using either a Cu-Bi liquid electrolyte (Supporting Figure 12.1.7) or a Cu-Bi gel-like electrolyte (Figure 2) that contains hydroxyethylcellulose to increase solution viscosity ($9.5 \text{ Pa}\cdot\text{s}$) is similar, which is important because a viscous electrolyte is needed to manufacture practical, well-sealed dynamics windows.

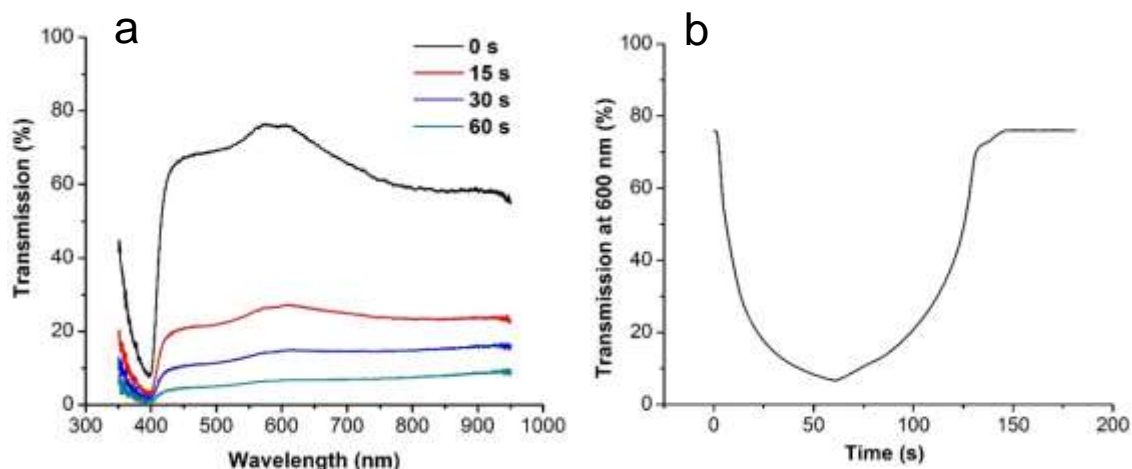


Figure 2.2. Transmission Profile of 25 cm² Hybrid Dynamic Window. a,

Transmission of a 25 cm² dynamic window with a Pt-modified ITO on glass working electrode, a LiNiO_x on ITO on glass counter electrode formed using electrodeposition, and a Cu-Bi gel electrolyte as a function of wavelength after 0 s (black), 15 s (red), 30 s (blue), and 60 s (teal) of window tinting at -2.5 V. **b,** Transmission of the same window at 600 nm during 60 s of metal electrodeposition at -2.5 V and 120 s of metal stripping at 0 V.

We next assessed the durability of metal-based NiO hybrid dynamic windows. Supporting Figure 12.1.8 illustrates that the difference between the maximum and minimum transmission of a device during switching degrades over the course of 100 cycles from about 75% to about 60% due to side reactions of metal electrodeposition occurring on the counter electrode. During cycling, the transparency of the NiO-coated ITO counter electrode decreases, and the electrode visibly greys. When 0 V is applied to turn the window clear, lithiation of NiO occurs on the counter electrode, but some Cu and Bi electrodeposition also occurs on top of the NiO as evidenced by SEM-EDX analysis (Supporting Figure 12.1.9), which diminishes the maximum transparency of the window during cycling.

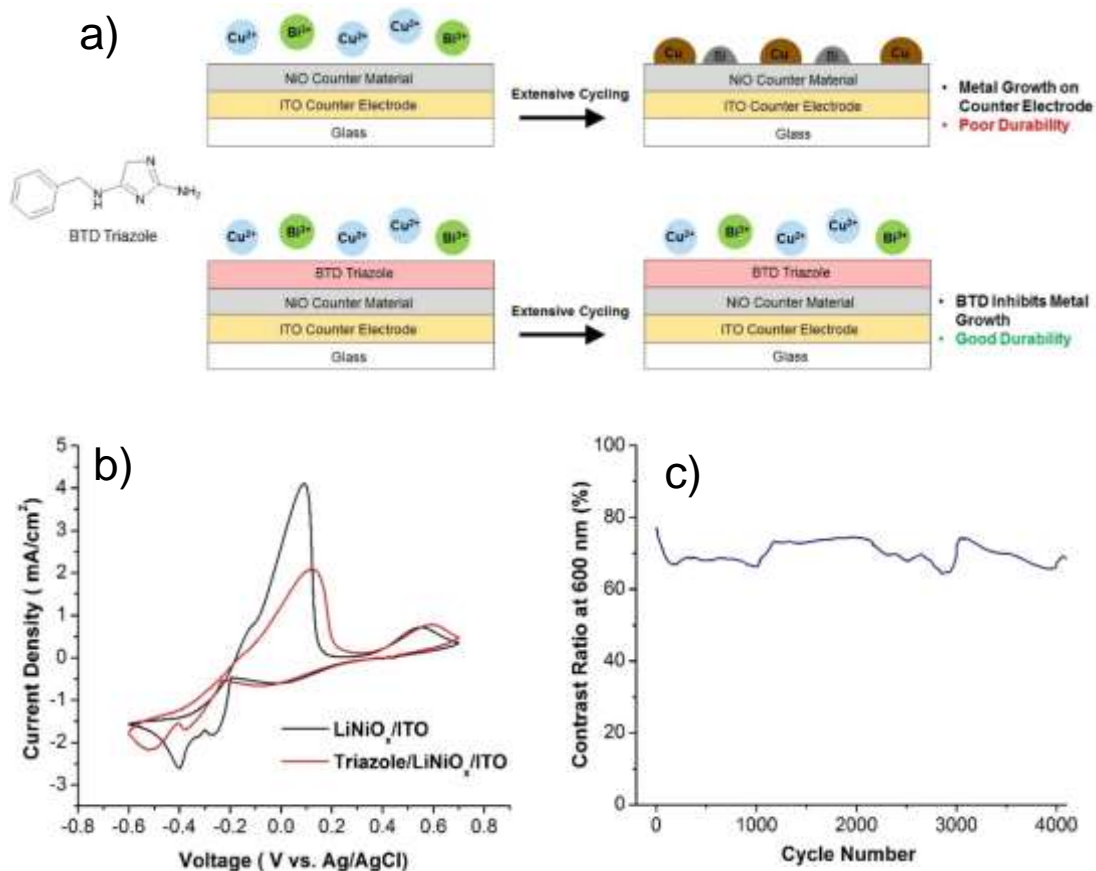


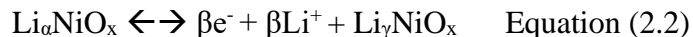
Figure 2.3. A Metal Inhibitor on LiNiO_x Improves Device Durability. **a**, Schematic of LiNiO_x counter electrode in a metal-based dynamic window after extensive cycling. Cu²⁺ and Bi³⁺ metallic ions (blue and green, respectively) are reduced to Cu⁰ and Bi⁰ solid metal (brown and grey, respectively) on the surface of the unmodified LiNiO_x (top panels). When the LiNiO_x counter electrode is modified with BTD, a triazole-based metal inhibitor, metal deposition does not occur on the LiNiO_x, which improves device durability. **b**, Cyclic voltammograms of LiNiO_x (black) and BTD-coated LiNiO_x (red) on ITO on glass in a three-electrode cell with a Cu-Bi liquid electrolyte at a scan rate of 50 mV/s. **c**, Contrast ratio of dynamic window with a Pt-modified ITO on glass working electrode and a BTD-coated LiNiO_x on ITO on glass counter electrode over the course of 4,000 cycles.

To improve the durability of the hybrid dynamic windows, we developed a strategy to impede metal electrodeposition on the counter electrode. We explored using metal electrodeposition inhibitors, which bind to metal ions and decrease

electrodeposition kinetics. [57, 58] In particular, we spin-coated a ~450 nm-thick thin film of *N*₅-benzyl-1H-1,2,4-triazole-3,5-diamine (BTD) on the NiO counter electrode since triazoles are well known to be potent Cu electrodeposition inhibitors. [59] We selected BTD (Figure 3a) as the metal inhibitor to protect the NiO since it is transparent, it forms a porous film (as shown in the SEM image in Supporting Figure 12.1.10) permeable to Li⁺ ions, and its hydrophobic benzyl group renders it insoluble in the aqueous Cu-Bi electrolyte. Cyclic voltammetry data demonstrate that the addition of a BTD overlayer significantly increases the overpotential and decreases the current density for Cu and Bi electrodeposition on a NiO-coated ITO electrode (Figure 3b). These results show that a BTD thin film decreases the kinetics of electrodeposition on NiO surfaces, and hence should limit the extent to which metal electrodeposition occurs as a side reaction on the NiO counter electrode in two-electrode systems, thus increasing the durability of hybrid dynamic windows (Figure 3a). Indeed, metal-based dynamic windows containing BTD-coated NiO on ITO counter electrodes switch without significant change in contrast ratio over the course of 4,000 cycles (Figure 3c).

As discussed previously, to develop large-scale windows in which metal ions diffuse transversely as opposed to laterally, the counter electrode must be oriented parallel to the plane of the working electrode. Previous approaches to achieving this orientation have relied upon the oxidation of Br⁻ to Br₃⁻ on a bare transparent conducting oxide as the counter electrode reaction.[60] However, this strategy is unsuitable with an aqueous electrolyte because Br₃⁻ causes the electrolyte to turn yellow during cycling (Supporting Figure 12.1.11). Hence, we hypothesized that the presence of a NiO thin film on the counter electrode could allow for Li⁺ insertion to occur as a more suitable counter

electrode reaction. NiO thin films have been previously shown to electrochromically cycle in Li-containing electrolytes through a two-step process. [50, 61-64] The first step involves an initial “activation” of the material followed by reversible Li insertion between bleached and colored states.



Where $\beta + \gamma = \alpha$ and $\text{Li}_\alpha\text{NiO}_x$ is the bleached state and $\text{Li}_\gamma\text{NiO}_x$ is the opaque state.

To determine the reaction occurring at the NiO counter electrode in our devices, we performed spectroelectrochemical measurements of NiO-coated ITO on glass electrodes in three-electrode cells since NiO is an anodically-coloring material.[45] In other words, while reductive metal electrodeposition turns the working electrode dark, oxidative processes occur that simultaneously turn the NiO counter electrode dark. This complimentary-darkening counter electrode increases the contrast ratio of hybrid dynamic windows. When a NiO on ITO-coated glass electrode is switched in a LiBr electrolyte, its contrast ratio at 600 nm is ~15% (Figure 4). Control experiments lithiating and delithiating a bare ITO electrode show that there is very little change in the transmission of the electrode (Supporting Figure 12.1.12). This experiment demonstrates that lithiation and delithiation of NiO is the chemistry that occurs during two-electrode device operation.

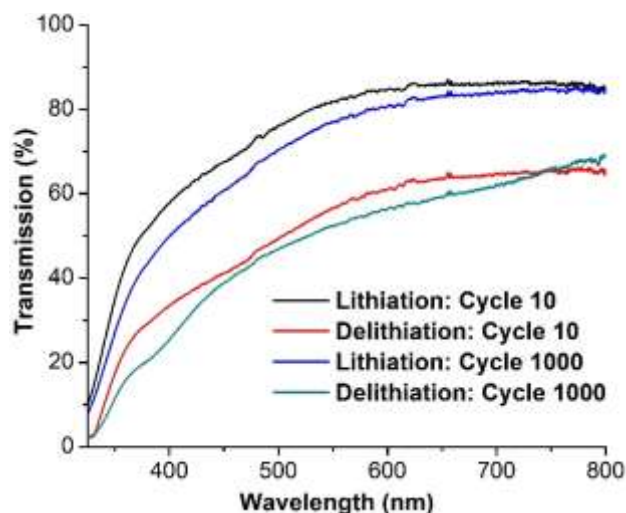


Figure 2.4. Transmission of LiNiO_x during Lithiation and Delithiation. Transmission of a 200-nm-thick NiO film on an ITO on glass working electrode in a three-electrode cell using a 1 M LiBr electrolyte. A voltage of -0.01 V was applied for 180 s to lithiate the electrode and 0.67 V was applied for 60 s to delithiate the electrode.

Additionally, the results of the half-cell measurements in Figure 5 and cyclic voltammetry (Supporting Figure 12.1.13) show that the spectroelectrochemical behavior of the NiO film does not change substantially over the course of 1,000 lithiation and delithiation cycles. Analogous experiments conducted with a BTD-coated NiO substrate are similarly durable (Supporting Figure 12.1.14), indicating that the BTD layer does not significantly perturb the lithiation and delithiation process during cycling.

Hybrid dynamic windows using NiO as a counter electrode enable the construction of devices on flexible polyethylene terephthalate (PET) substrates (Figure 5). Flexible dynamic windows are useful for curved applications such as car sunroofs, sunglasses, and displays, and they also allow for inexpensive roll-to-roll manufacturing techniques to be utilized along with windows that can be cut to specified sizes. Although we electrodeposited NiO ITO-coated glass substrates to form the counter electrodes, this

approach was not suitable for ITO-coated PET substrates due to nonuniform NiO electrodeposition that occurs as a result of the high sheet resistance ($30 \Omega \text{ sq}^{-1}$) and increased heterogeneity of the ITO on PET surfaces. Therefore, we deposited NiO on ITO-coated PET substrates using a low cost, scalable chemical bath deposition technique modified from a literature procedure, [65] which enables the construction of well-functioning flexible hybrid dynamic windows (Supporting Figure 12.1.15).

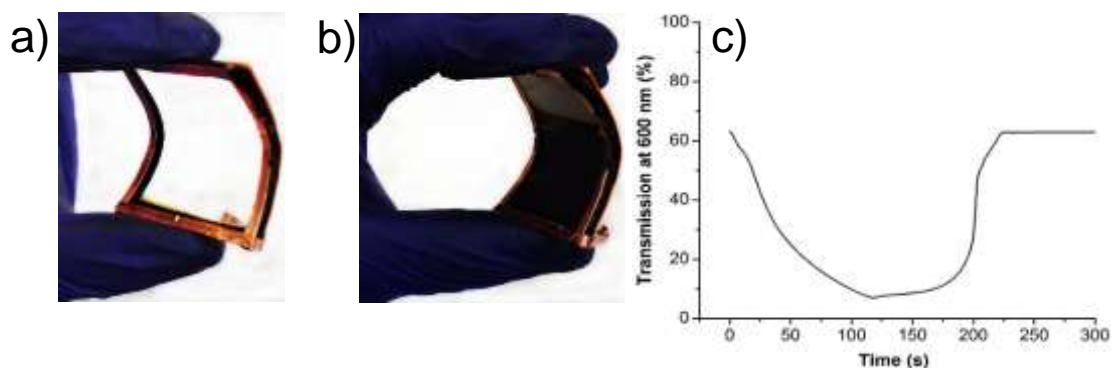


Figure 2.5. Flexible Hybrid Dynamic Windows. Photographs of a 25 cm^2 flexible dynamic window after 0 s (a) and 120 s (b) of metal electrodeposition using a Pt-modified ITO on PET working electrode and a LiNiO_x on ITO on PET counter electrode formed using a chemical bath deposition technique. c, Transmission at 600 nm of the window during 120 s of metal electrodeposition at -2.5 V and 180 s of metal stripping at 0 V .

2.2.3. Large-Scale Hybrid Dynamic Windows

To test the scalability of the hybrid dynamic windows developed here, we constructed 100 cm^2 windows using a spray-coating process to deposit the NiO on the counter electrode. Photographs and transmission data recorded at the center and edge of the device highlight that the window switches to its dark state uniformly (Figure 6 and Supporting Figure 12.1.16). The uniform nature of device switching enables these windows to access any intermediate state of grey while maintaining an aesthetically-pleasing view through the window. Strikingly, the transmission at 600 nm of a 100 cm^2

window decreases from about 75% to about 9% within 60 s (Figure 6c). In comparison, the transmission at 600 nm of a 25 cm² window decreases to about 6% within 60 s (Figure 2b). These results indicate that quadrupling the area of the window only slightly decreases device switching speed. Previous dynamic windows using reversible metal electrodeposition that contain a metal frame counter electrode rely upon the lateral diffusion of metal ions across the length and width of the windows. In contrast, in hybrid metal-based windows, ions must only diffuse across the thickness of the device during window operation. In short, this architecture enables 100 cm² windows to switch rapidly and uniformly.



Figure 2.6. 100 cm² Hybrid Dynamic Windows. Photographs of a 100 cm² dynamic window after 0 s (**a**) and 120 s (**b**) of metal electrodeposition using a Pt-modified ITO on glass working electrode and a LiNiO_x on ITO on glass counter electrode. **c**, Transmission at 600 nm through the edge (black) and the center (red) of the window during switching at -2.5 V for 60 s followed by 0 V for 120 s.

2.2.4. Outlook and Comparison to other Dynamic Window Technologies

Currently, the most successful dynamic windows utilize transition metal oxides, typically WO₃ on the working electrode and other metal oxides such as NiO on the counter electrode. [45] We assert that the metal-based windows developed here are a

promising alternative to these traditional electrochromic approaches. Whereas WO_3 switches between clear and blue, metals such as the mixture of Bi and Cu electrodeposited in this work are color neutral. Furthermore, the high extinction coefficients of metals allow metal-based dynamic windows to turn almost completely opaque ($<0.1\%$ transmission), [36] enabling them to be used for privacy applications. Additionally, we anticipate that the cost of these windows will be competitive with existing technologies. The windows contain an inexpensive aqueous-based electrolyte, and the optically active components of both electrodes are entirely solution processed, which is advantageous over the expensive sputtering techniques often used for WO_3 . We note that the organic components of these windows such as BTB will likely undergo degradation by ultraviolet (UV) sunlight over the 20-30 years needed for windows in many applications. UV filters similar to those used in car windows could be used to protect the organic components of the window. Future work will focus on developing all inorganic versions of this device architecture to enhance durability towards UV light.

The development of robust large-scale dynamic windows has been an incredible challenge and ongoing quest by academia and especially industry for several decades. [66] One of the grand impediments to the commercialization of large dynamic windows is switching speed. By integrating Ohm's Law over a two-dimensional electrode, it becomes clear that doubling the length of a dynamic window quadruples the voltage difference that exists between the center and edge of the window. At large scales (e.g. 1 m^2), this voltage difference causes nonuniform tinting that can only be avoided by dramatically decreasing device current such that switch speeds are 10-30 minutes.

Kinestral Technologies, Inc. has recently developed patterned transparent conducting oxide electrodes for electrochromic windows that have variable resistance. They deliberately increase the voltage drop, but engineer the voltage to vary linearly across the electrodes in such a way that the voltage difference between the two electrodes is the same throughout the window. [67] The hybrid dynamic window architecture developed here is entirely compatible with these patterned electrodes and possess the added benefits of neutral color and high optical contrast associated with electrodeposited metals.

2.3. Experimental:

2.3.1. Electrochemical Methods

Chemicals were received from commercial sources and used without further purification. BTD was synthesized in two steps from benzylamine following a literature procedure. [68] Electrochemical studies were conducted using a VSP-300 Biologic potentiostat. For experiments using three electrodes, electrochemical potentials were measured and reported with respect to a “no-leak” Ag/AgCl (3 M KCl) reference electrode (eDAQ) and utilized a Pt wire counter electrode. ITO electrodes (Xinyan Technology, $15 \Omega \text{ sq}^{-1}$) were cleaned by successively sonicating in de-ionized H₂O with 5% Extran solution for 5 minutes and isopropanol for 5 minutes. The electrodes were subsequently dried under a stream of air. Pt nanoparticles (Sigma-Aldrich) used to modify the working electrodes had average diameters of 3 nm. After cleaning, the ITO substrates were immersed in a solution of 3-mercaptopropionic acid (10 mM in ethanol) for 24 hours. The electrodes were next rinsed with ethanol and H₂O before they were immersed for at least 24 hours in the Pt nanoparticle dispersion that was diluted 1:4 with

H₂O. Lastly, ITO on glass substrates were annealed in air at 275°C for 30 minutes before use.

2.3.2. Dynamic Window Assembly

Two-electrode 25 cm² dynamic windows were constructed using a Pt-modified ITO working electrode and a LiNiO_x on ITO or a BTD-coated LiNiO_x on ITO counter electrode. Two-electrode 100 cm² dynamic windows used fluorine-doped tin oxide (15 Ω sq⁻¹) electrodes prepared in the same manner as the ITO electrodes. The aqueous liquid Cu-Bi electrolyte consisted of 5 mM BiCl₃, 15 mM CuCl₂, 10 mM HCl, and 1 M LiBr. The Cu-Bi gel electrolyte was made by adding 3.0% hydroxyethylcellulose by weight to the liquid electrolyte and has a viscosity of 9.5 Pa-s as measured using a NDJ-5S viscometer. To make uniform electrical contact, Cu tape with conductive adhesive was applied across the perimeter of both the working and counter electrodes. Butyl rubber Solargain edge tape separated the two device electrodes with an interelectrode spacing of ~3 mm. For durability studies, for each cycle, -2.5 V was applied for 60 s to induce metal electrodeposition and 0 V was applied for 120 s for metal stripping.

2.3.3. Thin Film Synthesis

To test the generality of NiO-based dynamic windows using reversible metal electrodeposition, thin films of LiNiO_x were deposited using either electrodeposition, a chemical bath deposition method, or a spray-coating technique. To fabricate LiNiO_x films using electrodeposition, a modified literature protocol was followed.[69] Chronoamperometry at +1 V for 30 minutes was performed in an aqueous solution of 500

mM NiSO₄ that was adjusted to pH 7.5 using 1 M KOH. The ITO substrates were subsequently rinsed with H₂O, dried under a stream of air, and annealed in air for 1 hour at 300°C. Next, the NiO_x films were lithiated using chronoamperometry at -1 V for 10 minutes in an aqueous solution of 1 M LiBr. The films were then rinsed with H₂O and dried under a stream of air. The thickness of the LiNiO_x films were measured using a KLA Tencor D-100 Stylus Profilometer. Electrodes containing BTD were fabricated by spin-coating LiNiO_x substrates at 4000 rpm for 60 s using a solution of BTD in tetrahydrofuran (10 mg/mL). As measured by profilometry, the BTD films had an average thickness of ~450 nm. LiNiO_x films were also fabricated using a chemical bath deposition method modified from the literature. [70] In this approach, an aqueous solution containing 500 mM NiSO₄, 94 mM K₂S₂O₈, and 3.1-3.5% ammonia was first formed by mixing the constituent chemicals together vigorously for 2-3 minutes. Next, the nonconductive side and edges of the ITO substrates were temporarily covered with Kapton tape, and the substrates were immersed in the chemical bath and mechanically shaken for 20 minutes at 80 rpm using an American Rotator V Model R-4140 shaker. Finally, the electrodes were rinsed gently with H₂O, dried in a stream of air, and heated in air for 1.5 hours at 300°C. LiNiO_x films on the 100 cm² substrates were prepared using a spray pyrolysis technique. The NiO precursor solution consisted of Ni(NO₃)₂ dissolved in water at a concentration of 50 mM. The precursor solution was sprayed onto ITO substrates, which were placed on a hot plate (300°C), at a flow rate of 100 μL/min for 10 minutes. The spray-coated NiO substrates were then lithiated using chronoamperometry at -1V for 40 minutes in an aqueous solution of 0.5 M LiBr. The films were then rinsed with H₂O and dried under a stream of N₂. CeO₂ thin films on ITO-coated glass were

fabricated following a literature procedure. [71] V_2O_5 thin films were prepared by spin coating a solution containing 14 μL vanadium(V) oxytriisopropoxide and 286 μL isopropanol on ITO-coated glass at 4000 rpm for 60 s. The thin films were subsequently annealed in air for 30 minutes at 275°C.

2.3.4. Materials Characterization

Most transmission spectra were measured with an Ocean Optics FLAME-S-VIS-NIR or an Ocean Optics FLAME-S-UV-VIS-ES spectrometer coupled with an Ocean Optics halogen light source (HL-2000-FHSA) or an Ocean Optics DH-mini UV-Vis-NIR light source. Optical data measured between 1000-1800 nm was measured using a Varian Cary 500 Scan UV-Vis-NIR spectrometer equipped with a Labsphere DRA-CA-5500 integrating sphere. Photographs of windows were taken with a Nikon D5000 Digital Camera. Scanning electron micrographs (SEM) and energy-dispersive X-ray (EDX) spectra were obtained using a JEOL JSM-6010LA microscope operated at an accelerating voltage of 20 kV.

2.4. Conclusion

In conclusion, we describe a class of dynamic windows that combine reversible Bi and Cu electrodeposition with Li^+ insertion in a NiO counter electrode. This approach harnesses the advantageous optical properties of metals while facilitating transverse ion diffusion, which enables robust devices to be constructed on a large scale. We demonstrate that 100 cm^2 versions of these hybrid dynamic windows uniformly switch between clear and black states with ~65% optical contrast in one minute. Furthermore,

the windows cycle at least 4,000 times without significant degradation when a small-molecule inhibitor of metal electrodeposition is used to prevent metal growth on the NiO counter electrode. Taken together, these results indicate that hybrid metal-based dynamic windows are a promising alternative to those based on traditional electrochromic materials.

Chapter 3: Cuprous Oxide Electrodeposited with Nickel for the Oxygen Evolution Reaction in 1 M NaOH

3.1. Introduction

Energy storage technologies are instrumental in facilitating our transition away from fossil fuels and towards renewable energy sources. Hydrogen gas is an attractive fuel for clean energy storage if the hydrogen utilized is produced using renewable processes.[72] Hydrogen could be produced in a green manner via the electrolysis of water.[73] However, the design of robust and inexpensive electrocatalysts for the oxygen evolution reaction (OER) is a key hurdle in developing practical water electrolyzers. [74] High-performing OER catalysts are also critical in the design of metal-air batteries.[75, 76]

In an effort to develop superior OER electrocatalysts, various metal and metal oxide materials for the OER have been studied. [77] Despite much theoretical and experimental research, the discovery of an ideal OER catalyst, one that is durable, inexpensive, and operates at a low overpotential with high current density, remains elusive. Traditional OER catalysts are based on Ru and Ir, but the precious nature of these metals limits their practical utility. [78] As an alternative, metal oxides containing Ni, Co, Fe, and Mn have been developed as stable OER electrocatalysts at high pH. [79] Regardless of the catalyst employed, the high overpotential for the OER limits the efficiency of water electrolysis. Recently, bimetallic catalysts have been explored as a strategy to reduce the overpotential for the OER. [80, 81] Studies show that bimetallic Ni-Fe and Ni-Co electrocatalysts are particularly effective at lowering the OER

overpotential. [82-84] Other examples of bimetallic Ni-based catalysts include those that contain Ce or W. [85-88]

In this manuscript, we develop bimetallic OER electrocatalysts based on Ni and Cu that operate under basic conditions. These catalysts are synthesized via the electrodeposition of Ni and Cu₂O. We chose to electrodeposit Ni because Ni-based OER catalysts are among the most active known due an optimal difference in the free energy associated with the adsorption of O and OH species on NiO_x surfaces. [89] Furthermore, previous studies have shown that bimetallic Ni-based catalysts modified with Fe and Co exhibit improved performance. [90] With the proper composition and morphology, the Ni-Cu₂O catalysts developed here rival those containing Ni-Fe and Ni-Co in terms of minimizing the OER overpotential.

3.2. Experimental

3.2.1. Chronoamperometric Electrodeposition of Cuprous Oxide

Cu₂O was electrodeposited onto a tin-doped indium oxide (ITO, Xin Yan, Inc.) glass slide at 50°C for 30 minutes using a published procedure. [91] A one-compartment, three-electrode electrochemical cell was used with ITO as the working electrode, Cu foil as the counter electrode, and Ag/AgCl (3 M KCl, eDAQ, Inc.) as the reference electrode. The sheet resistance of the ITO electrode was 10 Ω/sq, and the immersed geometric surface area of the electrode was 2 cm². The electrodeposition bath consisted of 7.5 M lactic acid and 0.66 M CuSO₄ adjusted to pH 12 with NaOH. The electrodeposition was carried out in the dark at a constant voltage of -0.45 V vs. Ag/AgCl. The thin film was left to dry in ambient atmosphere after electrodeposition and rinsed gently with DI water

to remove any residual CuSO_4 on the surface. Then, the thin film was either electrodeposited with Ni or directly studied using linear sweep voltammetry (LSV).

3.2.2. Chronopotentiometric Electrodeposition of Nickel

Ni was electrodeposited on top of the Cu_2O thin film at room temperature. Similar to the Cu_2O electrodeposition method, a three-electrode cell was used except that a Pt wire was used as the counter electrode instead of Cu foil. The electrodeposition bath consisted of 0.5 M NiSO_4 and 0.4 M boric acid (H_3BO_3) that was adjusted to pH 3 using H_2SO_4 . Chronopotentiometry at -4 mA/cm^2 for varying time periods was conducted to electrodeposit Ni films of different thicknesses. Next, the ITO electrodeposited with Ni on top of Cu_2O was left to dry in ambient air.

3.2.3. Electrochemical Measurements

To evaluate the OER activity of the thin films, the working electrodes were studied using LSV in 1 M NaOH at room temperature using a one-compartment, three-electrode configuration. The thin film on ITO functioned as the working electrode, a Pt wire was used as a counter electrode, and a Ag/AgCl electrode was used as the reference electrode. The OER LSVs reported are IR corrected using the solution resistance value obtained from electrochemical impedance spectroscopy as discussed previously. [92] All values are reported versus the reversible hydrogen electrode (RHE). Onset potentials for the OER are determined when the slope of the I-V curve reaches $17 \text{ } \Omega^{-1} \text{ cm}^{-2}$. The onset overpotential (η) is defined as the difference in the measured onset potential (E_{onset}) and the thermodynamic potential ($E^\circ = 1.23 \text{ V vs. RHE}$) for the oxygen evolution reaction such that $\eta = E_{\text{onset}} - E^\circ$. All electrochemical measurements were performed using a VSP-

300 Biologic Potentiostat. All experimental results were at least triplicated. Error bars presented signify one standard deviation of experimental results. Representative voltammograms are shown.

3.2.4. Material Characterization

Scanning electron microscope (SEM) images were obtained for each sample using a Hitachi S-4700 II Field Emission SEM with an Energy Dispersive Spectrometer (EDS) at an acceleration voltage of 15 kV. X-Ray diffraction (XRD) was performed using a Bruker D2 X-Ray Diffractometer. Atomic force microscopy (AFM) images were obtained using a Nanosurf EasyScan 2 microscope operated in contact mode using a silicon tip with an aluminium reflective coating (ContAl-G, TedPella, Inc.).

3.3. Results and Discussion

3.3.1. Electrodeposition of Ni-Cu₂O Thin Films

Cu₂O thin films were formed on ITO electrodes using an electrodeposition procedure reported previously. [91] To modify these films with Ni, Ni was electrodeposited on top of the Cu₂O thin films using chronopotentiometry at -4 mA/cm² in a Ni plating bath. By varying the electrodeposition time, the thickness of Ni on top of the Cu₂O can be tuned. Assuming a uniform Ni overlayer, we calculate the thickness of the layer from the charge passed during chronopotentiometry using equation 3.1 below

$$\text{Thickness} = \frac{QM}{AF\rho n} \quad (\text{Equation 3.1})$$

in which Q is charge, M is molecular weight, A is electrode area, F is Faraday's constant, ρ is the density of Ni, and $n = 2$ is the number of electrons transferred in the reaction $\text{Ni}^{2+} + 2 e^- \rightarrow \text{Ni}_{(s)}$. Table 3.1 lists the calculated thicknesses of the Ni overlayer for five different plating times studied in this work. We note that SEM images (*vide infra*) indicate that the Ni layer electrodeposited is not uniform, and thus the calculated thickness values can only be interpreted as average thicknesses across the entire sample area.

Time (s)	Calculated Ni Thickness (μm)	Calculated Cu ₂ O:Ni Mass Ratio
20	0.7	38.5:1
100	3.2	8.4:1
160	5.3	5.1:1
200	6.8	4.0:1
500	15	1.8:1

Table 3.1: Calculated thicknesses of Ni obtained during electrodeposition for various plating times and calculated Cu₂O: Ni mass proportions of the samples.

3.3.2. OER Activity of Ni-Cu₂O Thin Films

Figure 3.1 compares IR-corrected LSVs of an unmodified Cu₂O thin film with Cu₂O substrates that have been electrodeposited with Ni for 100 s and 500 s. In all three voltammograms, the current abruptly rises once a positive enough potential is reached to allow the OER to commence. At high current densities ($> \sim 5 \text{ mA cm}^{-2}$), O₂ bubbles are vigorously generated from the electrode surface. However, the onset potentials of the LSVs for the samples with Ni are about 130 mV more negative than the unmodified

Cu₂O electrode (Figure 3.1B). Therefore, the addition of Ni to the electrode enhances the activity of the OER catalyst in terms of overpotential.

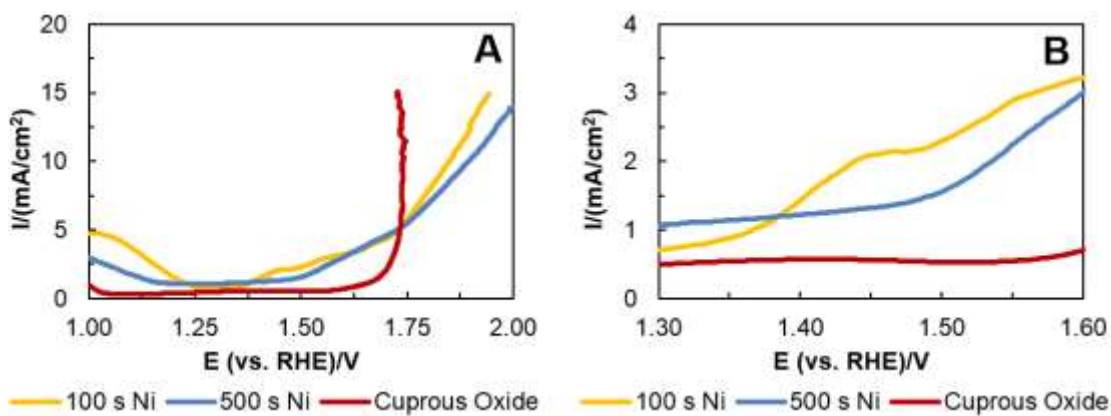


Figure 3.1: Linear sweep voltammograms of the oxygen evolution reaction in 1 M NaOH using Cu₂O on ITO working electrodes that have been electrodeposited with Ni for 0 s (red line), 100 s (orange line), and 500 s (blue line) at a scan rate of 10 mV/s. Panel B is an inset of panel A.

We tested three additional Ni electrodeposition times (20 s, 160 s, and 200 s) in an effort to determine the optimal Ni thickness for the Ni-Cu₂O catalyst (Figure 3.2A). These three catalysts also exhibited more negative onset potentials for the OER as compared to the unmodified Cu₂O control, although the extent of the enhancement varied. Importantly, control experiments measuring the LSVs of Cu and Ni foils both show much more positive OER onset potentials as compared to any of the Ni-Cu₂O electrodes (Figure 3.2B).

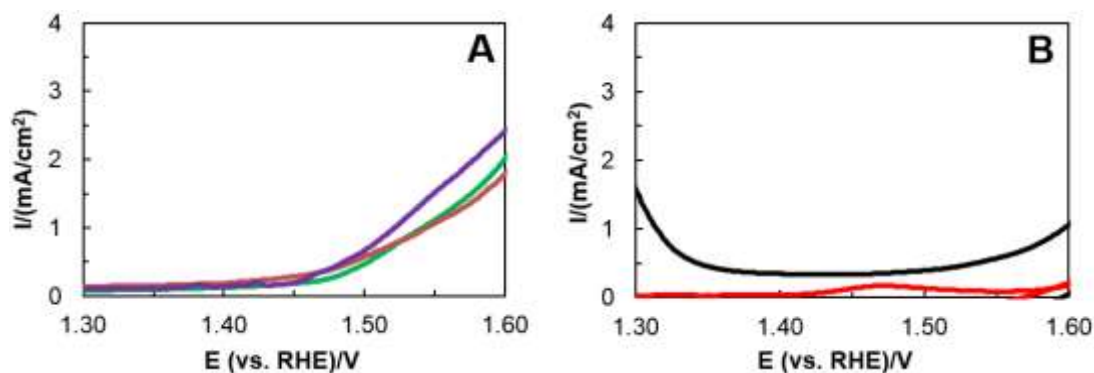


Figure 3.2: Linear sweep voltammograms of the oxygen evolution reaction in 1 M NaOH using Cu₂O on ITO working electrodes that have been electrodeposited with Ni for 20 s (A, green line), 160 s (A, red line), and 200 s (A, purple line) at a scan rate of 10 mV/s. Analogous experiments were also performed with Cu (B, black line) and Ni (B, red line) foils.

Figure 3.3 plots the calculated overpotential for the onset of the OER for Ni-Cu₂O catalysts with five different Ni overlayer thicknesses along with the overpotentials for control experiments. First, all of the Ni-Cu₂O catalysts possess an overpotential for the OER that is less than that of the Cu₂O, Cu, and Ni control experiments. Second, as the Ni electrodeposition time increases from 0 s to 20 s to 100 s, the OER overpotential decreases. However, once the Ni electrodeposition time exceeds 100 s, the OER overpotential increases. These results demonstrate that there is an optimal Ni to Cu₂O ratio to minimize the OER overpotential. The 100 s sample has the lowest overpotential (0.15 V), which is among the lowest for an OER catalyst operated under either acidic or basic conditions. Table S1 summarizes the overpotentials and current densities for a wide range of OER catalysts reported in the literature. The Ni-Cu₂O catalyst we developed has a comparable or lower overpotential than previously developed Ni-based OER catalysts.

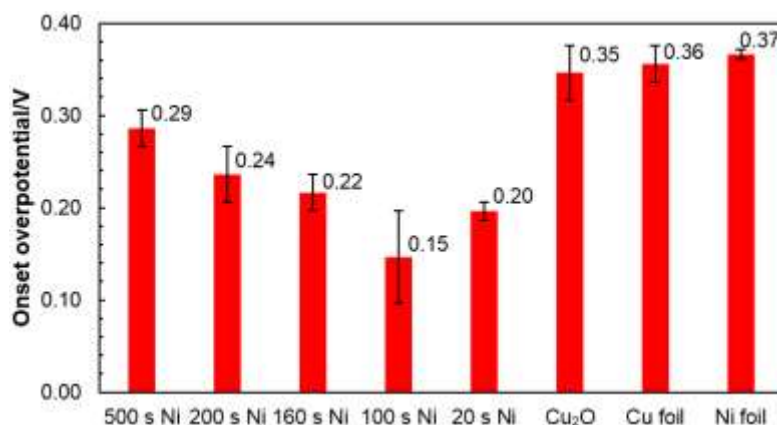


Figure 3.3: Plot of overpotentials for the onset of the oxygen evolution reaction using various working electrodes in 1 M NaOH.

3.3.3. Surface Characterization of Ni-Cu₂O Thin Films

In an effort to determine why the Ni-Cu₂O catalyst formed via 100 s of Ni electrodeposition has the optimal amount of Ni for decreasing the OER overpotential, we characterized the composition and structure of the catalysts using XRD, SEM-EDS, and AFM. We performed these characterization techniques on the samples after Ni electrodeposition but before OER voltammetry was conducted. The XRD spectrum of the Ni-Cu₂O catalyst confirms the presence of the ITO substrate and the electrodeposited films of Cu₂O and Ni on the electrode surface as expected (Figure 3.4). The positions of the peaks match the values previously reported for these three components. [91-94]

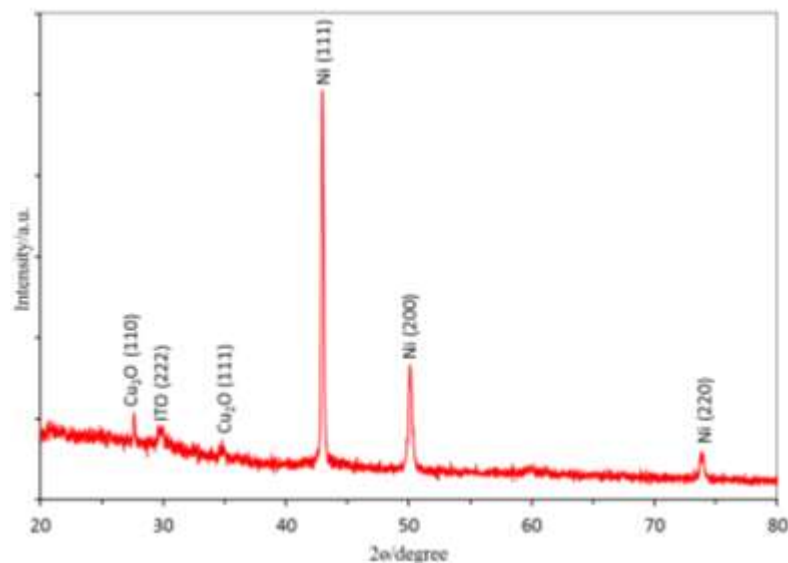


Figure 3.4: XRD spectrum of a Cu_2O on ITO electrode with a Ni overlayer formed using 100 s of Ni electrodeposition.

We next analyzed the morphology of Cu_2O electrodes modified with varying amounts of electrodeposited Ni using SEM. The unmodified electrodeposited Cu_2O thin film consists of triangular-shaped crystallites (Figure 3.5A) with (111) faces exposed as shown previously.[95] Figures 3.5B-3.5F show SEM images of Ni- Cu_2O thin films in order of increasing thicknesses of electrodeposited Ni. In all of these cases, the morphology obtained is different from the triangular facets observed without Ni. As the Ni electrodeposition time increases, the facets become sphere-like and agglomerate into larger-sized particles. We hypothesize that this agglomeration takes place due to etching of the Cu_2O crystals by the boric acid present in the Ni electrodeposition bath since Cu_2O is not stable in acid. Indeed, simply soaking a Cu_2O thin film in boric acid causes its original triangular morphology to change (Supporting Figure 12.2.1A). However, the morphological change induced by the boric acid does not significantly affect the OER

onset potential of the Cu_2O thin film (Supporting Figure 12.2.1B), indicating that Ni plays a role in the enhanced activity of the Ni- Cu_2O catalysts.

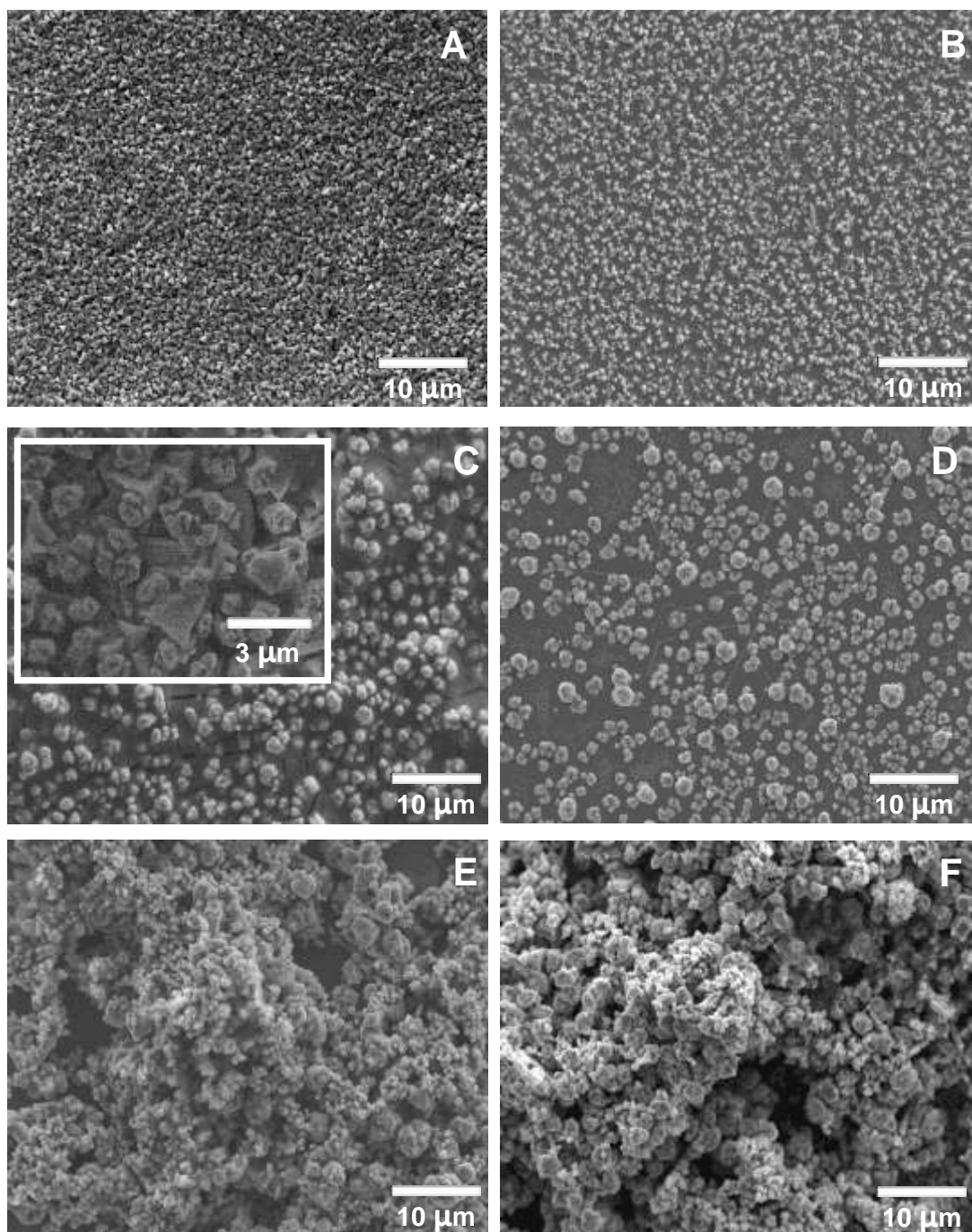


Figure 3.5: SEM images of Cu_2O on ITO electrodes with a Ni overlayer formed via 0 s (A), 20 s (B), 100 s (C), 160 s (D), 200 s (E), and 500 s (F) of Ni electrodeposition.

Since the Ni-Cu₂O catalyst formed using 100 s of Ni electrodeposition was found to have the lowest OER overpotential, we performed SEM-EDS mapping of this electrode (Figure 3.6, Supporting Figures 12.2.2 and 12.2.3). As a whole, the SEM-EDS mapping results indicate that the electrode contains Ni-modified Cu₂O particles. The overall EDS spectrum of the SEM image in Figure 3.6A is given in Figure 6B. The spectrum contains peaks associated with Ni, Cu, O, and S along with unlabelled In and Sn peaks from the ITO substrate. The first two elements come from the Ni and Cu₂O thin films, the O arises from both Cu₂O and ITO, and the S originates from NiSO₄ used in the Ni electrodeposition bath. An elemental map of the Cu content of the electrode shows that the bright sphere-like particles on the surface are Cu₂O (Figure 3.6C). Unlike the Cu coverage, the Ni distribution does not consist of discrete particles. Instead, Figure 3.6D shows that the Ni layer is fairly uniform across the surface although it is noticeably absent where the ITO substrate is exposed (e.g. see the top left of the image). The S elemental map mostly overlaps with the Ni distribution because the S originates from the Ni electrodeposition bath (Figure 3.6E). Lastly, the O content detected by EDS is greatest where bare ITO is present, and hence is roughly inversely correlated with the Ni distribution (Figure 3.6F).

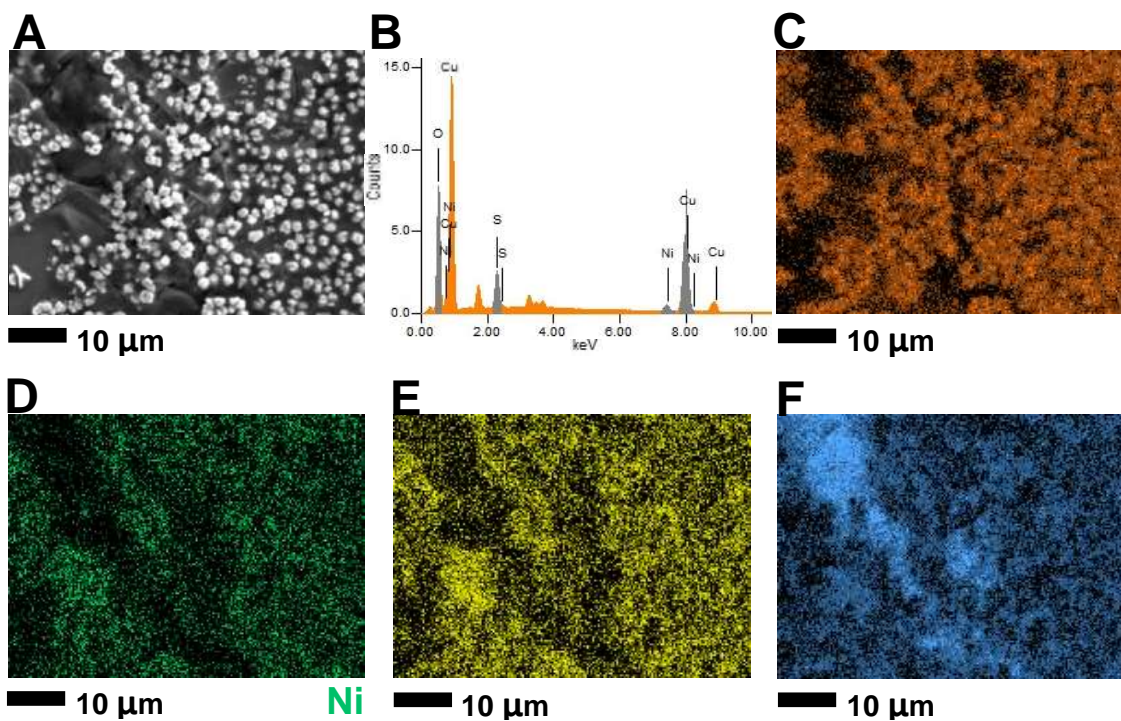


Figure 3.6: SEM image (A), EDS spectrum (B), and corresponding elemental distribution maps (C-F) as determined by EDS of a Cu_2O on ITO electrode with a Ni overlayer formed using 100 s of Ni electrodeposition. Brighter colors in the EDS maps represent higher relative elemental concentrations.

Lastly, we conducted AFM images of the Ni- Cu_2O electrode formed using 100 s of Ni electrodeposition (Supporting Figure 12.2.4). The AFM images confirm that there are low, smooth spots on the electrodes where bare ITO is present. The high-lying sphere-like particles are the agglomerates of Ni and Cu_2O .

Taking together the SEM, EDS mapping, and AFM results, we can now more fully understand the chemical identity of the components present in the SEM image of the optimal Ni- Cu_2O catalyst presented in Figure 3.5C formed via 100 s of Ni electrodeposition. The sphere-like particles can be assigned to Cu_2O , and the wispy-like platelets are Ni (Figure 3.5C, inset). This morphology contains a fairly uniform mixture of Cu_2O and Ni components, and this even distribution with many bimetallic sites may

explain why this surface structure leads to optimal OER electrocatalysis. Previous studies with OER catalysts have shown that bimetallic active sites often lead to lower OER overpotentials and outperform their monometallic counterparts.[96] For example, a synergistic effect between Ni and Fe sites in Fe-doped NiOOH leads to enhanced OER electrocatalysis.[97] Finally, we note that metallic Ni is unstable in the NaOH electrolyte we used for conducting the OER voltammetry.[98] The active catalyst during OER is therefore a mixture of Ni/Cu (oxy)hydroxides.

3.4. Conclusion

We synthesized a series of Ni-Cu₂O electrocatalysts for the OER by sequentially electrodepositing Cu₂O and Ni on ITO substrates. By altering the amount of Ni on the surface, the activity of the electrocatalysts varies substantially. An optimal thickness of Ni yields a catalyst with an improved onset overpotential of 0.15 V. Characterization using XRD, SEM, EDS, and AFM demonstrates that the composition and morphology of the electrocatalysts are dependent upon the amount of Ni electrodeposition and dictate catalyst performance.

Chapter 4: Dynamic Windows based on Reversible Metal Electrodeposition with Enhanced Functionality

4.1. Introduction

Increasing the energy efficiency of buildings and automobiles is a crucial component of fostering the transition of our energy economy away from fossil fuels and towards renewable energy sources. [1] Dynamic windows, which possess electronically tunable transmission, are one promising technology to increase the energy efficiency of spaces. Previous studies have demonstrated that the incorporation of robust dynamic windows into buildings leads to a 10% average reduction in energy consumption due to heating, cooling, and lighting savings. [32, 56] Additionally, dynamic windows are more aesthetically pleasing than traditional window blinds and their switching can be automated.

Recently, dynamic windows utilizing reversible metal electrodeposition have emerged as an intriguing alternative to those based on other technologies such as electrochromic materials, polymer dispersed liquid crystals, and thermochromic materials. These windows function via the reversible electrochemical transfer of metal between a metal window frame and a transparent conducting pane. [47, 99-103] Advantages of metal-based dynamic windows include high optical contrast, color neutral switching, the use of nontoxic aqueous electrolytes, and the potential for manufacturing using low-cost solution-processed techniques. [48]

One challenge hindering the practical adoption of metal-based dynamic windows is the difficulty of uniformly electroplating metals over a large electrode area. [104, 105] A self-assembled monolayer (SAM) of Pt nanoparticles was previously used to control the nucleation of metal electrodeposition on tin-doped indium oxide (ITO) surfaces. [40] This approach allowed for the construction of 25 cm² dynamic windows that possess uniform metal electrodeposition, giving rise to uniform device tinting. Currently, these windows harness the electrodeposition of Cu from an aqueous-based gel electrolyte along with a second metal such as Bi or Ag. [36]

In this work, we expand upon the traditional metal-based dynamic window architecture to create dynamic windows with enhanced switching speed and functionality. In particular, we construct windows that elicit metal electrodeposition on both window panes to increase switching speed. We also design windows that facilitate selective reversible metal electrodeposition such that the devices darken in a tailored pattern on the macro and microscales.

4.2. Experimental

All chemicals were obtained from commercial sources and used as received. Electrochemical studies utilized a VSP-300 Biologic potentiostat. Half-cell experiments with three electrodes consisted of a “no-leak” Ag/AgCl (3 M KCl) reference electrode (eDAQ, Inc.), a Pt wire counter electrode, and a Pt-modified or unmodified ITO on glass working electrode (Xinyan Technology, 15 Ω sq⁻¹). Half-cell experiments utilized an aqueous Ag-Cu electrolyte described previously.[40]

ITO substrates were cleaned through sonication in water with 5% Extran solution for 5 minutes followed by sonication in isopropanol for 5 minutes. The substrates were next dried using a stream of air. To modify the ITO surfaces with Pt nanoparticles, the substrates were placed in an ethanolic solution of 10 mM 3-mercaptopropionic acid for approximately 24 hours. Next, the surfaces were rinsed with ethanol followed by water before they were immersed in a solution of Pt nanoparticles that had an average diameter of 3 nm (Sigma-Aldrich) for at least 24 hours. The as-received Pt nanoparticle solution was diluted 1:4 with water before use. After the surfaces were treated with Pt nanoparticles, they were rinsed with water, dried under a stream of air, and annealed in air at 275°C for 20-30 minutes.

Practical full-cell dynamic windows were constructed using either one working electrode and one counter electrode or two working electrodes and one counter electrode. For devices with one working electrode, the working electrode was a 25 cm² Pt-modified ITO on glass substrate, and the counter electrode consisted of Cu foil with a nonconductive glass backing. To ensure uniform electrical contact to the working electrode, Cu tape with conductive adhesive was placed along the electrode perimeter. Butyl rubber was used as a sealant and maintained a ~3 mm spacing between the two electrodes. For devices with two working electrodes, the nonconductive glass backing was replaced with an additional 25 cm² Pt-modified ITO on glass working electrode. The two working electrodes were wired together during device operation. After sealing the devices, an aqueous-based gel electrolyte containing Bi³⁺ and Cu²⁺ ions was injected through the sealant. The electrolyte contained 5 mM BiCl₃, 15 mM CuCl₂, 10 mM HCl, and 1 M LiBr with 3% by weight hydroxyethylcellulose.

Transmission spectra were measured with an Ocean Optics FLAME-S-VIS-NIR spectrometer coupled with an Ocean Optics DH-mini UV-Vis-NIR light source. Photographs of windows were taken with a Nikon D5000 Digital Camera. Electrochemical impedance spectroscopy was performed at open circuit potential between 200 kHz and 100 mHz using a voltage amplitude of 10 mV. Scanning electron micrographs (SEM) were obtained using a JEOL JSM-6010LA microscope operated at an accelerating voltage of 20 kV. False coloring was added to the images using Adobe Photoshop.

Patterning on a macroscopic scale was accomplished using Parafilm cut out by hand or an Orafol vinyl sticker cut using a vinyl cutter. The Parafilm or sticker was placed on the ITO on glass before immersing it in the 3-mercaptopropionic acid and Pt nanoparticle solutions. After surface modification, the mask was carefully removed, and a dynamic window was assembled using the patterned Pt-modified ITO as the working electrode. Patterning on a microscopic scale was performing using polystyrene beads (100 μm diameter, Sigma-Aldrich). A cleaned ITO on glass substrate (2 cm by 2 cm) was modified with polystyrene beads by spin-coating a solution containing 80 μL of the as-received polystyrene bead suspension, 80 μL of Polysorbate 20, and 240 μL of water at 1000 rpm for 10 s. This spin-coating process was repeated five times to ensure a dense layer of beads assembled on the surface. After spin-coating, the substrate was annealed in air at 110°C for 1 hour. Metal electrodeposition was elicited using a Ag-Cu electrolyte previously described using chronoamperometry at -0.6 V for 120 s. [40] The surface was rinsed with water and dried with air before SEM imaging.

4.3. Results and Discussion

4.3.1. Dynamic Windows with One and Two Working Electrodes

Traditional dynamic windows based on reversible metal electrodeposition utilize the architecture displayed schematically in Figure 4.1. [106] During window darkening, a negative voltage is applied to the device with respect to the Pt-modified ITO working electrode. This voltage causes metal ions in the electrolyte (such as Cu^{2+}) to reduce to elemental metal on the Pt-modified ITO surface. Simultaneously, oxidation occurs at the Cu counter electrode window frame and generates Cu^{2+} . The net reaction during window tinting is therefore the electrochemical movement of metal on the window frame to the Pt-modified ITO electrode. To turn the window clear, a positive voltage is applied to the device with respect to the working electrode, and the opposite reaction occurs, and metal is replated on the counter electrode frame.

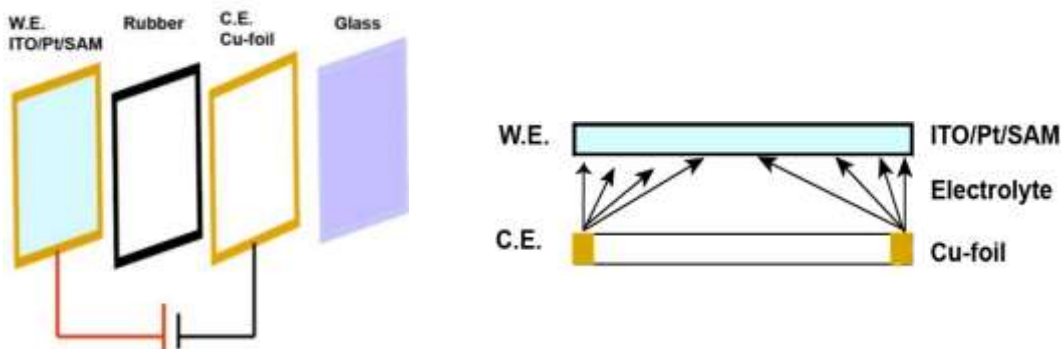


Figure 4.1: Schematic of the architecture of a dynamic window based on reversible metal electrodeposition that contains one Pt-modified ITO on glass working electrode and a glass back pane. Metal electrodeposition only occurs on the ITO during window tinting.

We sought to improve upon this architecture for metal-based dynamic windows by incorporating a second Pt-modified ITO on glass working electrode (Figure 4.2). With

this design, metal electrodeposition can occur simultaneously on both working electrodes, thus improving the contrast ratio and switching speed of the device.

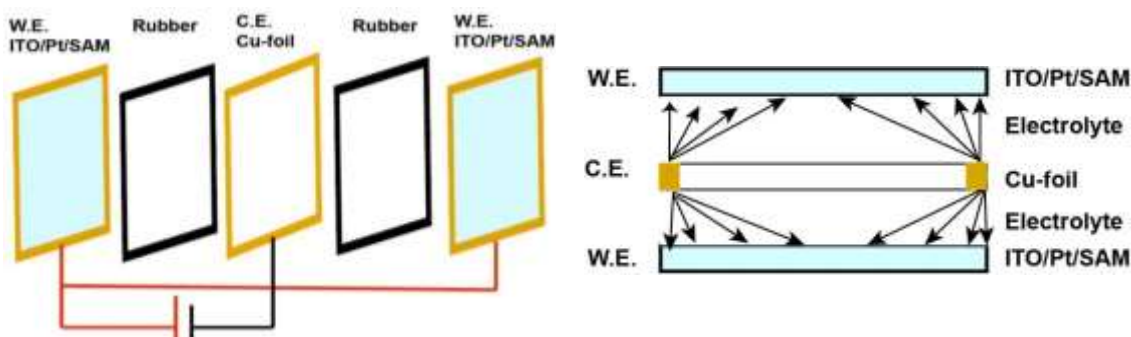


Figure 4.2: Schematic of the architecture of a dynamic window based on reversible metal electrodeposition that contains two Pt-modified ITO on glass working electrodes. Metal electrodeposition occurs on both ITO electrodes during window tinting.

Figure 4.3 displays a comparison of the transmission changes measured of dynamic windows containing one and two working electrodes that possess a Bi-Cu electrolyte. For the device with a single working electrode, the initial transmission at 600 nm of ~82% decreases to ~30% after 30 s of Bi and Cu electrodeposition at -0.6 V. By comparison, the window with two working electrodes has a similar initial transmission but decreases to ~15% using the same switching parameters. The increased contrast ratio of the device with double deposition is due to both panes of the window tinting. The contrast ratios of both devices can be improved by increasing the metal electrodeposition time (Supporting Figure 12.3.1).

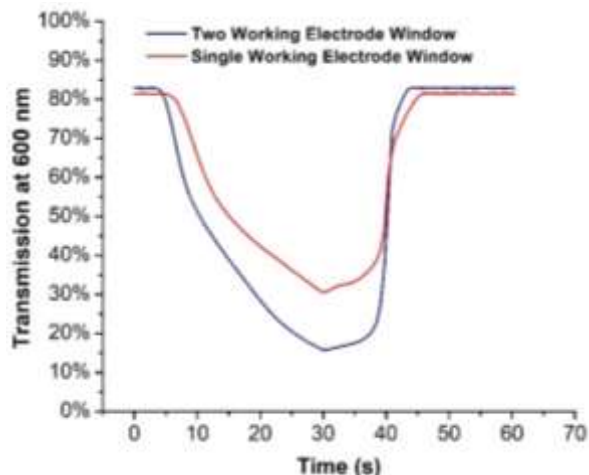


Figure 4.3: Transmission of 25 cm² metal-based dynamic windows with two (blue) and one (red) working electrodes during switching at -0.6 V for 30 s and +0.8 V for 30 s.

To further understand the switching speed of the window containing two working electrodes, we compared the chronoamperometry of the devices during switching (Figure 4.4). The initial current density and the amount of charge passed through the window with two working electrodes during metal electrodeposition is roughly double the device with one working electrode, as expected.

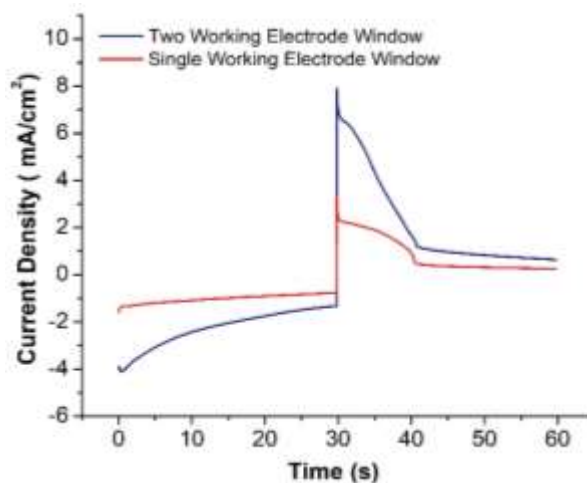


Figure 4.4: Chronoamperometry of 25 cm² metal-based dynamic windows with two (blue) and one (red) working electrodes during switching at -0.6 V for 30 s and +0.8 V for 30 s.

4.3.2. Modeling the Switching Speed of a Two Working Electrode Window

Assuming metal electrodeposition occurs at equal rates on both working electrodes, the switching speed of the window with two working electrodes can be modeled based upon the switching speed of the single working electrode device using Equation 4.1 below

$$T(t)_{double} = \left(\frac{T(t)_{single}}{T(0)_{single}} \right)^2 T(0)_{double} \quad (\text{Equation 4.1})$$

where $T(t)_{double}$ and $T(t)_{single}$ are the transmissions of windows with two and one working electrodes as a function of time, respectively, and $T(0)_{double}$ and $T(0)_{single}$ are the initial transmissions of the devices. This simple model generates a transmission curve for the double working electrode device that fairly accurately matches the experimental finding (Figure 4.5, red dashed line compared to black line). To increase the predictiveness of the model, we incorporated the chronoamperometry data into an equation describing the transmission of the window with two working electrodes. The modified Equation 4.2 is shown below

$$T(t)_{double} = \left(\frac{T(t)_{single}}{T(0)_{single}} \right)^{\frac{i(t)_{double}}{i(t)_{single}}} T(0)_{double} \quad (\text{Equation 4.2})$$

where the newly added variables $i(t)_{double}$ and $i(t)_{single}$ are the current densities as a function of time for the windows with two and one working electrodes, respectively. This second model takes into account slight changes in the relative switching rates between the two devices over time. Experimentally, $i(t)_{double}$ is not exactly twice that of $i(t)_{single}$ and varies from 1.7 to 3 during metal electrodeposition. The predictiveness of this second model is superior to the first (Figure 4.5, blue dashed line). However, both models do not perfectly match the experimental transmission curve, which was obtained by measuring

the transmission of the center of the 25 cm² device. In contrast, the chronoamperometry data are measures of current across the entire device. This discrepancy causes deviations in the transmission across the window area to lead to inaccuracies in the modeling.

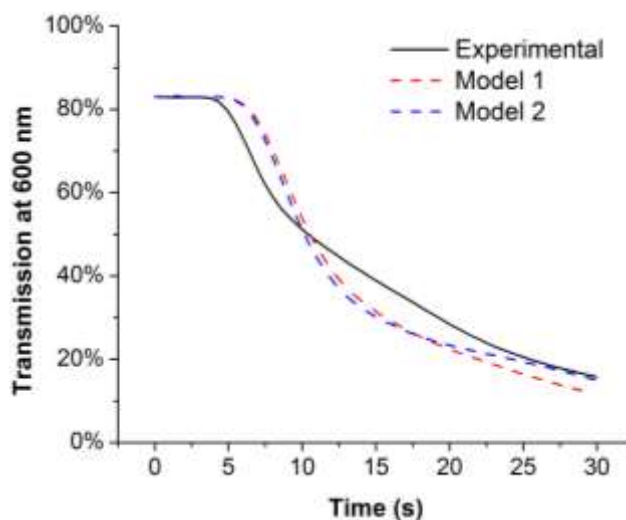


Figure 4.5: Transmission at 600 nm of a 25 cm² metal-based dynamic window with two working electrodes during switching at -0.6 V for 30 s (black). The dashed lines represent the predicted transmission curves with two different models.

4.3.3. Effect of Voltage on Metal Electrodeposition

Having understood the behavior of the dynamic windows containing two and one working electrodes, we next sought to increase the switching speed of the devices by increasing the switching voltage. Figure 4.6 displays a comparison of the transmission curves of devices with two and one working electrodes using -1.2 V for metal electrodeposition instead of -0.6 V. The data for the single deposition device show that the transmission reaches ~30% after 30 s of metal electrodeposition, which is almost identical to the value obtained when -0.6 V is applied (compare Figure 4.6, red line to Figure 4.3, red line). At -0.6 V, metal electrodeposition on the Pt-modified ITO working

electrode is limited by the diffusion of metal ions to the surface, and further increasing the voltage to -1.2 V does not accelerate metal electrodeposition. Instead, the extra voltage goes towards the H_2 evolution reaction, which results in the formation of bubbles inside the device (Supporting Figure 12.3.2A-B). In contrast, the switching speed of a device with two working electrodes is increased significantly when the magnitude of the voltage is increased to -1.2 V (Figure 4.6, blue line). With two working electrodes, the doubled electrode surface area causes the device current to not be diffusion-limited at -0.6 V, and thus increasing the voltage to -1.2 V results in a faster switching time. In this case, the additional voltage goes towards additional metal electrodeposition and not towards the formation of H_2 (Supporting Figure 12.3.2C-D).

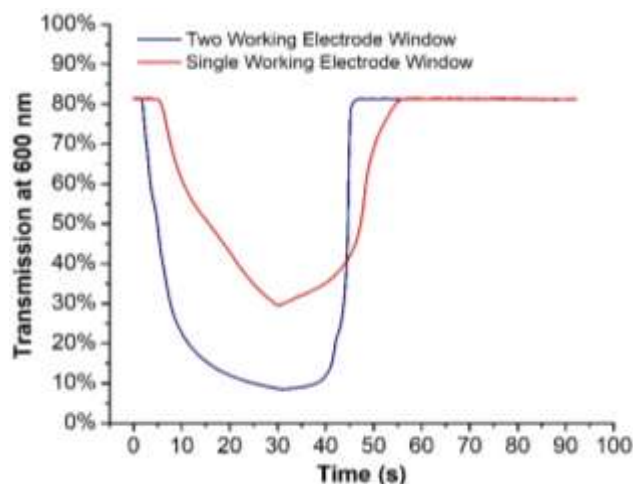


Figure 4.6: Transmission of 25 cm^2 metal-based dynamic windows with two (blue) and one (red) working electrodes during switching at -1.2 V for 30 s and $+0.8$ V for 60 s.

We systematically investigated the effect of electrodeposition voltage on device switching time (Supporting Figures. 12.3.3-12.3.5). An increase in the magnitude of the switching voltage improves the switching time of the device until -1.2 V. Further increasing the switching voltage to -1.5 V causes H_2 formation in both devices with one

and two working electrodes and also degrades the ITO electrodes, thus hampering device switch time (Supporting Figure 12.3.5) and durability.

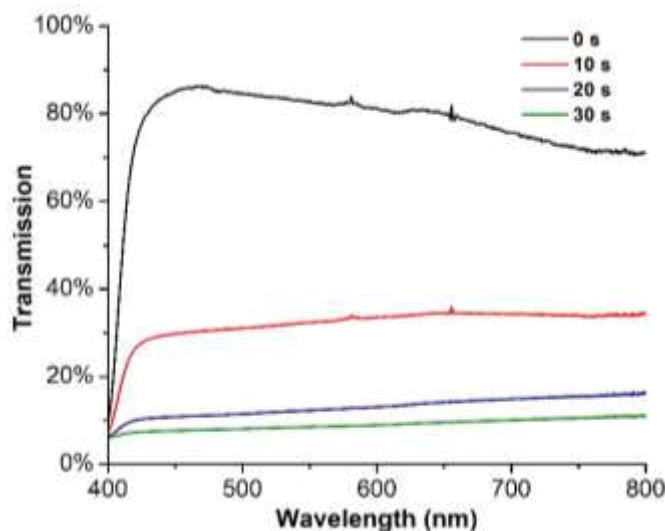


Figure 4.7: Transmission of a 25 cm² metal-based dynamic window with two working electrodes as a function of wavelength after 0 s (black), 10 s (red), 20 s (blue), and 30 s (green) of window darkening at -1.2 V.

Having established that -1.2 V is the optimal voltage for switching the window with two working electrodes, we next evaluated the performance of the device using this voltage. Using -1.2 V, the dynamic window with two working electrodes possesses an impressive contrast ratio of ~74 % and reaches ~8 % transmission at 600 nm in 30 s, making it one of the fastest reported dynamic window based on metal electrodeposition on the 25 cm² scale.[36] In addition, the transmission profile across visible wavelengths of light is relatively flat, which results in an aesthetically-pleasing black color of the windows in their tinted states (Figure 4.7). Furthermore, the windows effectively modulate near-infrared light, a property that is useful in controlling heat flow in and out of buildings and automobiles. The photographs in Figure 4.8 demonstrate that a window

with two working electrodes switches rapidly and uniformly between clear and dark states.

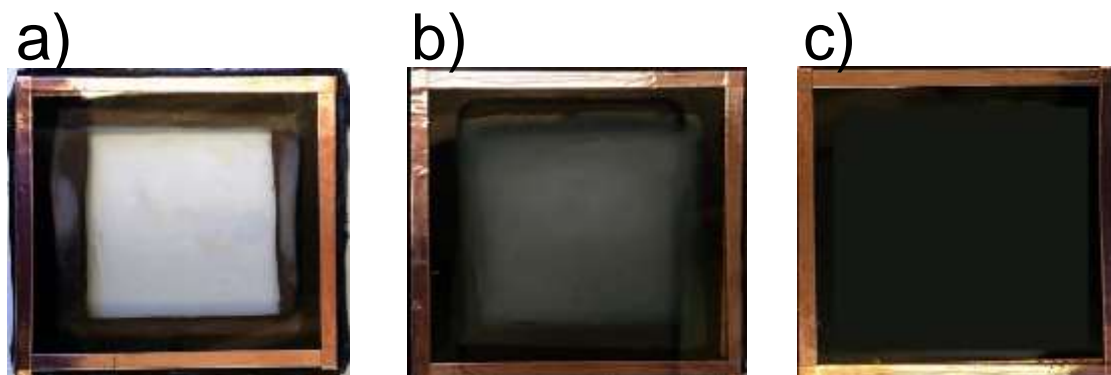


Figure 4.8: Photographs of a 25 cm² metal-based dynamic window during switching at -1.2 V for 0 s (a), 15 s (b), and 30 s (c).

Lastly, we evaluated the cycle life of devices based on reversible metal electrodeposition that contain two working electrodes. Windows with this architecture switch more than 1,000 times without significant degradation in contrast ratio (Figure 4.9).

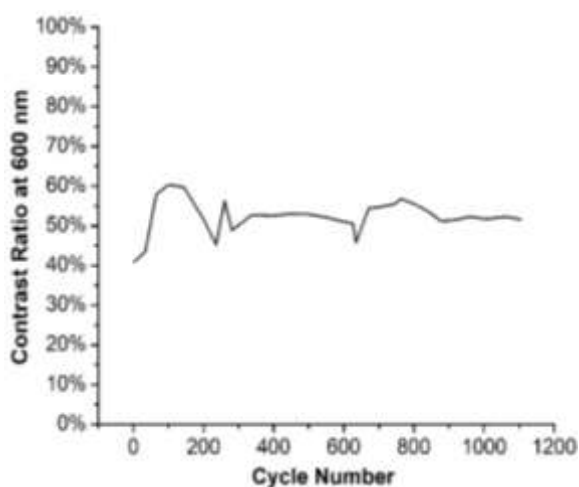


Figure 4.9: More than 1,000 cycles of a 4 cm² dynamic window based on reversible metal electrodeposition with two working electrodes. Each switching cycle consisted of applying -1 V for 3 s and +0.8 V for 7 s.

In an effort to further understand the different voltage behavior of devices with one and two working electrodes, we performed electrochemical impedance spectroscopy (Figure 4.10). The impedance spectrum of a device with one working electrode dramatically differs from the spectrum obtained for a device with two working electrodes (Figure 10, black and red). We hypothesize that when the working electrode area is doubled with two working electrodes, the switching kinetics become limited by reactions on the counter electrode. To test this hypothesis, we calculated the resistance of the counter electrode for the different device architectures using the first equivalent circuit previously discussed by Nara et al. for full cell devices.[107]The calculated resistance of the counter electrode increases from 29 Ω to 53 Ω when increasing the number of working electrodes from one to two. With two working electrodes, more IR drop occurs on the counter electrode due to its higher resistance, and thus the voltage that goes to the electrolyte to induce metal electrodeposition is diminished. In contrast, with one working electrode, the IR drop through the counter electrode is less, and so more voltage is applied to the electrolyte. This difference in IR drop explains why applying -1.2 V to the single deposition device causes H₂ formation, but the device with two working electrodes does not produce H₂ (Supporting Figure 12.3.2).

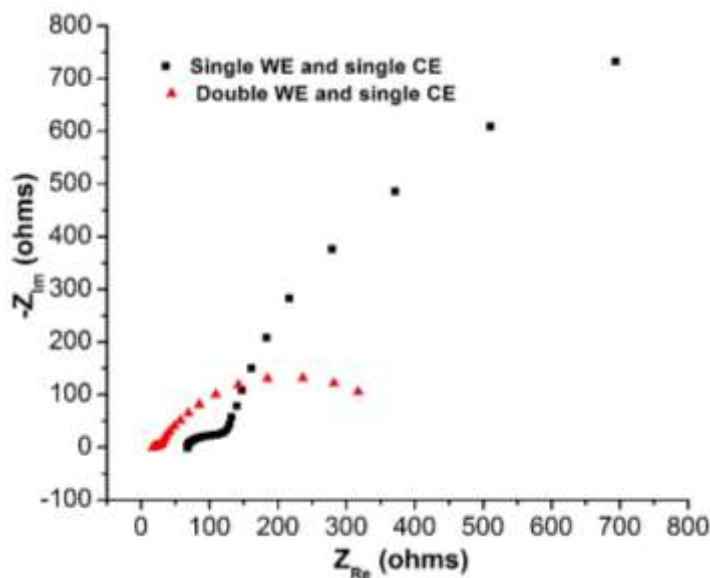


Figure 4.10: Electrochemical impedance spectroscopy of 25 cm² metal-based dynamic windows with one working electrode and one counter electrode (black), and two working electrodes and one counter electrode (red). The resistances of the counter electrode anode were calculated to be 29 Ω , and 53 Ω for these three devices, respectively.

For the dynamic window with two working electrodes, we can increase the area of the counter electrode by adding a second counter electrode metal frame. As expected, doubling the counter electrode area decreases the calculated resistance of the counter electrode as determined by electrochemical impedance spectroscopy. The decrease in counter electrode resistance results in less IR drop across the counter electrode, and thus there is a greater voltage applied towards the electrolyte, which causes H₂ formation (Supporting Figure 12.3.6).

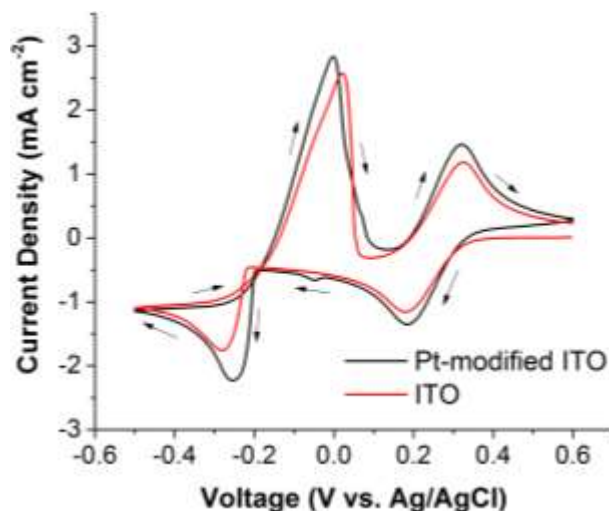


Figure 4.11: Cyclic voltammograms in a Ag-Cu electrolyte using a Pt-modified ITO on glass (black) and unmodified ITO on glass (red) working electrode at 20 mV/s.

As discussed in the Introduction, a SAM of Pt nanoparticles is used on the working electrode to provide an even distribution of nucleation sites and elicit uniform metal electrodeposition across the 25 cm² device area. The Pt nanoparticles function as nucleation sites because metal electrodeposition occurs more readily on another metal such as Pt than on heterogeneous metal oxide surfaces like ITO. For example, cyclic voltammograms conducted in a Ag-Cu electrolyte indicate that metal electrodeposition occurs more readily on Pt-modified ITO than unmodified ITO (Figure 4.11). On both electrodes, the peaks centered at about +0.25 V are due to the Cu(II)/Cu(I) redox couple. At about -0.25 V, there is a sharp increase in cathodic current due to metal electrodeposition. However, the onset potential for metal electrodeposition on the Pt-modified ITO electrodes occurs about 30 mV more positive than on the unmodified ITO electrode, indicating that it is more favorable for metal electrodeposition to occur on the

Pt nanoparticles. The peaks at about 0 V on both electrodes are due to stripping of the electrodeposited metals.

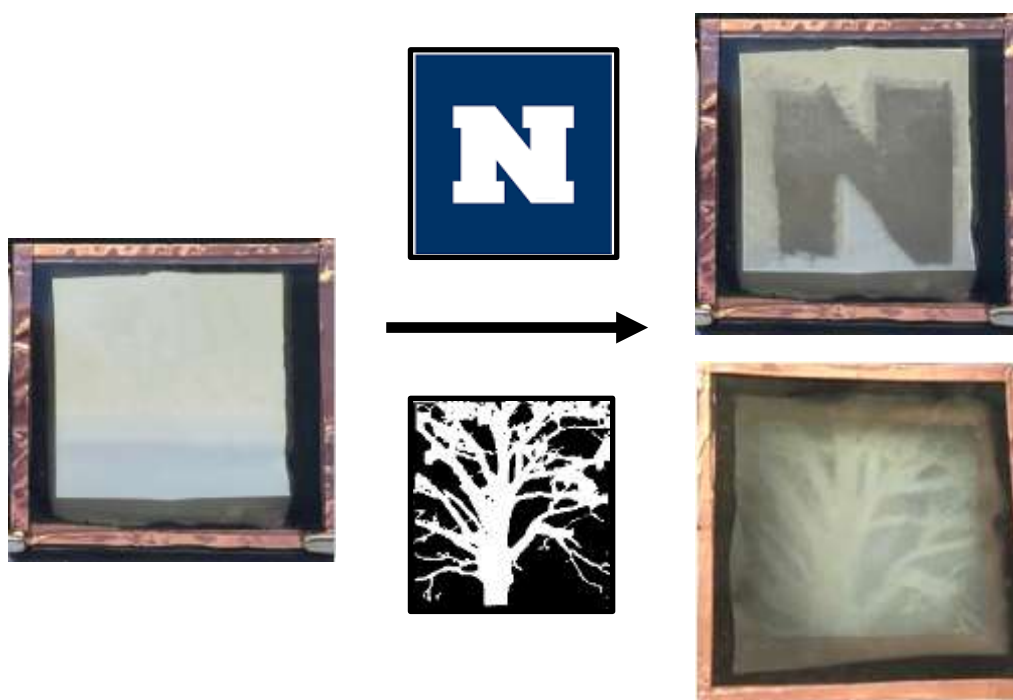


Figure 4.12: Photographs of a 25 cm² dynamic window in its clear state (left) and after 60 s of metal electrodeposition at -0.6 V using ITO on glass working electrodes with two different patterns of SAMs of Pt nanoparticles (right).

The difference in the onset potentials for metal electrodeposition on the Pt-modified and unmodified ITO electrodes suggests that it is possible to selectively electrodeposit metal on the SAM of Pt nanoparticles. To test this hypothesis, we constructed dynamic windows with ITO working electrodes that were patterned with Pt nanoparticles through masked self-assembly. By covering the ITO substrate with a mask (e.g. a hand-cut N-shaped piece of Parafilm wax or a vinyl-cut tree-shaped sticker) during Pt SAM formation, the Pt SAM is formed only on portions of the ITO electrode not covered by the mask. The photographs in Figure 4.12 demonstrate that the darkening of 25 cm² dynamic windows containing these patterned working electrodes occurs only in

areas where the Pt SAM is present, indicating that reversible metal electrodeposition devices can be constructed with electrodeposition occurring in any desired pattern on a macroscopic scale.

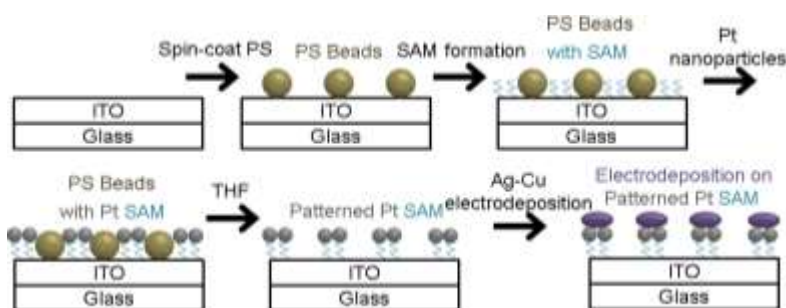


Figure 4.13: Schematic showing the fabrication of micro-patterned metal electrodeposition with a SAM of Pt nanoparticles templated by polystyrene beads.

Having demonstrated the ability to macroscopically pattern reversible metal electrodeposition, we next evaluated if selective electrodeposition could also be elicited on the microscale. Figure 4.13 shows a schematic of how we fabricated a micropatterned Pt SAM. First, spherical polystyrene (PS) beads 1 μm in diameter were spin-coated on ITO-coated glass to give close-packed clusters of beads as indicated by optical microscopy (Figure 4.14a). Next the PS-modified surface was immersed in a solution of 3-mercaptopropionic acid to form a SAM followed by a solution of Pt nanoparticles, which covalently bind to the thiol groups of the SAM. The PS beads were subsequently removed by immersing the surface in THF to yield the patterned Pt SAM electrode. The false color SEM image in Figure 4.14b shows that electrodeposition of Cu and Ag (colored purple) occurs in the void spaces left by the mask of the close-packed PS

spheres (black circles). This result indicates that selective metal electrodeposition using patterned Pt SAMs can also be performed on the microscale.

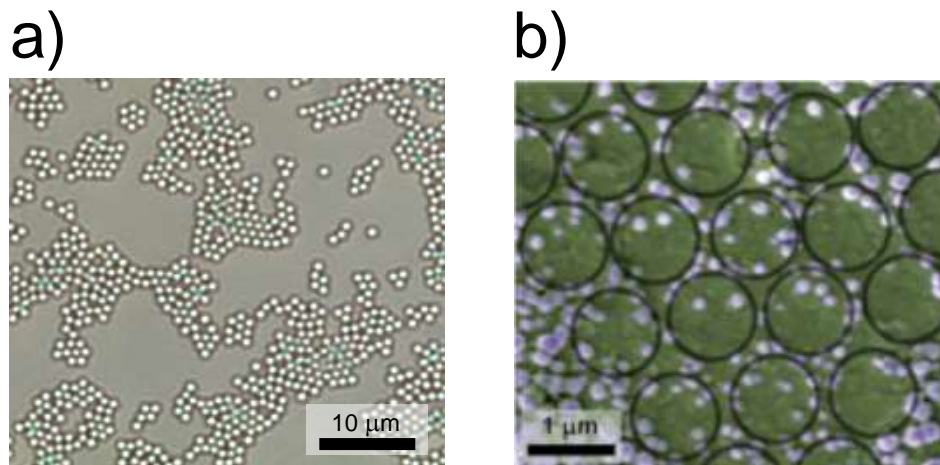


Figure 4.14: Optical microscopy of 1 μm polystyrene spheres spin-coated on ITO on glass (a). False-color SEM image of Ag-Cu electrodeposits (B, purple) on ITO with a Pt SAM patterned with 1 μm polystyrene spheres. The Pt SAM does not deposit where the polystyrene spheres once were (indicated by black circles), leaving bare ITO (B, green). For the most part, the Ag-Cu electrodeposits grow selectively on the Pt SAM.

The ability to pattern reversible metal electrodeposition for dynamic windows on the microscale could be used to tune the optical properties of metal-based dynamic windows. For example, reversible diffraction gratings, which have applications in various optical devices, could be constructed by patterning the Pt SAM on the microscale in the shape of diffraction gratings.[108] Further improvements of the concept shown here could enable nanoscale electrodeposition patterning, which would allow for device optics to be tuned through plasmonic effects if a plasmonically active metal such as Ag is electrodeposited.

4.4. Conclusion

In conclusion, we have demonstrated that there is significant flexibility in the architecture of dynamic windows based on reversible metal electrodeposition. The use of a metal frame counter electrode allows windows with two working electrodes to be constructed. Since metal electrodeposition occurs on both window panes, these devices possess superior contrast ratios to their single deposition counterparts. We also show that metal electrodeposition selectively occurs on the Pt nanoparticles used to modify ITO electrodes. This selectivity enables the patterning of reversible metal electrodeposition on both the macroscopic and microscopic scale.

Chapter 5: Dual Tinting Dynamic Windows using Reversible Metal Electrodeposition and Prussian Blue

5. 1. Introduction

Energy efficiency is a crucial component in fostering the transition to a renewable energy economy. [31] Dynamic windows, which possess electronically controlled transparency, are a promising technology to increase the energy efficiency of buildings. Studies have shown that the incorporation of well-functioning dynamic windows leads to an average energy savings of 10% in buildings due to reductions in lighting, heating, and cooling uses. [32] Although dynamic windows utilizing electrochromic materials have been investigated for over 30 years, these devices are not commercialized on a large scale due to the difficulty of a single technology achieving the durability, cost, color, switching time, and dynamic range needed for practical windows. [44, 47]

Compared to electrochromic windows, reversible metal electrodeposition is an underdeveloped strategy for constructing dynamic windows that offers several important advantages.[60, 104, 105] In one form, these devices darken via the electrochemical movement of metal from a metal counter electrode frame to the center of a transparent conducting pane of tin-doped indium oxide (ITO) on glass. [106] To turn the windows transparent, the polarity of the voltage applied to the device is switched such that the metal on the ITO redissolves into the electrolyte and replates on the counter electrode frame. Since metals are almost completely opaque at a thickness of only 20-30 nm, metal-based dynamic windows switch rapidly with high optical contrast. [39, 48] Furthermore, many metals are photostable, chemically inert, and color neutral. [55] These

properties enabled us to develop 100 cm² dynamic windows that switch between clear and black states in one minute and do not degrade after thousands of cycles. [36, 109]

The major challenging hindering the development of robust dynamic windows based on metal electrodeposition is the difficulty associated with electrodepositing uniform metal thin films on a large scale. We previously demonstrated that a self-assembled monolayer (SAM) of Pt nanoparticles functions as an array of transparent inert seeds for metal electrodeposition on ITO electrodes. [40] Although the presence of Pt nanoparticles significantly increases device uniformity, the requirement for metal ions to migrate laterally across the device area during switching still limits device scalability. To overcome this issue, we recently reported a new architecture for metal-based dynamic windows that pairs metal electrodeposition on the working electrode with a NiO counter electrode that intercalates Li⁺ ions. [109] The NiO counter electrode facilitates transverse ion migration between the two window panes as opposed to lateral ion migration from the window frame. Although NiO is an electrochromic material that tints upon OH⁻ intercalation, the acidic nature of reversible metal electrodeposition electrolytes requires the NiO to intercalate cations such as Li⁺, a process which only gives rise to very weak electrochromism. [50, 61-64]

In this manuscript, we develop dynamic windows that combine reversible metal electrodeposition on the working electrode with an electrochromic Prussian blue counter electrode that both compensates for charge passed during switching and becomes dark during metal electrodeposition. In this manner, both the working and counter electrodes tint during device switching, which dramatically increases the switching speed of these devices while still maintaining the transverse ion migration needed for large scale devices.

We demonstrate that 25 cm² devices using Prussian blue switch states with high optical contrast (~67.5%) in 3 s, which is nearly 20 times faster than previous metal-based dynamic windows using NiO.[109]

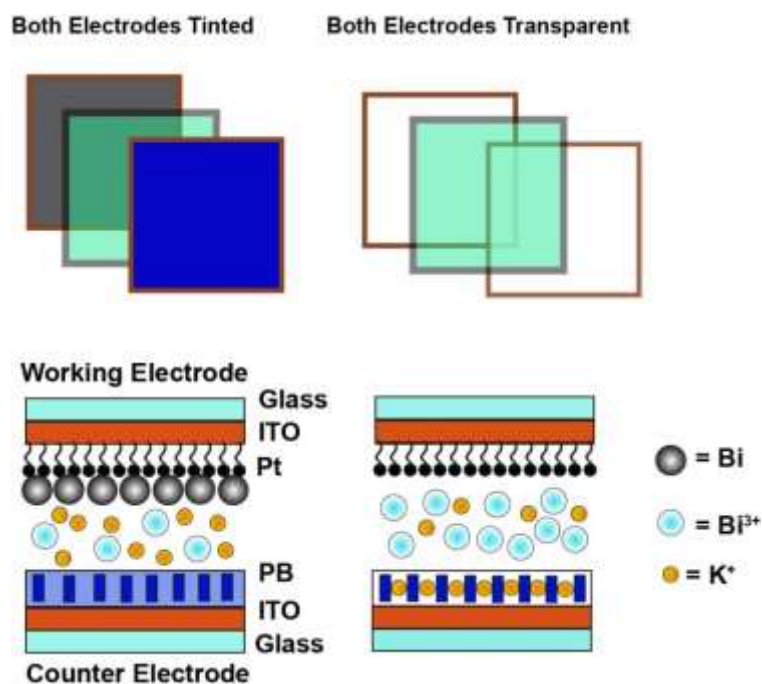
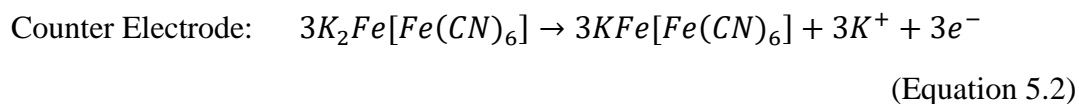
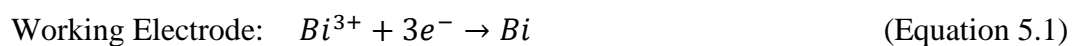


Figure 5.1. Schematic of dual tinting dynamic windows that facilitate reversible Bi metal electrodeposition on an ITO on glass working electrode modified with a SAM of Pt nanoparticles and a Prussian blue on ITO on glass counter electrode.



5. 2. Result and Discussion

5. 2. 1. Dual Tinting Device Architecture

Figure 5.1 displays a schematic of dynamic windows that combine reversible metal electrodeposition with Prussian blue counter electrodes. The working electrode consists of ITO modified with a SAM of Pt nanoparticles, which facilitate uniform metal electrodeposition on the microscale. [36, 40] The counter electrode consists of ITO coated with a ~150 nm thick layer of Prussian blue that serves as both an ion intercalation layer and an anodically tinting material. In between the two window panes lies an aqueous-based gel electrolyte containing Bi^{3+} ions needed for metal electrodeposition and K^+ ions needed for intercalation into the Prussian blue electrode (Equations 5.1-5.2).

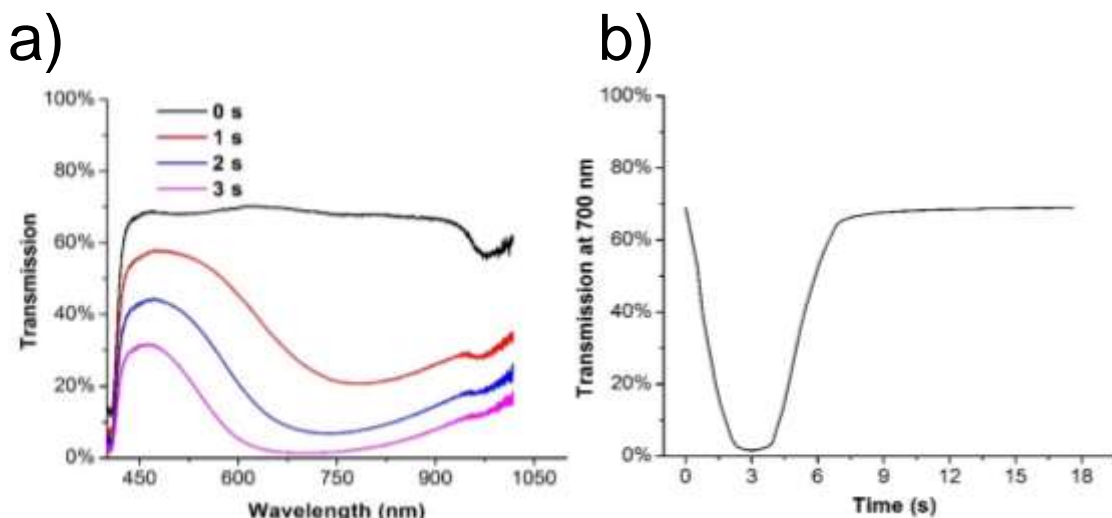


Figure 5.2. Transmission of a 25 cm² dynamic window with a Pt-modified ITO on glass working electrode, a PB on ITO on glass counter electrode formed using 6 minutes of electrodeposition, and a Bi gel electrolyte as a function of wavelength after 0 s (black), 1 s (red), 2 s (blue), and 3 s (pink) of window tinting at -2 V (a). Transmission of the same window at 700 nm during 3 s of window tinting at -2 V followed by 15 s of window lightening at +1.5 V (b).

We constructed 25 cm² metal-based dynamic windows using a Prussian blue counter electrode and evaluated their optical properties. In their clear state, the windows

possess about 60-70% transmission from 425-1000 nm (Figure 5.2a, black line). Upon application of -2 V for 3 s, the transmission of the devices decreases significantly (Figure 5.2a and Supporting Figure 12.4.1). Due to the Prussian blue counter electrode, the optical contrast of the device from 425-550 nm is not as large as from 550-1000 nm, which results in a dark blue appearance of the windows in their tinted state. Future work will explore the use of mixtures of Prussian blue analogs containing transition metals other than Fe that are known to exhibit superior color neutrality.[110-112] Figure 5.2b displays the transmission of the device during switching at 700 nm, the wavelength at which the window exhibits maximum optical contrast. The transmission at 700 nm decreases from ~69% to ~1.5% (~67.5% optical contrast) during the 3 s of device tinting at -2.0 V. This result demonstrates that dynamic windows using reversible metal electrodeposition and Prussian blue counter electrodes switch faster than any other metal-based dynamic window at this scale. By comparison, the previous fastest reported metal-based 25 cm² dynamic windows take ~17 s to switch to the same optical contrast (~67.5%).[113] Furthermore, previously reported 25 cm² dynamic windows combining reversible metal electrodeposition with a NiO ion-intercalation counter electrode take ~55 s to reach the same optical contrast.[109] Switching the polarity of the windows described here to +1.5 V causes the transmission at 700 nm to return to its original value within 15 s. However, the first 90% of the device lightening profile is particularly fast and occurs within 3.5 s. Importantly, both the metal electrodeposition and Prussian blue darkening processes occur uniformly, which allow for the window to be switched to any desired intermediate transparency (Figure 5.3).



Figure 5.3. Photographs of a 25 cm² metal-based hybrid dynamic window with a Prussian blue counter electrode during switching at -2 V for 0 s (a), 1 s (b), and 3 s (c).

5. 2. 2. *Thin Film Characterization*

To determine the origin of device tinting, we imaged the electrodes in their darkened states using scanning electron microscopy-energy-dispersive X-ray spectroscopy (SEM-EDX). A SEM image of the ITO working electrode contains an array of irregularly-shaped particles that are ~500 nm in size (Figure 4a). EDX analysis of the electrode demonstrates that these particles are electrodeposited Bi metal (Supporting Figure 12.4.2). A SEM image of the Prussian blue counter electrode displays a platelet-like morphology similar to previously reported images, and X-ray diffraction (XRD) analysis further confirms the presence of Prussian blue (Supporting Figure 12.4.3).[114] Atomic force microscopy (AFM) images of the Prussian blue counter electrode display a similar morphology and show that the film is ~150 nm thick (Supporting Figure 12.4.4). The use of thicker or thinner Prussian blue films in dynamic windows give devices that possess inferior optical contrast (Supporting Figure 12.4.5-12.4.6). Taken together, these results demonstrate that metal electrodeposition occurs on the working electrode while the Prussian blue counter electrode tints when the windows darken at -2 V. Photographs

of a device with a liquid electrolyte in a cuvette further prove that both electrodes tint upon application of -2 V (Supporting Figure 12.4.7).

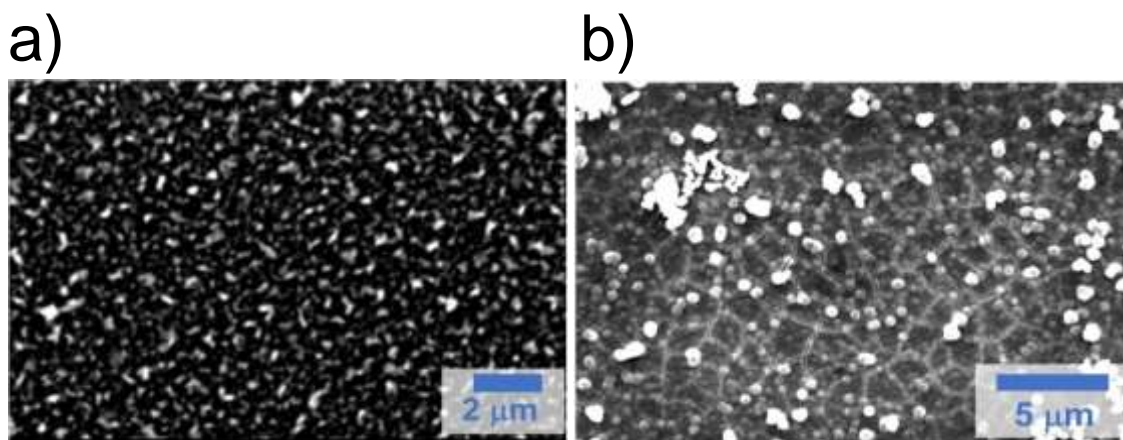


Figure 5.4. Scanning electron microscopy images of the working (a) and counter (b) electrodes of a hybrid dynamic window in its tinted state.

5. 2. 3. *Electrolyte Design*

Many previously reported windows based on reversible metal electrodeposition utilize Bi-Cu electrolytes containing BiCl_3 , CuCl_2 , LiBr , and a low concentration of HCl .^[104, 105] The LiBr and HCl aid in dissolving Bi^{3+} ions by favoring the formation of soluble Bi bromide complexes and eliminating the formation of insoluble $\text{Bi}(\text{OH})_3$, respectively.^[36] To evaluate the chemical reactions and cycling stability of the Prussian blue thin films in this electrolyte, we performed spectroelectrochemistry in three-electrode cells using various components of the Bi-Cu electrolyte. First, we conducted cyclic voltammetry (CV) using a Prussian blue on ITO working electrode in an electrolyte containing LiBr and HCl (Figure 5.5a). The CVs show one redox couple with a midpoint potential of about +0.08 V, which is due to the oxidation and reduction of $\text{Fe}(\text{CN})_6^{4-}/\text{Fe}(\text{CN})_6^{3-}$ in Prussian blue. The current density of both the anodic and cathodic peaks decreases as the electrode cycles, which is indicative of film degradation.

Furthermore, the voltage separation between the two peaks is about 220 mV, and the average full width at half maximum (FWHM) of the peaks is 126 mV. The theoretical peak separation for redox centers adsorbed onto electrodes is 0 mV since diffusion to the electrode surface does not dictate the shape of the CV.[115] For a one electron redox couple adsorbed onto an electrode, the theoretical FWHM of the peaks is 90.6 mV at room temperature. [116] Both the peak separation and FWHM values for the Prussian blue thin film cycled in an electrolyte containing LiBr and HCl are significantly greater than these theoretical values. These findings indicate that Li⁺ intercalation is kinetically slow and not fully reversible. Figure 5.5b displays the transmission at 700 nm of the Prussian blue-modified electrode during four CV cycles. The initial transmission of the electrode is ~10% and increases to a maximum of ~77% upon oxidation and conversion to the Prussian white form. However, the minimum electrode transmission steadily increases during cycling (Figure 5.5b, red arrow). This finding further demonstrates that Li⁺ intercalation in the Prussian blue film is not fully reversible.

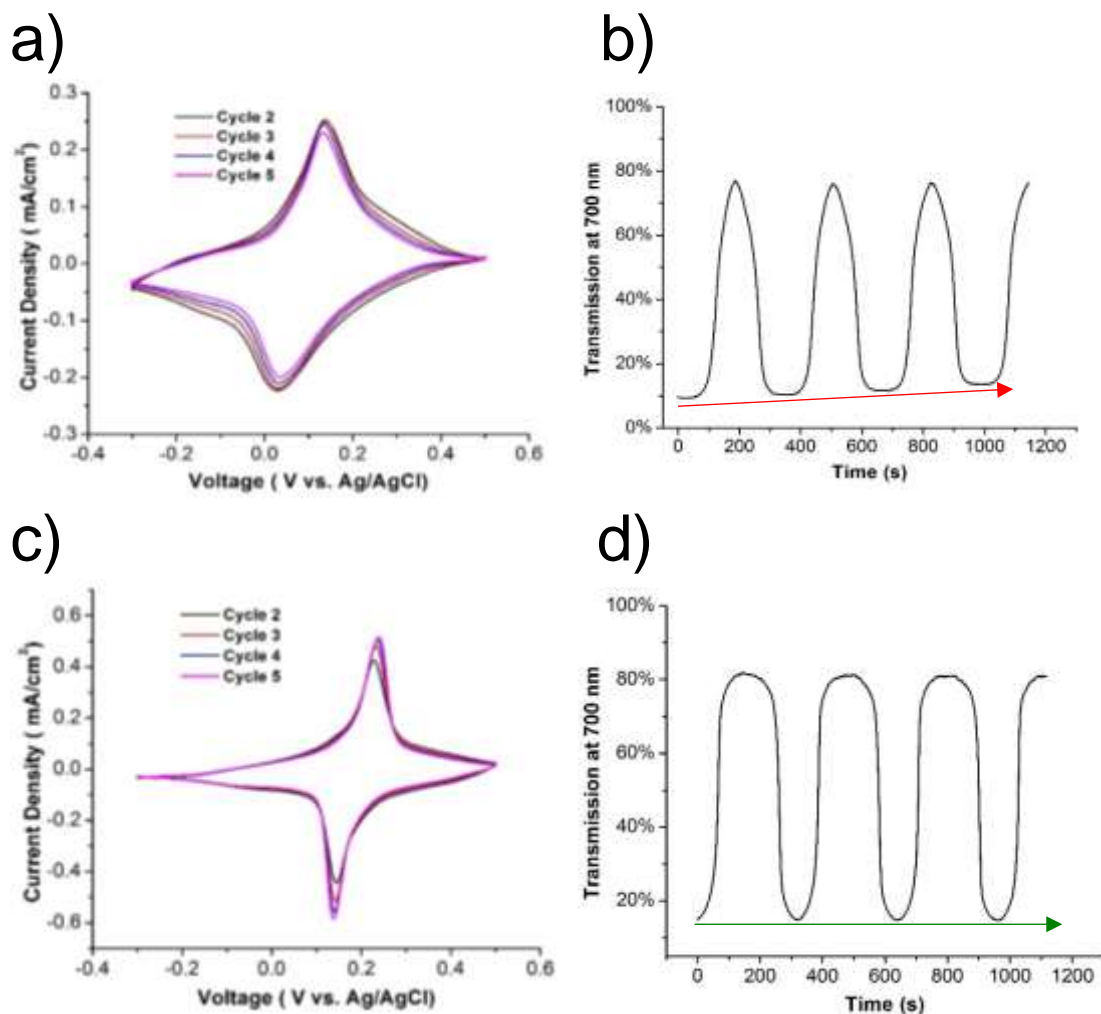


Figure 5.5. Cyclic voltammograms (a, c) and transmission at 700 nm (b, d) of a Prussian blue on ITO on glass working electrode in a three-electrode cell in a liquid electrolyte containing 0.2 M LiBr (a, b) or KBr (c, d) with 100 mM HCl at a scan rate of 5 mV/s.

In an effort to increase the reversibility of the insertion chemistry of Prussian blue, we evaluated the spectroelectrochemistry of the Prussian blue on ITO working electrode in an electrolyte containing KBr and HCl. CVs in this electrolyte display a redox couple with a midpoint potential of about +0.19 V, which is also due to the oxidation and reduction of $\text{Fe}(\text{CN})_6^{4-}/\text{Fe}(\text{CN})_6^{3-}$ (Figure 5c). This shift in redox potential compared to the CVs in the LiBr electrolyte is consistent with previous studies, which

show that the nature of the alkali metal ion inserted into Prussian blue structures can significantly alter their redox potentials.[117] Unlike the CVs using LiBr, the peak current densities increase gradually over the course of four cycles due to a narrowing of the peak FWHMs. For the CVs in the KBr electrolyte, the average FWHM of the peaks is 84 mV, and the peak separation is 57 mV. These values are closer to the theoretical values discussed previously for surface-adsorbed redox centers and indicate that K^+ intercalation in Prussian blue is more kinetically facile and reversible than Li^+ intercalation. Moreover, the transmission at 700 nm of the electrode is fully reversible and cycles consistently between ~15% and ~82% (Figure 5.5d). Taken together, these results indicate that K^+ intercalation in Prussian blue is reversible both electrochemically and optically.

Having demonstrated the reversibility of K^+ intercalation in Prussian blue, we next determined if the electrodes are compatible with a modified version of the Bi-Cu electrolyte known to facilitate rapid and reversible metal electrodeposition that contains KBr instead of LiBr. The black line in Figure 5.6 displays a CV of a Prussian blue working electrode in the Bi-Cu electrolyte with KBr.[36] The large cathodic feature with an onset potential of about -0.1 V is due to Bi and Cu electrodeposition on top of the Prussian blue thin film. The correspondingly large anodic peak at about +0.07 V is due to the oxidation of the electrodeposited Bi and Cu metal to Bi and Cu ions. The shapes of these two main features of the CV are typical for metal electrodeposition and stripping processes.[51] The CV also contains a highly asymmetric wave centered around +0.3 V, which is due to K^+ intercalation in the Prussian blue. Since we demonstrated K^+ intercalation is reversible in Prussian blue in electrolyte without Bi^{3+} and Cu^{2+} (Figure

5.5c and 5.5d), the irreversibility of this wave in the Bi-Cu electrolyte indicates that the K^+ intercalation process is impeded by the presence of Bi^{3+} and Cu^{2+} . A CV of Prussian blue in an electrolyte with Cu^{2+} and K^+ shows peaks indicative of reversible Cu electrodeposition, but does not display any redox wave associated with K^+ intercalation (Figure 5.6, blue line). This result demonstrates that Cu^{2+} is incompatible with K^+ intercalation in Prussian blue. We hypothesize that Cu^{2+} reacts with the Prussian blue to form a Cu-substituted Prussian blue analog that is redox inactive in this electrolyte (Equation 5.3), which causes the electrode to exhibit very little electrochromism during cycling (Supporting Figure 12.4.8). Indeed, previous researchers have synthesized Cu-substituted Prussian blue analogs by adding Cu^{2+} to Prussian blue.[118] A CV of Prussian blue in an electrolyte with Bi^{3+} and K^+ exhibits peaks associated with reversible Bi electrodeposition and also displays a reversible K^+ intercalation redox couple centered around +0.3 V (Figure 5.6, red line). This result indicates that the presence of Bi^{3+} does not hinder K^+ intercalation in Prussian blue and further corroborates the finding that Cu^{2+} is incompatible with K^+ intercalation. Previous studies fabricating K^+ batteries using Bi anodes and Prussian blue cathodes further suggest that Bi^{3+} is compatible with K^+ intercalation in Prussian blue albeit in a nonaqueous electrolyte. [119]

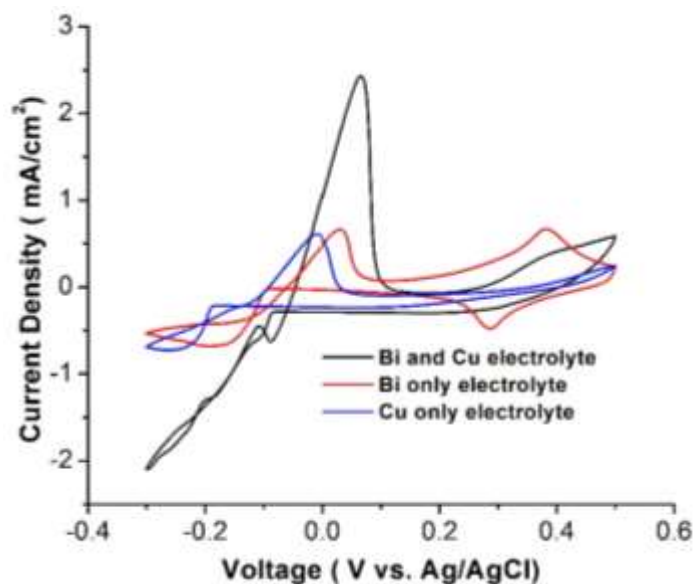
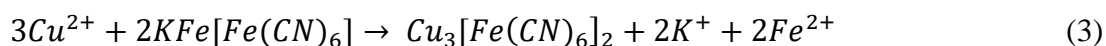


Figure 5.6. Cyclic voltammograms of Prussian blue on ITO on glass working electrode in the Bi-Cu (black), Bi only (blue), and Cu only (red) electrolytes in a three-electrode cell at a scan rate of 5 mV/s.



5. 2. 4. Cycling Durability

Conclusions drawn from the three-electrode spectroelectrochemical data above allowed us to design an electrolyte for two-electrode dynamic windows that facilitates both reversible metal electrodeposition on the working electrode and reversible K^+ intercalation in the Prussian blue counter electrode. This electrolyte contains BiCl_3 , KBr , and HCl without any CuCl_2 since we determined Cu^{2+} is incompatible with Prussian blue. Using this electrolyte, we evaluated the cycle life of 25 cm^2 dynamic windows (Figure 5.7). The windows switch with high optical contrast with minimal degradation over the course of 1,500 cycles. We note that the maximum transmission decreases from an initial value of $\sim 70\%$ to $\sim 66\%$ during the 1,500 cycles (Figure 5.7, red line). This degradation in

the transparency of the clear state is due to the slow metal dissolution kinetics of metal electrolytes containing only Bi. [36] In other words, Bi metal slowly accumulates on the working electrode during cycling, which decreases its maximum transmission. To overcome this issue, future work will focus on the development of Bi electrolytes modified with chelating ligands that accelerate the kinetics of Bi metal electrodisolution.

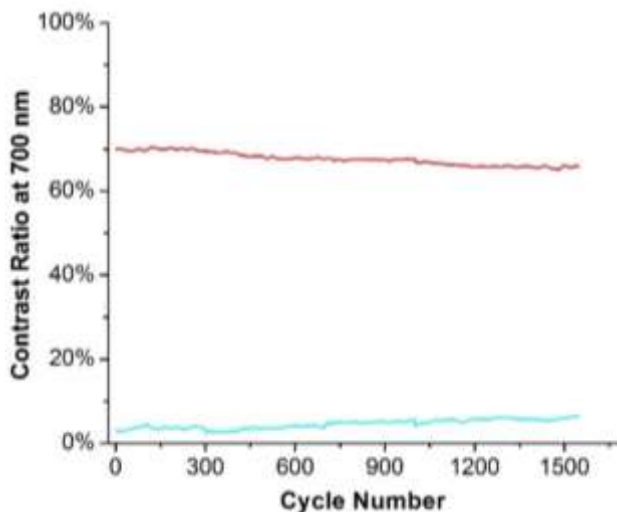


Figure 5.7. Maximum (red line) and minimum (cyan line) transmission of a 25 cm² dynamic window with a Pt-modified ITO on glass working electrode and a Prussian blue on ITO on glass counter electrode over the course of 1,500 cycles.

5. 3. Experimental

5.3.1. General Procedures

Chemicals were received from commercial sources and used without further purification. A VSP-300 Biologic potentiostat was used for conducting electrochemical studies. Tin-doped indium oxide (ITO) substrates were received from Xinyan Technology, Inc. with reported sheet resistances of 15 Ω sq⁻¹. For three-electrode experiments, the reference electrode used was a ‘no-leak’ Ag/AgCl (3 M KCl) reference electrode (eDAQ), and Pt wire was used as a counter electrode. ITO substrates were cleaned by sonicating with an

aqueous solution containing 5% Extran for 5 min followed by sonication in isopropanol for 5 min. The substrates were then rinsed with isopropanol and dried using a stream of air.

To form Pt-modified ITO substrates, cleaned ITO substrates were immersed in a solution of 10 mM 3-mercaptopropionic acid in ethanol for 24 h. This molecule is known to form a thiol-terminated self-assembled monolayer (SAM) on ITO substrates.[40] After rinsing the substrates with ethanol and de-ionized (DI) water, they were immersed in a Pt nanoparticle (3 nm diameter, Sigma-Aldrich) dispersion diluted with water in a ratio of 1:4. Finally, the ITO substrates were rinsed with DI water and annealed in air at 250 °C for 20 min.

5.3.2. Electrodeposition of Prussian Blue Thin Films

Prussian blue thin films were deposited electrochemically on ITO on glass surfaces using a modified literature procedure.[120] First, the edges of the ITO substrates were covered with conductive Cu tape. The Cu tape on the perimeter was subsequently covered with two layers of Kapton tape to ensure no Cu ions contaminated the electrolyte. Prussian blue was electrodeposited on the ITO electrode by applying +0.5V for 1 min, 6 min, or 10 min in an aqueous electrolyte containing 5 mM FeCl₃, 5 mM K₃Fe(CN)₆, and 200 mM KCl. Finally, the Prussian blue-modified ITO substrates were rinsed gently with water and set to dry in air.

5. 3. 3. Electrodeposition of Bi Thin Films

For Bi electrodeposition on Pt-modified ITO substrates, clean Pt-modified ITO surfaces were covered with Cu tape around the perimeter followed by two layers of Kapton tape to ensure no Cu ions were contaminated the electrolyte during window switching. The aqueous electrolyte used for Bi electrodeposition contained 5 mM BiCl₃, 1 M KBr, and 10 mM HCl. Chronoamperometry at -0.6 V was applied for 60 s in this electrolyte to electroplate Bi.

5. 3. 4. Construction of 25 cm² Two-Electrode Dynamic Windows

Dynamic windows were constructed in their opaque state using a Bi- and Pt-modified ITO on glass working electrode and a Prussian-blue modified ITO on glass counter electrode. The Bi gel electrolyte was made by adding 3.0% hydroxyethylcellulose by weight to an aqueous liquid electrolyte containing 15 mM BiCl₃, 3 M KBr, and 10 mM HCl. Butyl rubber Solargain edge tape separated the two device electrodes with an interelectrode spacing of ~3 mm.

5. 3. 5. Materials Characterization

Transmission spectra were measured with an Ocean Optics FLAME-S-VIS-NIR or an Ocean Optics FLAME-S-UV-VIS-ES spectrometer coupled with an Ocean Optics halogen light source (HL-2000-FHSA) or an Ocean Optics DH-mini UV-Vis-NIR light source. Photographs of windows were taken with a Nikon D5000 Digital Camera. Atomic force microscopy (AFM) images were obtained using a Nanosurf EasyScan 2 microscope operated in contact mode using a silicon tip with an aluminum reflective coating

(ContAl-G, TedPella, Inc.). SEM and EDX spectra were obtained using a JEOL JSM-6010LA microscope operated at an accelerating voltage of 20 kV. X-ray diffraction (XRD) was performed using a Bruker D2 X-ray Diffractometer.

5. 4. Conclusion

In summary, we constructed dynamic windows that combine reversible Bi electrodeposition on the working electrode with an anodically coloring Prussian blue counter electrode. The simultaneous tinting of both window panes enables 25 cm² devices to switch with an optical contrast of ~67.5% in 3 s, making them the fastest reported metal-based dynamic windows on this scale. This work demonstrates that combining the advantageous optical properties of electrodeposited metals with traditional electrochromic materials is a promising design for fast-switching dynamic windows.

Chapter 6: Optically Switchable Thin Films based on Reversible Cu and Au Electrodeposition

6. 1. Introduction

Electronically controllable thin films that switch between transparent and opaque states have applications in dynamic windows, tintable sunglasses, and optical gating devices.[121, 122] To date, the majority of research on dynamic thin films has focused on electrochromic materials, which change transmission properties upon application of a voltage.[47, 66] The most widely studied class of electrochromic materials are the transition metal oxides such as WO_3 . [45, 123] Electrochromic organic polymers including polythiophenes and polypyrroles and small molecule organic compounds such as viologens and triphenylamines. [43, 46, 124, 125] However, devices harnessing electrochromic materials, be they inorganic or organic, suffer from problems associated with less-than-ideal optical contrast, poor durability, high cost, or poor color rendering.[44, 50]

Dynamic thin films containing polymer dispersed liquid crystals (PDLCs) are an alternative to those containing electrochromic materials. Although many PDLCs possess impressive millisecond switching times, they switch between a transparent state and a bright hazy state, making them unsuitable for many applications where maintaining image fidelity is important. [101]

Reversible metal electrodeposition is a third strategy used to create dynamic thin films. This approach relies upon the electrochemical movement of metal between a solid metal electrode and a transparent conducting electrode that is facilitated by an electrolyte

containing metal ions. [106] The geometry of the solid metal electrode is typically engineered such that it is oriented around the perimeter of the transparent electrode so that it does not obstruct its transparency. One advantage of using metal for dynamic thin films is the high extinction coefficients of metals, which causes smooth metal films that are only 20-30 nm thick to be almost completely opaque. [39, 109] Electrochromic materials, on the other hand, must be several hundreds of nanometers thick to achieve similar optical contrast. [123] Furthermore, many metals are inert and color neutral, which together with their opacity, make them promising candidates for light-modulating devices. [55]

One large challenge hindering the development of metal-based dynamic thin films is enabling fully reversible metal electrodeposition on transparent conducting electrodes such as tin-doped indium oxide (ITO) and fluorine-doped tin oxide (FTO) on glass. These transparent electrodes contain heterogeneous surface chemistry that frequently results in nonuniform metal nucleation and growth that is difficult to control. [126] We previously demonstrated that by modifying ITO electrodes with a self-assembled monolayer (SAM) of Pt nanoparticles, the electrodeposition morphology could be more readily controlled and that the tinting uniformity of the device correspondingly increased. [40, 48] The Pt nanoparticles function as a uniformly distributed array of inert metal seeds on which metal electrodeposition nucleation preferentially occurs.

To achieve reversible metal electrodeposition, these Pt-modified transparent electrodes must be coupled with electrolytes that also facilitate reversible and uniform metal electrodeposition and dissolution. Towards this end, both aqueous and nonaqueous electrolytes containing metal ions have been investigated. [60, 104, 105] Halide-based

aqueous electrolytes are among the most promising and take advantage of improved reversible electrodeposition kinetics imparted by the stabilization of Cu(I) intermediates by halides during both deposition and stripping processes. [127] However, aqueous electrolytes that contain Cu as the only redox-active metal ion are inadequate for two reasons. First, the red color of Cu renders it unsuitable for most optical applications, and second, simple halide-based Cu electrolytes are not fully optically reversible (*vide infra*).

To improve both the color neutrality of the electrodeposits and the optical reversibility of the electrodeposition and dissolution processes, a second redox active metal ion can be incorporated into the electrolyte. Initial work using this approach for dynamic window applications focused on Pb or Ag as the secondary metal. [40] However, the use of Pb is impractical due to its toxicity, and the solubility of Ag ions is limited in halide-based aqueous systems. Other studies targeting display applications and more recent work aimed at dynamic window applications utilized mixtures of Cu and Bi ions. [37, 104, 105] Although these Cu-Bi electrolytes enable rapid and reversible metal electrodeposition, highly acidic electrolytes are needed to solubilize the Bi ions. The low pH values ($\text{pH} \leq 2$) of these electrolytes increases the propensity for H_2 production, thus limiting the electrochemical window of the devices.

In this manuscript, we develop a new class of binary Cu aqueous electrolytes that facilitate optically reversible metal electrodeposition on ITO on glass electrodes. As opposed to Pb, Ag, or Bi, these electrolytes contain Au as the secondary metal. We demonstrate that the addition of Au ions to the electrolyte increases the optical reversibility of metal electrodeposition and stripping processes. Au ions possess good solubility in aqueous halide systems without added acid and are nontoxic. Although Au is

prohibitively expensive for large window applications, its use may be suitable for other small optoelectronic devices.

6.2. Experimental

Chemicals were received from commercial sources and used without further purification. Electrochemical studies were carried out using a VSP-300 Biologic potentiostat. For experiments utilizing three electrodes, electrochemical potentials were measured and reported with respect to a “no-leak” Ag/AgCl (3 M KCl) reference electrode (eDAQ). Electrodes consisting of ITO on glass (Xin Yan, Inc., $10 \Omega \text{ sq}^{-1}$) were cleaned by successively sonicating in de-ionized H₂O with 5% Extran solution for 5 min and isopropanol for 5 min. The electrodes were subsequently dried under a stream of air. The cleaned ITO on glass electrodes were first immersed in an ethanolic solution of 10 mM 3-mercaptopropionic acid for 24 hours. Subsequently, the substrates were rinsed with ethanol and water before immersing them for 24 hours in a Pt nanoparticle solution (Sigma Aldrich, 1000 ppm Pt nanoparticles 3 nm in diameter) that was diluted 1:4 with water. Two-electrode devices utilized a Pt-modified ITO on glass working electrode and a Au wire counter electrode. For all experiments, the immersed geometric surface area of the working electrode was 1.74 cm^2 , and electrochemical cells were assembled in a 2.0 cm by 2.0 cm by 2.0 cm glass cuvette. The standard Cu-Au electrolyte consisted of NaCl (3000 mM), NaAuCl₄ (5 mM), CuCl₂ (22.5 mM), NaBr (400 mM), and NaI (1 mM) dissolved in de-ionized water. Transmission spectra were measured with an Ocean Optics FLAME-S-VIS-NIR or FLAME-S-UV-VIS-ES spectrometer coupled with an Ocean Optics light source (HL2000-FHSA or DH-MINI).

6.3. Results and Discussion

6.3.1. Two-Electrode Studies of the Cu-Au Electrolyte

The Cu-Au electrolyte we developed facilitates optically reversible metal electrodeposition and contains CuCl_2 , NaAuCl_4 , NaCl , NaBr , and NaI dissolved in water. To demonstrate the optical reversibility of this electrolyte, we first conducted spectroelectrochemical measurements using a cell containing a practical two-electrode device with an ITO on glass working electrode modified with a SAM of Pt nanoparticles and a Au wire counter electrode. The transmission at 600 nm of the working electrode decreases when a reducing potential of -1.65 V is applied to induce Cu and Au electrodeposition (Figure 6.1a). As metal electrodeposition occurs, the transmission at 600 nm of the working electrode decreases from ~91% to ~32% over the course of 60 s. Reversing the polarity to an oxidizing potential of +1.2 V rapidly restores the transparency of the working electrode to its original value. This restoration of optical transparency is due to metal dissolution back into the electrolyte and the formation of Cu^{2+} and Au^{3+} on the working electrode with concomitant metal electrodeposition occurring at the counter electrode. The metal stripping processes off of the Pt-modified ITO working electrode is particularly fast, and it only takes ~4 s for the electrode to switch 90% of the way to its original transparency. Figure 1b displays the corresponding chronoamperometry during the switching process. By integrating the charge passed during the metal electrodeposition portion of the chronoamperometry and comparing it to the magnitude of charge passed during metal stripping, the Coulombic efficiency, which is the measure of the electrochemical reversibility of a reaction, is calculated. In this case,

the calculated Coulombic efficiency is only ~52% with substantially more deposition charge passed than stripping charge. Taken together, the results in Figure 1 demonstrate that although the Cu-Au electrolyte enables optically reversible metal electrodeposition, the process is not electrochemically reversible. In order to interrogate the discrepancy between the optical reversibility of the electrolyte and its lack of electrochemical reversibility, we performed an array of cyclic voltammetry (CV) experiments using a variety of different electrolyte compositions (*vide infra*).

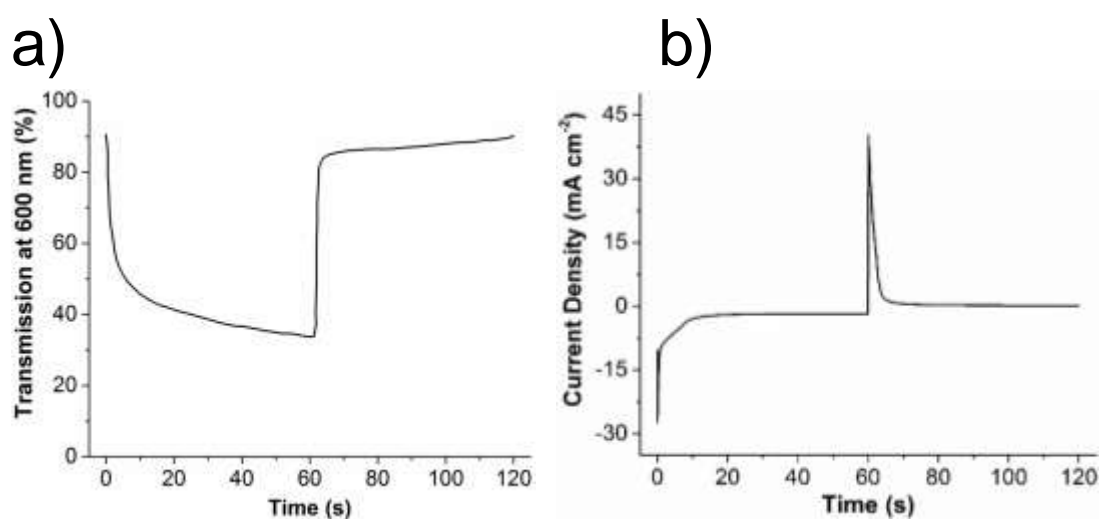


Figure 6.1: Transmission at 600 nm (a) and current density (b) during the first switching cycle of a Pt-modified ITO on glass working electrode in the Cu-Au electrolyte in a two-electrode cell with a Au wire counter electrode. The potential was held at -1.65 V for 60 s to induce metal electrodeposition followed by +1.2 V for 60 s to elicit metal stripping.

Figure 6.2a displays the transmission as a function of wavelength during metal electrodeposition in the two-electrode cell with the Cu-Au electrolyte. The data show that the metal electrodeposition effectively modulates light across the visible light spectrum.

However, the transmission profiles from 400-800 nm are not entirely flat with a noticeable peak in transmission at ~550 nm (Figure 6.2a red and blue lines). Figure 6.2b displays transmission curves for a 20 nm thick pure Au film (black line) and a 20 nm thick pure Cu film (red line) that are calculated using previously reported optical constants.[128] These transmission curves are compared to the transmission profile obtained after 60 s of metal electrodeposition on the Pt-modified ITO working electrode. A thin Cu film exhibits a transmission peak at ~575 nm, which gives rise to the characteristic red color of Cu. Similarly, a thin Au film possesses a transmission peak at ~500 nm, giving rise to gold's characteristic color. The optical data recorded for the 60 s metal electrodeposition thin film exhibits a peak transmission value (~550 nm) that is in between those of the positions of the peaks for the pure Cu and Au thin films because a mixture of Cu and Au is electrodeposited from the Cu-Au electrolyte.

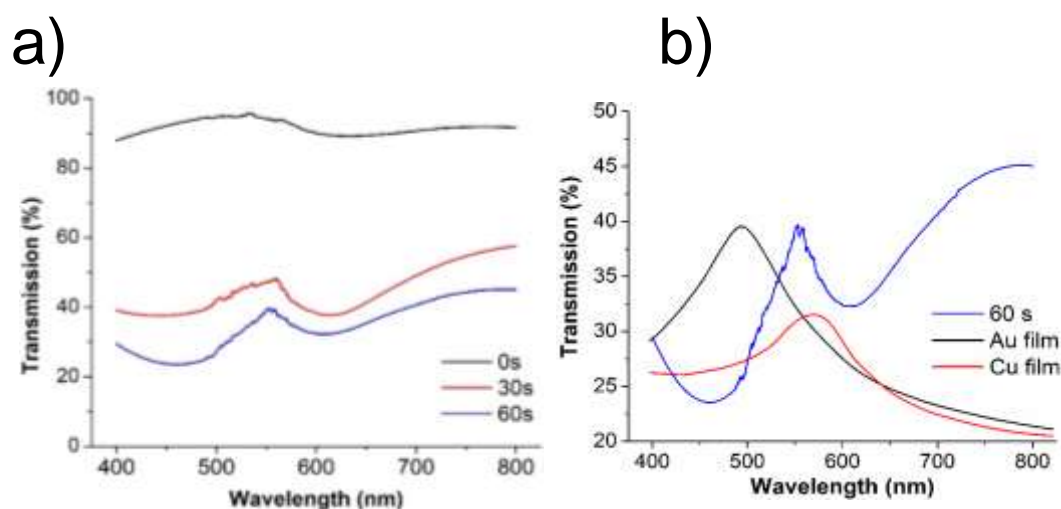


Figure 6.2: Transmission as a function of wavelength during metal electrodeposition on a Pt-modified ITO on glass working electrode in the Cu-Au electrolyte in a two-electrode cell with a Au wire counter electrode (a). The potential was held at -1.65 V for 60 s to induce metal electrodeposition. Calculated transmission values (b) of 20 nm thick films of Au (black) and Cu (red) as compared to the Cu-Au film obtained after 60 s of electrodeposition (blue).

Having demonstrated that the Cu-Au electrolyte supports optically reversible metal electrodeposition in a practical two-electrode configuration, we next evaluated the cycleability of the system. Figure 6.3 displays the maximum and minimum transmission values at 600 nm as well as the optical contrast, which is defined as the difference between the maximum and minimum transmission values, over the course of 100 chronoamperometric cycles. Although the contrast ratio remains relatively constant during the cycling, there is significant variation in both the maximum and minimum transmission values suggesting that dynamic processes occur. These processes include side reactions as evidenced by the <100% Coulombic efficiency of the electrolyte that alter the optical properties of the electrolyte during cycling.

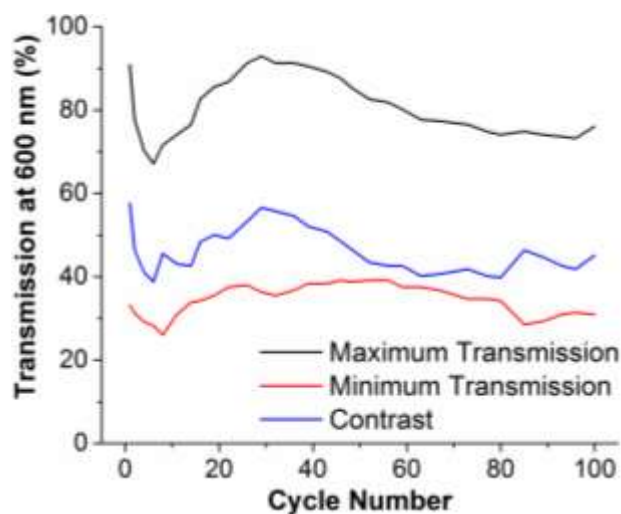


Figure 6.3: Maximum (black line) and minimum (red line) transmission values at 600 nm of the Pt-modified ITO on glass working electrode in the Cu-Au electrolyte in a two-electrode cell with a Au wire counter electrode over 100 switching cycles. For each cycle, the potential was held at -1.65 V for 60 s to induce metal electrodeposition followed by +1.2 V for 60 s to elicit metal stripping. The blue line plots the optical contrast or difference between the maximum and minimum transmissions during the 100 switching cycles.

6.3.2. Three-Electrode Studies of the Cu-Au Electrolyte

To interrogate the electrochemical reactions occurring in the Cu-Au electrolyte during metal electrodeposition and stripping, we performed systematic CV experiments in conjugation with optical measurements in three-electrode cells. The CV of a Pt-modified ITO on glass working electrode exhibits a number of different cathodic and anodic features (Figure 6.4a). The first reductive peak that occurs at about +0.5 V elicits a corresponding decrease in the transmission at 600 nm of the working electrode (Figure 6.4b). The second reductive peak in the CV occurring at about +0.25 V does not correspond to a similar inflection point in the transmission-voltage curve but rather the transmission continues to decrease at a constant rate. At around -0.25 V, the onset of a third reductive feature in the CV occurs which elicits a second inflection point in the transmission-voltage curve wherein the transmission of the electrode decreases more rapidly. From these spectroelectrochemical data, the first and third metal reductive peaks in the CV can be ascribed to metal electrodeposition since these processes result in a decrease in electrode transmission. Based on the relative redox potentials of Au and Cu, the first reduction peak at about +0.5 V can be assigned to Au electrodeposition and third reductive at around -0.35 V can be ascribed to Cu electrodeposition. The second reductive peak therefore is not due metal electrodeposition but is due to the reduction of Cu(II) to Cu(I) species. The stabilization of Cu(I) species is known to occur in halide-containing Cu electrolytes studied in other electrochemical contexts. [51, 127] Upon reversing the polarity of the sweep of the CV, four anodic peaks are obtained. The anodic peak occurring at around -0.1 V elicits an increase in the transmission of the electrode and corresponds to an inflection point in the transmission-voltage curve, which suggests

that the peak is due to metal stripping. The presence of two anodic peaks (at around -0.1 V and +0.1 V) at voltages related to the cathodic Cu electrodeposition peak suggest that there are energetic differences associated with stripping pure Cu and a Cu-Au alloy. The third anodic peak in the CV does not elicit any inflection point in the transmission-voltage curve and its position at about +0.35 V indicates that this peak is due to the oxidation of Cu(I) to Cu(II). The last anodic peak at about +0.7 V does cause an inflection point in the transmission-voltage curve and causes the transmission of the working electrode to decrease, which enables us to assign this peak to Au dissolution. We note that performing CV of this Cu-Au electrolyte in a three-electrode gives rise to optically reversible metal electrodeposition. In other words, the transmission at 600 nm of the electrode at the beginning of the CV starts at ~90% transmission and upon completion of the CV returns to its original value. However, the Coulombic efficiency for the CV of the Cu-Au electrolyte is only ~34% which indicates there is significantly more charge passed during the reductive portions of the CV as compared to the oxidative portions of the CV.

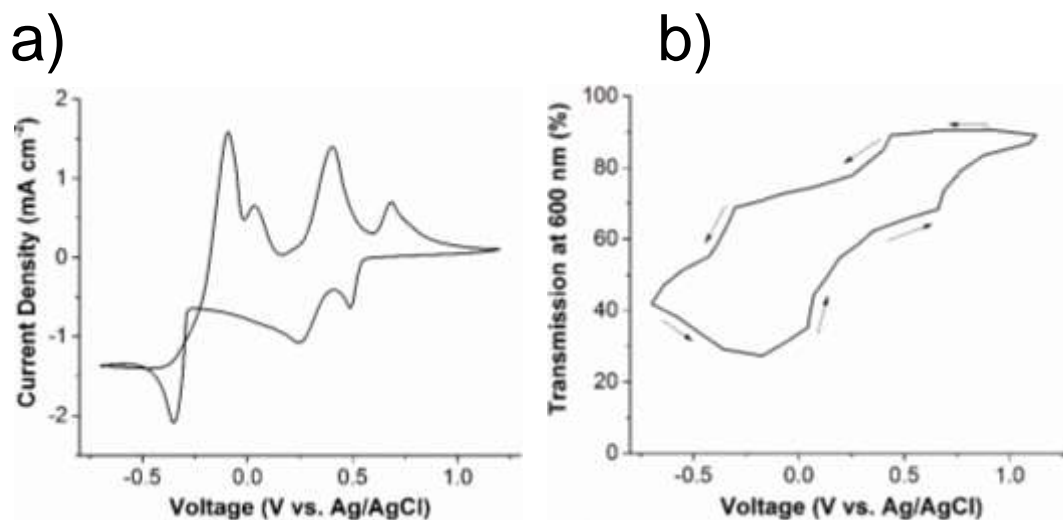


Figure 6.4: Cyclic voltammetry at a scan rate of 10 mV/s (a) and corresponding transmission at 600 nm (b) of a Pt-modified ITO on glass working electrode in a Cu-Au electrolyte in a three-electrode cell.

In an effort to determine the side reactions occurring in the Cu-Au electrolyte that account for its low Coulombic efficiency in both the CV performed in a three-electrode cell and the chronoamperometry performed in a two-electrode cell, we performed CV of the Pt-modified ITO on glass working electrode in electrolytes containing NaCl, NaBr, and NaI without the redox-active Cu and Au salts. The pH of this electrolyte was adjusted to 3.4 with HCl which is the pH of the Cu-Au electrolyte. The acidic nature of the Cu-Au electrolyte is caused by the Lewis acidities of Cu²⁺ and Au³⁺. The CV of the electrolyte without Cu and Au displays very little current density as compared to the electrolyte containing Cu and Au. The hydrogen evolution reaction (HER) is one side reaction that commonly occurs in aqueous metal electrodeposition electrolytes.[51] At a pH of 3.4, the thermodynamic value for the HER is -0.41 V vs. Ag/AgCl as calculated from the Nernst equation. Indeed, there is some reductive current observed at potentials more negative than -0.41 V, but since the current densities are so

low in this CV, the data show that the HER cannot fully account for the low Coulombic efficiency in the Cu-Au electrolyte.

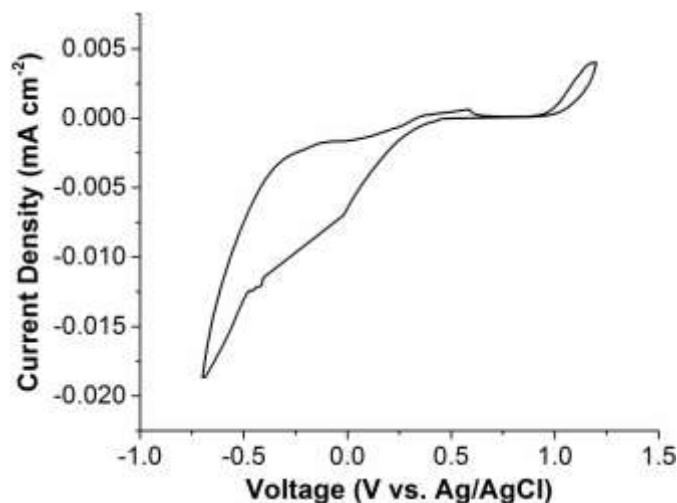


Figure 6.5: Cyclic voltammetry at scan rate of 10 mV/s of a Pt-modified ITO on glass working electrode in an electrolyte containing 3 M NaCl, 400 mM NaBr, and 1 mM NaI adjusted to pH 3.4 with HCl.

To further understand the electrochemical nature of the Cu-Au electrolyte, we performed CV of the electrolytes containing only Cu and only Au as the redox-active metals (Figure 6.6). These experiments further validate the peak assignments previously described for the complete Cu-Au electrolyte, the CV of which is reproduced as the black line in Figure 6.6. The Au only electrolyte (Figure 6.6, blue line) exhibits one redox wave associated with Au electrodeposition and dissolution. This wave is centered around +0.65 V and overlaps with the Au electrodeposition and stripping peaks also present in the Cu-Au electrolyte. The electrolyte containing only Cu (Figure 6.6, red line) displays a reductive feature that peaks around -0.35 V, which is assigned to Cu electrodeposition, and also displays a Cu stripping peak. Strikingly, however, the CV only exhibits a single metal stripping peak and the smaller stripping peak at about +0.1 V observed in the Cu-

Au electrolyte is not present when Au is removed (Figure 6.6, black). This results corroborates the interpretation that the second anodic peak in the Cu-Au electrolyte is due to the stripping of Cu-Au alloy. Lastly, the Cu(I)/Cu(II) couple is present as expected with a midpoint potential of about +0.3 V. In addition to the appearance of the Cu-Au alloy stripping peak, we also note that the Au electrodeposition and stripping peaks exhibit significantly lower current density in the Cu-Au electrolyte as compared to the electrolyte containing only Au, further demonstrating that some of the Au in the Cu-Au electrolyte goes toward making an alloy and that the Cu-Au electrolyte is not simply acting as a Cu electrodeposition system superimposed with a Au electrodeposition system. In other words, Cu and Au are acting synergistically, likely due to the formation of mixed Cu-Au species in the electrolyte, which give rise to mixed potentials at which metal electrodeposition and stripping process occur.

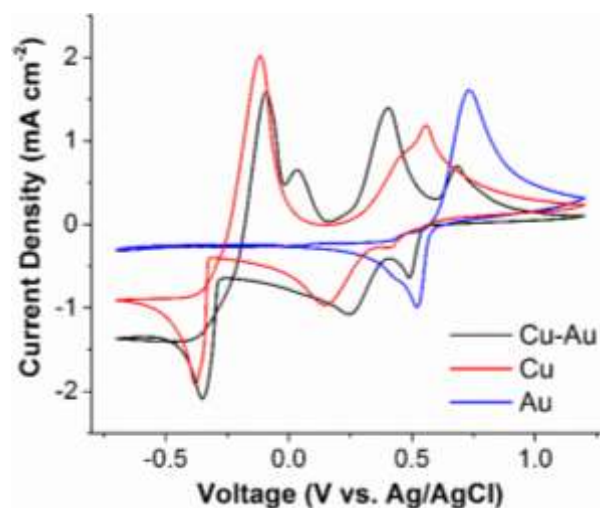


Figure 6.6: Cyclic voltammetry at a scan rate of 10 mV/s of a Pt-modified ITO on glass working electrode in the Cu-Au electrolyte (black line) and electrolytes containing only Cu (red line) and only Au (blue line) as the redox active metals.

We next evaluated the optical reversibility of the electrolytes containing only Cu and Au over the course of seven CV cycles (Figure 6.7). In both the Cu only and Au only electrolytes, the transmission at 600 nm of the working electrode is not completely reversible, and the maximum transmission value obtained decreases steadily as the electrolyte cycles. This result is in sharp contrast to the optical reversibility of the Cu-Au electrolyte (Figure 6.4b). The combination of these results further suggests that there is a synergetic effect between Cu and Au that enables the optical reversibility of the Cu-Au electrolyte that is not present when either of these metals is electrodeposited on their own.

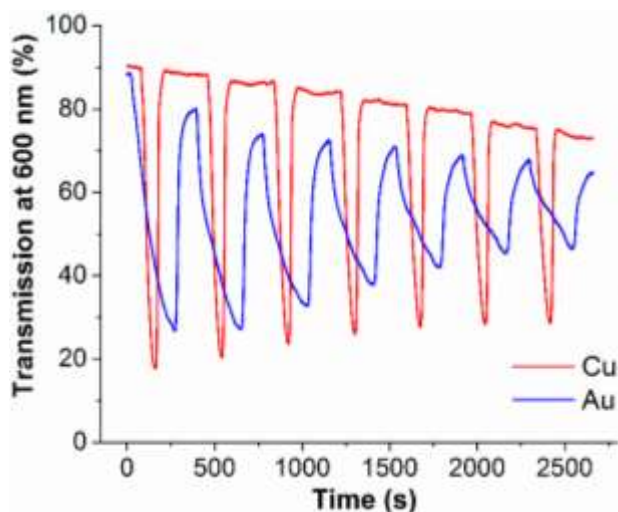


Figure 6.7: Transmission at 600 nm during seven cycles of cyclic voltammetry at a scan rate of 10 mV/s of a Pt-modified ITO on glass working electrode in electrolytes containing only Cu (red line) and only Au (blue line) as the redox active metals.

We next evaluated the electrochemistry of the Cu-Au, Cu only, and Au only electrolytes in water in the absence of NaCl, NaBr, and NaI to elucidate the effect of the supporting halide salts in these electrolytes (Figure 6.8). Taken as a whole, the CVs in

Figure 8 without NaCl, NaBr, and NaI are dramatically different than those containing high concentrations of sodium halides (Figure 6.6). In particular, the Au only electrolyte displays very little current, suggesting that halides are necessary to accelerate the metal electrodeposition process (Figure 6.8, blue line). It is known in the Au electroplating literature that halides facilitate Au electrodeposition. [129] Furthermore, there is not much of an anodic feature in the CV of the Au only electrolyte without NaCl, NaBr, and NaI. The nobility of Au renders its dissolution kinetically slow, and the presence of large concentrations of sodium halides accelerate the metal dissolution process. For the case of the Cu only electrolyte without additional halides (Figure 6.8, red line), the metal electrodeposition and stripping processes are both quite different from the case with added halides (Figure 6.6, red line). In particular, the onset potential for Cu electrodeposition is about 0 V as compared to around -0.3 V with added halides, indicating that Cu electrodeposition is more thermodynamically favorable in the absence of large concentrations of Cu halide complexes. These results match with the fact that the redox potential of $\text{Cu}(\text{H}_2\text{O})_6^{2+}$ is more positive than those of CuCl_4^{2-} and CuBr_4^{2-} . [130, 131] Lastly, for the case of the Cu-Au electrolyte without added halides, the onset of metal electrodeposition shifts even more positive to about +0.2 V because a mixture of Cu and Au electrodeposition occurs.

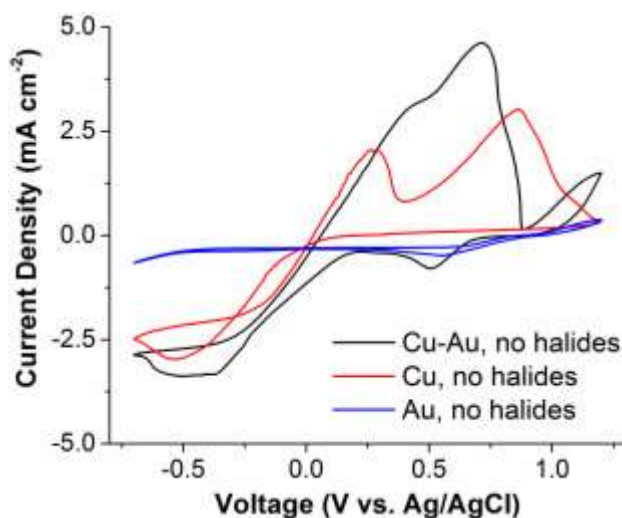


Figure 6.8: Cyclic voltammetry at a scan rate of 10 mV/s of a Pt-modified ITO on glass working electrode in electrolytes without halides containing Cu-Au (black line), only Cu (red line), and only Au (blue line) as the redox active metals.

Although the voltammetry results indicate that metal electrodeposition from the Cu-Au electrolyte is more thermodynamically favorable in the absence of NaCl, NaBr, and NaI, the transmission values at 600 nm of the working electrode during seven CV cycles demonstrate that without added NaCl, NaBr, and NaI the electrolyte is not optically reversible (Figure 6.9). Instead, the maximum transmission measured decreases significantly during each subsequent cycle, indicating that metal is not completely stripped off the electrode after each CV cycle. In contrast, the complete Au-Cu electrolyte with NaCl, NaBr, and NaI is optically reversible when cycled using CV or chronoamperometry (Figures 6.3 and 6.4b). Taken together, these results indicate that a high concentration of halides increases the kinetics of Cu and Au dissolution. One possible mechanism explaining the increased metal stripping kinetics in the presence of halides is that Br^- is oxidized to Br_2 , which is known to chemically dissolve both Cu and Au.[55] The redox potential for Br_2 formation is +0.88 V vs. Ag/AgCl so a mechanism

involving Br_2 is thermodynamically feasible since we scan up to +1.2 V in the CVs. [131] However, since the voltammetry in an electrolyte with NaCl, NaBr, and NaI as the only salts exhibits little anodic current density (Figure 6.5), dissolution via Br_2 cannot be the primary metal stripping mechanism. The data instead indicate that metal stripping is accelerated with halides due to the formation of metal halide complexes. Indeed, halides are known to stabilize Cu and Au in their +1 oxidation states, which are the first intermediates that form during the metal stripping process. [127, 129, 132]

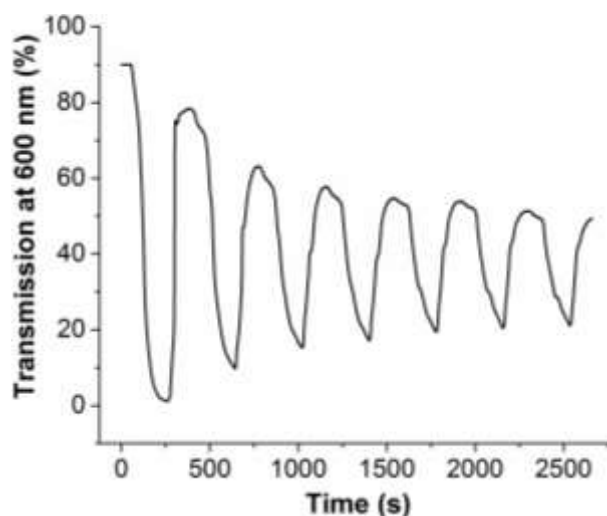


Figure 6.9: Transmission at 600 nm during seven cycles of cyclic voltammetry at a scan rate of 10 mV/s of a Pt-modified ITO on glass working electrode in the Cu-Au electrolyte without halides.

To further elucidate the role of halides in the Cu-Au electrolyte, we performed CV of the electrolytes containing various concentrations of NaBr. As the concentration of Br^- is increased in the electrolyte, the onset of the main metal electrodeposition (Cu-Au alloy formation) peak shifts progressively more negative (Figure 6.10). This result matches typical trends in the reported redox potentials of metal electrodeposition from

metal halide complexes in which metal bromide complexes possess more negative redox potentials than analogous metal chloride complexes.

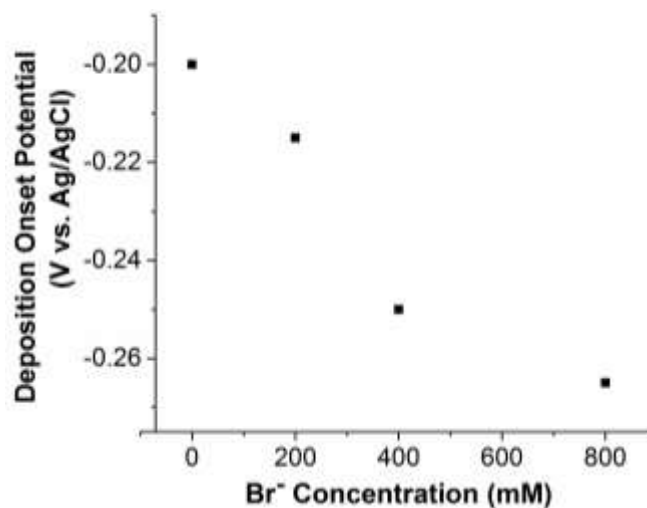


Figure 6.10: Onset potential for Cu-Au electrodeposition as determined by cyclic voltammetry at a scan rate of 10 mV/s of a Pt-modified ITO on glass working electrode in the Cu-Au electrolyte with various concentrations of NaBr.

Figure 6.11 compares the CVs of the Cu-Au electrolyte with and without NaBr. The presence of NaBr shifts the onset potentials of both the main metal electrodeposition (Cu-Au alloy formation) process and the Au electrodeposition process negative. However, the slopes of the current density-voltage curves for the both Cu and Au electrodeposition and stripping processes are steeper in the presence of NaBr, giving rise to a faster switching optical film.

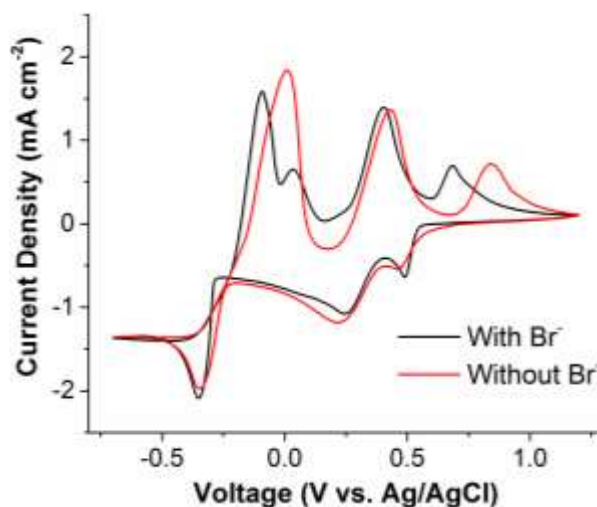


Figure 6.11: Cyclic voltammetry at a scan rate of 10 mV/s of a Pt-modified ITO on glass working electrode in the Cu-Au electrolyte with (black line) and without (red line) NaBr.

In other words, there is a decrease in the Tafel slope of both metal electrodeposition processes in the presence of NaBr (Figure 6.12).

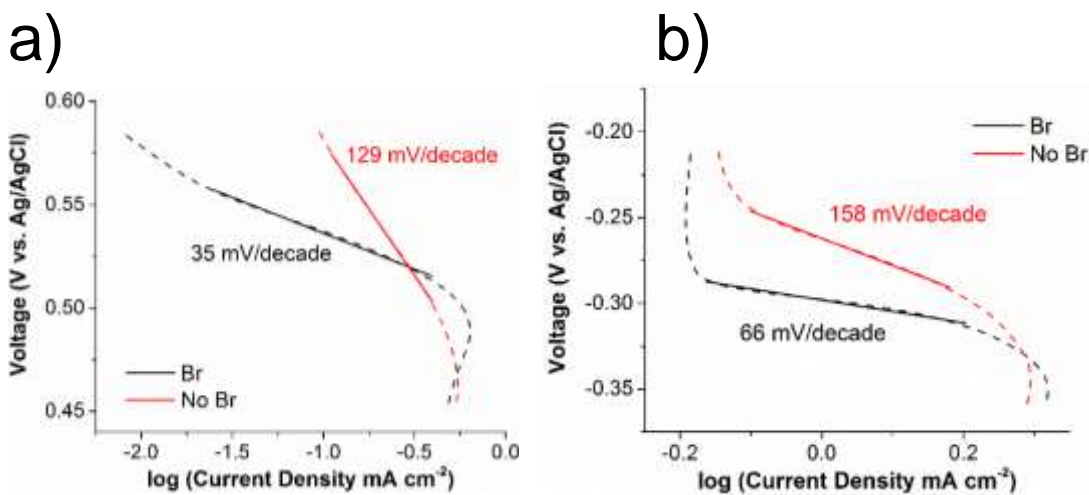


Figure 6.12: Tafel slopes extracted from cyclic voltammetry of the Cu-Au electrolyte with (black lines) and without (red lines) NaBr for Au electrodeposition at c.a. +0.55 V (a) and Cu/Au electrodeposition at c.a. -0.3 V (b). The solid lines represent the linear fits used to calculate the Tafel slopes.

6. 4. Conclusion

We develop an aqueous electrolyte that supports the optically reversible electrodeposition of Cu and Au on transparent ITO on glass electrodes modified with Pt nanoparticles. Through systematic voltammetry experiments with various electrolyte compositions, we find that Cu and Au act synergistically to facilitate the optical reversibility of the process and that analogous electrolytes with either metal alone are not optically reversible. Furthermore, we demonstrate that halides are key to the reversibility of the electrolyte due to their ability to facilitate electron transfer to metal electrodeposition and stripping intermediates.

Chapter 7: Hybrid Dynamic Windows with Color Neutral and Fast Switching using Reversible Metal Electrodeposition and Cobalt Hexacyanoferrate Electrochromism

7.1. Introduction

Energy efficient devices can play a vital role in transitioning our energy economy towards renewable energy that decreases greenhouse gas emissions. [31] Dynamic windows, which can switch to any transmission level on demand by application of a potential, are a promising technology for increasing the energy efficiency of buildings and automobiles. [42] Buildings are responsible for ~40% of the total energy consumption in the USA. [34] Studies have found that the incorporation of dynamic windows in a building saves ~10% of energy consumption by reducing heating, cooling, and lighting demand. [32] Moreover, coupling transparent solar cells and dynamic windows in modern high-rise buildings, which have large quantities of exterior glass, can reduce costs without sacrificing architectural aesthetics. [133, 134] Electrochromic materials, which are most commonly transition metal oxides, change color in their different oxidation states upon application of a voltage. [121, 135] Over the last thirty years, researchers have explored different kinds of electrochromic materials, but electrochromic devices are not widely commercialized because no technology simultaneously fulfills the requirements of color neutrality, long-term durability, low power consumption, low cost, and fast switching time. [44, 47]

Compared to electrochromic devices, reversible metal electrodeposition (RME) is a relatively underexplored and promising technology for dynamic window applications. Devices based on RME consist of an electrochemical system wherein the application of a

reductive potential causes metal ions to be reduced to an opaque metallic film on a transparent conductive electrode. To turn the device clear, an oxidative potential is applied to this electrode to convert the metal film back to metal ions. A counter electrode, typically a metal electrode frame, undergoes the reverse reactions during device switching to charge balance the system.

RME technology has several important advantages over electrochromic devices based on transition metal oxides. [60, 104, 105] Firstly, the most common electrochromic transitional metal oxide is tungsten oxide, which tints to an undesirable blue color, compared with RME devices that possess color neutral clear-to-black transitions. [35, 36] Secondly, due to the high extinction coefficient of metals, RME devices can theoretically block visible and infrared light completely at a thickness of 20-30 nm. In contrast, metal oxides in electrochromic devices need to be 100-1,000 nm thick to block the same amount of light, which often increases device cost and complexity. [39, 40] Lastly, the deposition of transition metal oxides uses sputtering deposition, a vacuum-based technique that is difficult to perform on the large substrates needed for most architectural windows. By comparison, the active components of RME devices can be fabricated using simple solution-based methods. [113, 136]

Although RME devices have numerous advantages for dynamic window applications, one of the main challenges hindering the development of RME devices is eliciting uniform metal electrodeposition on a large scale with a fast switching speed. In our previous work, we demonstrated that metal electrodeposition uniformity increases by seeding metal growth with a self-assembled monolayer (SAM) of inert Pt nanoparticles on tin-doped indium oxide (ITO). [40] A typical RME device is constructed with a Pt-

modified ITO substrate as the working electrode and a Cu frame as the counter electrode. Although the Pt-modified ITO on glass helps uniform electrodeposition on the ITO, metal ions still need to migrate laterally from the edge to the center of the device during tinting. To overcome this problem, instead of using a Cu frame, we recently introduced a new counter electrode architecture in which an intercalation-based material facilitates transverse ion migration across the thickness of the device. [109, 137] Transverse ion migration is important because the migration path length of the ions remains constant regardless of device scale. In addition, it is possible that the counter electrode can simultaneously tint anodically during device switching, which further improves switching speed. We call these devices that combine RME on the working electrode with electrochromism on the counter electrode “hybrid dynamic windows.” [109, 137]

Previously, we used NiO and Prussian blue (PB) counter electrodes in hybrid dynamic windows. Each of these materials has its own advantages and drawbacks. NiO exhibits good stability in an acidic Bi-Cu electrolyte, one of the most commonly used electrolytes for RME devices and supports Li^+ intercalation. Using this approach, we were able to build 100 cm^2 devices that switch uniformly. [109] However, as an electrochromic material, NiO shows best performance with alkaline electrolytes that support OH^- intercalation.[138] Later, we used PB-modified ITO as a counter electrode, which is a fast switching electrochromic material operating via K^+ ion intercalation. The switching speed of the PB-based devices dramatically increased compared to the NiO-based windows, but we found that PB is not compatible with Bi-Cu electrolytes and that Cu^{2+} irreversibly reacts with PB. Therefore, our PB devices contained electrolytes with Bi as the only redox-active metal. Unfortunately, reversible Bi electrodeposition is

intrinsically slower than the reversible Bi-Cu coelectrodeposition, and we determined that slow Bi stripping kinetics caused the maximum device transparency to progressively decrease over 1,000 switching cycles. Moreover, PB is not color neutral, and the hybrid PB-metal devices are blue in their dark state.[137]

In this work, we construct fast-switching color-neutral hybrid dynamic windows that use cobalt hexacyanoferrate ($\text{KCo}[\text{Fe}(\text{CN})_6]$, CoHCF) on an ITO substrate as the counter electrode coupled with RME on Pt-modified ITO as the working electrode. In CoHCF, Co and Fe can both be either in the +2 or +3 oxidation state. The resulting mixed state compound consists of $\text{KCo}^{3+}[\text{Fe}^{2+}(\text{CN})_6]$, which absorbs at ~ 400 nm and $\text{KCo}^{2+}[\text{Fe}^{3+}(\text{CN})_6]$, which absorbs at ~ 550 nm. These two absorption process give rise to a relatively color neutral brown dark state. Upon oxidation, colorless $\text{Co}^{3+}[\text{Fe}^{3+}(\text{CN})_6]$ is formed.[110] Moreover, CoHCF shows stability with Bi-Cu acidic electrolytes. In our hybrid devices that couple CoHCF with RME, both the counter and working electrodes switch from clear to dark by applying a negative potential with respect to the working electrode and vice versa by applying a positive potential. In addition to their improved cycle life and color neutrality, which we quantify using the La^*b^* color scale, 25 cm^2 devices switch in 20 s with an optical contrast of 58%.

7.2. Results and Discussion

7.2.1. Hybrid Dynamic Window Architecture

A schematic of a dual tinting hybrid dynamic window is shown in Figure 7.1 in which RME and electrochromism operate in tandem to maximize optical contrast. In this device architecture, the working electrode is a Pt-modified transparent conductive electrode (TCE) such as ITO or fluorine-doped tin oxide (FTO). A SAM of Pt nanoparticles on the TCE enables uniform nucleation of electrodeposited metal on the TCE.[40]

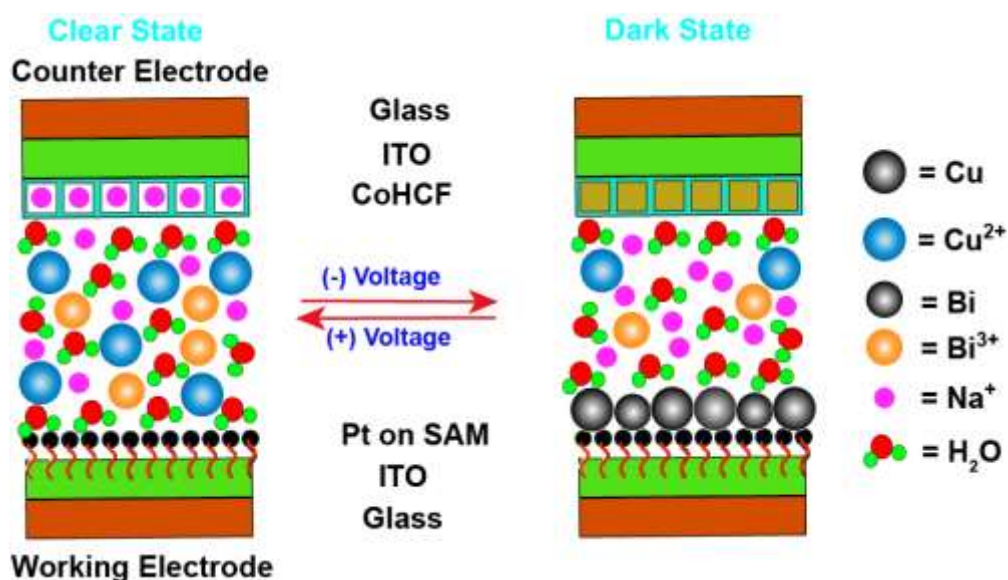


Figure 7.1: Schematic of a hybrid dynamic window that facilitates reversible Bi and Cu metal electrodeposition on an ITO on glass working electrode modified with a SAM of Pt nanoparticles and migration of Na⁺ on a CoHCF on ITO on glass counter electrode.

The counter electrode of the hybrid device is a TCE modified with a thin film of electrochromic CoHCF. When a negative potential is applied with respect to the working electrode, metal ions deposit on the working electrode, and at the same time the counter

electrode changes from clear to dark due to the oxidative potential at the counter electrode. When the polarity of the device is flipped, the electrodeposited metal on the working electrode oxidizes to form soluble metal ions and reduction at the counter electrode causes CoHCF to revert to its clear state (Equations 7.1 and 7.2, where A represents an alkali metal).

Working electrode: $Cu^{2+} + Bi^{3+} + 5e^{-} \rightarrow Cu + Bi$ (Equation 7.1)

Counter Electrode: $5ACo[Fe(CN)_6] \rightarrow 5A^{+} + 5Co[Fe(CN)_6] + 5e^{-}$ (Equation 7.2)

Clear state \rightarrow Dark state

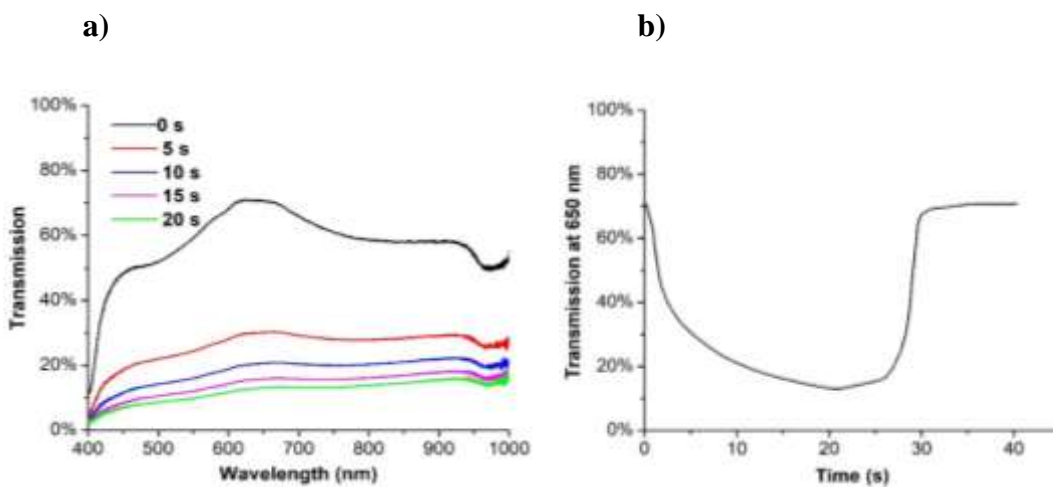


Figure 7.2: Transmission of a 25 cm² hybrid dynamic window with a Pt-modified ITO on glass working electrode, a CoHCF on ITO on glass counter electrode, and a Bi-Cu-NaBr gel electrolyte as a function of wavelength after 0 s (black), 5 s (red), 10 s (blue), 15 s (magenta), and 20 s (green) of window tinting at -2.5 V (a). Transmission of the same window at 650 nm during 20 s of window tinting at -2.5 V followed by 20 s of window lightening at 0.75 V (b).

Figure 7.2 presents optical data of a 25 cm² hybrid dynamic window, which was constructed using a Pt-modified ITO working electrode and a ~3.5 μm thick film of CoHCF on ITO as the counter electrode. In the clear state, the window possesses 50-70%

transmission from 450-1000 nm (Figure 7.2a). The dark state spectrum of the device is relatively flat over the visible and near-infrared region, which results in a color neutral opaque state. Figure 7.2b shows how the transmission at 650 nm changes during device switching. After applying -2.5 V for 20 s, the transmission of the window decreases from 71% to 13%, giving a contrast ratio of 58%. Although the switching speed of PB hybrid dynamic windows is faster than this CoHCF device, CoHCF is more color neutral than PB (see section 7.2.2). Like CoHCF, NiO is also an anodically darkening material that is color neutral in its opaque state. By comparison, 25 cm² hybrid dynamic windows with NiO counter electrodes take more than 30 s to achieve a 58% contrast ratio at 650 nm. [109, 137] To switch the CoHCF hybrid dynamic windows back to their clear state, a voltage of 0.75 V was applied for 20 s. By comparison, NiO-based devices require 120 s to complete this same transition. These findings demonstrate that for devices of the same area, CoHCF-based hybrid dynamic windows possess faster darkening and lightening kinetics than those using NiO.[109] Photographs of a 25 cm² hybrid dynamic window with CoHCF during darkening demonstrate that these devices switch uniformly and with good color neutrality (Figure 7.3).

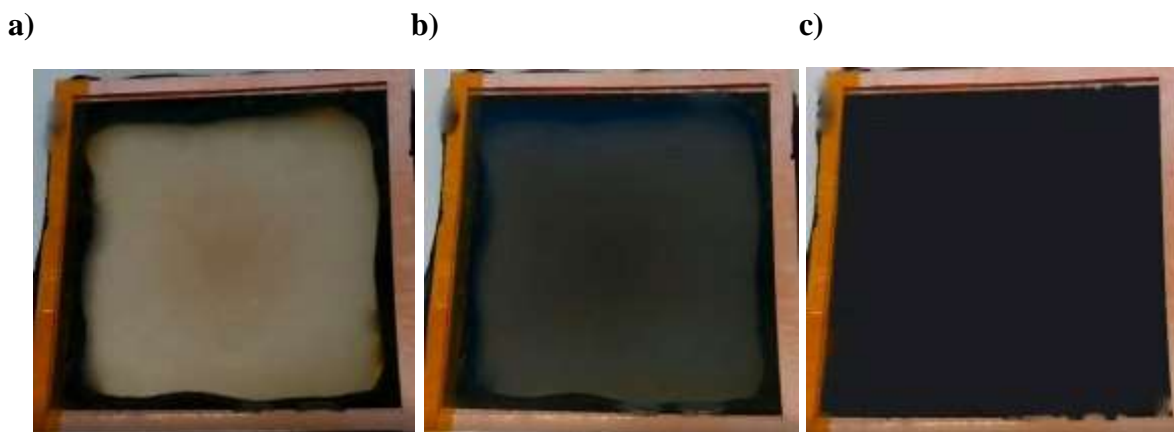


Figure 7.3: Photographs of a 25 cm² metal-based hybrid dynamic window with a CoHCF counter electrode during switching at -2.5 V for 0 s (a), 10 s (b), and 40 s (c).

7. 2. 2. *Color Neutrality of CoHCF Hybrid Dynamic Windows*

We quantified the color neutrality of the CoHCF hybrid dynamic windows during switching using the $L^*a^*b^*$ scale. This color scale provides an objective color measure that is proportional to the eye's sensitivity to different visible wavelengths of light. [139, 140] When determining object color, a standard lighting condition must be used because the color of an object depends upon the color of light used for illumination. Here, we use the standard D65 10° illuminant, which is the light profile for average clear sky conditions in Western Europe within a 10° arc of the fovea of the eye.[141] For the $L^*a^*b^*$ scale, L is the object lightness and ranges from 0 (pure black) to 100 (pure white). a^* is a measure of the redness/greenness of an object and ranges from -128 (pure green) to +128 (pure red). In a similar way, b^* reflects the yellowness/blueness of an object and varies from -128 (pure blue) to +128 (pure yellow). By factoring in the sensitivity of the eye, lighting, and device optics, the color of transmitted light through a window can be objectively measured. The color neutrality (C^*) of any $L^*a^*b^*$ color is also easily

calculated by applying the Pythagorean Theorem to the (a^* , b^*) coordinates to find the distance the color is from the grey origin at (0, 0). La^*b^* colors can also be converted to the best corresponding RGB colors that can be electronically displayed or printed. Because the color gamut of electronic displays and printer inks is limited and does not fully encompass the color portfolio of the eye, we note that these RGB colors are only approximations of the true perceived colors.



Prussian Blue				
				
Time (s)	Lightness (L)	Red/Green (a^*)	Blue/Yellow (b^*)	Color Neutrality (C^*)
0	69	-0.5	2.4	2.4
1	50	-9.1	-2.2	9.4
2	29	-19	-13	23
3	13	-26	-31	40
CoHCF				
				
0	62	4.0	11	12
5	26	3.1	13	14
10	17	3.8	16	16
15	13	4.0	17	18

Table 7.1: RGB color profiles and $La^*b^*C^*$ values for 25 cm² hybrid dynamic windows based on reversible metal electrodeposition and a counter electrode containing Prussian Blue (top, calculated from data in reference 20) and CoHCF (bottom).

Table 7.1 displays the $La^*b^*C^*$ color values for PB (top) and CoHCF (bottom) hybrid dynamic windows along with the corresponding RGB profiles during device

darkening. It is clear from these values that the PB device is highly green and blue in its dark state, whereas the CoHCF device is yellow and slightly red when dark, which results in a brown appearance. Importantly though, when comparing the dark states of the two devices ($L = 13$), the CoHCF device has a C^* value of only 18 as opposed to 40 for the PB device. In other words, in the dark state, the CoHCF hybrid dynamic window is greater than two times more color neutral than the analogous PB window.

7. 2. 3. Thin Film Characterization

Figure 7.4 shows scanning electron microscopy (SEM) images of the two electrodes of the CoHCF hybrid dynamic window in its dark state. On the working electrode, Bi and Cu metal electrodeposits are visible that possess particle sizes of about 200 nm (Figure 7.4a). The morphology of these electrodeposits is similar to those reported previously in RME dynamic windows using a metal frame counter electrode and an analogous electrolyte. [36] A SEM image of the CoHCF counter electrode (Figure 7.4b) shows a platelet-like structure, which is similar to our previously reported PB morphology. [137] The energy-dispersive X-ray spectrum (EDS) of the counter electrode confirms the presence of Co, Fe, N, and K, which are all elements present in CoHCF (Supporting Figure 12.5.1). We also analyzed the CoHCF thin film using X-ray diffraction (XRD, Supporting Figure 12.5.2), which matches previously reported spectra for CoHCF. [110]

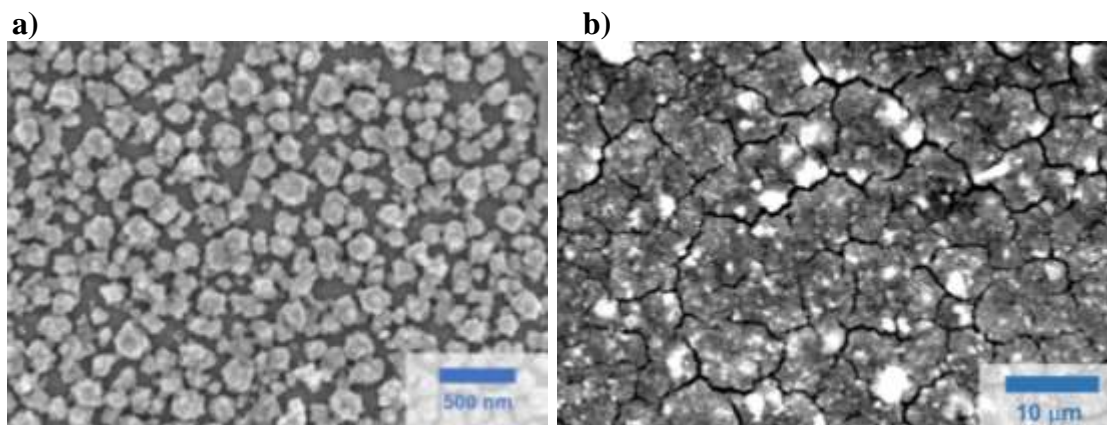


Figure 7.4: Scanning electron microscopy images of the working (a) and counter (b) electrodes of a CoHCF hybrid dynamic window in its tinted state.

Atomic force microscopy (AFM) images of the counter electrode are presented in Supporting Figure 12.5.3. The thickness of the CoHCF thin film fabricated via spin-coating at 1500 rpm was determined to be $\sim 3.5 \mu\text{m}$ from an AFM image of the CoHCF-bare ITO interface (Figures S3c and S3d). Using different spin-coating rotation speeds (Supporting Figure 12.5.4), we optimized the thickness of the CoHCF thin film. Films that are too thick possess an initial transmission that is lower than ideal. On the other hand, films that are too thin do not switch to a dark enough opaque state (Supporting Figure 12.5.5).

To further confirm the optical modulation of the two electrodes in the hybrid dynamic windows, we photographed the electrodes in an open, unsealed cuvette with liquid electrolytes. These photographs show that the CoHCF thin film changes color upon redox cycling in an electrochemical half cell as expected (Supporting Figure 12.5.6). Furthermore, photographs of a hybrid dynamic window in a cuvette demonstrate that both electrodes darken during device tinting (Supporting Figure 12.5.7).

7.2.4. Ion Intercalation and Electrolyte Design

Several previous RME dynamic windows use an electrolyte that contains 5 mM BiCl_3 , 15 mM CuCl_2 , 1 M LiBr , and 10 mM HCl to reversibly electrodeposit Bi and Cu. [36, 40, 109, 113, 137] The addition of LiBr and HCl increases the solubility of Bi^{3+} by forming Bi bromide complexes and preventing the precipitation of insoluble $\text{Bi}(\text{OH})_3$, respectively.[39] To understand the effect of the Bi-Cu electrolyte in our devices, we used spectroelectrochemistry to systematically study CoHCF electrochromism in solutions containing different alkali metal cations. Figure 5a displays a CV of a CoHCF on ITO working electrode in an electrolyte with LiBr (Figure 7.5a). The CV contains a reduction peak at 0.38 V and an oxidation peak at 0.78 V. These peaks are due to the Co/Fe redox behavior of CoHCF as depicted in Equation 7.2. There is also an anodic shoulder at 0.55 V. This lower magnitude oxidation process is due to a secondary CoHCF structure that forms during Li^+ deintercalation. [142] For this CV, the separation between the two main peaks is about 400 mV, in contrast to the theoretical 0 mV peak separation for an adsorbed redox active film. [115] This large peak separation indicates that electron transfer kinetics to and from the film are significantly impeded. Additionally, the current densities of the peaks decrease slightly with increasing cycle number, suggesting that the film is degrading during cycling. The transmission of the CoHCF film at 500 nm shows only ~5% modulation with each cycle (Figure 7.5b). These results indicate that the intercalation and deintercalation of Li^+ in CoHCF in this electrolyte is not fully reversible and only exhibits weak electrochromism.

The intercalation dynamics of Na^+ in CoHCF are much different than those of Li^+ . The CV of CoHCF in an electrolyte containing NaBr shows only one oxidation peak

without the shoulder observed in the LiBr electrolyte (Figure 7.5c). The reduction and oxidation processes possess peak positions of 0.45 V and 0.82 V, respectively. This values give a peak separation of 370 mV, which is less than that for the LiBr electrolyte. Importantly though, as opposed to the LiBr electrolyte, the magnitude of the peak current densities of the CoHCF electrode in the NaBr electrolyte increase as the electrode is cycled as a result of the peaks becoming more narrow. These findings indicate that under these conditions, Na⁺ intercalation in CoHCF is more reversible than Li⁺ intercalation. The optical contrast ratio of the electrode at 500 nm is about 15% during each CV cycle (Figure 7.5d), which is three times higher than the weak electrochromism observed with Li⁺.

Lastly, CVs of the CoHCF thin film with KBr exhibit very broad peaks with relatively low current densities (Figure 7.5e). Furthermore, like the CVs with the LiBr electrolyte, the peak current densities decrease with increasing cycle number. In addition, the transmission at 500 nm shows very little modulation during cycling (Figure 7.5f). These results indicate that the kinetics of K⁺ intercalation and deintercalation in CoHCF are slower than those of both Li⁺ and Na⁺, and that these processes are also not very reversible.

From the CVs of CoHCF in the three electrolytes, the midpoint potentials for CoHCF in LiBr, NaBr, and KBr solutions are 0.58 V, 0.64 V, and 0.73 V, respectively. This trend is the same as reported previously and can be explained by considering the different ionic radii of the alkali metal cations.[143-145] While the ionic radii of the dehydrated alkali metal ions increase with increasing atomic weight (0.06 nm for Li⁺, 0.10 nm for Na⁺, and 0.13 nm for K⁺), the radii of the hydrated ions possess the opposite

trend (0.24 nm for K^+ , 0.36 nm for Na^+ , and 0.42 nm for Li^+) due to the greater charge density of the smaller ions, which results in a larger hydration network. [146, 147] Because Na^+ displays faster and more reversible intercalation dynamics than Li^+ and K^+ , we hypothesize that the intermediate hydration size of Na^+ is optimal for fitting into open sites of the CoHCF lattice. Indeed, previous studies suggest that hydrated alkali metal ions play an important role in determining the structure of CoHCF. [148]

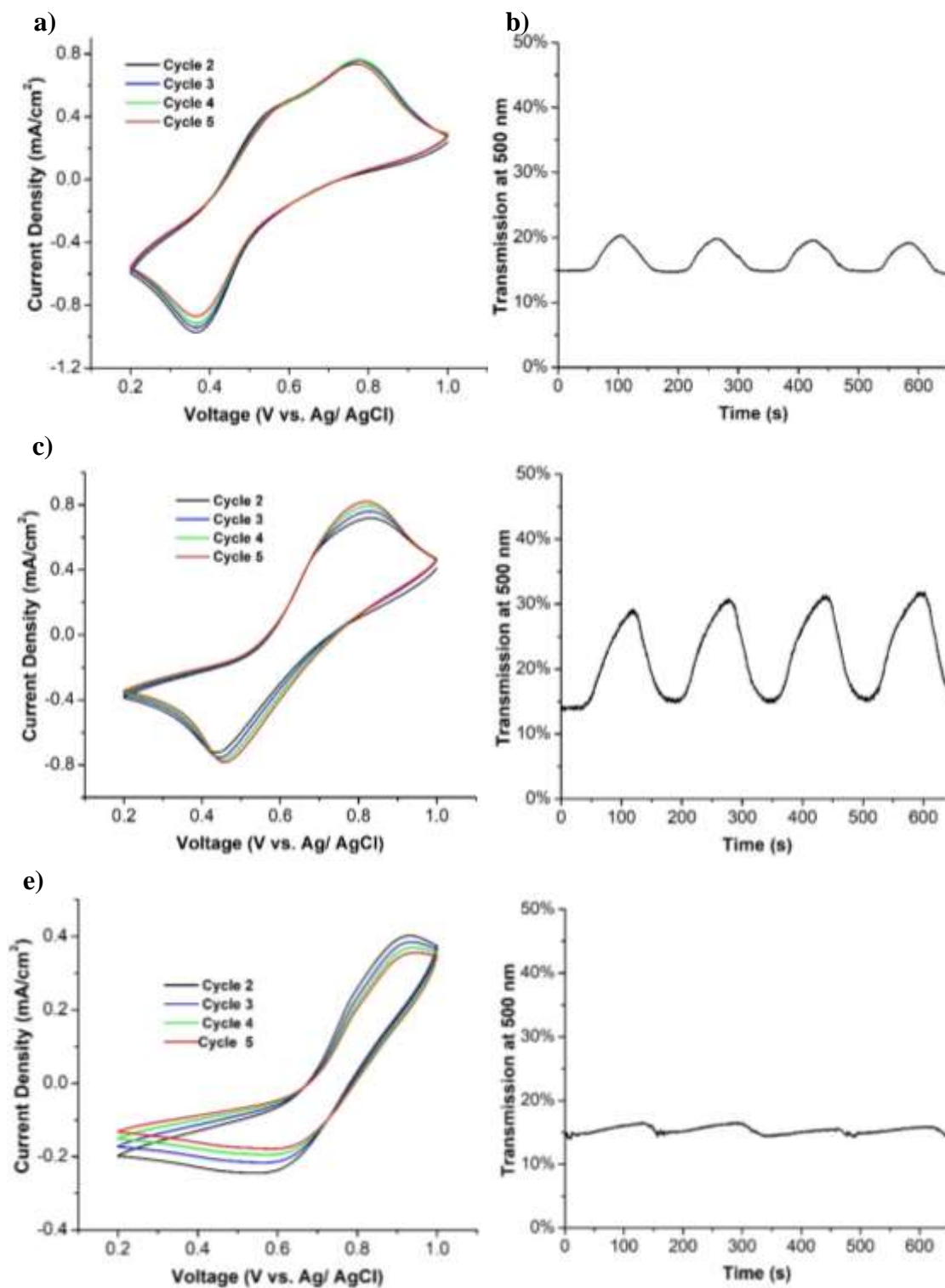


Figure 7.5: Cyclic voltammograms (a, c, e) and transmission at 500 nm (b, d, f) of a CoHCF on ITO on glass working electrode in a three-electrode cell in an electrolyte containing 1M LiBr (a, b), NaBr (c, d), or KBr (e, f) at a scan rate 10 mV/s.

Having established that Na^+ intercalation dynamics are superior to those of Li^+ and K^+ intercalation, we performed spectroelectrochemistry of a CoHCF thin film using a Bi-Cu-NaBr electrolyte (Figure 7.6). This experiment allows us to assess if Bi and Cu electrodeposition occurs under the same conditions as Na^+ intercalation in CoHCF, conditions that are necessary for the construction of a dual-tinting hybrid dynamic window. The CV in Figure 7.6a shows a reductive peak at +0.18 V denoted as (a), which is due to the intercalation of Na^+ into CoHCF. Beginning at potentials more negative than 0 V (b), Bi and Cu electrodeposition occurs on top of the CoHCF. On the positive-going scan, an anodic peak at +0.2 V (c) is due to the oxidation of Bi and Cu to soluble Bi^{3+} and Cu^{2+} . Lastly, Na^+ deintercalation occurs at +0.8 V (d). In situ optical data (Figure 7.6b) of the electrode shows that during regime (a) when Na^+ intercalates into CoHCF, the electrode transmission increases as the CoHCF turns from opaque to clear. During regime (b), the electrode transmission decreases as a result of Bi and Cu electrodeposition. Subsequently during regime (c), the dissolution of the metal electrodeposits causes the transmission to return to a similar value as during regime (a). Finally during regime (d), deintercalation of Na^+ causes the CoHCF to turn opaque and the electrode transmission to return to a value similar to that at the beginning of the CV cycle. This spectroelectrochemical study proves that CoHCF is compatible with the Bi-Cu-NaBr electrolyte.

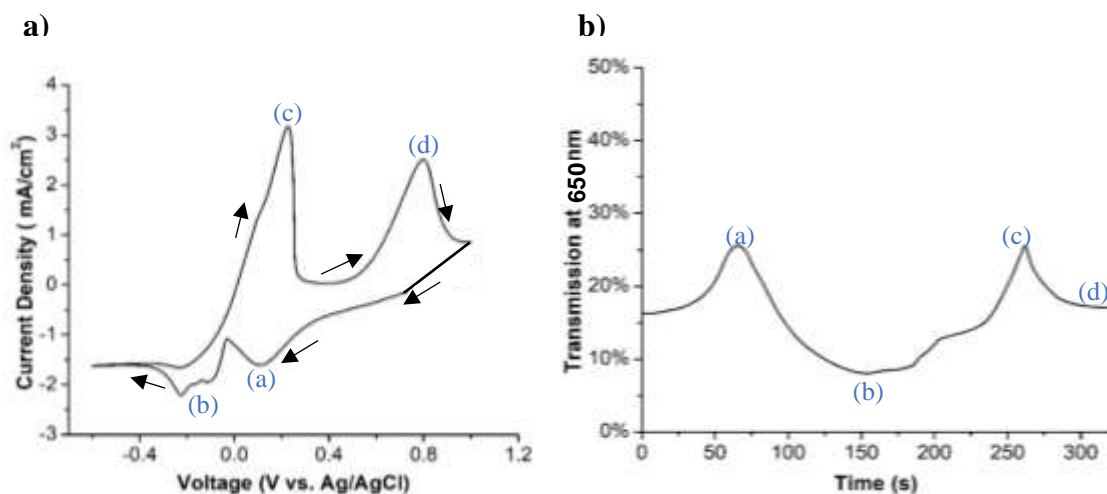


Figure 7.6: Cyclic voltammogram (a) and transmission at 650 nm (b) of a CoHCF on ITO on glass working electrode in a three-electrode cell in a liquid electrolyte containing Bi-Cu-NaBr at a scan rate of 10 mV/s.

7.2.5. Cycling Durability

After understanding and optimizing the electrochemistry of CoHCF thin films using half cells, we evaluated the cycle life of a two-electrode 25 cm² hybrid dynamic window with a Bi-Cu-NaBr electrolyte. Figure 7.7 demonstrates that the contrast ratio of this device at 650 nm remains relatively constant during 1,000 switching cycles. This result is in contrast to the durability of PB hybrid dynamic windows, which steadily degrade during cycling.[137] The improved performance of the CoHCF-based windows presented here is due to the ability of CoHCF windows to operate with a Bi-Cu electrolyte. PB-based windows are not compatible with Cu ions, and the resulting Bi electrolytes that must be used do not facilitate completely reversible metal electrodeposition. The presence of Cu in Bi-Cu electrolytes is known to improve metal electrodeposition reversibility by altering metal electrodeposit morphology.[40]

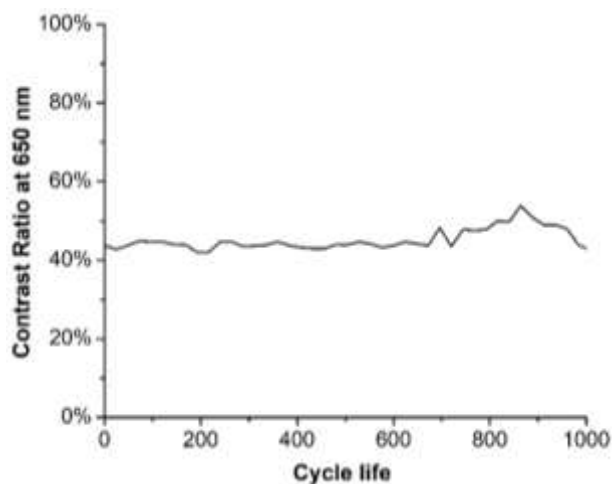


Figure 7.7: Contrast ratio of a hybrid dynamic window with CoHCF over the course of 1000 cycles.

7.3. Conclusion

In conclusion, we successfully combined RME with electrochromism to create hybrid dynamic windows that are compatible with Bi and Cu electrodeposition. By systematically studying CoHCF thin films using three-electrode spectroelectrochemistry, we demonstrated that Na^+ intercalation results in superior electrochromism as compared to Li^+ and K^+ intercalation. The combination of Bi and Cu RME on the working electrode and CoHCF electrochromism on the counter electrode enables 25 cm^2 devices to switch rapidly with high color neutrality and good cycle life.

7.4. Experimental

7.4.1. General Procedures

All chemicals were obtained from commercial sources and used without additional purification. Modified ITO substrates (Xinyan Technology, reported sheet resistance of $15 \Omega/\text{sq}$) were used as both the working and counter electrodes for two

electrode devices. For three electrode studies, a modified ITO substrate was used as the working electrode, Ag/AgCl (3 M KCl) 'no-leak' (eDAQ) used as the reference electrode, and Pt wire was used as the counter electrode. ITO substrate were first cleaned by sonicating them in an aqueous solution of Extran for 5 minutes and washed with de-ionized water followed by isopropanol. The substrates were then sonicated in a solution of isopropanol for 5 minutes and washed with isopropanol followed by water. Finally, the substrates were dried using a stream of air. FTO working electrodes were used for long-term cycling studies.

For the preparation of Pt-modified ITO substrates, cleaned ITO substrates were first immersed in a 10 mM solution of 3-mercaptopropionic acid in ethanol for 24 h, which forms a self-assembled monolayer (SAM) on top of the bare ITO surfaces. After successively rinsing the substrates with ethanol and water, the ITO substrates were immersed in a diluted aqueous dispersion of Pt nanoparticles (3 nm diameter, Sigma-Aldrich) for at least 24 h. The commercial nanoparticle dispersion was diluted fourfold with water. Lastly, the ITO substrates were washed with water and annealed in air for 20 min at 250°C.

7. 4.2. Synthesis and Deposition of CoHCF Thin Films

For the preparation of CoHCF thin films on ITO substrates, CoHCF nanoparticles were first synthesized using a water dispersive method following a modified literature procedure.[110] 0.06 M of $\text{CoCl}_2 \cdot 6\text{H}_2\text{O}$ and 0.03 M $\text{K}_3\text{Fe}(\text{CN})_6$ were dispersed in water and stirred for 1 h. A red-brown precipitate of CoHCF formed during this time. To purify the CoHCF, three successive centrifuges at 3600 rpm were performed followed by

washing with water. The CoHCF nanoparticles were then dried in a vacuum oven at 75°C overnight. The obtained powder was then grinded with a mortar and pestle before being dispersed in 0.1 M $\text{K}_3\text{Fe}(\text{CN})_6$ in water. The mass ratio of the 0.1 M $\text{K}_3\text{Fe}(\text{CN})_6$ in water and CoHCF was 1:10 for the 3 cm² ITO substrate and 1: 15 for 25 cm² ITO substrate. This mixture was then stirred for at least 24 h to form a homogenous and well-dispersed ink. The ink was then filtered through a 200 μm Nylon mesh. The filtered CoHCF ink was deposited on ITO substrates by using a spin coater with a rotation speed of 1200 rpm, 1500 rpm, or 1800 rpm for 3 cm² ITO substrates and 1000 rpm for 25 cm² ITO substrates for 200s. After deposition of CoHCF, we observed that if we use 120°C for drying up the thin film electrochromism properties of CoHCF decrease dramatically (Supporting Figure 12.5.8). This degradation in optical performance is likely due to dehydration of the CoHCF lattice.[148, 149] By taking this into consideration, we dry the thin film by letting any residual solution evaporate in air.

7. 4.3. Electrodeposition of Bi Thin Films

First, the perimeter of Pt-modified ITO substrates were covered by conductive Cu tape. The substrates were then immersed in an electrolyte containing 5 mM of BiCl_3 , 1 M NaBr, and 10 mM of HCl. Bi electrodeposition was then conducted in a three-electrode cell in which a Pt-modified ITO substrate was the working electrode, Pt wire was the counter electrode, and Ag/AgCl was the reference electrode. To elicit Bi electrodeposition a constant potential of -0.6 V was applied for 60 s. After electrodeposition, the substrates were dipped gently in water and dried under open air.

7.4.4. Construction of 25 cm² Two-electrode Hybrid Dynamic Windows

The hybrid dynamic windows were constructed with both electrodes in their dark state. Bi electrodeposited on Pt-modified ITO was used as the working electrode, and CoHCF on ITO was used as the counter electrode. The aqueous Bi-Cu-NaBr gel electrolytes were prepared with 5 mM BiCl₃, 15 mM CuCl₂, 10 mM HCl, and 1 M NaBr as previously reported. The gel was made by adding 3% of hydroxyethylcellulose followed by magnetic stirring. The viscosity of the gel was found to be 9.5 Pa-s using a NDJ-5S viscometer. After construction of the device, we switch the hybrid windows to their clear state by applying +0.5V for 60s.

7.4.5. Materials Characterization

For all electrochemical studies, A VSP-300 Biologic potentiostat was used. Optical studies were carried out using an Ocean Optics FLAME-S-VIS-NIR spectrometer coupled with an Ocean Optics DH-mini UV-Vis-NIR light source. A Nikon D5000 Digital Camera were used for taking photographs of the windows. The SEM image and EDS spectra of CoHCF thin film were obtained using a JEOL JSM-6010LA microscope where accelerating voltage was 10kV. Bi-Cu thin film SEM image was obtained using a FEI Magellan 400 XHR microscope where accelerating voltage of the machine was 5kV. A Bruker D2 X-ray diffractometer was used performing XRD. AFM images of the CoHCF thin film was obtained using a Nanosurf EasyScan 2 microscope operated in contact mode whereby using an aluminum reflective coating silicon tips (ContAl-G, TedPella, Inc.). The thickness measurement of the CoHCF was done from the AFM interface data using WSxM 5.0 development software.[150]

Chapter 8: Aqueous Alkaline Electrolytes for Dynamic Windows based on Reversible Metal Electrodeposition with Improved Durability

8.1. Introduction

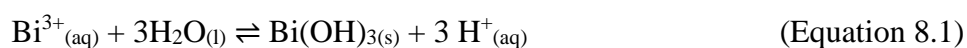
Energy efficiency is a crucial component of fostering our society's transition to a renewable energy economy. Dynamic windows, which can be electronically switched between clear and opaque states, are a promising technology to increase the energy efficiency of buildings and automobiles. The tunable transmission properties of dynamic windows enable them to reduce energy consumption in buildings by an average of about 10% due to savings in lighting, heating, and cooling costs. [32, 56] By implementing dynamic windows in the sunroofs of cars, energy usage from air conditioning can be diminished, which is especially important in extending the battery range of electric vehicles. [42]

The majority of research on electronically controlled dynamic windows over the past three decades has focused on electrochromic materials, which change transmission upon application of a voltage. [47, 125] Classes of electrochromic materials include transition metal oxides, polymers, small organic molecules, and nanoparticles. [43, 44, 121, 124] With all of these approaches, however, it is difficult to construct dynamics windows that simultaneously possess the optical contrast, color, durability, and manufacturing requirements for widespread commercial adoption. [50, 66]

Recently, our group has explored dynamic windows based on reversible metal electrodeposition as a promising alternative to electrochromic windows. [48, 109, 113] These metal-based windows function via electrodeposition of metals on a transparent

conducting surface using an electrolyte containing aqueous metal ions. During window tinting, the metal cations are reduced to elemental metal on the transparent electrode. In some device architectures, this reduction reaction is balanced by concomitant oxidation of a metal frame counter electrode to metal ions. The reverse reactions to lighten the window occur upon flipping the polarity of the applied voltage.

Current state-of-the-art metal-based dynamic windows utilize tin-doped indium oxide (ITO) on glass electrodes with electrolytes that facilitate Bi and Cu electrodeposition. The ITO electrodes are modified with a self-assembled monolayer (SAM) of Pt nanoparticles, which serve as a seed layer that enables uniform metal electrodeposition over a large electrode area.[37] The composition of the Bi-Cu electrolytes enables fast, reversible, and color neutral metal electrodeposition to occur over thousands of cycles.[36] All previously studied Bi-Cu electrolytes are acidic [36, 37, 104, 105] to avoid the precipitation of insoluble Bi(OH)_3 , [55] which occurs under neutral or alkaline conditions according to Equation 8.1:

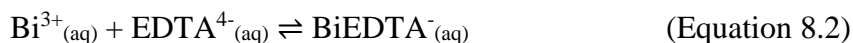


The excess H^+ present at low pH prevents the formation of insoluble Bi(OH)_3 according to Le Chatelier's principle. Despite the excellent optical performance of these Bi-Cu electrolytes, the acid present introduces two drawbacks. The first issue is that ITO slowly degrades in acidic solutions. As a result, the sheet resistance of the ITO working electrodes increases over time at open circuit potential. This increase in sheet resistance

causes the device switching speed and contrast ratio to diminish over the course of several days.

The second issue of acidic metal electrodeposition electrolytes is that they have a limited electrochemical window due to their propensity to evolve H₂. The thermodynamic potential for H₂ evolution in the typically used Bi-Cu electrolytes (pH ~ 2) is -0.33 V vs. Ag/AgCl. The negative voltage limit of the electrolytes can be expanded by using more basic electrolytes according to the Nernst equation. Expanding the electrolyte voltage range is essential for scaling up dynamic windows based on reversible metal electrodeposition. As device area increases, the voltage difference between the perimeter and the center of the device increases due to a buildup of resistance across the transparent working electrode according to Ohm's law. [37] To maintain uniform metal electrodeposition across a large-area window, the voltage at the center of the electrode must be high enough to elicit diffusion-limited metal electrodeposition currents without evolving H₂ at the perimeter of the device where the voltage is higher. Therefore, more basic metal electrodeposition electrolytes enable the construction of larger devices by pushing the onset of H₂ production to a more negative voltage.

To develop alkaline electrolytes that increase both the durability and scalability of metal-based dynamic windows, we design Bi-Cu electrolytes using the chelating agent ethylenediaminetetraacetic acid (EDTA) instead of acid to solubilize Bi³⁺ ions (Equation 8.2).



This strategy allows us to reversibly electrodeposit metals from electrolytes containing Bi³⁺ and Cu²⁺ ions at a more basic pH of 8.5. The thermodynamic potential for

H₂ formation shifts negative to -0.71 V vs. Ag/AgCl in these more basic electrolytes according to the Nernst equation. Furthermore, the electrolytes we develop do not chemically degrade ITO, which allows us to construct practical two-electrode dynamic windows with improved durability.

8.2. Experimental

Chemicals were received from commercial sources. Half-cell experiments were conducted with a three-electrode system using a Ag/AgCl (3 M KCl) reference electrode (eDAQ, Inc.), a Pt wire counter electrode, and a Pt-modified ITO on glass working electrode. Electrochemical experiments were performed using a VSP-300 Biologic potentiostat. Transmission data were collected with an Ocean Optics FLAME-S-VIS-NIR spectrometer coupled with an Ocean Optics DH-mini UV-Vis-NIR light source. Spectroelectrochemical and electrochemical data were plotted by aligning data timestamps to match up corresponding electrical and optical data points. Scanning electron microscope (SEM) images were obtained using a JOEL JSM-6010LA microscope with a working voltage of 20 kV. Sheet resistance measurements were conducted using a universal four-point probe instrument connected to a Jandel RM3 Test Unit. Photographs were taken using a Samsung Galaxy S9 cell phone camera.

Pt-modified ITO on glass electrodes were prepared as follows. ITO on glass substrates (Xinyan Technology, nominally 15 Ω /sq) were sonicated in 5% Extran for 5 minutes and rinsed with water and isopropanol. The substrates were next sonicated in isopropanol for 5 minutes and rinsed with isopropanol. The samples were then dried under a stream of air and immersed in 3-mercaptopropionic acid in ethanol (10 mM) for

24 hours. Next, the ITO on glass substrates were rinsed with ethanol followed by water. The samples were then transferred into a dispersion of Pt nanoparticles, which was prepared by diluting a stock solution of 3 nm in diameter Pt nanoparticles (Sigma Aldrich) fourfold with water, for 24 hours. The Pt-modified ITO on glass substrates were then rinsed with water, dried under a stream of air, and annealed at 250°C for 20 minutes.

To construct two-electrode 25 cm² dynamic windows, Cu tape with conductive adhesive was applied along the perimeter of the Pt-modified ITO on glass to make electrical connection to the working electrode. The counter electrode consisted of Cu foil together with a plain, nonconductive glass backing. Butyl rubber was applied around the perimeter of the device stack to seal the device.

8.3. Results and Discussion

Our initial approach to develop an alkaline reversible metal electrodeposition electrolyte was inspired by a Bi electrodeposition electrolyte previously reported by Zhou et al. that contains Bi(NO₃)₃, EDTA, potassium sodium tartrate, 5-sulfosalicylic acid, and KCl. The authors studied reversible Bi electrodeposition from this electrolyte on a carbon electrode. In an effort to elicit reversible metal electrodeposition in an alkaline electrolyte on a transparent electrode, we first evaluated the capability of this electrolyte to support reversible Bi electrodeposition on a Pt-modified ITO-coated glass working electrode. We conducted cyclic voltammograms (CVs) of a Pt-modified ITO working electrode in this alkaline electrolyte (Figure 8.1A) while simultaneously measuring the transmission at 500 nm of the electrode (Figure 8.1B). The CVs display reductive current with an onset potential of about -0.6 V vs. Ag/AgCl (Figure 8.1A), which is due to Bi electrodeposition

on the Pt-modified ITO surface as evidenced by a corresponding decrease in electrode transmission (Figure 8.1B). On the forward scan of the CVs, there is an anodic peak at about -0.15 V, which is ascribed to Bi oxidation to Bi^{3+} . The blue line in Figure 1B shows that the transmission of the electrode increases from its minimum value during this oxidative feature as is expected for a metal dissolution process. However, the electrode transmission only increases to about 4%, a value much less than the original 94% ITO transmission. This difference indicates that most of the Bi remains on the electrode during the oxidative portion of the CV. In other words, Bi electrodeposition is almost completely irreversible on a Pt-modified ITO surface using this electrolyte. This irreversibility is maintained during subsequent cycling of the electrode.

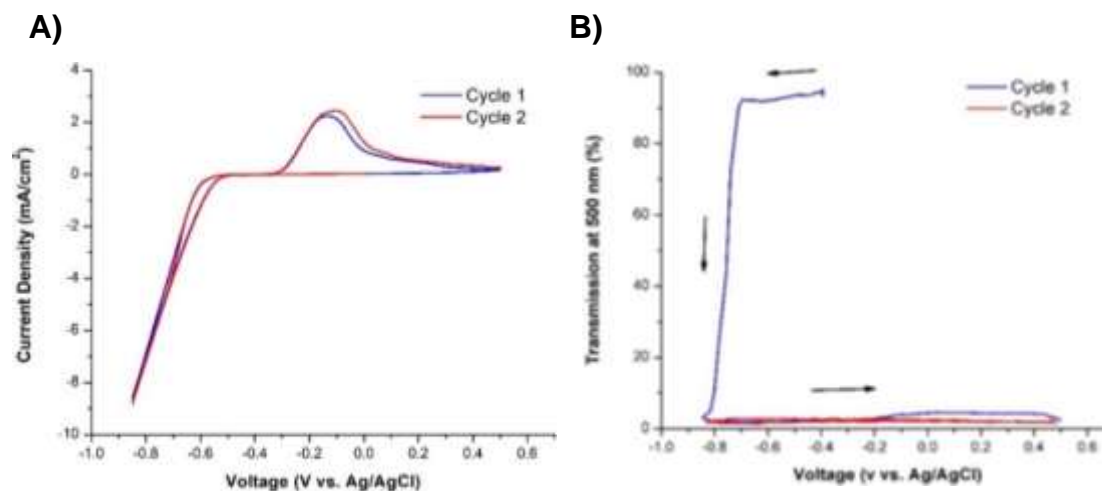


Figure 8.1: Cyclic voltammetry (A) and corresponding transmission at 500 nm (B) of a Pt-modified ITO on glass working electrode in an electrolyte containing 202 mM $\text{Bi}(\text{NO}_3)_3$, 308 mM EDTA, 550 mM 5-sulfosalicylic acid, 266 mM potassium sodium tartrate, and 107 mM KCl adjusted to pH 8.5 with NaOH.

Previously, we demonstrated that the addition of Cu^{2+} ions in an acidic Bi electrolyte improves metal stripping kinetics.[36] A galvanic displacement reaction

between Cu^+ and Bi metal causes the electrodeposits to be more spherical, which allows for more complete and faster metal dissolution. In an attempt to develop an analogous alkaline electrolyte with improved stripping kinetics, we added various amounts of CuCl_2 to the alkaline Bi electrolyte. However even at low CuCl_2 concentrations (e.g. 1 mM), the addition of Cu^{2+} results in the formation of insoluble compounds. Precipitates form in the presence of either 5-sulfosalicylic acid or potassium sodium tartrate, indicating that these precipitates consist of copper (II) 5-sulfosalicylate and copper (II) tartrate, both of which are known to be insoluble in water.[151, 152] Removing 5-sulfosalicylic acid, potassium sodium tartrate, and EDTA from the electrolyte also results in a precipitate. This precipitation is due to the formation of insoluble $\text{Bi}(\text{OH})_3$, which forms according to Equation 8.1. This result demonstrates that EDTA is necessary for solubilizing Bi^{3+} under alkaline conditions through chelation as shown in Equation 8.2. To avoid precipitation while including both Bi^{3+} and Cu^{2+} , we tested an alkaline electrolyte with EDTA to enable Bi solubility but removed potassium sodium tartrate and 5-sulfosalicylic acid to allow for Cu solubility. Although no precipitates form in this electrolyte, metal stripping does not occur to any appreciable extent (Solution A, Table 8.1). To accelerate metal stripping, we tested analogous electrolytes with NaBr or NaI in place of KCl. The electrolyte containing bromide exhibits improved stripping kinetics as compared to the electrolyte with chloride, but still does not support complete dissolution of the electrodeposited metals (Solution B, Table 8.1). The iodide-containing electrolyte, however, does elicit fully reversible metal electrodeposition and stripping (Solution C, Table 8.1). This trend in halide reactivity can be rationalized by considering the oxidation potentials of the halides. Since the voltage needed to oxidize the halides increases with

$\text{Cl}^- > \text{Br}^- > \text{I}^-$, I_2 or related species such as I_3^- can readily form that facilitate the metal stripping process.

Solution	$\text{Bi}(\text{NO}_3)_3$ (mM)	CuCl_2 (mM)	EDTA (M)	Halide (M)	Bi:Cu Ratio	Switching Characteristics	Solution Appearance
A	400	100	1.5	1 M KCl	4	Incomplete metal stripping	Dark blue
B	400	100	1.5	1 M KBr	4	Incomplete metal stripping	Dark blue
C	400	100	1.5	1 M NaI	4	Reversible	Dark blue
D	100	25	1.5	1 M NaI	4	Reversible	Blue
E	80	20	1.5	1 M NaI	4	Reversible, slower kinetics	Light blue
F	120	5	1.5	2 M NaI	24	Reversible	Light blue
G	120	5	1.5	-	24	Incomplete metal stripping	Light blue
H	-	5	1.5	2 M NaI	-	Very slow kinetics	Light blue
I	120	-	1.5	2 M NaI	-	Reversible, slower kinetics	Transparent

Table 8. 1: Composition of some of the various EDTA electrolytes studied.

Although the presence of iodide in Solution C enables optically reversible metal electrodeposition, due to the high concentration of CuEDTA^{2-} complexes, the solution has a dark blue color that limits its use in dynamic windows. To create a more transparent electrolyte, we decreased the Cu^{2+} and Bi^{3+} concentration by a factor of four (Solution D, Table 8.1). This reduced metal ion concentration maintained the established Bi:Cu ratio, but resulted in a lighter blue color than Solution C without significantly sacrificing switching speed. In Solution E, we further reduced the total metal ion concentration, but found that the switching kinetics decreased noticeably. These results suggest that at a total Cu^{2+} and Bi^{3+} ion concentration of 125 mM (Solution D), the rate of reversible metal electrodeposition is limited by diffusion of the ions to the electrode surface. In contrast, at lower metal ion concentrations (Solution E), the kinetics of the system are no longer

limited by diffusion and instead are controlled by the speed of an (electro)chemical step at the electrode. In other words, to ensure the fastest possible switching speed with this electrolyte chemistry, the total Bi^{3+} and Cu^{2+} concentration should not fall below 125 mM.

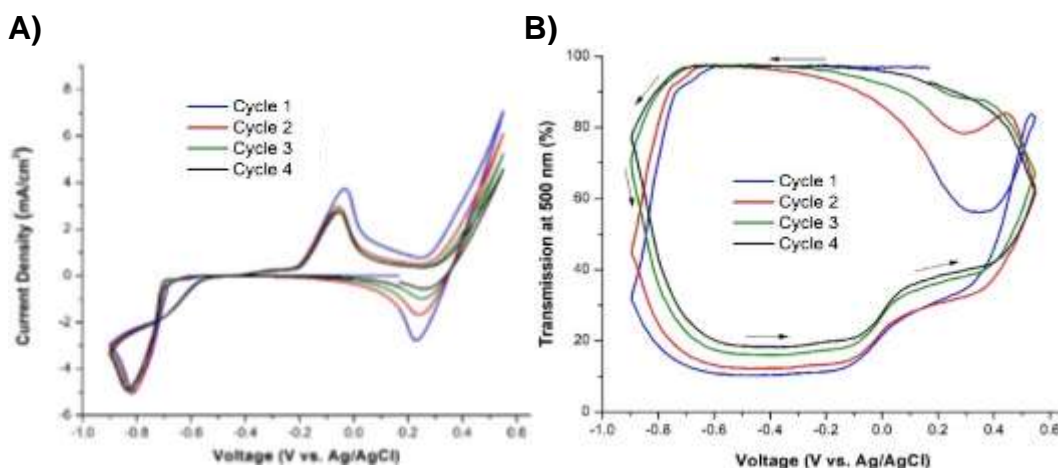


Figure 8.2: Cyclic voltammetry (A) and corresponding transmission at 500 nm (B) of a Pt-modified ITO on glass working electrode in an electrolyte containing 120 mM $\text{Bi}(\text{NO}_3)_3$, 5 mM CuCl_2 , 1.5 M EDTA, and 2.0 M NaI adjusted to pH 8.5 with HCl.

We further optimized the switching speed and transparency of the electrolyte by modifying the Bi:Cu ratio and NaI concentration (Solution F). Figure 8.2A presents CVs of reversible metal electrodeposition elicited from Solution F. Starting from the open circuit potential (OCP) of about +0.2 V and scanning the potential negative, the current density remains near zero until around -0.6 V at which point Bi and Cu electrodeposition commence. The metal electrodeposition wave peaks at around -0.8 V, indicating that the process becomes limited by diffusion of metal ions to the surface. On the reverse scan, a metal stripping peak occurs at a voltage of about -0.05 V followed by an anodic process starting around +0.3 V, which is due to the oxidation of I^- to I_2 . Once

the electrode is swept back to the negative direction, a cathodic peak at around +0.25 V appears due to the reduction of I_2 back to I^- . While performing the voltammetry, we also measured the transmission at 500 nm of the electrode (Figure 8.2B). During metal electrodeposition, the electrode transmission decreases from about 95% to 10-20% due to opacity of the metal electrodeposits. As expected, the transmission of the electrode increases throughout the metal stripping peak. However, the transmission only increases to 30-40%. The production of I_2 causes the transmission of the electrode to return fully to its original 95% value. The data show that this electrolyte supports optically reversible metal electrodeposition over the four CV cycles measured. Furthermore, these results demonstrate that I_2 is instrumental in enabling reversible optics.

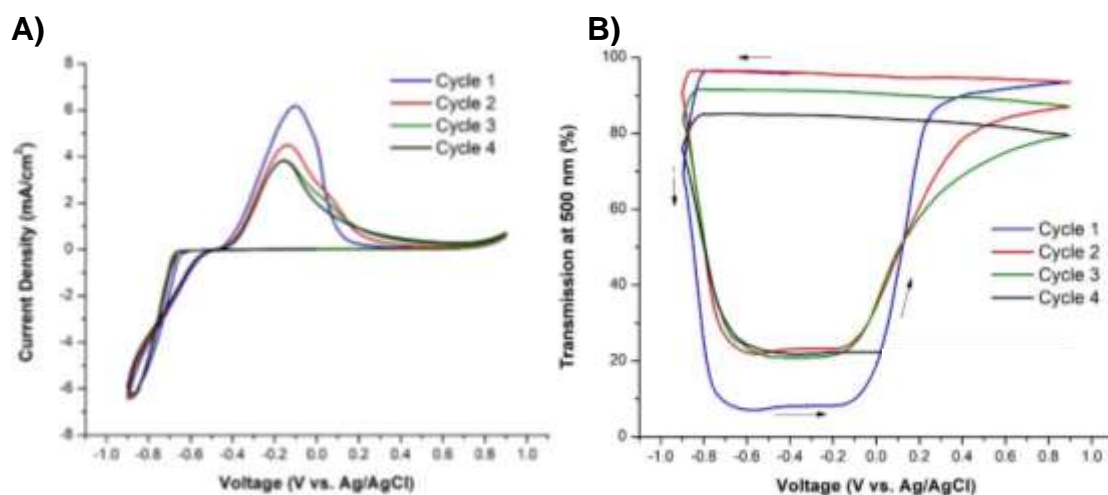


Figure 8.3: Cyclic voltammetry (A) and corresponding transmission at 500 nm (B) of a Pt-modified ITO on glass working electrode in an electrolyte containing 120 mM $Bi(NO_3)_2$, 5 mM $CuCl_2$, and 1.5 M EDTA adjusted to pH 8.5 with HCl.

To further understand the electrochemical behavior of the optimized Bi-Cu EDTA electrolyte (Solution F), we performed spectroelectrochemistry on a series of

modified electrolytes with various components removed. Figure 8.3A displays CVs of the Bi-Cu EDTA electrolyte without NaI (Solution G). Without NaI, the CVs still exhibit well-defined metal electrodeposition and stripping processes, but as expected, there are not peaks associated with I_2 redox. Because I_2 aids in metal stripping, the transmission of the electrode is not fully reversible during cycling (Figure 3B). Specifically, the maximum attainable electrode transmission decreases from about 95% to about 80% over the course of four CV cycles.

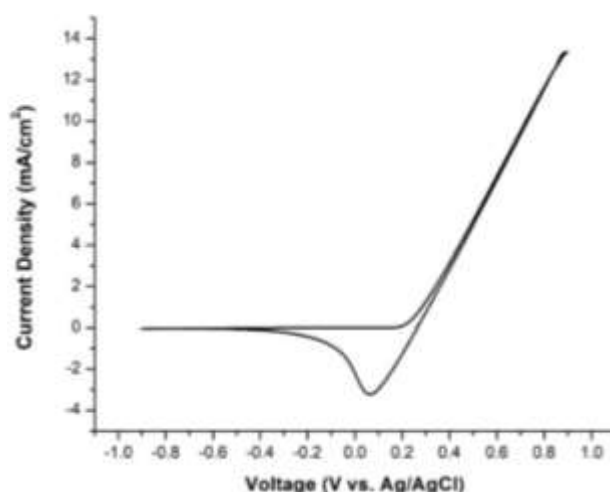


Figure 8.4: Cyclic voltammetry of a Pt-modified ITO on glass working electrode in an electrolyte containing 1.5 M EDTA and 2.0 M NaI adjusted to pH 8.5 with HCl.

To confirm that the anodic process that begins at about +0.3 V is due to I_2 formation, we performed a CV in an electrolyte without Bi and Cu salts (Figure 8.4). As expected, the CV does not show metal electrodeposition and stripping processes, but otherwise possesses very similar features to those present in the complete Bi-Cu EDTA electrolyte. This experiment further demonstrates that the anodic process beginning at

+0.3 V is due to the oxidation of I^- to I_2 and the cathodic peak is caused by the reduction of formed I_2 to I^- .

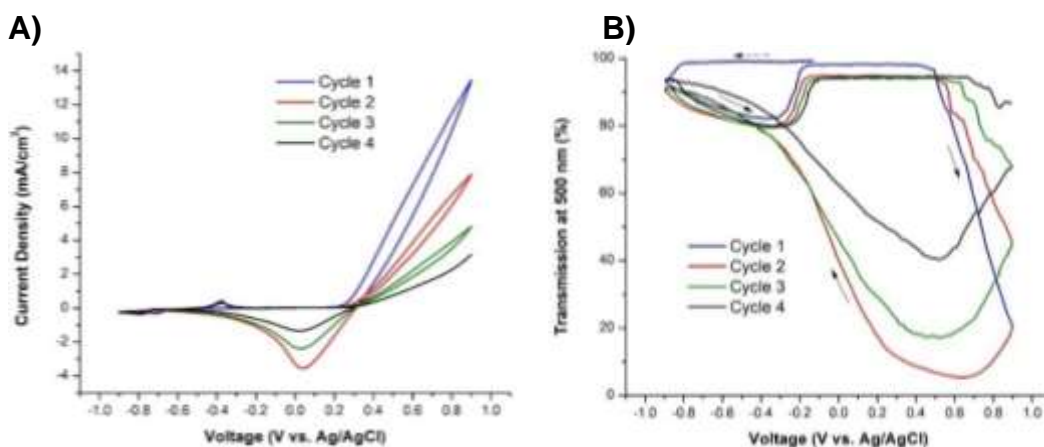


Figure 8.5: Cyclic voltammetry (A) and corresponding transmission at 500 nm (B) of a Pt-modified ITO on glass working electrode in an electrolyte containing 5 mM $CuCl_2$, 1.5 M EDTA, and 2.0 M NaI adjusted to pH 8.5 with HCl.

Next, we performed spectroelectrochemistry of the Bi-Cu EDTA electrolyte without $Bi(NO_3)_3$ (Solution H). CVs of this electrolyte only possess minor electrodeposition and stripping features because the Cu concentration in the electrolyte is only 5 mM (Figure 8.5A). As a result, the metal optics do not change dramatically during these processes (Figure 8.5B). However, the I_2 redox processes are still present and without Bi deposition, the formed I_2 does not have any metal to strip and instead goes into bulk solution. The bulk I_2 formed during I^- oxidation causes the solution to turn the characteristic yellow-red color of I_2 , which causes the electrode transmission to decrease substantially.

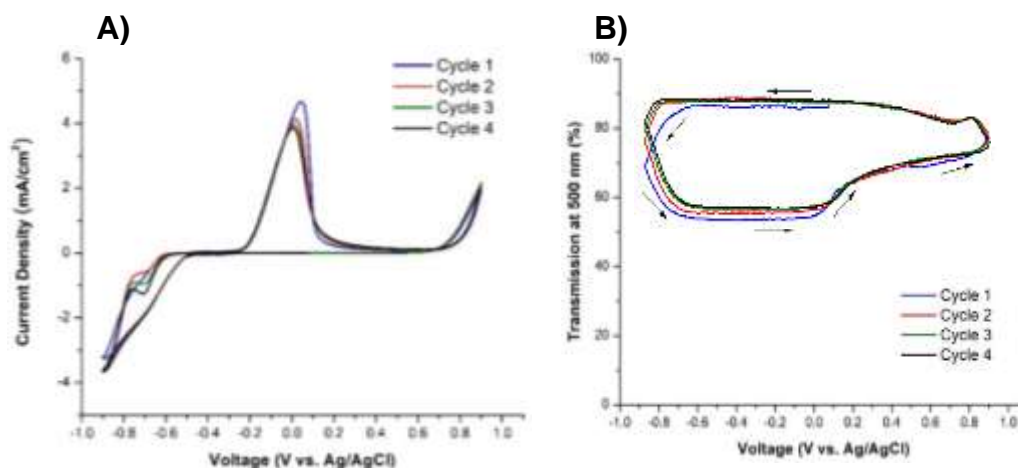


Figure 8.6: Cyclic voltammetry (A) and corresponding transmission at 500 nm (B) of a Pt-modified ITO on glass working electrode in an electrolyte containing 120 mM $\text{Bi}(\text{NO}_3)_2$, 1.5 M EDTA, and 2.0 M NaI adjusted to pH 8.5 with HCl.

Lastly, we performed CVs of the Bi-Cu EDTA electrolyte without CuCl_2 (Solution I, Figure 8.6A). The CVs contain Bi electrodeposition and stripping features. However, the transmission of the electrode only decreases to about 55% by the end of Bi electrodeposition (Figure 8.6B). By comparison, the electrode transmission decreases to 10-20% in the complete Bi-Cu EDTA electrolyte (Solution F, Figure 8.2B). These results indicate that although the concentration of CuCl_2 added to the complete electrolyte is low (5 mM), the addition of Cu has a profound effect on the switching speed of the electrode. Furthermore, we note that the absence of Cu substantially decreases the kinetics of I_2 formation. The exact origin of this difference is unclear, but it may be due to the formation of iodine-containing Bi complexes of EDTA that are favored without Cu. [153]

A)

B)

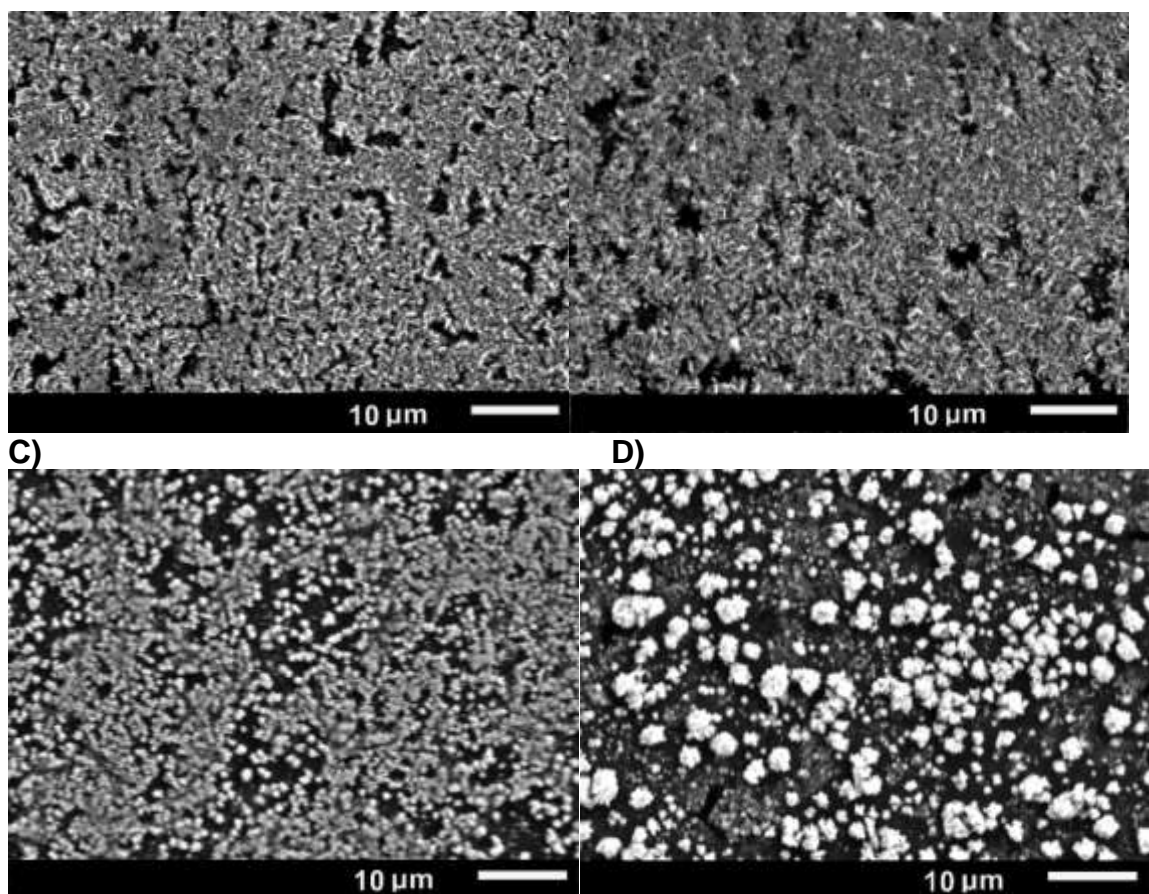


Figure 8.7: Scanning electron microscope images of metal electrodeposits on Pt-modified ITO on glass working electrodes electrodeposited from an electrolyte containing 120 mM $\text{Bi}(\text{NO}_3)_2$, 1.5 M EDTA, and 2.0 M NaI adjusted to pH 8.5 with HCl without (A, B, Solution I) and with 5 mM CuCl_2 (C, D, Solution F). Electrodeposition was performed at -0.9 V for 30 s (A, C) or 60 s (B, D).

In an effort to understand why the addition of a low concentration of CuCl_2 (5 mM) to the electrolyte significantly increases the optical contrast of the working electrode during CV, we analyzed the morphology of the metal electrodeposits using SEM-EDX. EDX spectra confirm the presence of Bi and Bi-Cu metals when using Solutions I and F, respectively (Supporting Figure 12.6.1). Pt is also present in the EDX spectra due to the presence of Pt nanoparticles on the ITO electrodes. SEM images in the

absence of CuCl_2 (Solution I) show that the Bi electrodeposits formed after 30 s (Figure 8.7A) and 60 s (Figure 8.7B) of metal electrodeposition consist of dendrite-like particles with numerous protrusions. Previous SEM images from studies of Bi electrodeposits from acidic Bi electrolytes without Cu exhibit a similar dendritic morphology.[36] In contrast, the Bi-Cu electrodeposits formed after 30 s (Figure 8.7C) and 60 s (Figure 8.7D) of metal electrodeposition are much more spherical. A similar transition from dendritic to spherical morphologies upon Cu addition in acidic electrolytes has been observed and is due to Galvanic displacement of the Bi by the Cu. [36] Evidently, these spherical Bi-Cu particles block light more effectively than the dendritic Bi electrodeposits. Furthermore, more metal is electrodeposited when Bi and Cu are codeposited, which also explains the higher contrast ratio observed for the complete Bi-Cu electrolyte (Solution F). When Cu is present (Solution F), an average of 68 mC/cm^2 of charge are passed during the metal electrodeposition portion of the CV whereas only 58 mC/cm^2 are passed without Cu (Solution I). In other words, the charge passed during metal electrodeposition increases by 17% upon addition of 5 mM of CuCl_2 . In contrast, adding this low concentration of CuCl_2 only increases the total Bi^{3+} and Cu^{2+} concentration by 4%. This finding demonstrates that Cu accelerates the intrinsic kinetics of metal electrodeposition. The increased optical contrast observed with Cu is therefore due to both the increased metal electrodeposition kinetics and the change in electrodeposit morphology.

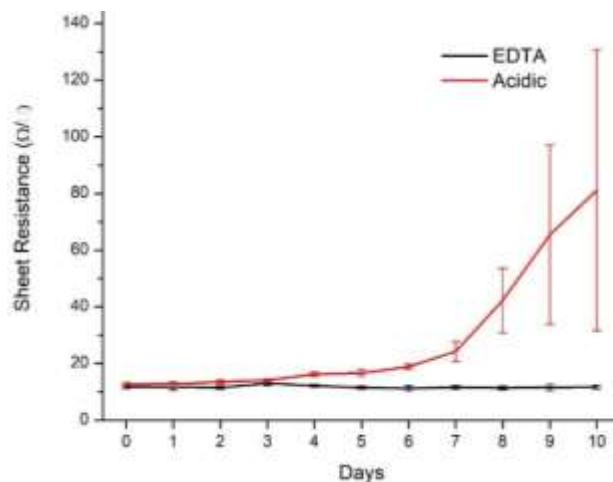


Figure 8.8: Sheet resistances of ITO on glass substrates over time measured using a four-point probe when immersed in an electrolyte containing 5 mM BiCl₃, 15 mM CuCl₂, 10 mM HCl, and 1.0 M LiBr (red line, acidic electrolyte) and an electrolyte containing 120 mM Bi(NO₃)₂, 5 mM CuCl₂, 1.5 M EDTA, and 2.0 M NaI adjusted to pH 8.5 with HCl (black line, EDTA electrolyte, Solution F).

Having developed an alkaline electrolyte that supports reversible metal electrodeposition, we next sought to implement the electrolyte in practical two-electrode 25 cm² dynamic windows. As discussed in the Introduction, we hypothesize that metal-based dynamic windows with alkaline electrolytes would have improved durability over those with acidic electrolytes because ITO slowly degrades under acidic conditions. To test the validity of this hypothesis, we first measured the sheet resistances over time of ITO on glass substrates immersed in the Bi-Cu EDTA electrolyte (Solution F) and an acidic Bi-Cu electrolyte studied previously (Figure 8.8).[36, 37] After three days of immersion in the acidic electrolyte, the sheet resistance of the ITO substrate begins to increase above its original ~12 Ω/sq value and sharply increases over the next seven days (Figure 8.8, red line). The standard deviations of the sheet resistance measurements across the sample areas also significantly increases with time, indicating that the

uniformity of the ITO decreases with increasing sheet resistance. These results suggest that the acidic Bi-Cu electrolyte slowly etches the ITO off of the glass substrates. In sharp contrast, the sheet resistance of an ITO substrate immersed in the alkaline Bi-Cu electrolyte does not significantly change over the course of ten days (Figure 8.8, black line). This result demonstrates that ITO is more stable in the alkaline electrolyte.

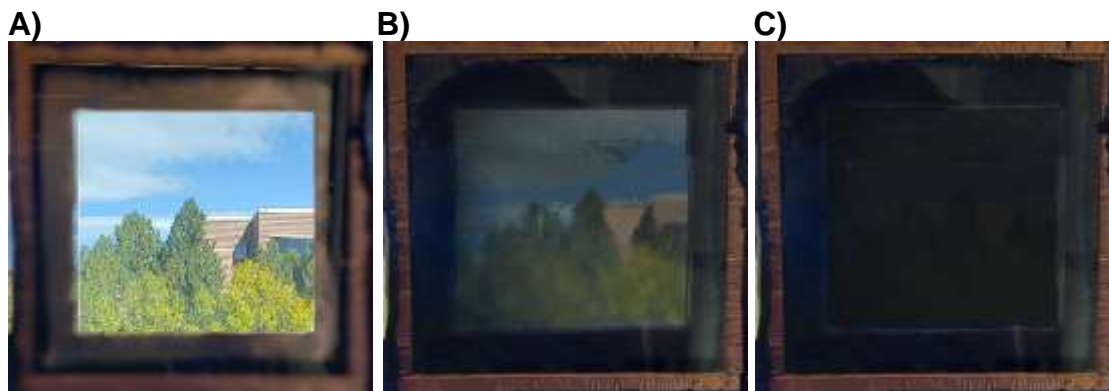


Figure 8.9: Photographs of a 25 cm² window containing the Bi-Cu EDTA electrolyte (Solution F) after 0 s (A), 30 s (B), and 60 s (C) of metal electrodeposition at -0.9 V.

Because ITO exhibits superior stability in the Bi-Cu EDTA electrolyte as compared to the acidic electrolyte, we next constructed 25 cm² dynamic windows with each electrolyte to evaluate their durability. Figure 8.9 displays photographs of a dynamic window containing the Bi-Cu EDTA electrolyte during the metal electrodeposition process. To test the durability of the window, we switched the device between clear and dark states six times each day (Supporting Figures 12.6.2 and 12.6.3). Figure 8.10 displays the average contrast ratio of the six switching cycles for windows containing the acidic and alkaline electrolytes. Immediately after device construction (day 0), the window with the acidic electrolyte possessed a superior contrast ratio (~71%) compared

to the device with the alkaline electrolyte (~25%). After resting under open circuit for one day, however, the contrast ratio of the window with the acidic electrolyte decreased substantially to ~45%. The contrast ratio of the acidic window fairly consistently decreased over the course of seven days. After eight days (data not shown), the window failed to switch at all. By comparison, the contrast ratio of the alkaline window did not change as dramatically as the acidic window (Figure 8.10, black circles). There is some variation in the contrast ratio over the seven days for the alkaline window. The exact origin of this variation is unknown, but it could be due to changes in small amounts of residual metal left on the ITO electrode after cycling that affect the kinetics of metal electrodeposition during each subsequent day. Taken as a whole, however, the data demonstrate that the alkaline Bi-Cu EDTA electrolyte does indeed improve the durability of practical two-electrode dynamic windows.

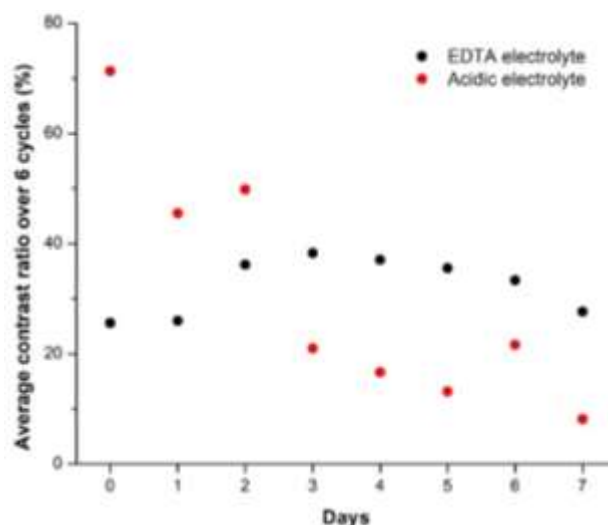


Figure 8.10: Contrast ratio of Pt-modified window with electrolyte solution containing 5 mM BiCl₃, 15 mM CuCl₂, 10 mM HCl, and 1.0 M LiBr (red dot, acidic electrolyte) and an electrolyte containing 120 mM Bi(NO₃)₂, 5 mM CuCl₂, 1.5 M EDTA, and 2.0 M NaI adjusted to pH 8.5 with HCl (black dot, EDTA electrolyte, Solution F).

8.4. Conclusion

We develop electrolytes that support the reversible electrodeposition of Bi and Cu on ITO on glass electrodes for use in dynamic windows. The key innovation is the design of an alkaline electrolyte that is chemically compatible with ITO. The enabling component of the electrolyte is the chelating agent EDTA, which allows for the development of soluble Bi electrolytes at basic pH values. Two-electrode 25 cm² dynamic windows with an alkaline Bi-Cu electrolyte exhibit improved durability over their acidic electrolyte counterparts. In future work, we will explore the use of chelating agents other than EDTA that may facilitate improved metal electrodeposition and stripping kinetics while maintaining Bi³⁺ solubility.

Chapter 9: Dynamic Windows using Reversible Zn Electrodeposition in Neutral Electrolytes with High Opacity and Excellent Resting Stability

9. 1. Introduction

Dynamic windows possess electronically tunable transmission that enable control of light and heat flow into buildings and other spaces. Buildings are responsible for ~40 % of total energy demand in the USA and the UK. [34, 154] Dynamic windows are promising technologies because they save up to ~10% of energy consumption in buildings by reducing lighting, heating, and cooling costs without compromising aesthetics. [155] Moreover, dynamic windows coupled with transparent solar cells could be used to generate large quantities of energy in high-rise buildings where rooftop space is often smaller than the window footprint. [133, 134] In addition to buildings, dynamic windows could also be used in automobiles, [156, 157] sunglasses, [40, 158] mirrors, [60, 159] displays, [66, 160] and transparent batteries [161, 162].

Over the last three decades, researchers have explored various types of electrochromic materials for dynamic window applications. [121, 135] The most common electrochromic materials are transition metal oxides, which switch color upon changing oxidation state. For example, tungsten oxide (WO_3) is colorless in its +6 oxidation state and transitions to an opaque blue state when it is electrochemically reduced to the +5 oxidation state. Despite much research studying transition metal oxides and other electrochromic materials including polymers, [43] small molecules, [44] and nanoparticles, [163] there is not yet a single technology that fulfills the color neutrality, switching speed, low cost, and durability required for the widespread adoption of

dynamic windows. [47] Compared with electrochromic materials, reversible metal electrodeposition (RME) for dynamic window applications is an underexplored approach that has recently shown great promise. [60, 104, 105]

RME-based devices have several advantages over traditional electrochromic devices. First, metals have high extinction coefficients, which means that they uniform metal films are opaque at thicknesses of 20-30 nm. In contrast, electrochromic materials need to be 100-1000 nm thick to block the same amount of light, which can result in slower switching speeds and higher costs. [39, 45, 49] Second, electrochromic materials are typically deposited using expensive vacuum techniques, while RME devices are mostly solution processed. [40, 45, 136] Third, while the most extensively used electrochromic material, WO_3 , is blue in its opaque state, most electrodeposited metal thin films are black, and this color neutrality is desired for most applications. [36, 40, 113]

Dynamic windows harnessing RME are electrochemical devices in which the working electrode is a transparent conductive electrode such as tin-doped indium oxide (ITO) and the counter electrode is a metal frame or mesh. In between the two electrodes, RME devices contain a solution of transparent metal ions in a liquid or gel electrolyte. By applying a negative potential with respect to the working electrode, the metal ions in the electrolyte are reduced to elemental metal on the working electrode, which transforms the device from clear to dark. At the same, metal is oxidation on the counter electrode to form metal ions and charge balance the device. To switch dark to clear, a positive potential is applied to the working electrode to induce the opposite reactions.

Most previous RME dynamic windows operate the electrodeposition of a mixture of Bi and Cu. [37, 40, 109] Although these devices exhibit fast switching speeds and excellent color neutrality, one disadvantage is the limited solubility of Bi ions in aqueous electrolytes due to the formation of insoluble $\text{Bi}(\text{OH})_3$. As a result, Bi-Cu electrolytes are typically acidic such that the $\text{Bi}(\text{OH})_3$ is solubilized. The acid in these electrolytes, however, slowly etches the transparent conducting electrodes and as a result, the devices switch increasingly slowly over time even in the absence of continual cycling. In other words, devices with acidic electrolytes possess poor resting stability, which is one of the biggest challenges hampering the durability of RME dynamic windows. [164]

Most aqueous RME electrolytes contain metal ions with positive standard reduction potentials vs NHE such as Bi^{3+} , Cu^{2+} , and Ag^+ . Due to their positive reduction potentials, these metal ions can thermodynamically electrodeposit before H_2 is evolved from H_2O . In contrast, the standard reduction potential of Zn^{2+}/Zn is -0.76 V vs NHE. [165] From a thermodynamic standpoint, this negative reduction potential means that H_2 generation will occur before Zn electrodeposition. [166] However, neutral pH electrolytes and Zn metal's sluggish ability to evolve H_2 can kinetically impede this unwanted side reaction.[161, 167, 168] Furthermore, ZnO , which also can form during electrodeposition, prevents H_2 production.[169] The Zn aqueous battery literature shows that organic acids or surfactants in the electrolyte can adsorb on electrodes and further increase the overpotential for H_2 generation. [170, 171]

In this work, we develop dynamic windows based on reversible Zn electrodeposition with a pH neutral gel electrolyte. As a result of the neutral pH, the dynamic window functions for four weeks without any significant degradation, far

exceeding the resting stability of previous RME devices using acidic electrolytes. Furthermore, 100 cm² dynamic window switch with a ~80% contrast ratio within less than 20 s.

9.2. Results and Discussion

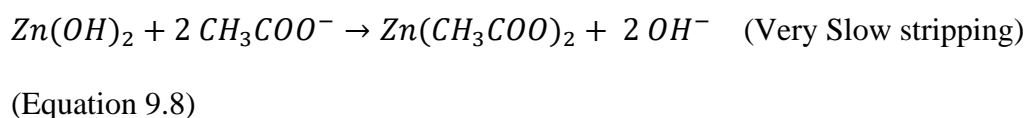
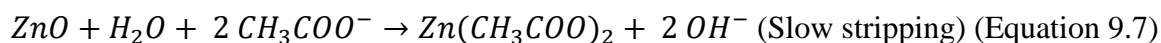
9.2.1. Dynamic Window Architecture and Reaction Mechanism

Figure 9.1 shows the device architecture of the Zn-based dynamic windows in which ITO is used as the working electrode and a Zn mesh serves as the counter electrode. In between these two electrodes, there is a gel-modified aqueous-based electrolyte, which contains Zn²⁺ ions for reversible metal electrodeposition and K⁺ ions for increasing the ionic conductivity of the electrolyte. The application of -1 V with respect to the working electrode switches the dynamic window from a clear to dark state. At a negative potential, Zn²⁺ ions are reduced to metallic Zn and electrodeposited on the ITO surface. At the same time, to counter this reaction, Zn metal from the counter electrode is oxidized to Zn²⁺. Upon flipping the polarity of the potential, the opposite reactions occur, and the dynamic window switches back to its original clear state.

Deposition mechanism:



Stripping mechanism:



Equation 9.1) represents Zn electrodeposition on the ITO surface during the application of a reductive potential at the working electrode. However, the presence of dissolved O_2 in the aqueous electrolyte can react with the electrodeposited Zn to form ZnO (Equation 9.2). In a subsequent step, ZnO can be electrochemically reduced to Zn (Equation 9.3) or be chemically converted to $\text{Zn}(\text{OH})_2$ (Equation 9.4). $\text{Zn}(\text{OH})_2$ can also be electrochemically reduced to Zn (Equation 9.5). It is known that the conversion of ZnO and $\text{Zn}(\text{OH})_2$ to Zn is kinetically sluggish (Equations 9.3 and 9.5). [172, 173]

When stripping occurs at the working electrode to turn the device clear, Zn metal is oxidized to soluble Zn^{2+} ions in a kinetically fast reaction (Equation 9.6). For ZnO and $\text{Zn}(\text{OH})_2$ to be removed from the electrode, they must chemically react with acetate in the electrolyte to form soluble $\text{Zn}(\text{CH}_3\text{COO})_2$ (Equations 9.7 and 9.8). The kinetics of dissolving the ZnO and $\text{Zn}(\text{OH})_2$ deposits depend upon their solubilities and their acidities (pK_a values) because they react with a base, $\text{CH}_3\text{COO}^{-}$. While the pK_a values of ZnO and $\text{Zn}(\text{OH})_2$ are similar, [174] the solubility of ZnO in water (20 μM) is significantly higher than that of $\text{Zn}(\text{OH})_2$ (1 μM). [175, 176] For this reason, we expect that ZnO dissolution is kinetically more favorable than $\text{Zn}(\text{OH})_2$ dissolution.

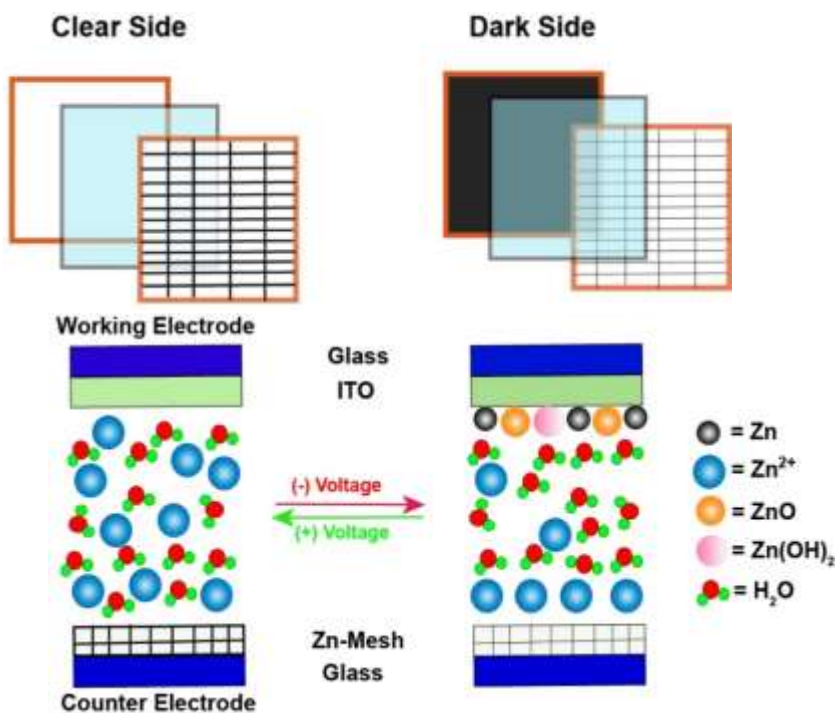


Figure 9.1: Schematic of a dynamic window that facilitates reversible Zn electrodeposition on an ITO on glass working electrode and a Zn mesh counter electrode.

9.2.2. Cycle Life and Durability

Using the above architecture and Zn chemistry, we constructed 25 cm² dynamic windows (Figure 9.2), which possesses 70%-78% transmission from 450 nm to 900 nm in their clear state. Upon application of -1 V for 30 s, the dynamic window transitions from its clear state to an opaque state. In its dark state, the dynamic window exhibits less than 0.1% transmission from 400 nm to 1000 nm (Figure 9.2a), resulting in an extremely dark appearance. This low transmission is important for dynamic window applications requiring privacy such as in residential settings. Moreover, the spectrum of the dynamic window over the visible and near-IR regions is relatively flat after 10 s and 15 s of electrodeposition and extremely flat at 30 s of electrodeposition, which is reflective of a

color neutral appearance throughout switching. The calculated color neutrality values (c^*) of the transmission spectra are 9, 9, and 3 after 10 s, 15 s, and 30 s, respectively (Supporting Figure 12.7.1), in which values less than 10 are considered color neutral for most purposes.[139]

Figure 9.2b shows the transmission of the dynamic window at 600 nm versus electrodeposition time. By applying -1 V for 30 s, the dynamic window transitions from 78% to less than 0.1% transmission after 20 s. This switching speed is the fastest reported for a metal-based dynamic window that has a dark state with less than 1% transmission. [36, 40, 41, 106, 109, 113, 137, 177] To switch the window to its clear state, 1 V was applied, and the window returned mostly to its original transmission after 40 s.

To understand the origin of the extreme opacity of the device, we conducted scanning electron microscopy (SEM) coupled with energy dispersive X-ray spectroscopy (EDX) of the working electrode after the window was switched to its dark state (Supporting Figure 12.7.2). The SEM image (Supporting Figure 12.7.2a) shows that the Zn electrodeposits are ~ 5 μm in size and are densely packed, which results in the high opacity of the films. The EDX spectrum confirms the presence of Zn metal on the electrode along with In and O from ITO (Supporting Figure 12.7.2b).

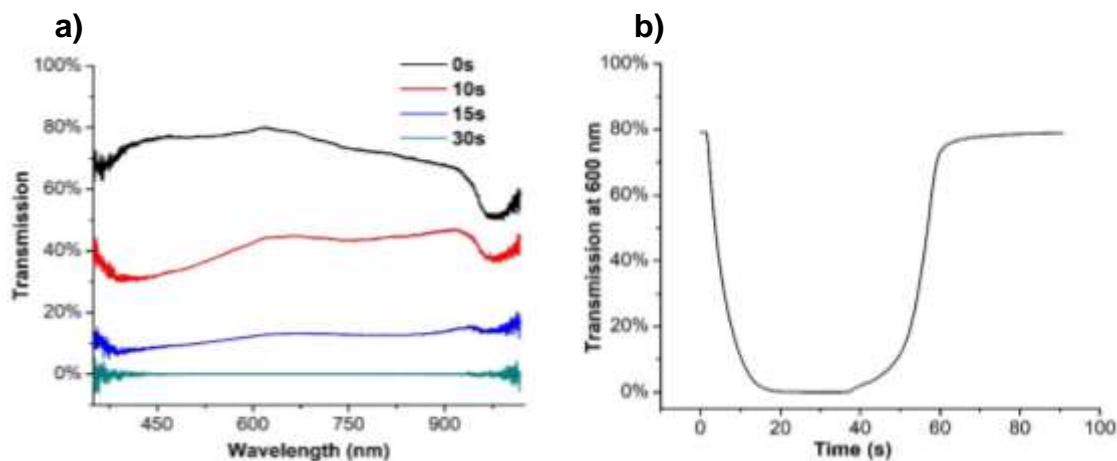


Figure 9.2: (a) Transmission of a 25 cm² dynamic window with an ITO on glass working electrode, a Zn mesh counter electrode, and a Zn acetate gel electrolyte as a function of wavelength after 0 s (black), 10 s (red), 15 s (blue), and 30 s (teal) of window tinting at -1 V. (b) Transmission of the same window at 600 nm during 30 s of metal electrodeposition at -1 V and 60 s of metal stripping at 1 V.

The majority of previous dynamic windows based on metal electrodeposition utilize acidic electrolytes ($\text{pH} < 3$) to improve metal ion solubility and reaction kinetics. [37, 109, 137, 177] A major problem of these acidic systems is that they slowly etch ITO in conjunction with halides also present in the electrolyte. For this reason, the windows have poor shelf life, and they exhibit slower switching speeds in the weeks following initial device construction. [41] Because the Zn acetate electrolyte used in this work is nearly neutral ($\text{pH} = 6.4$), we anticipated that the shelf life of the windows would be significantly improved.

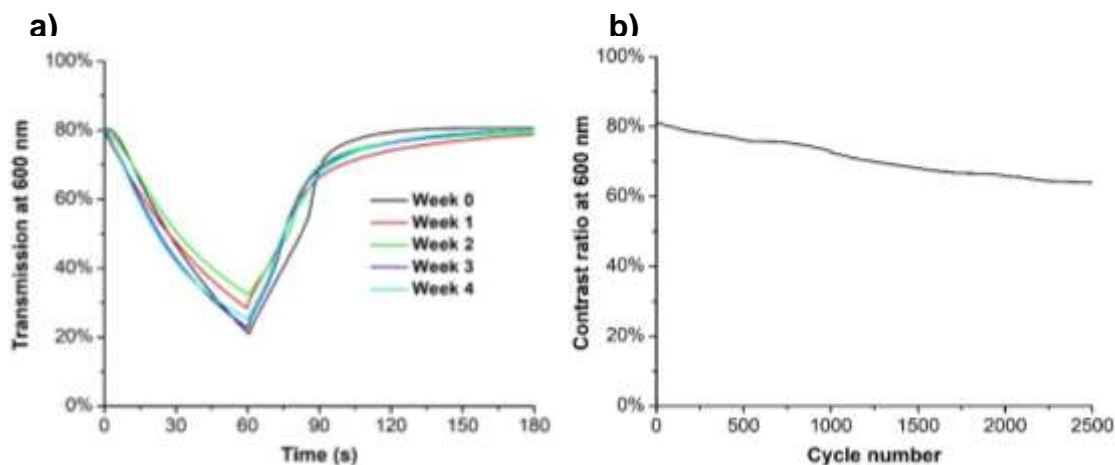


Figure 9.3: (a) Transmission of a 25 cm² dynamic window with an ITO on glass working electrode, a Zn counter electrode, and a Zn acetate gel electrolyte during switching. The device was switched once a week for four consecutive weeks. The window was darkened at -0.5 V for 60 s and lightened at 1 V for 120 s. (b) Contrast ratio at 600 nm of an analogous dynamic window with a Zn-Cu electrolyte over the course of 2,500 cycles.

Figure 9.3a shows the transmission at 600 nm of a 25 cm² Zn-based dynamic window while it switches over the course of four weeks. After applying -0.5 V for 60 s, the transmission of the dynamic window decreases to between 21%-34% each week. Although there are small variations in the minimum transmission reached each week, there is no clear trend, suggesting that the windows are not degrading over time in the Zn electrolyte. By contrast, a metal-based dynamic window using a standard acidic Bi-Cu electrolyte degrades substantially after one week (Supporting Figure 12.7.3). We ascribe the improved durability of the Zn electrolyte to its nearly neutral pH, which prevents ITO etching that occurs in acidic electrolytes.

Although the Zn-based dynamic windows possess excellent optical reversibility and long-term durability, they exhibit poor cycleability when continuously cycled without rest. For example, the contrast ratio of a 25 cm² dynamic window decreases

steadily over the course of 250 cycles when continuously switched (Supporting Figure 12.7.4a). XRD data show that ZnO and Zn(OH)₂ accumulate on the ITO electrode after this continuous cycling (Supporting Figure 12.7.4b). As described in section 2.1, ZnO and Zn(OH)₂ are chemically converted to soluble Zn²⁺ through kinetically slow reactions. As a result, ZnO and Zn(OH)₂ do not have time to fully dissolve into the electrolyte during continuous cycling, and thus they slowly accumulate on the ITO electrode, which decreases the transmission of the device in its clear state. A more detailed discussion of the chemical principles of these phenomena are described in section 2.4.

To overcome this problem, we explored the use of electrolyte additives to potentially slow down the formation of chemically sluggish ZnO and Zn(OH)₂. Bi and Pb are commonly used as electrolyte additives for enhancing Zn electrodeposition in aqueous battery applications. [178, 179] Because Bi and Pb have more positive reduction potentials than Zn, Bi and Pb electrodeposition occurs before Zn. The small amounts of Bi and Pb electrodeposits serve as nucleation sites for Zn electrodeposition that later occurs, and in this way, the amount of ZnO and Zn(OH)₂ formed is limited.

Due to its toxicity, we did not study Pb, and we found that Bi salts are insoluble in the Zn electrolyte due to the formation of a Bi(OH)₃ precipitate. For this reason, we used Cu as an electrolyte additive because Cu also has a more positive reduction potential than Zn. We found that the addition of 1 mM of Cu(CH₃COO)₂ in the electrolytes suppresses the formation of ZnO and Zn(OH)₂ during window switching. With this Zn-Cu electrolyte, the devices can cycle 2,500 times (Figure 3b). Even though the Cu additive greatly improve the cycle life of the dynamic windows, the contrast ratio still slowly degrades when continuously cycled 2,500 times. In future work, we will study additional

additives such as chelating ligands that may aid in ZnO and Zn(OH)₂ dissolution and further improve device cycle life.

9.2.3. 100 cm² Dynamic Window

To assess the scalability of Zn-based dynamic windows, we constructed a 100 cm² device using an ITO working electrode, a Zn-coated stainless steel grid as the counter electrode, and the Zn only electrolyte. The Zn grid provides a uniform distribution of Zn²⁺ during switching across the large electrode area. In principle, a transparent Zn grid could be designed to increase device aesthetics. For a sufficiently transparent grid that does not give rise to unwanted diffraction patterns, the grid lines would have to possess a thickness of ~10 μm and an interline spacing of hundreds of microns. However, the design and fabrication of a transparent Zn grid is outside the scope of this manuscript.

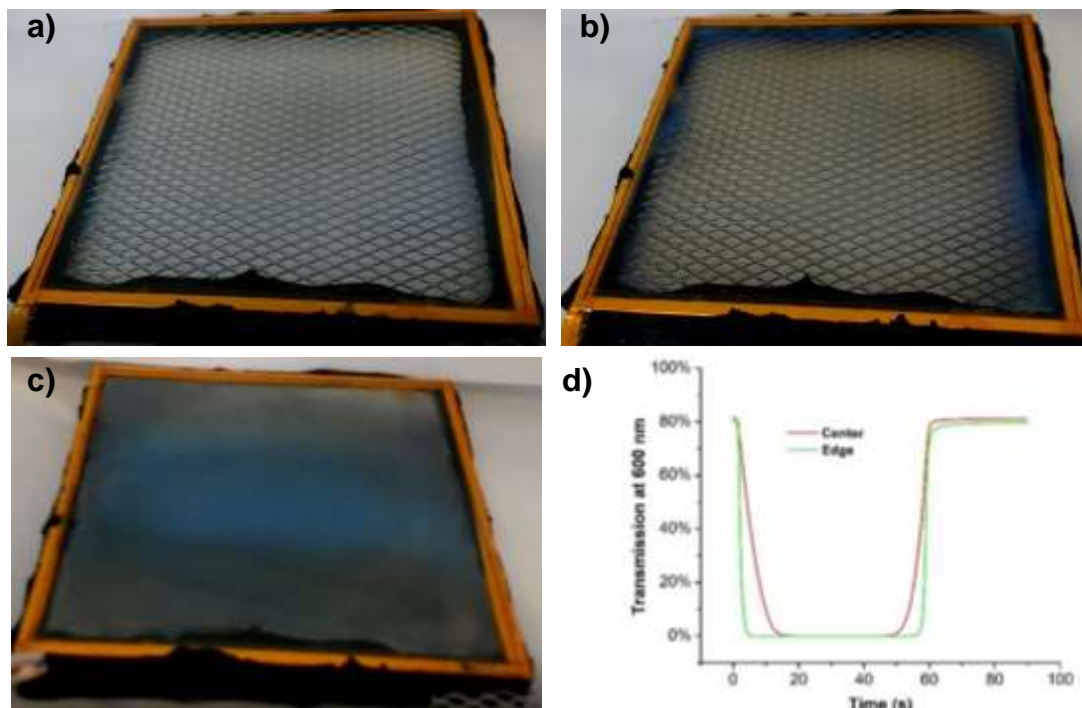


Figure 9.4: Photographs of a 100 cm² dynamic window after (a) 0 s, (b) 10 s, and (c) 30 s of metal electrodeposition using an ITO on glass working electrode and a Zn grid counter electrode. (d) Transmission at 600 nm through the edge (green) and the center (red) of the window during switching at -1 V for 30 s followed by 1 V for 60 s.

Photographs (Figure 9.4a-c) of the 100 cm² device during darkening show that the device switches relatively uniformly. Transmission data indicate that the window switches faster at its edge compared to its center (Figure 9.4d). This result is expected because the current of the device is collected along its perimeter, and there is a voltage drop that is established across the ITO working electrode toward its center. In future work, we will explore the coupling of reversible Zn electrodeposition on the working electrode with an electrochromic intercalation-based counter electrode such as those based on hexacyanoferrates. The use of an electrochromic counter electrode enables both electrodes of the device to darken during switching, and thus the amount of current

needed to achieve a given switching speed can be decreased. The decreased current requirement would result in a decreased voltage drop across the working electrode, thus increasing switching uniformity without sacrificing switching speed.

9.2.4. Study of Electrolytes

To understand how the Zn electrolyte supports reversible metal electrodeposition, we performed spectroelectrochemical studies of a 25 cm² dynamic window with an ITO working electrode and Zn metal frame counter/reference electrode. We conducted cyclic voltammetry (CV) from 2 V to -1 V at a slower scan rate of 5 mV/s and a faster scan rate of 50 mV/s (Supporting Figure 12.7.5) with *in situ* optical measurements shown in Figures 12.7.5a and 12.7.5b, respectively. At 5 mV/s, the device initially possesses 78% transmission at 600 nm. The transmission decreases to less than 0.1% due to the electrodeposition of Zn on the ITO surface during the reductive scan from 2 V to -1 V. On the reverse scan, metallic Zn is oxidized to soluble Zn²⁺ at potentials above 0 V. As a result, the electrode transmission increases and returns to 76%, close to but below its original value. The electrode transmission is not fully reversible due to the formation of small amounts of ZnO and Zn(OH)₂ on the ITO surface (*vide infra*).

By comparison, with a scan rate of 50 mV/s, the transmission of the electrode decreases to only ~10% during Zn electrodeposition because about 10 times less charge is passed during electrodeposition due to the faster scan rate. Interestingly, during the oxidative scan, the transmission only returns to 55%, which indicates that at this faster scan rate Zn electrodeposition is not reversible. We hypothesize that at this faster scan rate, a greater proportion of ZnO and Zn(OH)₂ deposit on the electrode as compared to

metallic Zn. At a slower scan rate, the greater amount of charge passed goes towards the electrochemical conversion of ZnO and Zn(OH)₂ to Zn (Equations 9.3 and 9.5). In other words, the amount of available O₂ dissolved in the electrolyte to form ZnO (Equation 9.2) and subsequently Zn(OH)₂ (Equation 9.4) is relatively small compared to the amount of Zn electrodeposited at the slower scan rate. As a result, at the slower scan rate, there is a larger amount of Zn as compared to ZnO and Zn(OH)₂, which enables the transmission of the electrode to be more reversible (Figure 9.5c) because the electrochemical dissolution of metallic Zn (Equation 9.6) is much faster than the chemical dissolution of ZnO and Zn(OH)₂ (Equations 9.7 and 9.8).

To probe the relative amounts of Zn, ZnO, and Zn(OH)₂ on the ITO surface under different conditions, we performed XRD. After conducting linear sweep voltammetry (LSV) at 5 mV/s and 50 mV/s from 2 V to -1 V, we recorded the XRD spectra of these two samples and compared the integrated peak areas associated with Zn, ZnO, and Zn(OH)₂ to estimate the composition of the electrodeposits (Supporting Figure 12.7.6). This analysis reveals that the percentage of metallic Zn in the electrodeposits at the slower scan rate is higher than those produced at the faster scan rate in accordance with the relative rates of Equations 9.1-9.5. Experiments analyzing the composition of electrodeposits produced in an Ar-sparged electrolyte versus an O₂-sparged electrolyte demonstrate that the percentage of Zn increases with the Ar-sparged electrolyte, which supports an electrodeposition mechanism that involves Equations 9.2 (Supporting Figure 12.7.7).

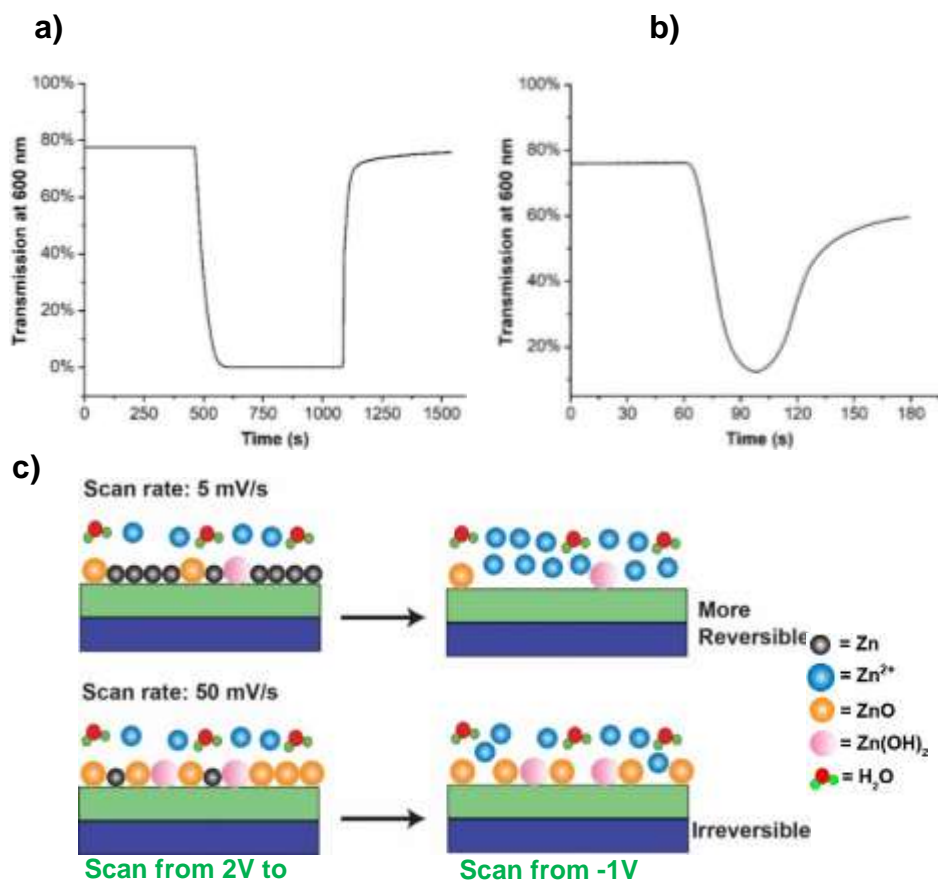


Figure 9.5. (a, b) Transmission at 600 nm during cyclic voltammetry scanning from 2 V to -1 V to 2 V of a 25 cm² dynamic window with an ITO on glass working electrode and a Zn metal frame as the counter and reference electrodes with a 0.5 M Zn acetate gel electrolyte. The scan rate was (a) 5 mV/s or (b) 50 mV/s. The corresponding CVs are shown in Supporting Figure 12.7.5. (c) Schematic of the working electrode during the deposition (left) and dissolution (right) portions of the CV at the two scan rates.

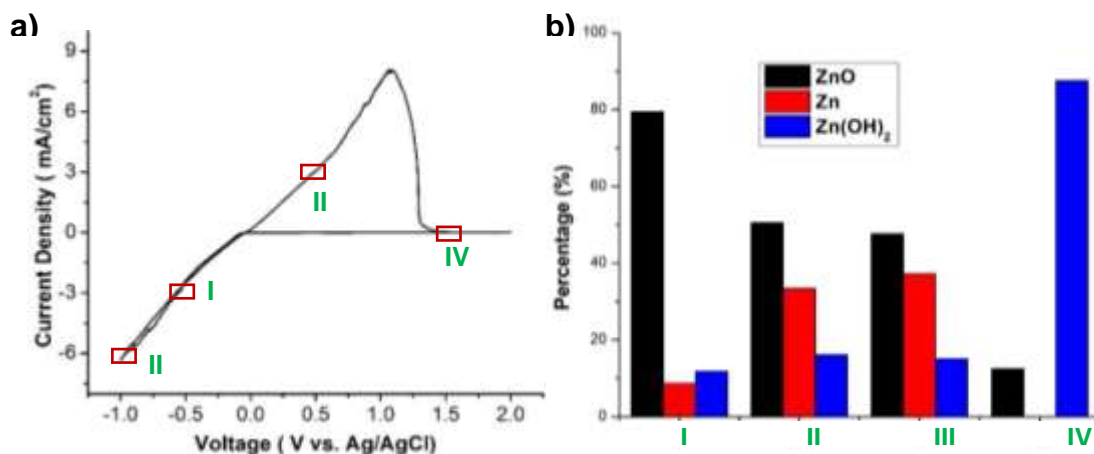


Figure 9.6. (a) Cyclic voltammogram at a scan rate of 5 mV/s of a 25 cm² dynamic window with an ITO on glass working electrode and a Zn metal frame as the counter and reference electrodes with a 0.5 M Zn acetate gel electrolyte. (b) Percentage of ZnO (black), Zn (red), and Zn(OH)₂ (blue) on the working electrode as determined by XRD analysis after performing voltammetry at 5 mV/s from (I) 2 V to -0.46 V, (II) 2 V to -1 V, (III) 2 V to -1 V to 0.5 V, and (IV) 2 V to -1 V to 1.45 V.

To understand further the dynamics of reversible Zn electrodeposition, we collected XRD spectra of the electrodeposits after halting a CV scan from 2 V to -1 V to 1 V at four different voltages (Figure 9.6a) and determined the relative compositions of Zn, ZnO, and Zn(OH)₂ (Figure 9.6b and Supporting Figures 12.7.8). At the early stages of electrodeposition (point I), the electrodeposits mostly consist of ZnO (80%). Because little charge has passed at this stage, there is a relatively large amount of O₂ available in the electrolyte. Most of the electrodeposited Zn thus reacts with this O₂ to form ZnO according to Equation 9.2. In contrast, during the latter stages of electrodeposition (point II), less O₂ is available in the electrolyte, and fresh Zn electrodeposits remain in their metallic state, and ZnO and Zn(OH)₂ are electrochemically converted back to Zn (Equations 9.3 and 9.5). As a result, the electrodeposits at point II contain less ZnO (50%) and more metallic Zn (33% vs. 9%). An additional experiment producing

electrodeposits by holding the potential at -1 V instead of performing a CV yields an even higher metallic Zn content (52%, Supporting Figure 12.7.9). This finding further demonstrates that the percentage of metallic Zn in the electrodeposits increases as more electrodeposition occurs.

At point III, the electrodeposits have undergone a small amount of electrochemical stripping, but their overall composition is similar to the values obtained at point II due to the small amount of stripping charge passed. At the end of stripping (point IV) though, the composition of the electrodeposits dramatically changes. At this stage, all of the metallic Zn has been removed from the electrode according to Equation 9.6 and only ZnO and Zn(OH)₂ remain. Because the transmission of the electrode has returned nearly to its original transparency at this stage (Figure 9.5a), the total quantity of ZnO and Zn(OH)₂ left on the electrode is small. Some ZnO and Zn(OH)₂ electrodeposits are left on the electrode because both of these compounds can only be removed from the surface through slow chemical dissolution steps (Equations 9.7 and 9.8). Of the electrodepositions that remain, however, most are comprised of Zn(OH)₂ (Figure 9.6b, rightmost bar). This finding confirms that the chemical dissolution of Zn(OH)₂ (Equation 9.8) is slower than that of ZnO (Equation 9.7). The chemical rationale for the difference in the rates of these two reactions is described in section 9.2.1. As discussed in section 9.2.2, it is the slow accumulation of Zn(OH)₂ on the electrode during cycling that explains why the maximum transmission of dynamic windows with a Zn only electrolyte decreases during hundreds of continuous cycles (Supporting Figure 12.7.4).

9.3. Conclusion

In conclusion, we studied reversible Zn electrodeposition on ITO electrodes and proposed mechanisms for the Zn deposition and dissolution processes. An understanding of reversible Zn electrodeposition dynamics allowed us to construct dynamic windows with promising device metrics. In particular, a pH neutral electrolyte resulted in a device with excellent resting durability and high optical contrast. 100 cm² dynamic windows switch between clear (~80% transmission at 600 nm) and dark (<0.1% transmission at 600 nm) states within 30 s. Additionally, the dynamic windows show promising cycleability when a Cu additive is included in the electrolyte. Taken together, these results demonstrate that reversible Zn electrodeposition is a promising alternative to current RME windows based on more noble metals.

9.4. Experimental

9.4.1. General Procedure

ITO substrates were cleaned by sonicating with a 5% Extran solution for 5 minutes. After rinsing the substrates with water followed by isopropanol, the surfaces were sonicated in isopropanol for 5 minutes. The substrates were then rinsed with isopropanol and water and dried under a stream of air. The Zn acetate electrolyte was prepared using 0.5 M Zn(CH₃COO)₂ and 0.9 M KCl in aqueous medium, and the acidic Bi-Cu electrolyte consisted of 5 mM BiCl₃, 15 mM CuCl₂, 1 M LiCl, and 10 mM HCl. [36, 162] After dissolving the solute, 2% of hydroxyethylcellulose (HEC) was added to the electrolyte, and the resulting suspension was stirred overnight to form a gel.

9.4.2. Material Characterization

Electrochemical studies were conducted using a VSP-300 Biologic potentiostat. Optical measurements were carried out with an Ocean Optics FLAME-S_VIS-NIR spectrometer coupled to an Ocean Optics DH-mini UV-vis-NIR light source. A Sony Xperia X Series phone camera was used for photography of the dynamic windows. A JEOL JSM-6010LA microscope operating with an acceleration voltage of 10 kV was used to collect SEM-EDX images. XRD measurements were conducted using a Bruker D2 X-ray diffractometer. All samples for XRD spectra were fabricated using a 3 cm² ITO on glass working electrode. For XRD spectra, peak assignments were used following literature precedent.[180, 181] The integral of the peaks were measured for Zn, ZnO, and Zn(OH)₂ and used to calculate percent compositions as compared to the total peak area for all three compounds.

9.4.3. Dynamic Window Assembly

100 cm² or 25 cm² Zn dynamic windows were constructed using ITO on glass as the working electrode, a galvanized Zn grid or a Zn metal frame as the counter electrode, and the Zn acetate gel electrolyte. The diameter of the wire of the Zn grid was 3 mm with a spacing of ~1 cm. A non-conducting piece of glass was used on the opposite side of the working electrode to hold electrolyte inside the device. Cu tape with conductive adhesive was applied around the perimeter of the ITO working electrode to ensure uniform electrical connection. Butyl rubber was used to seal the device and separate the working and counter electrodes. To construct 25 cm² Bi-Cu dynamic windows, we followed previous literature procedures.[36]

Three-electrode systems consisted of an ITO on glass working electrode, a Zn wire counter electrode, and a Zn wire reference electrode. A glass cuvette (2 cm × 2 cm × 2 cm) was used to contain the gel electrolyte, and the immersed area of the ITO working electrode was 3 cm².

Chapter 10: Electrolytes for Reversible Zinc Electrodeposition for Dynamic Windows

10.1. Introduction

One important method of reducing energy consumption is to increase the energy efficiency of buildings, which are responsible for about half of the electricity consumed in the United States.[34] A promising way of increasing building energy efficiency is to decrease lighting, heating, and cooling consumption by implementing dynamic windows with electronically tunable transmission. The replacement of energy-efficient low-emissivity static windows with dynamic windows leads to an average of 10% energy savings in buildings. [32, 56]

Devices containing electrochromic materials are the most common form of dynamic windows and have existed for decades. [45, 121, 123, 125] Electrochromics refer to any material that change their optical properties upon application of a voltage and include transition metal oxides, polymers, small molecules, and nanoparticles.[47] Electrochromic windows can possess high optical contrasts, long cycle lives, and fast switching speeds. [43, 182] However, many electrochromic devices do not possess all of these attributes along with the low production costs needed for widespread adoption. In addition to electrochromic materials, polymer dispersed liquid crystals (PDLCs) are also commonly used to construct dynamic windows. [183] Although PDLC devices possess millisecond switching times, they transition between a clear state and a bright hazy state, which is undesirable for many applications in which maintaining image fidelity is important. [184] Thermochromic windows, which turn opaque upon solar heating, have

also been investigated for decades, but these windows switch passively, and thus do not provide users with control over their transparency. [185, 186] Thus, all of these approaches have drawbacks, and the ideal set of attributes for a dynamic window has not been achieved yet through a single technology.

Reversible metal electrodeposition for dynamic windows is a burgeoning technology that is a promising alternative to electrochromics, PDLCs, and thermochromics.[187] Metals are promising materials for light modulation in dynamic windows due to several intrinsic properties. Most metals are chemically inert, color neutral, photostable, and highly opaque in their elemental form. [39, 55] An additional benefit is that many dynamic windows based on reversible metal electrodeposition can be constructed through inexpensive solution processing. [48, 113]

Metal-based dynamic windows consist of a transparent conducting working electrode such as tin-doped indium oxide (ITO), a counter electrode, and a gel or liquid electrolyte containing salts of colorless metal ions. [106] Upon applying a reductive potential to the working electrode, the metal ions in the electrolyte are reduced to elemental metal on the transparent conductor to turn the device dark. At the same time, oxidation occurs at the counter electrode to charge balance this reaction. In some embodiments, oxidation of a metal counter electrode frame or a transparent metal mesh occurs. [37, 41, 104] In other devices, the counter electrode facilitates intercalation chemistry through the oxidation of a transparent thin film host material such as NiO or a hexacyanoferrate. [109, 137, 177]

Previous dynamic windows harnessing reversible metal electrodeposition have relied upon the electrodeposition of Ag, Pb, Cu, Bi, and Au. [40, 60, 188] Each of these

metals has its own advantages and disadvantages. Among the most successful dynamic windows have been those based on the coelectrodeposition of Bi and Cu. [36, 41] However, Bi-based electrolytes possess limited ion solubility due to the proclivity to form insoluble $\text{Bi}(\text{OH})_3$ under aqueous conditions. [55] However, all of the metals used in these windows are relatively noble. Indeed, the focus on utilizing noble metals has been a guiding principle in the development of these devices. [40, 187] This principle stems from the fact that in aqueous electrolytes, the evolution of hydrogen must be avoided. The more noble the metal electrodeposited, the less thermodynamically favorable it is to generate hydrogen during device operation. For this reason, non-noble metals are not commonly explored for metal-based dynamic windows.

In this manuscript, we broaden the paradigm for which metals can be used in reversible metal electrodeposition electrolytes for dynamic windows by demonstrating fully functional Zn electrolytes. Despite the fact that Zn is a non-noble metal with a standard reduction potential of -0.76 V vs. NHE, we demonstrate that the hydrogen evolution reaction and other deleterious side reactions can be kinetically passivated in properly designed reversible Zn electrodeposition electrolytes. These Zn electrolytes possess high Coulombic efficiency and support the formation of a highly opaque metal film. In addition to probing the fundamental electrochemical properties of these electrolytes, their successful design allows us to construct practical two-electrode dynamic windows that possess high optical contrast. Although a recent publication utilized reversible Zn electrodeposition on a metal grid as a counter electrode, to the best of our knowledge, this work is the first to use reversible Zn electrodeposition on a transparent conducting oxide working electrode. [161] By harnessing a non-noble metal,

this work diversifies the chemical space of reversible metal electrodeposition on transparent conductors.

10.2. Experimental

Chemicals were received from commercial sources and used without further purification. Half-cell experiments were performed using a Zn metal (99.9%) reference electrode, a separate Zn metal counter electrode, and a Pt-modified ITO on glass working electrode with a geometric surface area of 3 cm². Electrochemistry was conducted using a VSP-300 Biologic potentiostat. All CV data presented is the second cycle unless otherwise stated. Transmission data were recorded with an Ocean Optics FLAME-S-VIS-NIR spectrometer together with an Ocean Optics DH-mini UV-Vis-NIR light source.

Various electrolytes were studied with their compositions listed in the figure captions. Solutions were prepared by adding the appropriate solids to 20 mL of de-ionized water. The pH values of the solutions were then adjusted to 4.8 ± 0.3 with the conjugate acid of an electrolyte anion. The solutions were next converted to gels by the addition of 2% wt. hydroxyethylcellulose (Sigma Aldrich, average $M_v \sim 90,000$) and overnight stirring.

Pt-modified ITO on glass electrodes were prepared by spraying coating a 3:1 mixture of water:Pt nanoparticles (Sigma Aldrich, 3 nm in diameter) on ITO on glass substrates (Xinyan Technology, 15 Ω sq⁻¹). The Pt-modified ITO on glass substrates were then heated under air at 250°C for 20 minutes.

For two-electrode 25 cm² dynamic windows, Cu tape with conductive adhesive was first placed along the edges of the Pt-modified ITO on glass to make uniform

electrical connection to the working electrode. The counter electrode was comprised of Zn foil placed on top a nonconductive glass backing. Butyl rubber was placed around the edges of the device stack to seal the two electrodes together with an interelectrode spacing of ~5 mm. The gel electrolyte was then injected into the device stack through the butyl rubber sealant via a syringe. The outside surfaces of the completed dynamic window were cleaned with glass cleaner before performing the optical measurements.

Scanning electron microscope (SEM) images were obtained using a JOEL JSM-6010LA microscope with an operating voltage of 20 kV. X-ray diffraction (XRD) was conducted using a Bruker D2 X-ray Diffractometer. To estimate the relative percentages of Zn and ZnO, the integral of the XRD peaks for Zn located at $\sim 39^\circ$ and $\sim 43^\circ$ were compared to the integral of the peak for ZnO located at $\sim 36^\circ$. The Zn/ZnO electrodeposits for SEM and XRD analysis were formed by conducting linear sweep voltammograms at a scan rate of 5 mV s^{-1} from 0 V to -1 V.

10. 3. Results and Discussion

10.3.1. Zn Haloacetate Electrolytes

As a starting point for designing reversible Zn electrodeposition electrolytes, we used an electrolyte containing 0.5 M ZnCl_2 and 0.5 M NaCH_3COO . This composition using relatively simple salts is inspired in part by a previous electrolyte containing ZnSO_4 and KCl used in dynamic windows that facilitate reversible Zn electrodeposition on a stainless steel mesh. [161] The acetate-chloride electrolyte evaluated here supports electrochemically (Figure 10.1, black line) and optically reversible Zn electrodeposition. On a Pt-modified ITO working electrode, an electrode commonly used to enhance metal

nucleation in reversible metal electrodeposition devices,[36] cyclic voltammetry (CV) shows that Zn electrodeposition commences at about -30 mV vs. Zn/Zn^{2+} . This onset potential, which is close to 0 V, indicates that Zn electrodeposition has a low overpotential in this electrolyte. After electrodeposition occurs, the positive current at voltages greater than 0 V is due to the oxidization of Zn off of the electrode to form Zn^{2+} . The rapid decrease in the current after the anodic peak around 1.3 V is due to the complete depletion of Zn from the electrode. The Coulombic efficiency, as defined by the ratio of the integrated anodic charge to the integrated cathodic charge in the CV, for this electrolyte is 98%, indicating good electrochemical reversibility.

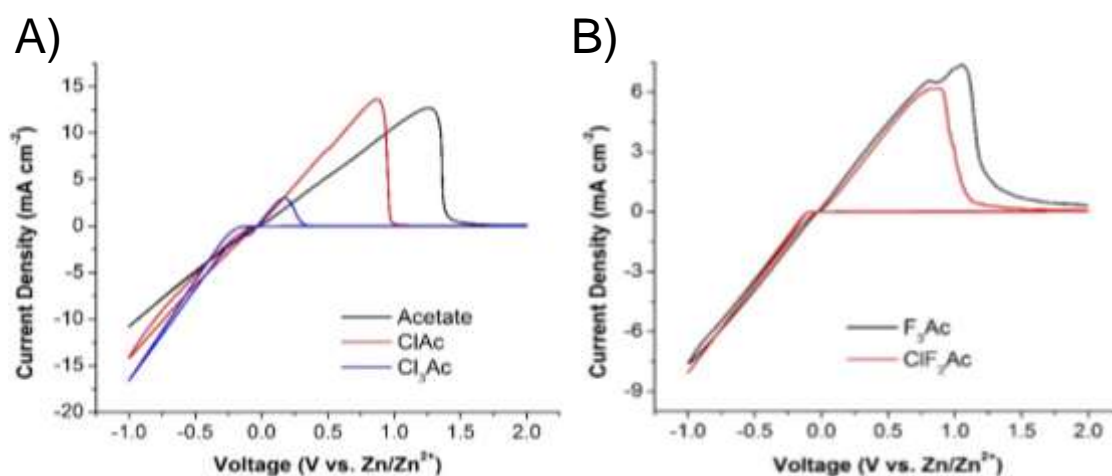


Figure 10.1: Cyclic voltammograms at a scan rate of 25 mV s^{-1} of Pt-modified ITO working electrodes in electrolytes containing 0.5 M ZnCl_2 and 0.5 M NaCH_3COO (sodium acetate, panel A, black line), $\text{NaCClH}_2\text{COO}$ (sodium chloroacetate, ClAc, panel A, red line), NaCCl_3COO (sodium trichloroacetate, Cl₃Ac, panel a, blue line), NaFCH_2COO (sodium fluoroacetate, panel B, black line), or NaClF_2COO (sodium chlorodifluoroacetate, panel B, red line).

In an effort to understand the electrochemical behavior of this electrolyte, we systematically altered the chemical identity of its acetate component. First, we evaluated

the electrochemistry of Zn electrolytes with halogen-substituted acetates. Substituting one of the hydrogen atoms of acetate with chlorine gives chloroacetate. Although the Zn electrolyte with chloroacetate possesses the same general Zn deposition and stripping features as the acetate electrolyte, there are important differences. First, the onset potential for Zn deposition is about -70 mV, a value that is 40 mV more negative than that of the acetate electrolyte. Second, the Coulombic efficiency obtained from the CV with the chloroacetate electrolyte is 60% as compared to the 98% value in the acetate electrolyte (Figure 10.2A). These findings indicate that both the Zn deposition and stripping processes are impeded with chloroacetate relative to acetate.

The complete chlorine substitution of acetate in a trichloroacetate electrolyte further inhibits the Zn deposition and stripping reactions. The onset potential for Zn deposition in the trichloroacetate electrolyte shifts further negative to -150 mV, indicating that there is a significant kinetic barrier for Zn deposition to occur using this electrolyte. Additionally, the Coulombic efficiency of the trichloroacetate CV further decreases to only 4% (Figure 10.2A), which signifies that the Zn stripping reaction is slow in the presence of trichloroacetate. Taken together, these results indicate that chlorine substitution on the acetate ligand decreases the kinetics of reversible Zn electrodeposition. Increasing the number of chlorine atoms on the conjugate acids of the acetates results in progressively stronger acids (acetic acid: $pK_a = 4.8$, chloroacetic acid: $pK_a = 2.9$, trichloroacetic acid: $pK_a = 0.7$). [189] As a result, the corresponding anions with chlorine substitutions used in the Zn electrolytes are weaker bases than acetate and thus will form weaker coordination complexes with Zn^{2+} , which is a Lewis acid.[190] Evidently, the basic nature of acetate facilitates the stripping of Zn through the formation

of soluble Zn acetate complexes at the electrode-electrolyte interface. The decreased stability of the analogous Zn chloroacetate and Zn trichloroacetate complexes likely explains the decreased Coulombic efficiencies in the chlorine-substituted electrolytes.

We next evaluated electrolytes with fluorine-substituted acetates. Figure 12.8.1B displays CVs of reversible Zn electrodeposition in electrolytes containing trifluoroacetate and chlorodifluoroacetate. Like the trichloroacetate electrolyte, these two electrolytes contain trihaloacetates. However, the Coulombic efficiencies of the two CVs are significantly higher than that of the trichloroacetate CV (Figure 10.2A). In particular, the trifluoroacetate CV possesses a higher Coulombic efficiency than the chlorodifluoroacetate CV, indicating that a greater number of fluorine substitutions enhances Zn stripping kinetics. These higher Coulombic efficiencies with fluoroacetates are observed despite the fact that trifluoroacetate and chlorodifluoroacetate are even weaker bases than trichloroacetate (trifluoroacetic acid: $pK_a = 0.2$, chlorodifluoroacetic acid: $pK_a = 0.3$).^[191] We hypothesize that noncovalent interactions between Zn and F, which are known to be particularly strong as compared to other Zn-halide interactions,^[192] enhance the stability of the Zn fluoroacetate coordination complexes, thus explaining the increased stripping kinetics of the fluoroacetate electrolytes relative to the chloroacetate electrolytes.

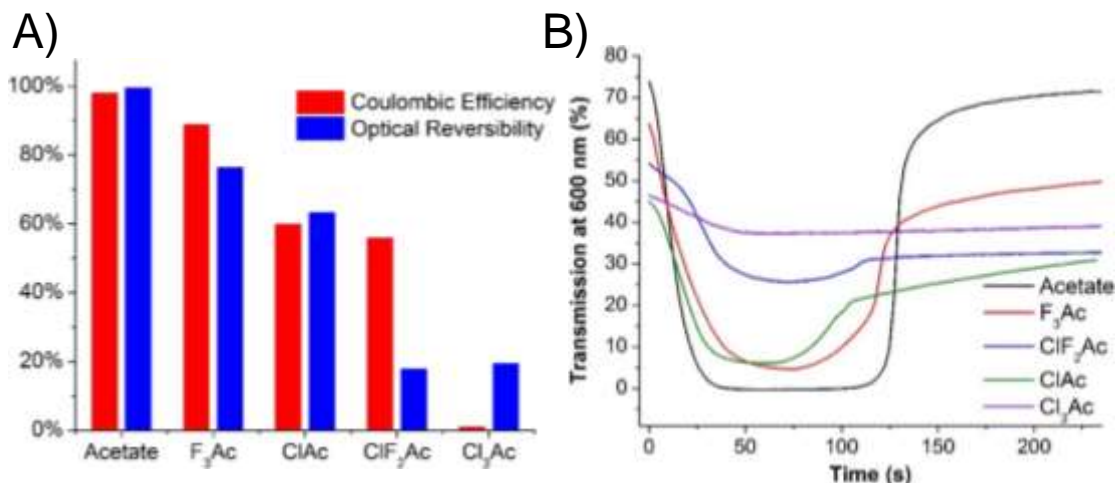


Figure 10.2: Coulombic efficiency and optical reversibility for Zn electrolytes containing different acetates (A) along with the transmission at 600 nm of the working electrode during the second cycle of CVs in these electrolytes (B). The corresponding CVs are displayed in Figure 1.

Figure 10.2B displays the transmission at 600 nm of the working electrodes during one CV cycle of reversible Zn electrodeposition in the various acetate electrolytes as measured in a spectroelectrochemical cell. For the electrolyte containing unsubstituted acetate, the transmission begins at about 74% and decreases to nearly 0% during metal electrodeposition (Figure 10.2B, black line). During the stripping portion of the CV, the transmission returns close to its original 74% value, indicating that reversible Zn electrodeposition from this acetate electrolyte is nearly completely optically reversible under these conditions. The optical reversibility of the electrode during the CV cycle is defined as the ratio of the transmission changes during the deposition and stripping processes, and is given by Equation 10.1, where $T_{initial}$ is the transmission at the beginning of the CV, T_{final} is the transmission at the end of the CV, and T_{min} is the minimum transmission recorded during the CV.

$$\frac{T_{final}-T_{min}}{T_{initial}-T_{min}} \quad (\text{Equation 10.1})$$

Electrodes using electrolytes with halide-substituted acetates do not get nearly as opaque as the electrode using the unsubstituted acetate electrolyte. Furthermore, the electrolytes with substituted acetates all possess optical reversibilities less than 100%. The lack of optical reversibility in these electrolytes correlates well with their decreased Coulombic efficiencies (Figure 10.2A), which is indicative of slower stripping kinetics. We note that in Figure 10.2B, the starting transmission values of all of the electrolytes differ substantially. These differences arise from the fact that the data analyzed were taken from the second CV cycles, and so optical irreversibility in the first CV cycle resulted in a decreased initial transmission value for the substituted acetate electrolytes. We chose to analyze the second cycle of the CVs because initial nucleation processes occur on the ITO working electrode during the first CV cycle that complicate analysis. [48]

10. 3. 2. Effects of Ligand Chain Length on Zn Electrolytes

In addition to studying the effect of haloacetates, we also investigated electrolytes containing ZnCl_2 and various chain lengths of carboxylates. Figure 10.3 displays CVs of the Zn electrolytes with formate, propionate, or butyrate in place of acetate. All three CVs exhibit the typical features associated with Zn electrodeposition and stripping. However, a clear trend emerges when analyzing the Coulombic efficiencies of the CVs, which increase using carboxylates with shorter chain lengths (Figure 10.4A, red bars). In

particular, the CV for the formate electrolyte possesses a Coulombic efficiency of 99% as compared to 98% for the acetate electrolyte, indicating that Zn stripping kinetics are accelerated with the formate anion.

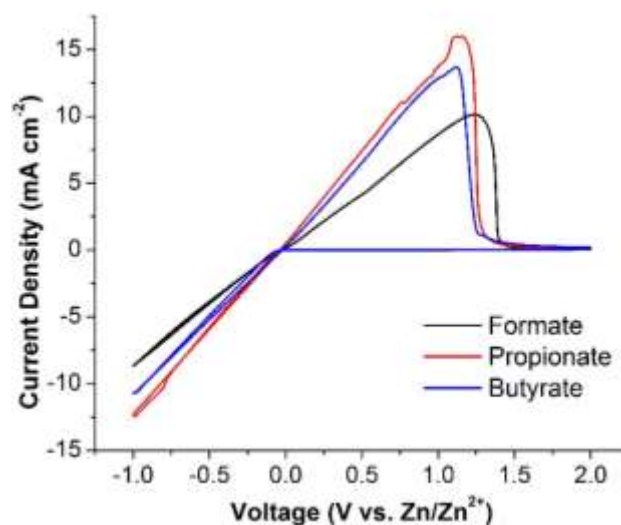


Figure 10.3: Cyclic voltammograms at a scan rate of 25 mV s^{-1} of Pt-modified ITO working electrodes in electrolytes containing 0.5 M ZnCl_2 and 0.5 M sodium formate (black line), sodium propionate (red line), or sodium butyrate (blue line).

As for the haloacetate electrolytes, the trend in the optical reversibilities of the electrolytes with different carboxylates also follows the Coulombic efficiency trend (Figures 10.2A and Figure 10.4A). In particular, the transmission of the working electrode when using the formate electrolyte returns back to its original $\sim 77\%$ value after the stripping portion of the CV is completed, indicating that this electrolyte exhibits complete optical reversibility (Figure 10.4B, black line). The good electrochemical and optical reversibility observed in the formate electrolyte is likely due to the sterically unencumbered nature of the small formate anion, which enhances Zn stripping kinetics. Formate is less basic than acetate [191] (formic acid: $\text{pK}_a = 3.7$, acetic acid: $\text{pK}_a = 4.8$)

and from the haloacetate results described in the previous section, the lower basicity of formate is expected to impede stripping kinetics. Evidently though, the smaller amount of steric hindrance with formate is a more impactful effect in dictating stripping kinetics. Furthermore, the importance of the steric effect is confirmed with experiments using the long-chained propionate and butyrate. These electrolytes possess slower stripping kinetics than acetate even though all three carboxylates have similar basicities (propionic acid: $pK_a = 4.9$, butyric acid: $pK_a = 4.8$).

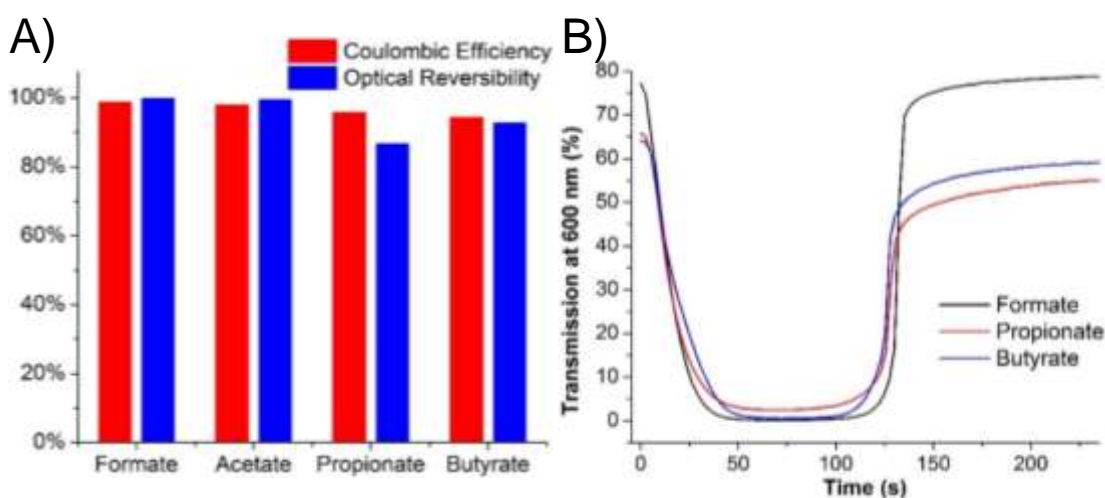


Figure 10.4: Coulombic efficiency and optical reversibility for Zn electrolytes containing different chain lengths of carboxylates (A) along with the transmission at 600 nm of the working electrode during the second cycle of CVs in these electrolytes (B). The corresponding CVs are displayed in Figure 3.

10.3.3. Effect of Halides on Zn Electrolytes

We next studied the effect of halide compositions on the Zn electrolytes. Because in the section above, we found that both the acetate and formate electrolytes possess good Coulombic efficiency and optical reversibility, we investigated the influence of halide

composition on both of these systems with a particular focus on the formate electrolytes due to their enhanced stripping kinetics.

Figure 10.5A displays CVs of Zn electrodeposition and stripping in formate electrolytes with ZnCl_2 , ZnBr_2 , and a 1:1 mixture of ZnCl_2 and ZnBr_2 . The CV of the electrolyte containing ZnBr_2 (red line) possesses approximately twice the deposition current as the CV of the ZnCl_2 electrolyte (black line), and as a result, the ZnBr_2 CV also exhibits about twice as much stripping current. In Cu electrodeposition baths, the bromide anion is known to be an accelerant for electrodeposition that operates via the formation of bridges halide complexes, [127, 129] and a similar phenomenon may explain the enhanced deposition current observed with the ZnBr_2 electrolyte. However, because bromide induces morphological differences in Zn electrodeposits, the ZnBr_2 electrolyte results in films that switch to their opaque states as quickly as those formed using ZnCl_2 (*vide infra*). For this reason, we also studied a 1:1 mixture of ZnCl_2 and ZnBr_2 with the intention of accelerating deposition kinetics while maintaining an optically favorable electrodeposit morphology. Interestingly, the CV of the ZnCl_2 - ZnBr_2 electrolyte (blue line) possesses similar currents as the CV of the ZnCl_2 electrolyte (black line). This result suggests that the ZnCl_2 - ZnBr_2 electrolyte is dominated by chlorine species from which electrodeposition occurs. Indeed, Zn-Cl bonds are significantly stronger than Zn-Br bonds, which explains the greater stability of Zn-Cl electrodeposition precursors.[192]

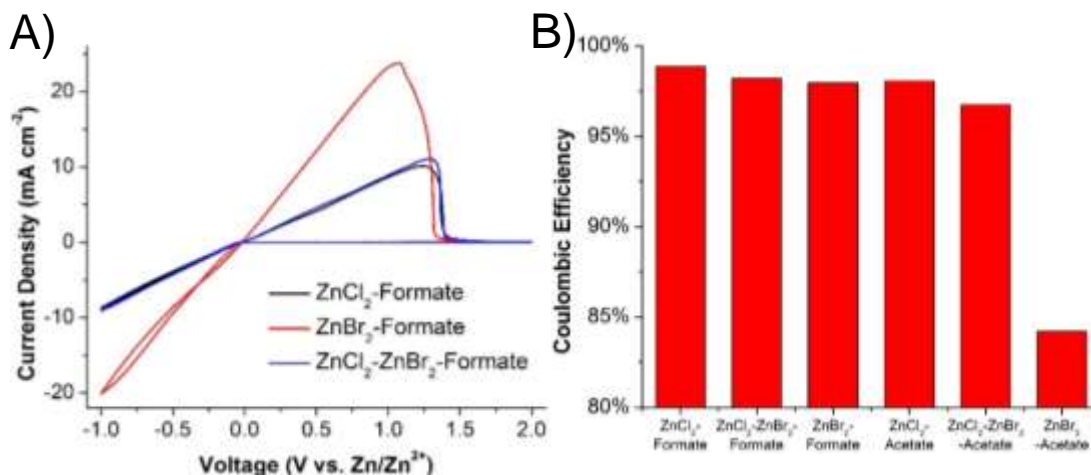


Figure 10.5: Cyclic voltammograms (A) at a scan rate of 25 mV s^{-1} of Pt-modified ITO working electrodes in electrolytes containing 0.5 M sodium formate and 0.5 M ZnCl_2 (black line), 0.5 M ZnBr_2 (red line), or 0.25 M ZnCl_2 and 0.25 M ZnBr_2 (blue line). Coulombic efficiencies (B) of the CVs of formate and acetate electrolytes with various halide compositions.

The Coulombic efficiencies of the CVs increase in the order of $\text{ZnCl}_2 > \text{ZnCl}_2\text{-ZnBr}_2 > \text{ZnBr}_2$ for both the formate and acetate electrolytes (Figures 10.5B and Supporting Figure 12.8.1). Furthermore, for a given halide composition, each formate electrolyte exhibits a higher Coulombic efficiency than the corresponding acetate electrolyte due to the enhanced stripping kinetics of formate as discussed previously. We hypothesize that the greater Coulombic efficiencies in the electrolytes containing ZnCl_2 is due to enhanced stripping kinetics of chloride that result from the greater stability of Zn-Cl coordination complexes.

We also tested an electrolyte containing ZnI_2 . The iodide-containing electrolyte produced a yellow-colored solution as a result of the oxidation of iodide to iodine during the anodic portion of the CV (Supporting Figure 12.8.2). This iodine formation interfered with measurements of the transmission of the working electrode (Supporting Figure

12.8.3), and thus ZnI_2 electrolytes were not studied further. ZnF_2 electrolytes could not be examined due to the insolubility of ZnF_2 in water.

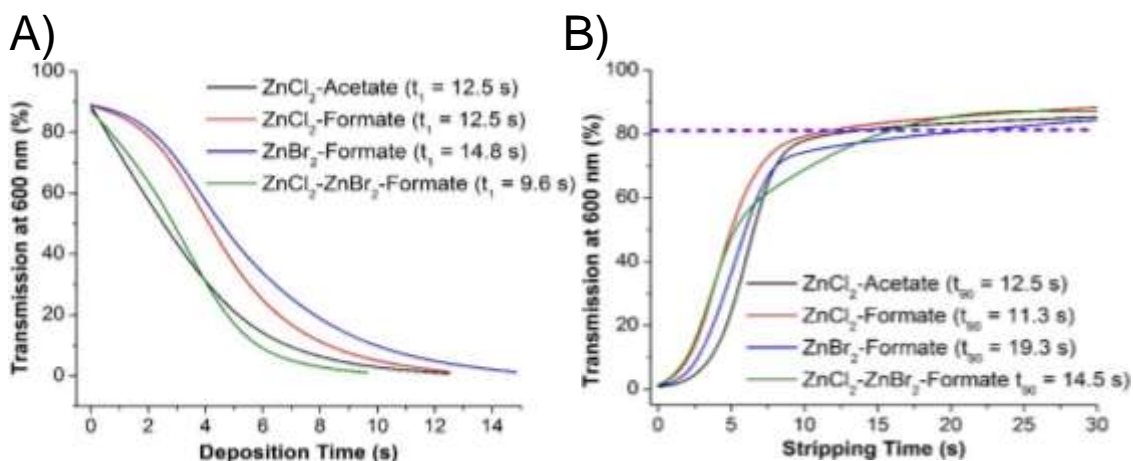


Figure 10.6: Transmission at 600 nm of the working electrode during Zn electrodeposition (A) and stripping (B) in electrolytes containing 0.5 M sodium acetate and 0.5 M ZnCl_2 (black line), or 0.5 M sodium formate and 0.5 M ZnCl_2 (red line), 0.5 M ZnBr_2 (blue line), or 0.25 M ZnCl_2 and 0.25 M ZnBr_2 (green line). To elicit Zn electrodeposition, chronoamperometry was conducted at -1.0 V until the transmission at 600 nm reached 1%. Next, Zn stripping was conducted at $+2.5$ V for 30 s.

Given the high Coulombic efficiencies ($\geq 98\%$) of the ZnCl_2 -acetate, ZnCl_2 -formate, ZnBr_2 -formate, and ZnCl_2 - ZnBr_2 -formate systems, we studied these four electrolytes using chronoamperometry to better assess their deposition and stripping speeds (Supporting Figure 12.8.4). Figure 6 displays the transmission of the working electrode at 600 nm during Zn electrodeposition and stripping. Electrodeposition was elicited by applying a potential of -1.0 V until the transmission reached 1% (Figure 6A). Upon reaching 1% transmission, the potential was switched to $+2.5$ V to induce metal stripping (Figure 10.6B). This procedure allows for the comparison of electrode

darkening and lightening speeds at a fixed contrast ratio (i.e. switching between a 88% clear state to a 1% dark state) among the four electrolytes.

For both the ZnCl_2 -acetate and ZnCl_2 -formate electrolytes, the time it takes to reach 1% transmission is 12.5 s (Figure 10.6A, black and red lines). However, the darkening speed decreases to 14.8 s with the ZnBr_2 -formate electrolyte (Figure 10.6A, blue line) despite the additional deposition current observed with ZnBr_2 (Figure 10.5A). This finding implies that the morphology of the Zn electrodeposits with the ZnBr_2 electrolyte are less effective at blocking light than the ZnCl_2 electrolyte. This supposition is confirmed by SEM analysis (*vide infra*). Strikingly, the fastest darkening speed of 9.6 s is obtained with the ZnCl_2 - ZnBr_2 -formate electrolyte. The interpretation of this result is discussed later in the manuscript.

Electrode lightening speeds were assessed by calculating the time it takes the electrode to complete 90% of its transmission change during metal stripping (t_{90} values, dashed purple line, Figure 10.6B). The t_{90} value for the ZnCl_2 -formate electrolyte (11.3 s) is less than for the ZnCl_2 -acetate electrolyte (12.5 s) due to the enhanced stripping kinetics by the less sterically bulky formate anion as discussed previously. The lightening speeds for the three formate electrolytes increase in the order of $\text{ZnCl}_2 > \text{ZnCl}_2\text{-ZnBr}_2 > \text{ZnBr}_2$. This trend directly correlates with the same order of increasing Coulombic efficiency (Figure 10.5B), which demonstrates the enhanced stripping kinetics imparted by chloride.

10. 3. 4. Surface Characterization of Zn Electrodeposits

To investigate the morphology of the Zn electrodeposits as a function of halide composition in the electrolyte, we use SEM to image the electrodeposits. The Zn electrodeposits obtained from the ZnCl_2 (Figures 10.7A and 10.7B) and $\text{ZnCl}_2\text{-ZnBr}_2$ (Figure 10.7E and 10.7F) electrolytes are relatively similar and consist of a uniform film of material decorated with protrusions approximately 1 μm in length. In contrast, the morphology of the electrodeposits obtained from the ZnBr_2 electrolyte is markedly different and consists of a lower density of larger particles (>10 μm in length) with visible gaps in between them. These images suggest that in the ZnBr_2 electrolyte, the metal nucleation density is lower than in the chloride-containing electrolytes, which gives rise to more nonuniform growth. Larger particles, however, grow in the ZnBr_2 electrolyte because of the enhanced deposition kinetics observed with bromide as discussed previously. These larger and less uniform particles that contain gaps are less effective at blocking light compared to the more uniformly distributed electrodeposits obtained from the chloride-containing electrolytes. These results explain why the ZnBr_2 -formate electrolyte exhibits a slower darkening time as compared to the ZnCl_2 -formate and $\text{ZnCl}_2\text{-ZnBr}_2$ -formate electrolytes (Figure 10.6A) despite the greater magnitude of current measured during the CVs (Figure 10.5A).

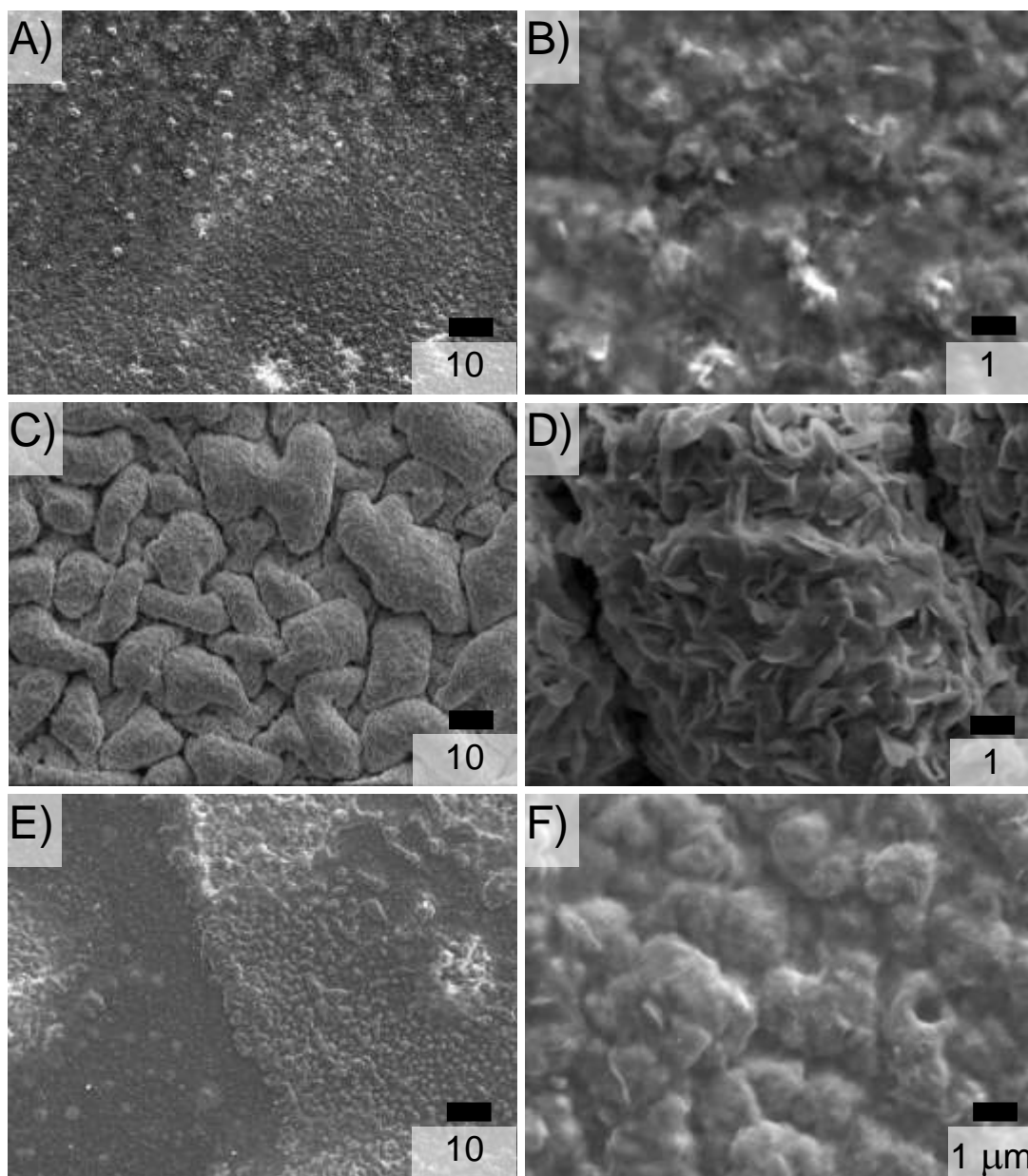


Figure 10.7: Scanning electron microscopy images of Zn electrodeposits obtained after a linear sweep voltammogram from 0 V to -1 V at 5 mV s^{-1} in an electrolyte containing 0.5 M sodium formate and 0.5 M ZnCl_2 (A, B), 0.5 M ZnBr_2 (C, D), or 0.25 M ZnCl_2 and 0.25 M ZnBr_2 (E, F).

However, given the fairly similar morphologies of the electrodeposits obtained from the ZnCl_2 and $\text{ZnCl}_2\text{-ZnBr}_2$ electrolytes, it is unclear at this stage of our analysis

why the $\text{ZnCl}_2\text{-ZnBr}_2$ electrolyte possesses a faster darkening speed (Figure 10.6A). To complement the SEM morphological data, we used XRD to probe the chemical composition of the electrodeposits. XRD analysis shows that the electrodeposits consist predominantly of Zn and ZnO (Supporting Figure 12.8.5). By comparing the ratios of the integrated peaks in the XRD spectra for Zn and ZnO, we were able to gauge the oxide content in the various electrodeposits (Figure 10.8).

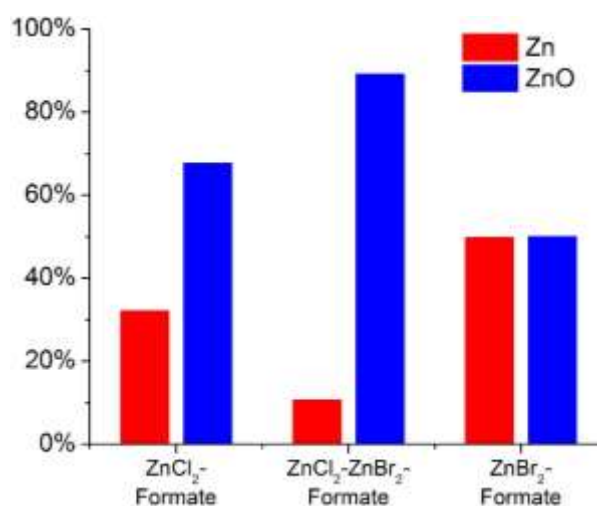


Figure 10.8: Relative compositions of Zn and ZnO as determined by X-ray diffraction of Zn electrodeposits obtained using the conditions described in Figure 7.

Interestingly, electrodeposits obtained from the $\text{ZnCl}_2\text{-ZnBr}_2$ electrolyte have a significantly higher percentage of ZnO than electrodeposits created from the ZnCl_2 or ZnBr_2 systems. Perhaps the greater quantity of ZnO causes the electrodeposits formed from the $\text{ZnCl}_2\text{-ZnBr}_2$ electrolytes to block light more effectively than the morphologically-similar electrodeposits obtained from ZnCl_2 . However, because the extinction coefficient of ZnO is substantially less than Zn, [193, 194] uniform thin films

of pure ZnO block less light than a uniform Zn film of the same thickness. This inconsistency means that a completely uniform thin film of Zn or ZnO is an inadequate way of modeling the optics of these electrodeposits. It is likely that more complex optical phenomena occur within the electrodeposits, which are highly heterogeneous both in terms of their physical and chemical structures.

10. 3. 5. The Electrochemical Window of ITO in Zn Electrodeposition Electrolytes

As mentioned in the introduction, dynamic windows based on reversible metal electrodeposition typically harness relatively noble metals such as Cu, Bi, and Ag. [187] These metals have standard reduction potentials more positive than H₂, and therefore, it is thermodynamically more favorable in aqueous electrolytes to electrodeposit these metals as opposed to generating H₂, which is not tolerable for window applications. Not only is there the potential issue of H₂ generation with less noble metals, electrodepositing metals with more negative reduction potentials can also lead to the application of voltages outside of the electrochemical window of transparent conductors like ITO. For instance, ITO is known to degrade at voltages more negative than about -0.3 V vs. Zn²⁺/Zn at neutral pH.[195]

Despite the instability of ITO and the thermodynamic possibility of H₂ generation at negative potentials, we do not observe ITO degradation or H₂ generation in any of the studied Zn electrolytes when cycling between +2.0 V and -1.0 V vs. Zn²⁺/Zn. These findings suggest that some property of the Zn electrolytes impedes H₂ evolution and ITO degradation, thus protecting the electrode from undergoing these unwanted side reactions.

We performed a series of CV experiments to interrogate how the Zn electrolytes protect the ITO electrode and prevent H₂ formation. These experiments have three distinct stages. In the first stage, we conducted a CV in the previously described electrolyte containing sodium formate, ZnCl₂, and ZnBr₂ (Figure 10.9A, black line). During the second cycle of this CV, the experiment was stopped at -0.1 V during the negative going sweep ($E_{\text{final}} = -0.1$ V). As a result, the working electrode at this stage contained a small amount of electrodeposited Zn on its surface.

In the second stage of the experiment, the electrode was removed from the first electrolyte and placed in a second electrolyte containing sodium formate without any Zn salts. The CV in this blank formate electrolyte still contains the characteristic reversible Zn deposition and stripping peaks (Figure 10.9A, red line). These peaks are due to the stripping and redepositing of Zn that was originally electrodeposited during the first stage. (In part, the peaks are also due to Zn²⁺ impurities in the blank electrolyte, which come from residual Zn electrolyte on the original wet electrode. We do not rinse the electrode before moving it to the blank formate electrolyte so as to not destroy the integrity of the electrodeposited Zn film.)

Finally, in the third stage of the experiment, the electrode is removed from the second electrolyte and placed in a third electrolyte, which is a freshly prepared solution containing sodium formate, ZnCl₂, and ZnBr₂. The CV of the electrode in this new ZnCl₂-ZnBr₂-formate electrolyte (Figure 10.9A, blue line) is similar the CV of the electrode in the first electrolyte (Figure 10.9A, black line). The similarity of the CVs before and after cycling in the blank formate electrolyte indicates that cycling in the blank formate electrolyte does not degrade the ITO electrode when $E_{\text{final}} = -0.1$ V.

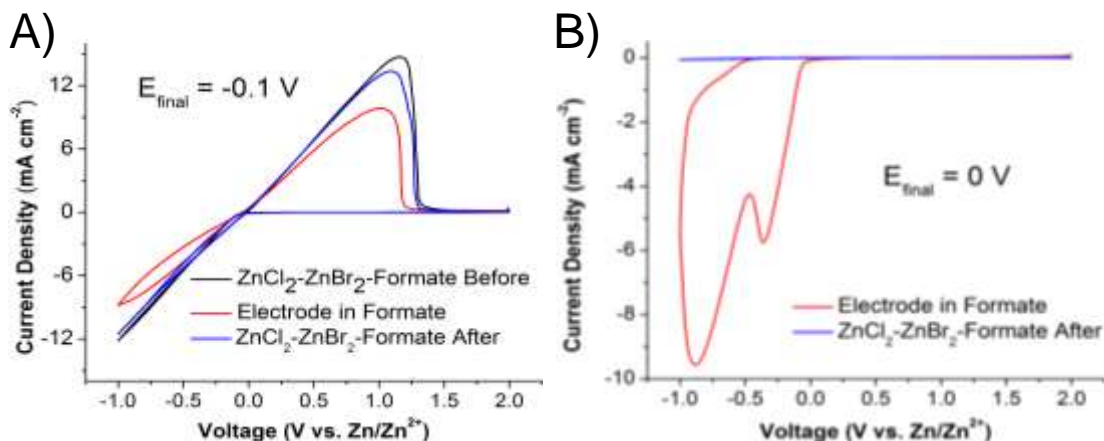


Figure 10.9: Cyclic voltammogram obtained using the ZnCl₂-ZnBr₂-formate electrolyte containing 0.5 M sodium formate, 0.25 M ZnCl₂, and 0.25 M ZnBr₂ (A, black line). The experiment was halted at -0.1 V (E_{final}) during the negative sweep of the second cycle.

After obtaining this voltammogram, the same working electrode was used in an electrolyte containing only 0.5 M sodium formate (A, red line). Lastly, the same working electrode was used a second time in the ZnCl₂-ZnBr₂-formate electrolyte (A, blue line). For panel B, a fresh working electrode was also first cycled in the ZnCl₂-ZnBr₂-formate electrolyte. The experiment was halted at an $E_{\text{final}} = 0$ V during the negative sweep of the second cycle. After obtaining this voltammogram, the same working electrode was used in an electrolyte containing only 0.5 M sodium formate (B, red line). Lastly, the same working electrode was used a second time in the ZnCl₂-ZnBr₂-formate electrolyte (B, blue line).

With a new working electrode, we next performed the same three-part experiment, but during the first CV in the ZnCl₂-ZnBr₂-formate electrolyte, the negative going sweep was halted at 0 V during the second cycle ($E_{\text{final}} = 0$ V). Because the experiment was halted before Zn electrodeposition occurred during the second cycle, the electrode did not contain a significant amount of Zn at this stage. Next, the electrode was placed in the blank formate electrolyte. The CV in the blank formate electrolyte does not contain the typical Zn electrodeposition and stripping peaks (Figure 10.9B, red line). Instead, the cathodic peaks observed are a combination of H₂ evolution and ITO degradation to metallic In and Sn. In the third stage of the experiment, the electrode was

placed back in the ZnCl_2 - ZnBr_2 -formate electrolyte. Notably, the CV in this case shows little current density throughout the scan (Figure 10.9B, blue line). This result indicates that the ITO electrode degraded and as such no longer supports reversible Zn electrodeposition.

In summary, H_2 evolution and ITO degradation occur when $E_{\text{final}} = 0$ V, but not when $E_{\text{final}} = -0.1$ V. These results demonstrate that Zn electrodeposits protect the ITO electrode from degradation and from evolving H_2 . During the second stage of the experiments in the blank formate electrolyte, the Zn electrodeposits are only present on the electrode when $E_{\text{final}} = -0.1$ V. It is known that Zn is a poor catalyst for the H_2 evolution reaction, and in this way the electrodeposited Zn prevents the system from generating H_2 even at relatively high magnitude cathodic potentials. Furthermore, the Zn electrodeposits protect the ITO from degrading into metallic In and Sn likely by physically blocking access of the electrolyte to the ITO surface. In this manner, the electrochemical window of ITO is expanded in the presence of reversible Zn electrodeposition electrolytes.

10. 3. 6. Practical Two-Electrode Devices using Reversible Zn Electrodeposition

Having designed and investigated reversible Zn electrodeposition electrolytes, we next constructed practical two-electrode 25 cm^2 dynamic windows using these electrolytes. We built these windows with the electrolyte containing ZnCl_2 , ZnBr_2 , and sodium formate because our studies described above determined that this electrolyte has a high Coulombic efficiency and fast switching times.

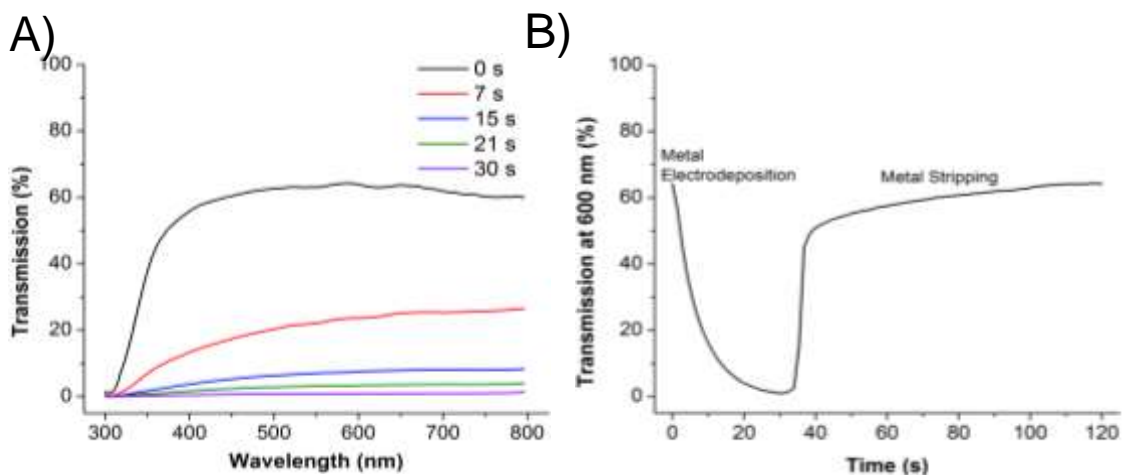


Figure 10.10: Transmission as a function of wavelength of a 25 cm^2 dynamic window based on reversible Zn electrodeposition after 0 s (black line), 7 s (red line), 15 s (blue line), 21 s (green line), and 30 s (purple line) of device darkening (A). Metal electrodeposition on the working electrode was elicited by applying -0.8 V for 30 s before $+2.3 \text{ V}$ was applied to induce metal stripping. The transmission at 600 nm during one cycle of switching is shown in panel B. The aqueous-based gel electrolyte used contained 0.5 M sodium formate, 0.25 M ZnCl_2 , and 0.25 M ZnBr_2 .

The application of -0.8 V for 30 s to the 25 cm^2 device causes the initial visible light transmission of the window to decrease from $\sim 60\%$ to $<0.1\%$ (Figure 10.10A). The high opacity of the window in its dark state is enabled by the dense morphology of the Zn electrodeposits on the ITO surface, which block light effectively. In its opaque state, the window appears black due to its flat transmission profile across the visible spectrum. Additionally, the window in its opaque state effectively blocks near-infrared light, which is desirable for building applications in which heat management is important. After 30 s of metal electrodeposition on the working electrode, switching the voltage of the device to $+2.3 \text{ V}$ elicits rapid metal stripping, which causes the device to return to its original clear state within 90 s (Figure 10.10B).

An important attribute of any dynamic window technology is device cycle life. Thus far, several different variants of dynamic windows based on reversible metal electrodeposition have been developed that cycle thousands of times without significant degradation. [40, 41, 137] Figure 10.11 displays the minimum and maximum transmission values of a dynamic window based on reversible Zn electrodeposition during consecutive switching cycles. From the data, it is clear that the maximum transmission value of the device steadily decreases over the course of 250 cycles. This less-than-optimal cycleability is in contrast to our previous work showing excellent cycle lives in windows using reversible Bi and Cu electrodeposition.

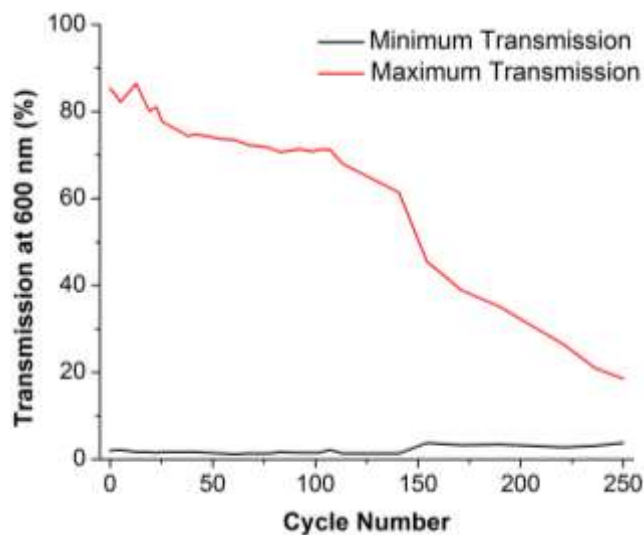


Figure 10.11: Minimum and maximum transmission values at 600 nm during cycling of a 3 cm² dynamic window based on Zn electrodeposition. The device was switched at -1 V for 5 s to induce metal electrodeposition and 1.5 V for 30 s to elicit metal stripping.

To understand the origin of the decrease in the maximum transmission value during cycling of the Zn windows, we conducted XRD on the working electrode after the

250 switching cycles. The XRD spectrum shows a prominent peak that is due to the presence of Zn(OH)_2 . Because the intensity of this peak is much larger than any Zn(OH)_2 peak observed after one cycle of Zn electrodeposition, this finding suggests that Zn(OH)_2 progressively accumulates on the working electrode and is responsible for the steady decrease in the transparency of the window in its clear state during cycling.

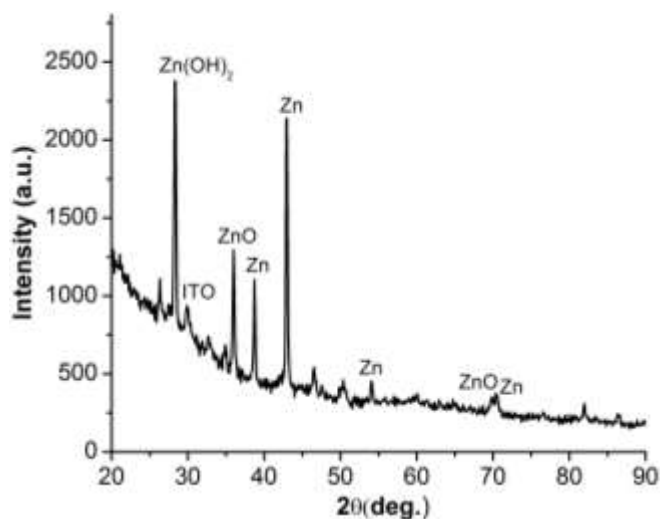


Figure 10.12: X-ray diffraction spectrum of ITO working electrode obtained after 250 switching cycles in a dynamic window.

In future work, we will carefully interrogate the origin of this accumulation of Zn(OH)_2 during cycling, and we will pursue several strategies to mitigate this problem including utilizing different voltage switching profiles and chemical additives such as chelating ligands that may facilitate Zn(OH)_2 dissolution. However, the focus on this manuscript is to interrogate the physicochemical parameters that allow for reversible Zn electrodeposition electrolytes, not to develop practical windows or optimal cycling parameters. Nonetheless, because the design of such electrolytes is still in its infancy, we

are hopeful that future versions of these electrolytes will enable the construction of robust and practical dynamic windows.

10. 4. Conclusion

In this manuscript, we investigated a variety of chemical and physical properties of reversible Zn electrodeposition on transparent conducting electrodes. In particular, we systematically studied the effect of the chain length of carboxylates, the halogen in haloacetate, and the identity of supporting halides on the electrochemical reversibility of Zn electrolytes. These studies enabled us to develop electrolytes that are both optically and electrochemical reversibility (Coulombic efficiency up to 99%). Using SEM and XRD analysis, we correlated electrolyte composition with electrodeposit morphology and composition, both of which effect the reversibility of the system. We also discovered how reversible Zn electrodeposition occurs in these electrolytes despite the fact that electrode degradation and H₂ production are thermodynamically favorable within the voltage regimes need to elicit Zn electrodeposition. Lastly, we applied these findings to the construction of practical 25 cm² dynamic windows based on reversible Zn electrodeposition.

Chapter 11: Nanographene Cathode Materials for Nonaqueous Zn-ion Batteries

11.1. Introduction

The advent of rechargeable Li-ion batteries in the twentieth century was a key technological breakthrough that powered the personal electronics revolution. [196] In this century, as the scope of the battery market expands to encompass the transportation and grid storage sectors, there is an increasing need to develop new battery chemistries beyond Li-ion, with superior performance. [18, 23, 131, 197-199] Batteries that utilize multivalent ions such as Mg^{2+} , Zn^{2+} , and Al^{3+} are promising, due to their high theoretical volumetric capacities. Compared to the practical volumetric capacities of commercial Li-ion batteries (500-700 mAh cm^{-3}), multivalent metal anodes have much higher theoretical volumetric capacities (3833 mAh cm^{-3} , 5851 mAh cm^{-3} , and 8046 mAh cm^{-3} for Mg^{2+} , Zn^{2+} , and Al^{3+} , respectively) due to their ability to transfer more than one electron per ion. [19, 20]

Over the last decade, much research progress has been made in designing electrolytes that facilitate reversible metal electrodeposition at multivalent metal anodes. Although some problems such as the formation of dendrites at high current densities—remain, significant progress in the field of multivalent metal anodes has been made. [200-203] Despite considerable effort, it has proved much more challenging to facilitate multivalent ion intercalation at the cathode with high capacity, high voltage, fast discharge rates, and with good reversibility. [25, 204, 205] Successful multivalent ion intercalation at the anode, which is much less studied, would also be useful in obviating the lingering problems of multivalent metal anode chemistry.

In Li-ion batteries, a wide variety of materials support reversible Li^+ intercalation with excellent electrochemical performance. Of all the systems discovered, Li^+ intercalation in graphite anodes is probably the most studied, as the process has been known since the 1990s.[206] On the other hand, reversible multivalent ion intercalation in graphite was, until a few years ago, thought to be impossible due to strong cation- π interactions between the highly charged cations and graphite aromatic rings. [207] Recently, a few publications have reported batteries with anodes that facilitate reversible Mg^{2+} or Ca^{2+} intercalation in graphite. However, the ions that intercalate are highly solvated, which decreases the electrode's energy density. Furthermore, the interpretations of some of these results have been called into question. [208-210] Nam et al. used triangular phenanthrenequinone as cathode materials for aqueous rechargeable Zn-ion batteries with high capacity. The resulting material has pores that allow for reversible Zn-ion intercalation. [211]

To overcome the obstacles associated with multivalent intercalation into graphite, we were inspired to design multivalent battery electrodes with molecularly-precise nanographene compounds. We hypothesize that these molecules, the bottom-up synthesis of which was recently pioneered by the Chalifoux group, [212-214] can be engineered to facilitate reversible multivalent ion intercalation due to their tailorable interlayer spacing and pore sizes. The nanographenes can also be modified with chemical diversity beyond the carbon of graphite. In principle, such chemical functionality allows for enhanced intercalation properties via the tuning of electronic and steric properties.

In this manuscript, we demonstrate the first example of a battery that operates via multivalent ion intercalation into a nanographene. In particular, we construct nonaqueous

Zn-ion batteries that contain a peropyrene cathode and a Zn metal anode. The high redox potential of the peropyrene (~ 1.5 V vs. Zn/Zn²⁺) enables it to operate as a cathode—in contrast to graphite, which traditionally functions as an anode. [215, 216] This proof-of-concept research using nanographenes opens up a new strategy for designing multivalent ion intercalation electrodes that will aid in the development of multivalent battery technologies.

11.2. Experimental

Peropyrene **1** was synthesized following a literature procedure, [214] and the characterization data are consistent with reported data. [213] Anhydrous acetonitrile was purchased from Sigma Aldrich. Anhydrous Zn(ClO₄)₂ was prepared following a literature procedure in which Zn(ClO₄)₂·6 H₂O is dried in a vacuum oven for four days at 100°C.[26] All electrochemical experiments were performed in an Ar-filled glove box with <1 ppm O₂ and <0.1 ppm H₂O. To prepare the cathode electrodes, stainless steel (alloy 316) substrates were first coated with a 15 μm thick layer of graphite using a doctor blade and a colloidal graphite dispersion (DAG EB-012, Ladd Research). The graphite was dried in a vacuum oven overnight at 80°C. The graphite serves as a conductive scaffold for the cathode material and itself does not participate in Zn ion intercalation as shown previously. [26] Alternatively, Cu foil without graphite was used as a substrate. Next, 15 mg polyvinylidene fluoride (PVDF, Kynarfex 2801), 7.5 mg of Vulcan XC-72 carbon, and 7.5 mg perylene, coronene, or the peropyrene were added into a vial. Acetone (0.36 mL for voltammetry experiments or 2.5 mL for two-electrode batteries) was then added, and the resulting slurry was mixed for at least 3 hours at room

temperature. The slurry was then deposited at a thickness of 15 μm using a doctor blade before it was punched into circular electrodes (4 mm in diameter).

To assemble two-electrode batteries, battery components were assembled in a polypropylene body with two stainless steel screws serving as terminals. A Zn metal (99.99%) anode followed by a glass separator (Whatman) soaked in 10 μL of electrolyte were placed on top of the bottom terminal. Then, the cathode electrode was added to the device stack followed by a stainless steel spring. The spring provides electrical connection from the top terminal to the back of the cathode.

Two pieces of Zn metal served as the reference and counter electrodes for voltammetry experiments. Scanning electron microscope (SEM) images were obtained using a Hitachi S-4700 II field emission SEM with an energy-dispersive spectrometer (EDX) at an acceleration voltage of 15kV.

11.3. Results and discussion

Chalifoux and coworkers have demonstrated the versatility of alkyne benzannulation for the synthesis of a broad scope of contorted nanographenes through the use of Brønsted and Lewis acid catalysts. [212-214, 217-219] Notable among their early work was the novel synthesis of contorted, functionalized, and processable peropyrenes. Nonaqueous solutions of these peropyrenes exhibit two reversible redox waves associated with the oxidation and reduction of the aromatic system to the corresponding radical cation and anion, respectively. [213] To construct a reversible Zn^{2+} battery, a cathode containing peropyrene **1** and a Zn metal anode, sandwich an electrolyte containing Zn^{2+} (Figure 11.1). To evaluate this battery architecture, we chose to study electrolytes

consisting of either $\text{Zn}(\text{CF}_3\text{SO}_3)_2$ or $\text{Zn}(\text{ClO}_4)_2$ in acetonitrile. Both of these electrolytes are known to facilitate reversible Zn electrodeposition with $\geq 99.9\%$ Coulombic efficiency.[26, 220] There are also examples of reversible Zn^{2+} intercalation into V_3O_7 and other cathode materials using these electrolytes. [26] [27] Lastly, acetonitrile is a desirable solvent because the peropyrene is insoluble, which allows stable electrode films to be cast. In the case of the $\text{Zn}(\text{CF}_3\text{SO}_3)_2$ electrolyte, acetonitrile also enables the electrolyte to have a much higher anodic stability (3.5 V vs. Zn/Zn^{2+}) as compared to aqueous electrolytes. [27]

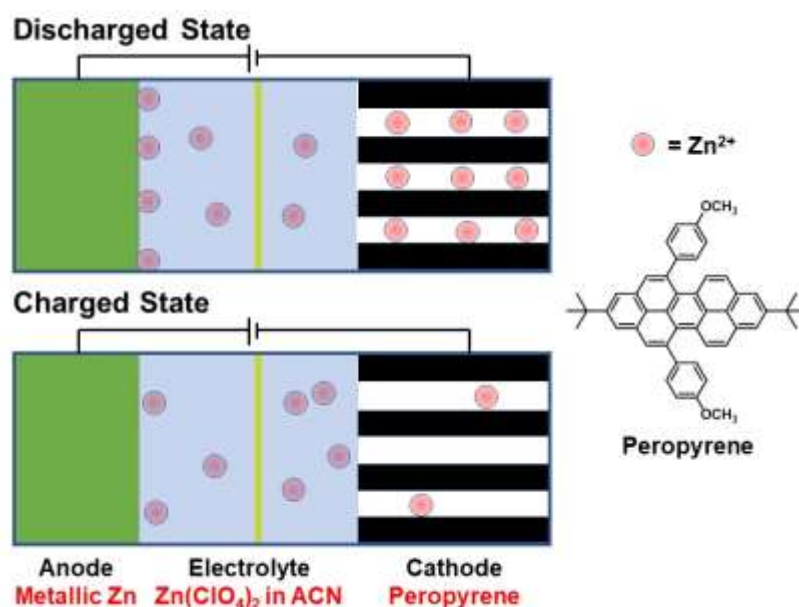


Figure 11.1. Schematic of a Zn^{2+} battery consisting of a peropyrene cathode and a Zn metal anode showing their nominal discharged and charged states.

The battery is constructed in a charged state with a metallic Zn anode and the peropyrene without any intercalated Zn^{2+} . Upon discharge, the Zn metal is oxidized at the

anode to form Zn^{2+} , which concurrently intercalates into a film of the reduced peropyrene radical anion. Upon charge, the reverse reactions occur, in which Zn^{2+} electrodeposits to form Zn on the anode and the peropyrene is oxidized. The peropyrene can be oxidized beyond its neutral form to a radical cation, which is charge balanced by the anion in the electrolyte (e.g. ClO_4^-).

Before testing a full battery, we sought to understand the Zn^{2+} intercalation dynamics in the peropyrene using cyclic voltammetry (CV). We first performed CV of the peropyrene cast with Vulcan XC-72 carbon and a PVDF binder on a Cu substrate in an electrolyte containing $\text{Zn}(\text{CF}_3\text{SO}_3)_2$ in acetonitrile (Figure 11.2a, black line). At a scan rate of 0.1 mV s^{-1} , the voltammogram exhibits a cathodic peak at $\sim 0.1 \text{ V}$ vs. Zn/Zn^{2+} and an anodic peak at $\sim 0.85 \text{ V}$ vs. Zn/Zn^{2+} , which we ascribe to Zn^{2+} intercalation and deintercalation, respectively. However, the large separation between the peak potentials— especially given the slow scan rate—indicates that the kinetics of Zn^{2+} intercalation are significantly impeded. A CV from a control experiment without the peropyrene in the electrode does not exhibit well-defined peaks, indicating that the voltammetric response is due to the peropyrene (Figure 11.2a, red line). Importantly, a CV from another control experiment using the peropyrene with tetrabutylammonium triflate ($\text{TBACF}_3\text{SO}_3$) instead of $\text{Zn}(\text{CF}_3\text{SO}_3)_2$ shows no redox behavior (Figure 11.2a, blue line). This result is expected, because the tetrabutylammonium ion is much larger than Zn^{2+} and presumably too large to intercalate within the pores of the peropyrene. Furthermore, an EDX spectrum of the peropyrene electrode, taken after halting the CV in the intercalated state (0 V), reveals the presence of Zn in the electrode (Figure 11.3a). The corresponding EDX spectrum of the electrode in the deintercalated state does not

display any peaks associated with Zn (Figure 11.3b). Taken together, these results indicate that, although the reaction is slow, Zn^{2+} reversibly intercalates into the peropyrene using an electrolyte containing $\text{Zn}(\text{CF}_3\text{SO}_3)_2$ in acetonitrile.

We additionally evaluated if Zn^{2+} intercalation is feasible in the smaller nanographene molecules, coronene and perylene, the structures of which are shown on the right side of Figure 11.2. Unlike the peropyrene, which possesses a twisted structure, coronene and perylene are relatively flat molecules. The smaller interlayer spacing of these molecules should make Zn^{2+} intercalation into these structures more difficult. Indeed, the CVs of electrodes with coronene (Figure 11.2, purple line) and perylene (Figure 11.2, green line) in the $\text{Zn}(\text{CF}_3\text{SO}_3)_2$ electrolyte confirm this hypothesis, as both CVs exhibit very low current density. The results of Figure 11.2a indicate that it is the unique structure of the peropyrene, with its larger interlayer spacing, that allows it to function as a reversible host for reversible Zn^{2+} intercalation. Under the same electrochemical conditions, Zn^{2+} intercalation does not occur in graphites (e.g. Vulcan XC-72) or flat nanographenes.

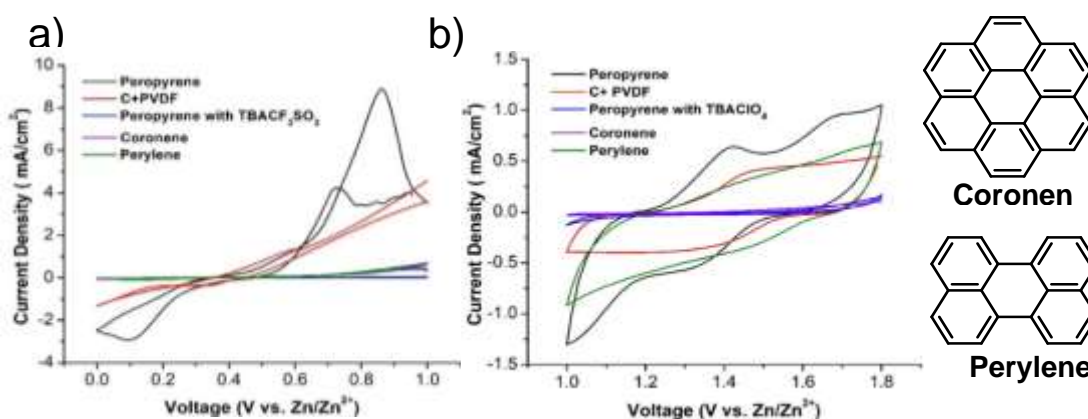


Figure 11.2. Cyclic voltammetry evaluating Zn^{2+} intercalation in the peropyrene (black), a control without any nanographene (red), coronene (purple), and perylene (green) cast

with Vulcan XC-72 carbon and PVDF. For panel a, the electrolyte used was 100 mM $\text{Zn}(\text{CF}_3\text{SO}_3)_2$ in acetonitrile, the cathode was cast on a Cu substrate, and the scan rate was 0.1 mV s^{-1} . For panel b, the electrolyte used was 100 mM $\text{Zn}(\text{ClO}_4)_2$ in acetonitrile, the cathode was cast on a graphite-coated stainless steel substrate, and the scan rate was 50 mV s^{-1} . The blue lines indicate voltammetry with the peropyrene using an electrolyte containing 100 mM $\text{TBACF}_3\text{SO}_3$ or TBAClO_4 in acetonitrile.

We next performed an analogous set of voltammetry experiments using an electrolyte in which $\text{Zn}(\text{ClO}_4)_2$ replaces $\text{Zn}(\text{CF}_3\text{SO}_3)_2$ (Figure 11.2b). For these experiments, the electrodes were cast on graphite-coated stainless steel substrates, not Cu. Cu substrates were found to be incompatible with the $\text{Zn}(\text{ClO}_4)_2$ electrolyte (Supporting Figure 12.9.1), and more information explaining this phenomenon can be found in the supporting information. Strikingly, the CV of the peropyrene electrode contains two well-defined sets of redox peaks at a much faster scan rate of 50 mV s^{-1} (Figure 11.2b, black line). Based on previous literature studying the solution-phase electrochemistry of this peropyrene, [218] the redox pair centered at $\sim 1.35 \text{ V}$ is ascribed to the neutral peropyrene and the corresponding radical anion, and the redox pair centered at $\sim 1.65 \text{ V}$ is assigned to the neutral peropyrene and the corresponding radical cation. The well-defined peaks at this faster scan rate indicate that Zn^{2+} intercalation dynamics are faster with the $\text{Zn}(\text{ClO}_4)_2$ electrolyte as compared to $\text{Zn}(\text{CF}_3\text{SO}_3)_2$. We hypothesize that the origin of this difference is due to greater ion disassociation in $\text{Zn}(\text{ClO}_4)_2$ compared to $\text{Zn}(\text{CF}_3\text{SO}_3)_2$. Previous reports studying Zn^{2+} intercalation in a V_3O_7 electrode, using $\text{Zn}(\text{CF}_3\text{SO}_3)_2$ in acetonitrile, determined that Zn^{2+} in this electrolyte remain largely ion-paired and heavily solvated, and that this solution structure resulted in slow Zn^{2+} intercalation kinetics. [27] For these reasons, a CV exhibiting Zn intercalation is only obtainable at a slower scan

rate using the $\text{Zn}(\text{CF}_3\text{SO}_3)_2$ electrolyte, whereas Zn intercalation occurs faster with the $\text{Zn}(\text{ClO}_4)_2$ electrolyte and hence a faster scan rate can be used. CVs of the control experiments without the peropyrene (Figure 11.2b, red line), with tetrabutylammonium perchlorate (TBAClO₄, Figure 11.2b, blue line), and with coronene and perylene (Figure 11.2b, purple and green lines) do not exhibit well-defined peaks like the CV of the peropyrene electrode. As for the $\text{Zn}(\text{CF}_3\text{SO}_3)_2$ electrolyte, these experiments indicate that the molecular structure of the peropyrene is responsible for facilitating reversible Zn^{2+} intercalation. While the intermolecular spacing of the smaller and flatter coronene and perylene molecules is too small to allow for reversible Zn^{2+} intercalation, the twisted peropyrene structure is less well-packed, which enables Zn^{2+} intercalation to occur. The crystal structures of coronene and perylene indicate that these molecules have intermolecular spacings of 3.40 Å and 3.47 Å, respectively. [221, 222] In contrast, the intermolecular spacing of a structurally similar peropyrene (n-hexyl ethers replace the methyl ethers) is much larger.[213] Although a greater intermolecular spacing in nanographenes improves the reversibility of intercalation, less densely-packed nanographenes reduce the volumetric energy density of the battery. In future research, we will more fully explore the relationship between intermolecular spacing, intercalation reversibility, and volumetric energy density.

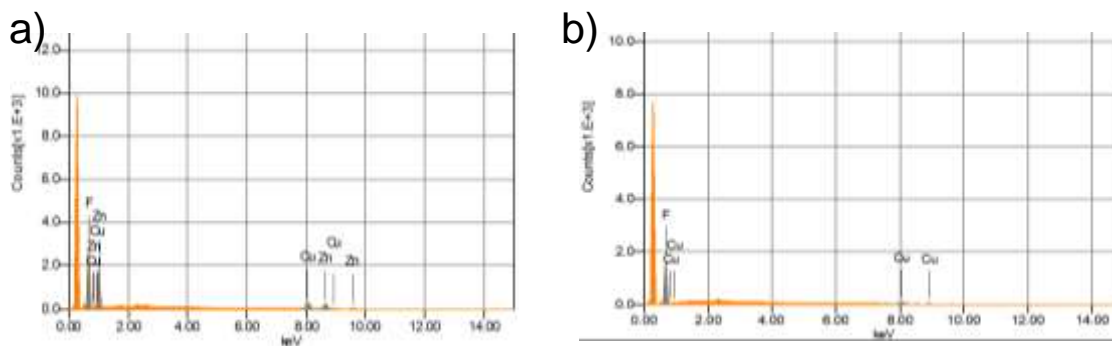


Figure 11.3. Energy-dispersive X-ray spectra of the peropyrene cathode cast on Cu foil in its intercalated (a) and deintercalated (b) states using an electrolyte containing $\text{Zn}(\text{CF}_3\text{SO}_3)_2$ in acetonitrile at a scan rate of 0.1 mV s^{-1} .

To probe the larger scale structure of peropyrene in the electrode composites, we used SEM. Figure 11.4a displays a SEM image of the peropyrene electrode as cast with Vulcan XC-72 carbon and PVDF binder. The rod-like structures (yellow arrows) are assigned to the peropyrene because they are not present in SEM images of the electrodes without the peropyrene (Figure 11.4b).

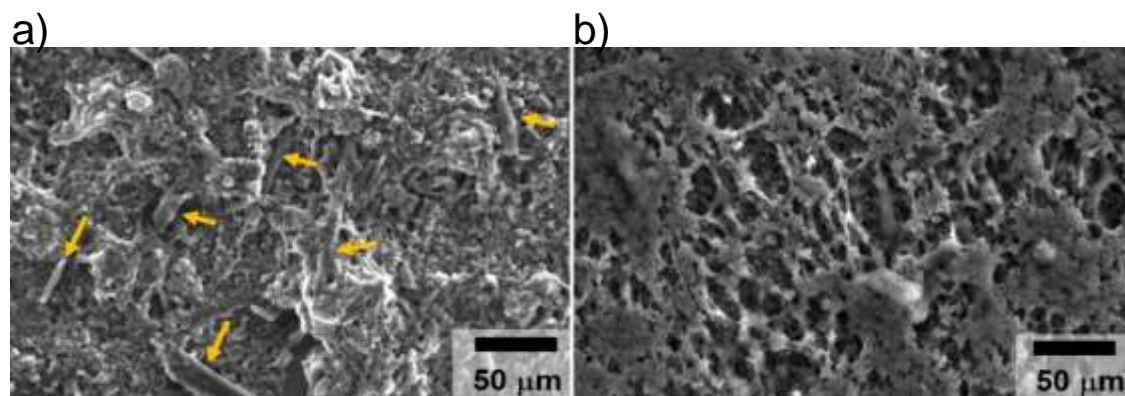


Figure 11.4. SEM images of electrodes with Vulcan XC-72 carbon, PVDF, and with (a) and without (b) the peropyrene. The yellow arrows in image a point to examples of the rod-like structures in the SEM, which are not present in image b and therefore are assigned to the peropyrene.

Having established that reversible Zn^{2+} intercalation occurs facily in the peropyrene with $\text{Zn}(\text{ClO}_4)_2$, we constructed a battery that uses the $\text{Zn}(\text{ClO}_4)_2$ electrolyte and pairs a peropyrene cathode with a Zn metal anode. The discharge-charge curves of the battery are displayed in Figure 11.5. The open circuit potential of the battery is $\sim 1.6 \text{ V}$, which corresponds well with the voltage of the redox peaks of the peropyrene as determined by CV (Figure 11.2b, black line). Based on the molar mass of the peropyrene

(650.32 g mol⁻¹) and the capacity for each peropyrene to store 2 e⁻ by cycling between the radical cation, neutral, and radical anion states, the theoretical capacity for the battery—which is limited by the cathode—is 82 mAh g⁻¹. The first two discharge-charge cycles of the battery (Figure 11.5, black and red lines) exhibit significantly higher capacities than this theoretical value. These large capacities are likely artificially inflated by a number of potential initial side reactions in the battery such as reactions with water or O₂ impurities in the electrolyte or solid-electrolyte interface formation. Higher than theoretical initial discharge-charge capacities are common in a wide range of battery chemistries including Zn-ion batteries.[203] From the third to fifth cycles, however, the charge and discharge curves begin to stabilize near the theoretical values. Although the discharge curves begin near the open circuit potential of 1.6 V, they steadily decrease through device discharging until the cutoff voltage of 0.3 V is reached. Because the overpotentials associated with Zn electrodisolution at the anode are known to be low,[26] this behavior indicates there is significant overpotential associated with Zn²⁺ intercalation at the cathode. Discharge curves were performed at a current of 100 mA g⁻¹, which, based on the battery's theoretical capacity, gives a rate of 1.2 C. In contrast, the charge curves were performed at a current of 500 mA g⁻¹ or a rate of 6 C. Even at this faster rate, the charge curves exhibit much less overpotential than the discharge curves (Figure 11.5b). For the majority of the capacity of the charge curves, the voltage ranges from 1.2-1.7 V, which is the same range that the redox peaks are observed in the peropyrene CV (Figure 11.2, black line). The lower overpotential associated with charging indicates that Zn²⁺ deintercalation is kinetically more favorable than Zn²⁺ intercalation. The fast deintercalation kinetics allow the battery to charge rapidly, which is an advantageous attribute of this battery chemistry.

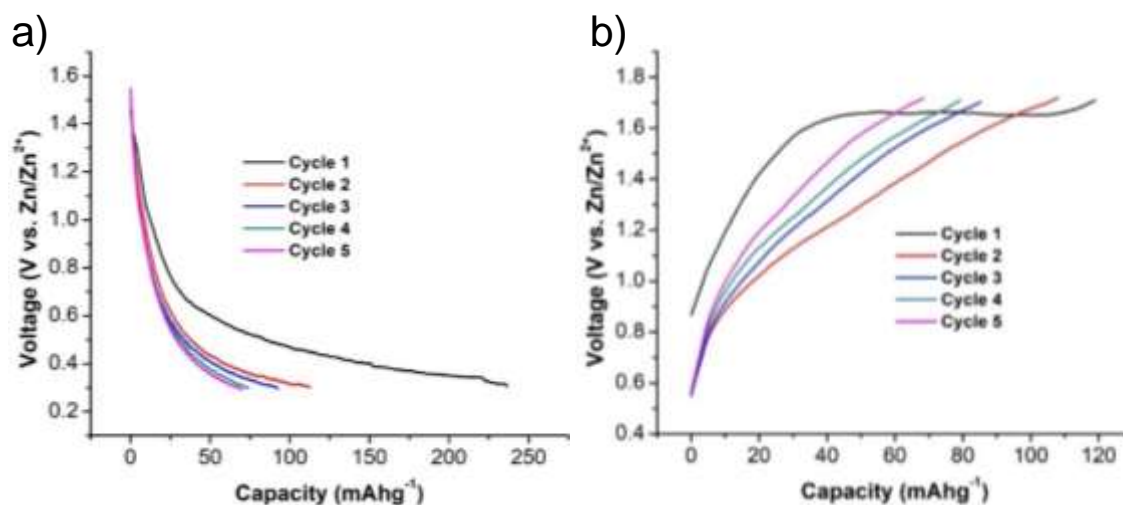


Figure 11.5. Discharge (a) and charge (b) curves of a Zn-ion battery with the peropyrene cathode, a Zn metal anode, and an electrolyte containing Zn(ClO₄)₂ in acetonitrile. Discharge and charge rates were 100 mA g⁻¹ and 500 mA g⁻¹, respectively.

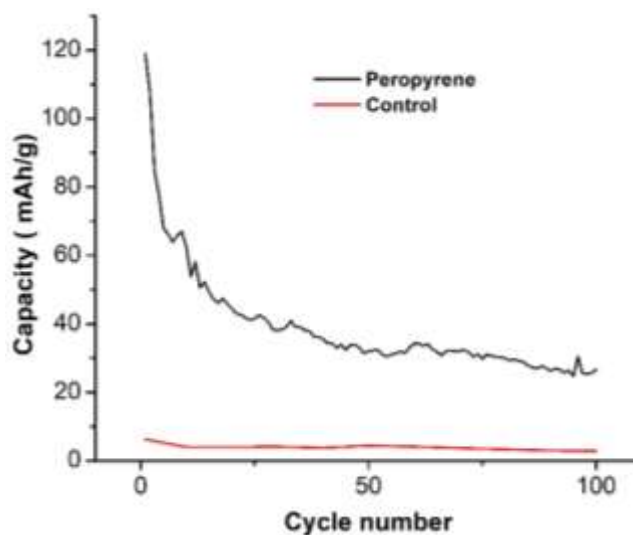


Figure 11.6. Capacity as a function of cycle number of Zn-ion batteries with a cathode cast using Vulcan XC-72 carbon and PVDF with (black) and without (red) the peropyrene.

Further discharge-charge curves of the battery beyond cycle 5 are shown in Supporting Figure 12.9.2, and the black line in Figure 6 plots the capacity of the battery

over the course of 100 cycles. The data indicate that the capacity of the battery steadily decreases during cycling. At this stage, the exact origin of this degradation is not clear. Oxidative degradation of the electrolyte, however, can be ruled out. Degradation during cycling is also evidenced by the less than 100% Coulombic efficiency of the device (Supporting Figure 12.9.3). From cycles 10-100, the Coulombic efficiency ranges between 89% and 94%. A CV of the peropyrene cathode in the $\text{Zn}(\text{ClO}_4)_2$ in acetonitrile electrolyte indicates that oxidative degradation does not occur until voltages more positive than 1.9 V (Figure 11.7), a value higher than the 1.7 V cutoff voltage used when cycling the batteries. This oxidative stability matches with previous reports studying reversible Zn electrodeposition in this electrolyte.[26] Importantly, a control experiment cycling a battery using a cathode with Vulcan XC-72 carbon and PVDF without the peropyrene indicates that this battery possesses a capacity less than 10 mAh g^{-1} throughout cycling (Figure 6, red line and Supporting Figure 11.4). This experiment proves that the peropyrene is responsible for the enhanced capacity of the Zn-peropyrene battery.

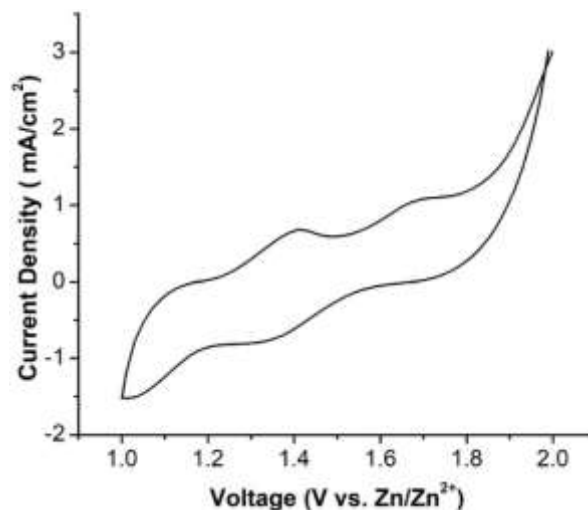


Figure 11.7. Cycle voltammetry of Zn^{2+} intercalation in the peropyrene cast with Vulcan XC-72 carbon and PVDF. The electrolyte used contained 100 mM $\text{Zn}(\text{ClO}_4)_2$ in acetonitrile, and the scan rate was 50 mV s^{-1} .

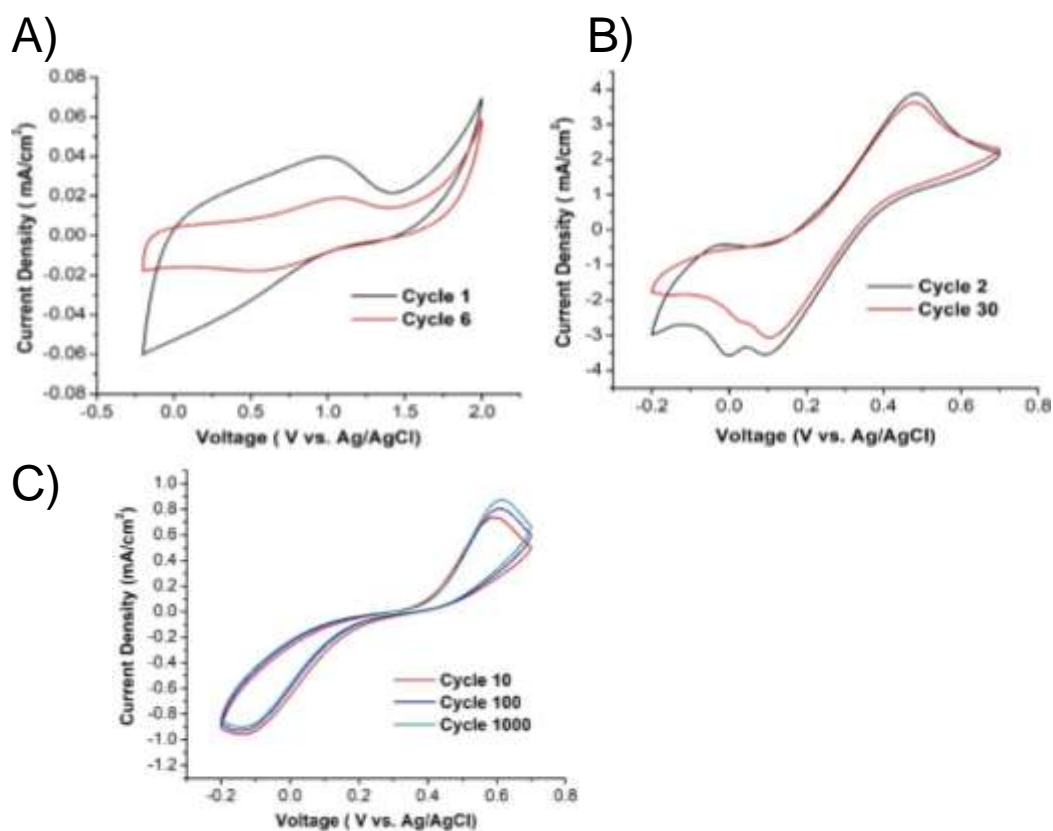
11.4. Conclusion

In terms of its capacity, discharge/charge rates, voltage, and cycle life, the Zn-peropyrene battery developed here is comparable to many other Zn-ion battery chemistries actively being researched. [20, 28, 223] For example, Chae et al. reported a Zn-ion battery in an organic electrolyte using a hexacyanoferrate-based cathode that cycled 40 times with a capacity between $45\text{-}55 \text{ mAh g}^{-1}$ at a much slower rate of 0.2 C.[26] Another hexacyanoferrate cathode using an aqueous electrolyte resulted in a battery that cycled 100 times with a capacity between $45\text{-}55 \text{ mAh g}^{-1}$ at 1 C. [224] A Zn-ion battery based on a Chevrel-type cathode in an aqueous electrolyte cycled 20 times with a marginally higher capacity, but at slower discharging rates. [225] In comparison, the battery developed here cycles at rates greater than 1 C about 60 times with a capacity between $30\text{-}60 \text{ mAh g}^{-1}$. Achieving adequate cycle life in new advanced battery chemistries is commonly challenging, and in future work, we will first seek to understand the origins of the decline in performance during the cycling of these nanographene batteries. Based on those results, the electrolyte and the nanographene will be modified in an effort to increase cycling performance. Beyond its performance, the key innovation presented in this manuscript is the use of a molecularly-precise nanographene cathode for nonaqueous multivalent ion intercalation. Compared to aqueous systems, there are relatively few examples of reversible multivalent ion intercalation in layered cathode

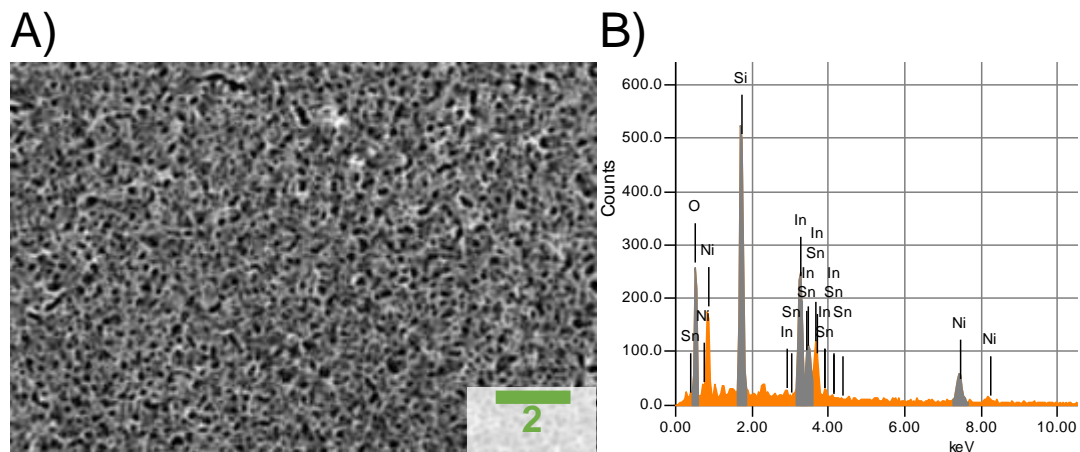
materials. This research introduces a new strategy to facilitate nonaqueous multivalent ion intercalation in graphitic materials. In future research, we will study the intercalation of other multivalent ions such as Mg^{2+} and Ca^{2+} in nanographenes. The variety of contorted nanographenes, including persistently chiral compounds, which can be produced using alkyne benzannulation allows us to explore alternative nanographenes to increase device performance moving forward.

Chapter 12: Appendices. Supporting Figures

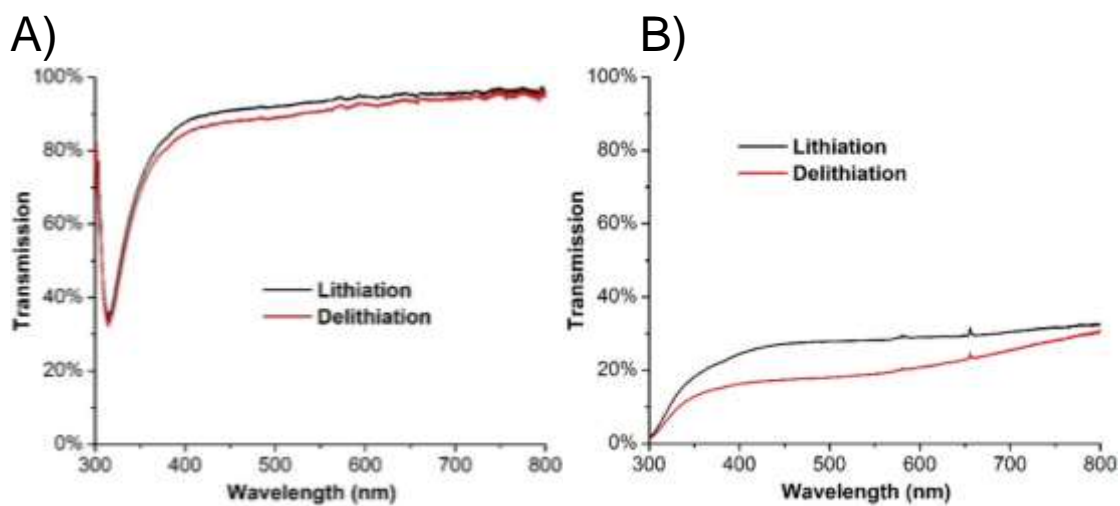
12.1. Supporting Figures for Chapter 2: Hybrid Dynamic Windows using Reversible Metal Electrodeposition and Ion Insertion



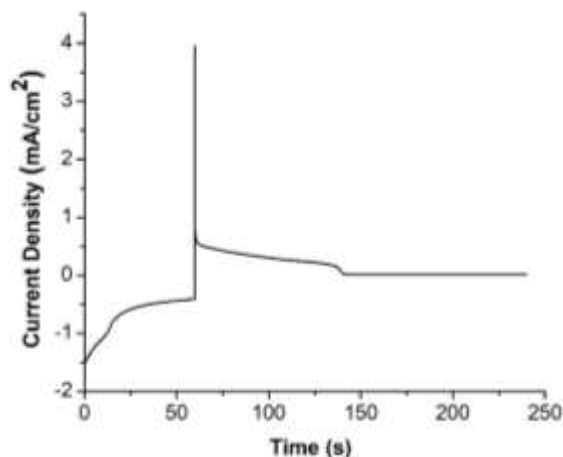
Supporting Figure 12.1.1: Cyclic voltammograms of ITO on glass electrodes coated with CeO₂ (A), V₂O₅ (B), and NiO (C) in the aqueous Cu-Bi electrolyte.



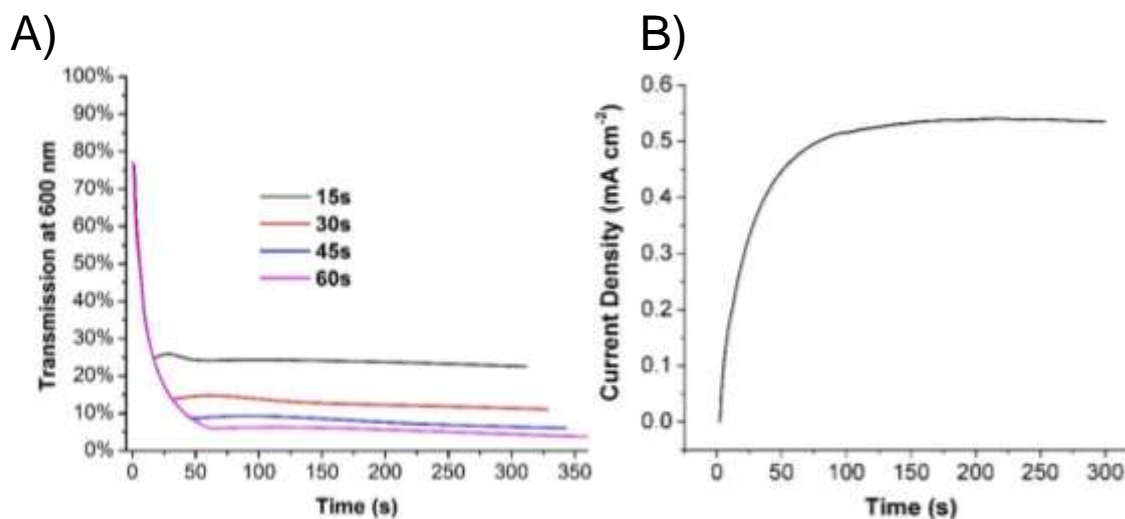
Supporting Figure 12.1.2: SEM image of LiNiO_x (A) and the corresponding EDX spectrum (B), which confirms the presence of NiO and also exhibits In and Sn peaks from ITO and Si peaks from the glass.



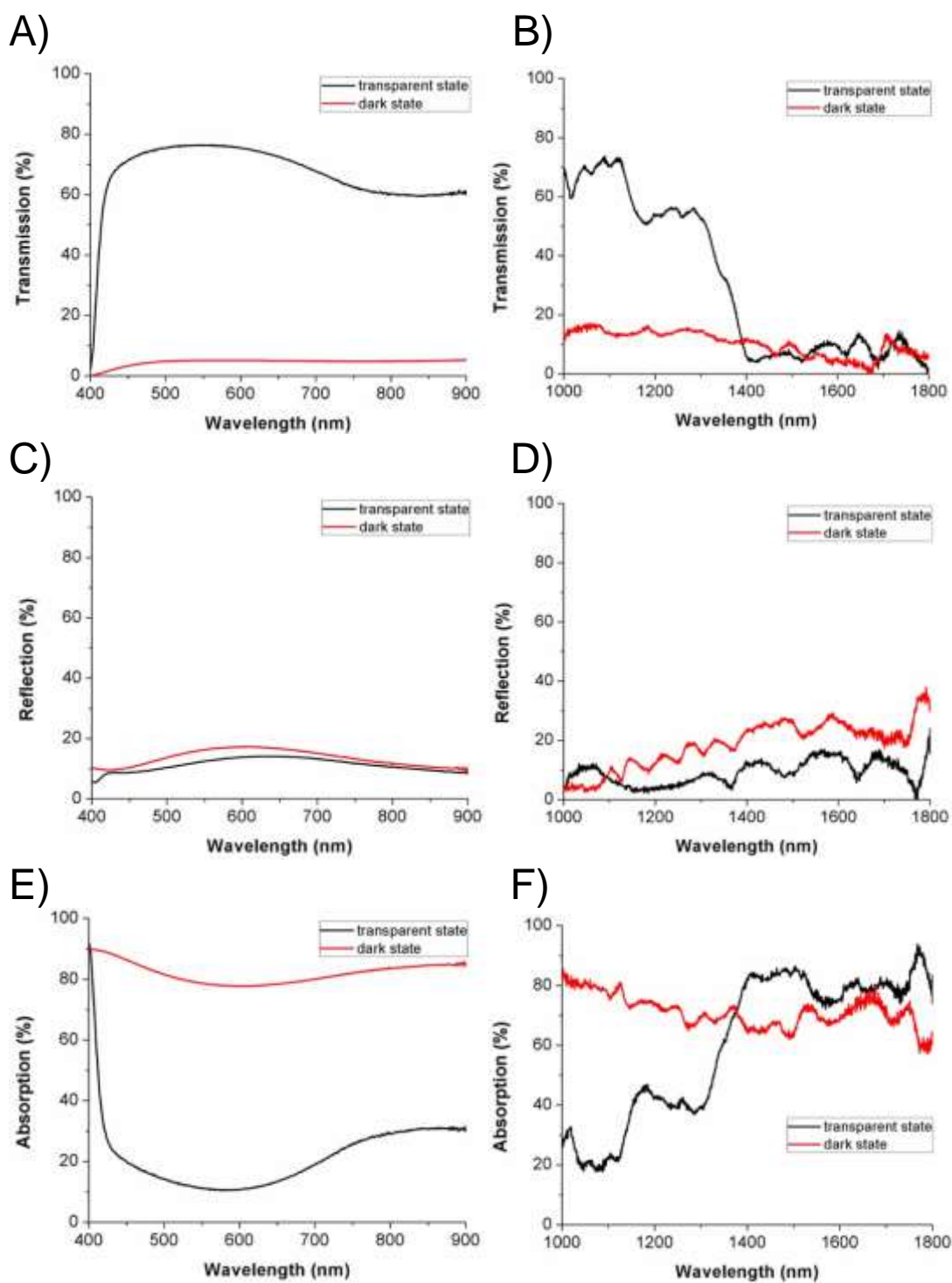
Supporting Figure 12.1.3: Transmission of a 60-nm-thick (A) and 1- μm -thick (B) NiO film on an ITO on glass working electrode in a three-electrode cell using a 1 M LiBr electrolyte. A voltage of -0.01 V was applied for 180 s to lithiate the electrode and 0.67 V was applied for 60 s to delithiate the electrode.



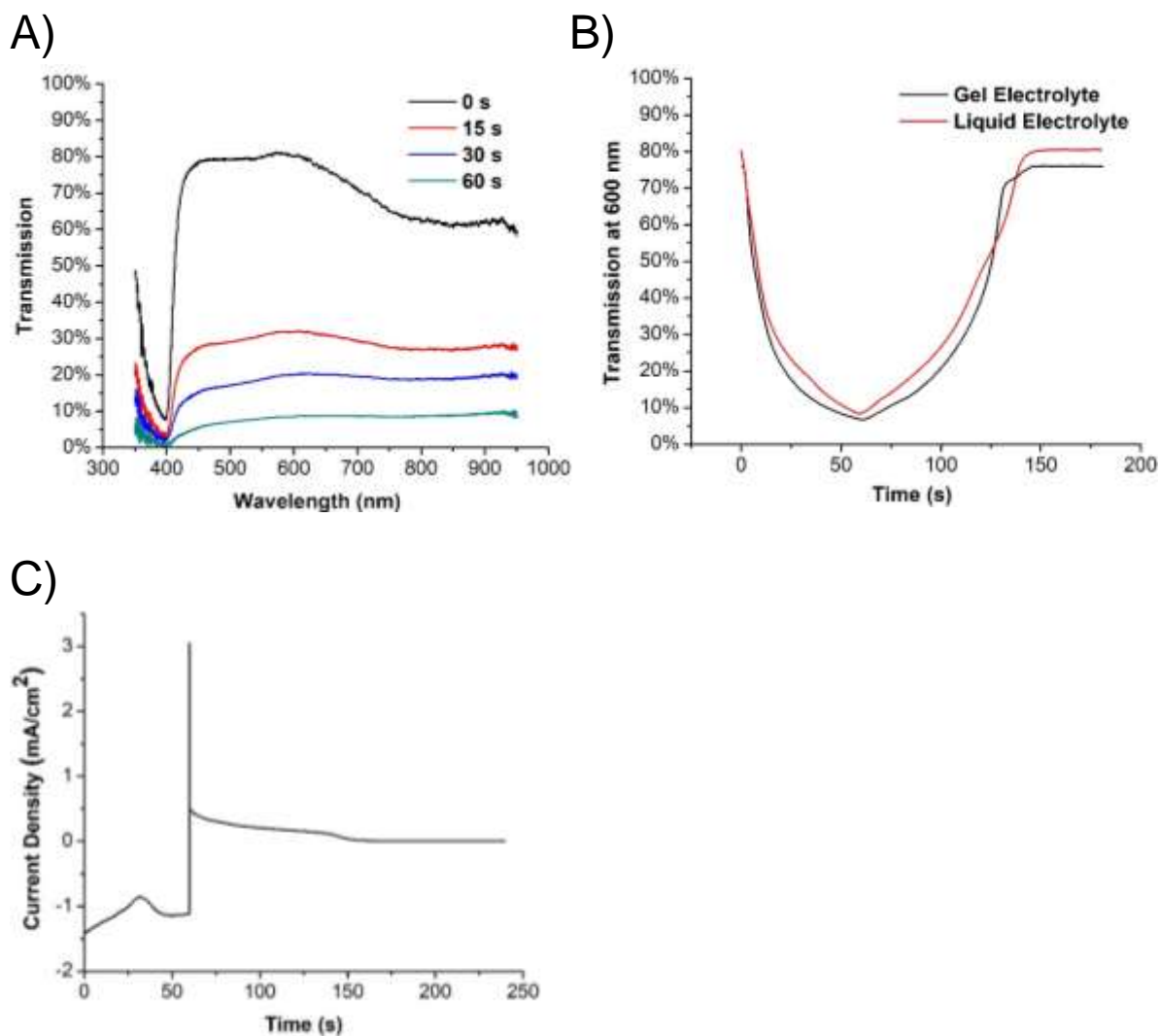
Supporting Figure 12.1.4: Chronoamperometry of a 25 cm² dynamic window with a Pt-modified ITO on glass working electrode, a LiNiO_x on ITO on glass counter electrode formed using electrodeposition, and a Cu-Bi gel electrolyte during 60 s of metal electrodeposition at -2.5 V and 120 s of metal stripping at 0 V.



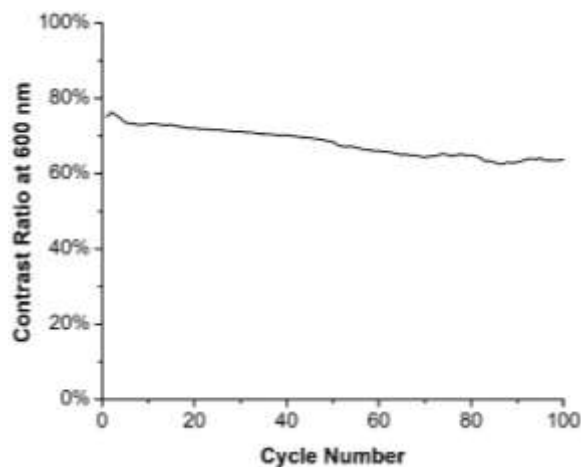
Supporting Figure 12.1.5: Transmission at 600 nm of a 25 cm² hybrid dynamic window that was darkened to an intermediate transmission state using 15 s (black), 30 s (red), 45 s (blue), or 60 s (pink) of metal electrodeposition at -2.5 V followed by 300 s at -0.55 V to keep the window in its intermediate state (A). Representative chronoamperometry at -0.55 V (B). By calculating the average current density from the chronoamperometry, the average power density is calculated to be 2.7 W m⁻² to keep the window in any dark state.



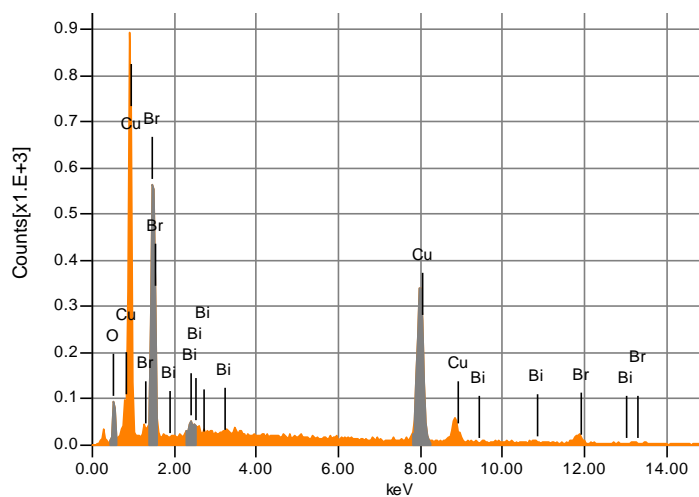
Supporting Figure 12.1.6: Transmission (A, B), reflection (C, D), and absorption (E, F) of a 25 cm² dynamic window with a Pt-modified ITO on glass working electrode, a LiNiO_x on ITO on glass counter electrode, and a Cu-Bi gel electrolyte as a function of wavelength after 0 s (black) and 60 s (red) of window tinting at -2.5 V.



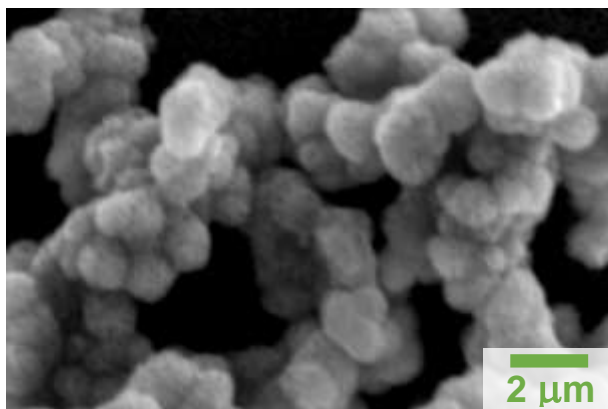
Supporting Figure 12.1.7: Transmission of a 25 cm² dynamic window with a Pt-modified ITO on glass working electrode, a LiNiO_x on ITO on glass counter electrode formed using electrodeposition, and a Cu-Bi liquid electrolyte as a function of wavelength after 0 s (black), 15 s (red), 30 s (blue), and 60 s (teal) of window tinting at -2.5 V (A). Transmission of the same window at 600 nm during 60 s of metal electrodeposition at -2.5 V and 120 s of metal stripping at 0 V (B). Chronoamperometry of the window during switching (C).



Supporting Figure 12.1.8: Contrast ratio of dynamic window with a Pt-modified ITO on glass working electrode and a LiNiO_x on ITO on glass counter electrode over the course of 100 cycles.



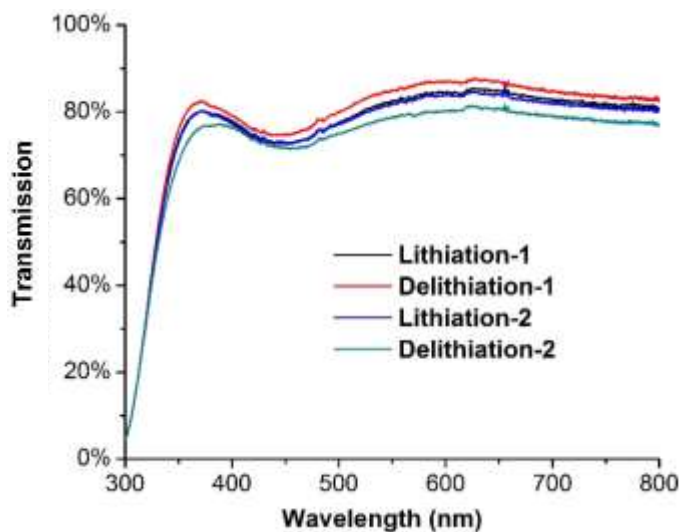
Supporting Figure 12.1.9: EDX spectrum of a NiO on ITO on glass counter electrode after device cycling. The presence of Bi and Cu in the spectrum indicates that metal deposits on the counter electrode, giving rise to the visible greying of the electrode that lowers the maximum transmission of the device during cycling. Br is also present due to LiBr in the electrolyte.



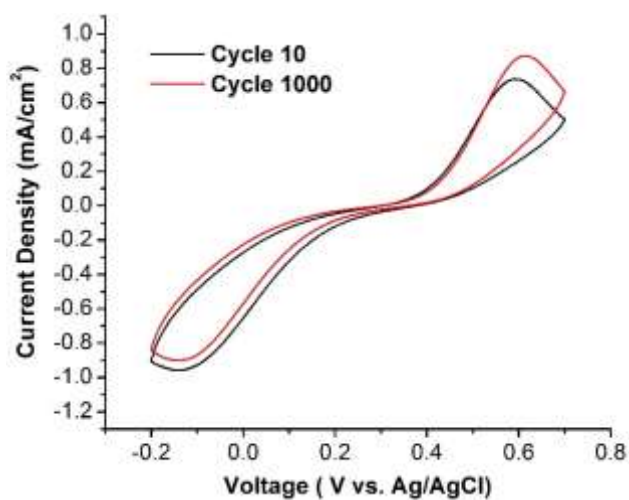
Supporting Figure 12.1.10: SEM images of BTM on NiO on ITO on glass.



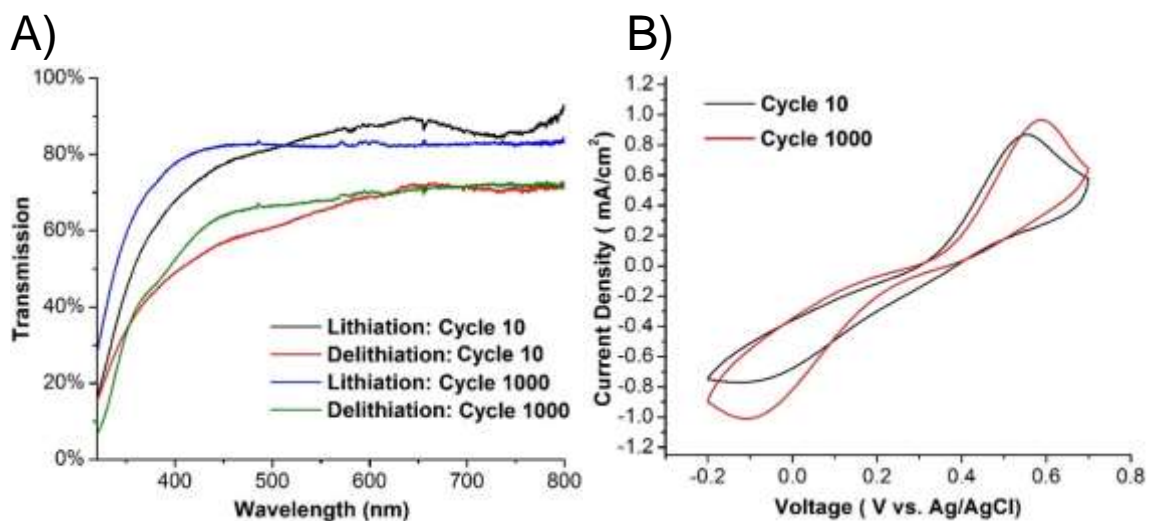
Supporting Figure 12.1.11: Photograph of a 25 cm² dynamic window utilizing an unmodified ITO counter electrode. Following 10 complete cycles of -2.5V for 30 s and 0V for 60 s, the device turns yellow due to the formation of Br₃⁻ in the electrolyte.



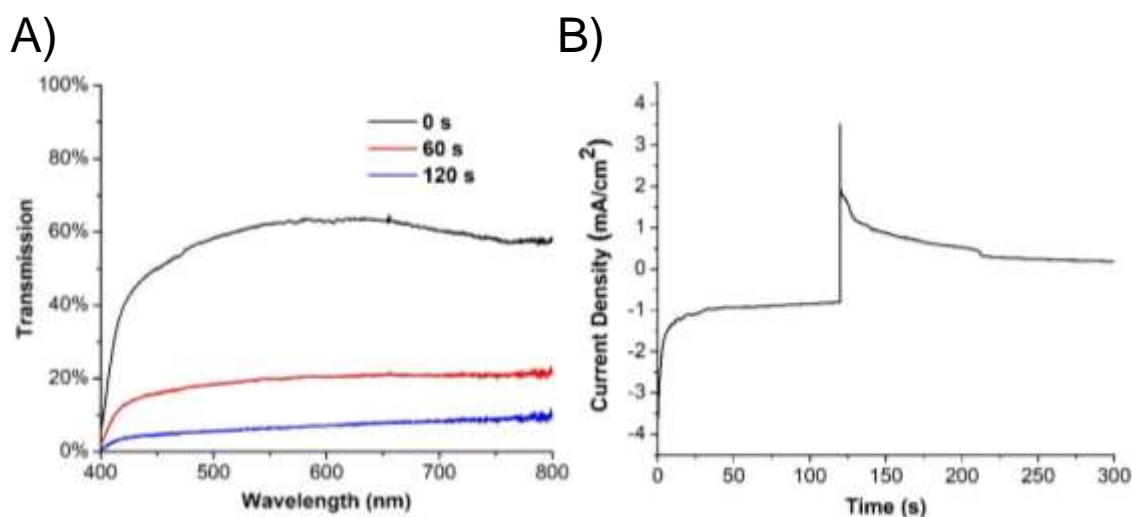
Supporting Figure 12.1.12: Transmission of a ITO on glass working electrode in a three-electrode cell using a 1 M LiBr electrolyte. A voltage of -0.01 V was applied for 180 s to lithiate the electrode and 0.67 V was applied for 60 s to delithiate the electrode.



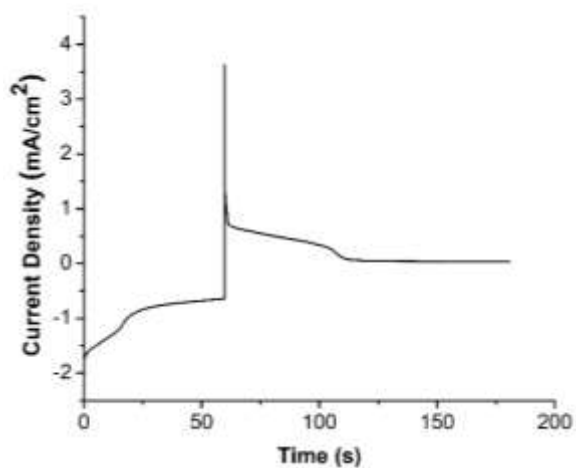
Supporting Figure 12.1.13: Cyclic voltammograms of ITO on glass electrodes coated with NiO in the aqueous Cu-Bi electrolyte at 50 mV/s.



Supporting Figure 12.1.14: Transmission of a BTD-coated NiO film on an ITO on glass working electrode in a three-electrode cell using a 1 M LiBr electrolyte (A). A voltage of -0.01 V was applied for 180 s to lithiate the electrode and 0.67 V was applied for 60 s to delithiate the electrode. Cyclic voltammograms of the same electrode in the aqueous Cu-Bi electrolyte at 50 mV/s (B).

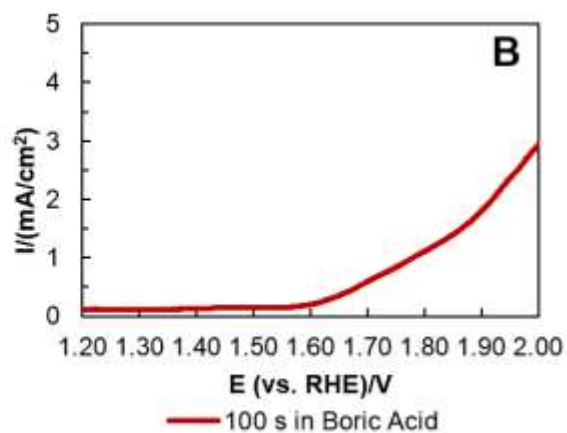
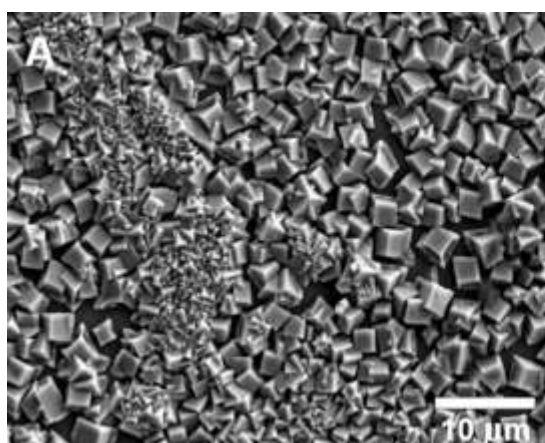


Supporting Figure 12.1.15: Transmission of a 25 cm² dynamic window with a Pt-modified ITO on PET working electrode, a LiNiO_x on ITO on PET counter electrode formed using chemical bath deposition, and a Cu-Bi liquid electrolyte as a function of wavelength after 0 s (black), 60 s (red), and 120 s (blue) of window tinting at -2.5 V (A). Chronoamperometry (B) of the same window during 120 s of metal electrodeposition at -2.5 V and 180 s of metal stripping at 0 V.

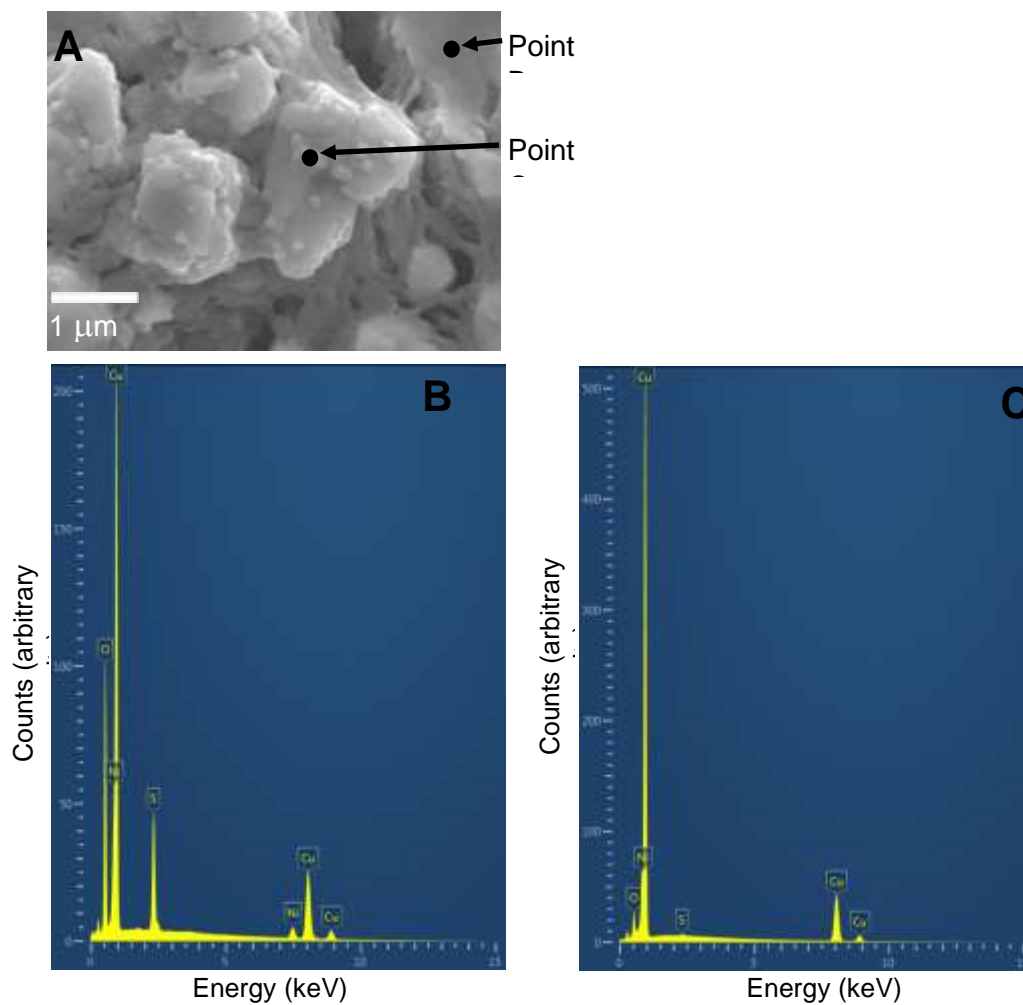


Supporting Figure 12.1.16: Chronoamperometry of a 100 cm² dynamic window using a voltage of -2.5 V for 60 s and 0 V for 120 s.

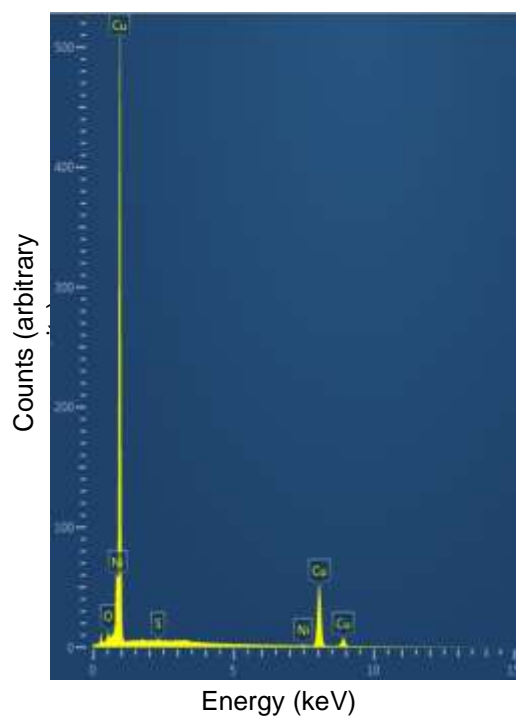
12.2. Supporting Figures for Chapter 3: Cuprous Oxide Electrodeposited with Nickel for the Oxygen Evolution Reaction in 1 M NaOH



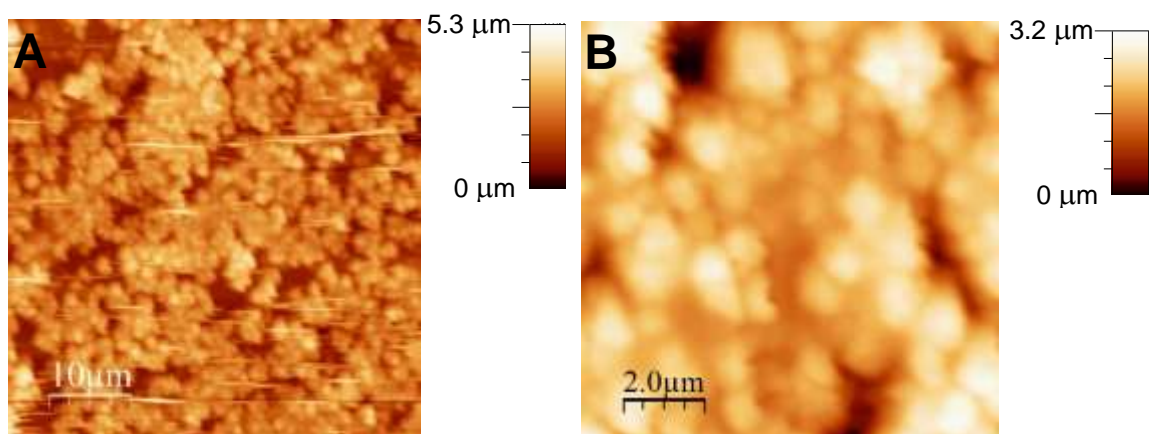
Supporting Figure 12.2.1: SEM images of a Cu₂O on ITO working electrode that has been soaked in 0.4 M boric acid for 100 s (A) and a linear sweep voltammogram of the same electrode in 1 M NaOH at a scan rate of 10 mV/s (B).



Supporting Figure 12.2.2: SEM image (A) of a Cu_2O on ITO electrode with a Ni overlayer formed using 100 s of Ni electrodeposition and EDS spectra taken at points B and C of the SEM image (B, C).



Supporting Figure 12.2.3: EDX spectrum of a Cu_2O on ITO electrode with a Ni overlayer formed using 500 s of Ni electrodeposition. The corresponding SEM image is shown in Figure 5F



Supporting Figure 12.2.4: AFM images of a Cu_2O on ITO electrode with a Ni overlayer formed using 100 s of Ni electrodeposition.

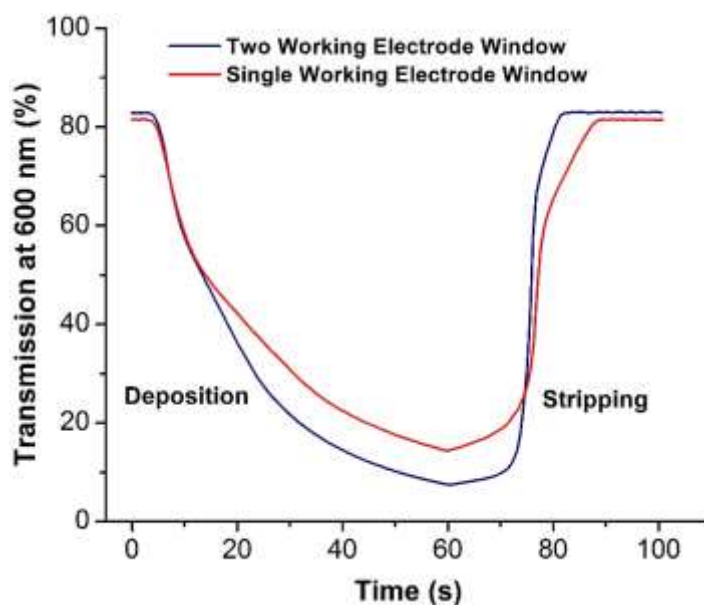
Catalyst	Electrolyte	Onset E (V_{RHE})	Onset overpotential ($V_{RHE} - 1.23$ V)	Overpotential (mV) at specific current density	Ref- erence
Precious metal					
Ru ₆₀ -Co ₄₀	0.1 M HClO ₄	1.41	0.18	-	[226]
Ru ₇₀ -Ir ₃₀	0.1 M HClO ₄	1.40	0.27	-	[226]
RuO ₂	0.1 M KOH	1.44	0.21	425 @ 20 mA/cm ²	[227]
IrO ₂	1 M KOH	1.51	0.28	340 @ 10 mA/cm ²	[80]
Spinel family					
CoFe ₂ O ₄ on GCE	0.1 M KOH	1.58	0.35	443 @ 10 mA/cm ²	[228]
Mn ₃ O ₄ on GCE	1 M KOH	1.68	0.45	>600 @ 3 mA/cm ²	[81]
Co ₃ O ₄ on Au	1 M KOH	1.56	0.33	400 @ 10 mA/cm ²	[229]
Mn _{2.1} Co _{0.9} O ₄	1 M KOH	1.64	0.41	490 @ 3 mA/cm ²	[81]
ZnCo ₂ O ₄ on Pt	1 M KOH (pH 13.8)	1.62	0.39	450 @ 20 mA/cm ²	[230]
Layer-structure type family					
CoOOH on PtO/AuO	0.1 M KOH/LiOH	1.48	0.25	450 @ 5 mA/cm ²	[231]
3D Ni-Fe LDH on Ni foam	0.1 M KOH	1.46	0.23	280 @ 30 mA/cm ²	[232]
Co-Ni LDH on FTO	0.1 M potassium phosphate (pH 7)	1.623	0.393	490 @ 1 mA/cm ²	[82]
Co-Co LDH	0.1 M potassium phosphate (pH 7)	1.638	0.408	610 @ 1 mA/cm ²	[82]
Zn-Co LDH on GCE	0.1 M KOH (pH 13)	1.57	0.34	-	[233]
Co-Fe LDH (1:0.35) on GCE	0.1 M KOH	1.52	0.29	350 @ 10 mA/cm ²	[234]

Co-Cr LDH (2:1) on GCE	0.1 M KOH	1.47	0.24	340 @ 10 mA/cm ²	[227]
Ni-Fe-Mn LDH on CFP	1 M KOH	1.43	0.20	289 @ 20 mA/cm ²	[83]
β -Ni(OH) ₂ nanoparticle film	0.1 M KOH	1.55	0.32	450 @ 30 mA/cm ²	[232]
Co-Ni based nanotubes/nanos heets on Cu	1 M KOH	1.50	0.27	280 @ 10 mA/cm ²	[232]
Exfoliated Ni-Fe nanosheets on GCE	1 M KOH	1.49	0.26	300 @ 10 mA/cm ²	[80]
Exfoliated Ni-Co nanosheets on GCE	1 M KOH	1.52	0.29	385 @ 10 mA/cm ²	[80]
Exfoliated Co- Co nanosheets on GCE	1 M KOH	1.53	0.30	390 @ 10 mA/cm ²	[80]
Fe-Ni nanoparticles on GCE	1 M NaOH	1.40	0.17	256 @ 1 mA/cm ² 311 @ 10 mA/cm ²	[235]
CNTs or carbon fiber supported					
NiFe-LDH/CNT	1 M KOH	1.45	0.22	149 @ 10 mA/cm ²	[236]
M-CNTs-Arc	1 M KOH	1.48	0.25	152 @ 10 mA/cm ²	[237]
NiFeO _x /CFP	1 M KOH	1.43	0.20	146 @ 10 mA/cm ²	[232]
20%Ir/C	1 M KOH	1.50	0.27	152 @ 10 mA/cm ²	[238]
Other					
Fe nanoparticles	1 M NaOH	1.56	0.33	421 @ 1 mA/cm ²	[235]
Ni nanoparticles	1 M NaOH	1.34	0.11	476 @ 1 mA/cm ²	[235]

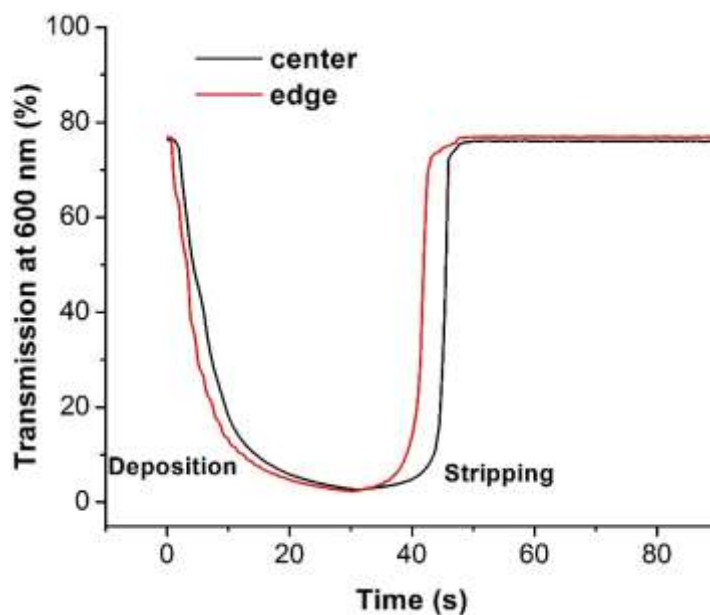
Ni-FeO _x /C (69:31) nanoparticle on carbon black	1 M KOH	1.41	0.18	280 @ 10 mA/cm ²	[84]
Ir/C catalyst	0.1 M KOH	1.50	0.27	390 @ 30 mA/cm ²	[232]

Supporting Table 12.2.1: Summary of performance of various OER electrocatalysts reported in the literature arranged by catalyst family.

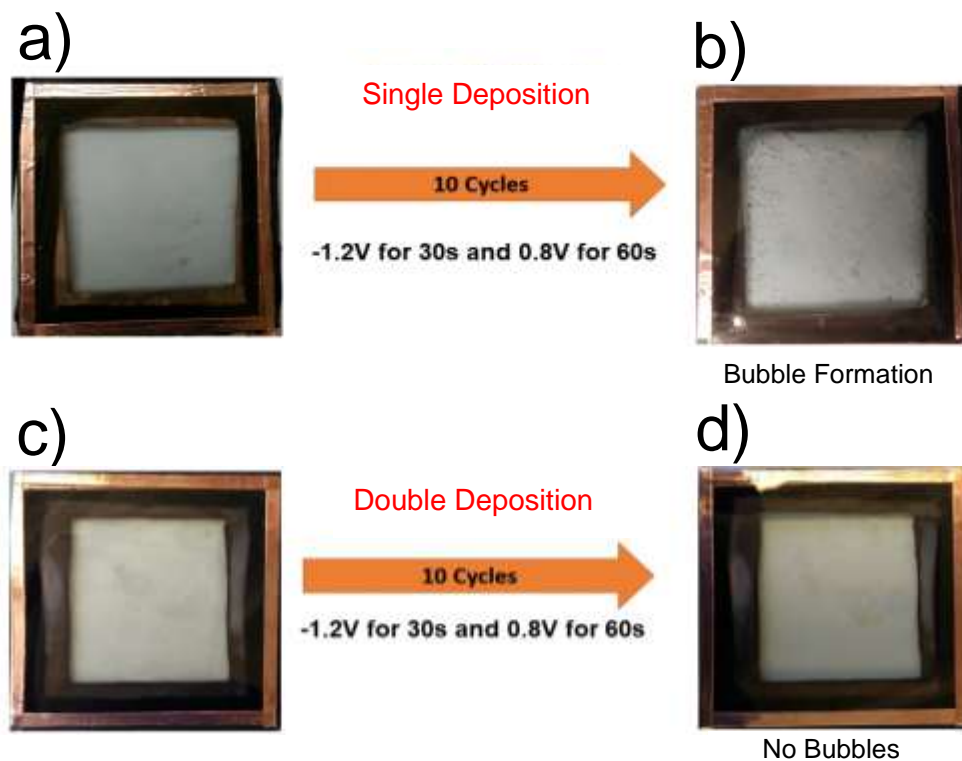
12.3. Supporting Information for Chapter 4: Dynamic Windows based on Reversible Metal Electrodeposition with Enhanced Functionality



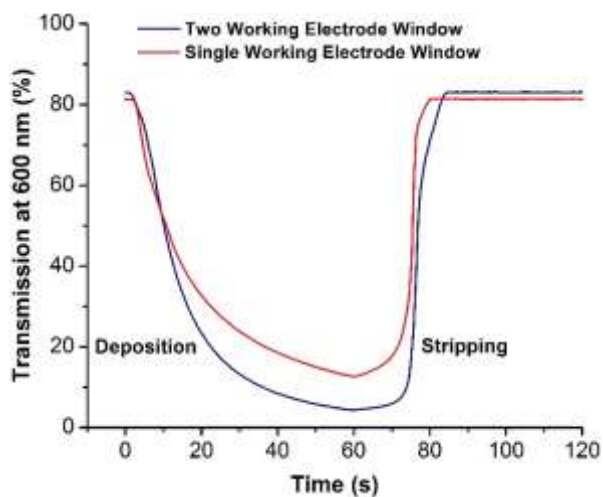
Supporting Figure 12.3.1: Transmission at 600 nm of 25 cm² metal-based dynamic windows with two (blue) and one (red) working electrodes during switching at -0.6 V for 60 s and +0.8 V for 40 s.



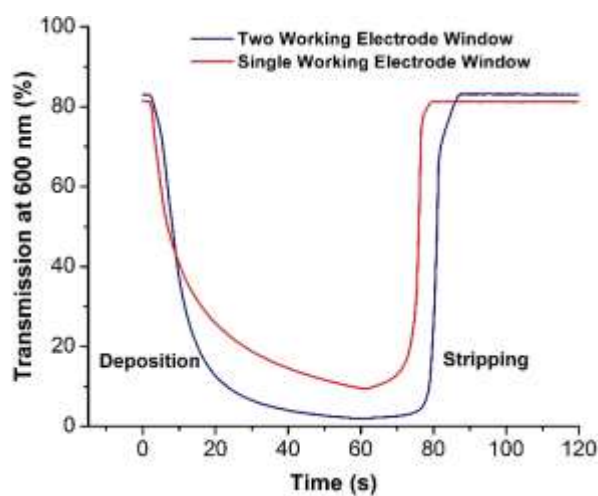
Supporting Figure 12.3.2: Transmission at 600 nm of the center (black) and edge (red) of a 25 cm² metal-based dynamic window with two working electrodes during switching at -1.2 V for 30 s and +0.8 V for 60 s.



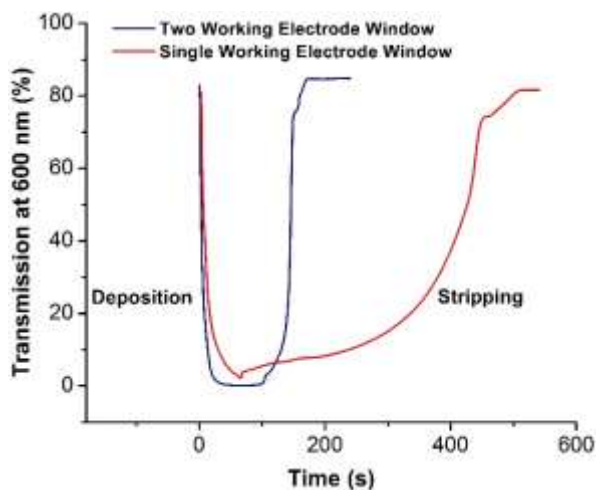
Supporting Figure 12.3.3: Photographs of 25 cm² metal-based dynamic windows with one (a, b) and two (c, d) working electrodes. The initially constructed windows (a, c) were cycled 10 times using -1.2 V for 30 s for metal electrodeposition and +0.8 V for 60 s for metal stripping.



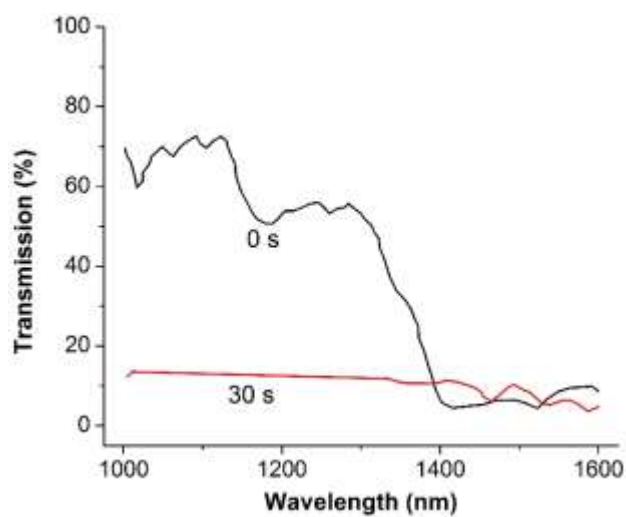
Supporting Figure 13.3.4: Transmission at 600 nm of 25 cm² metal-based dynamic windows with two (blue) and one (red) working electrodes during switching at -0.8 V for 60 s and +0.8 V for 60 s.



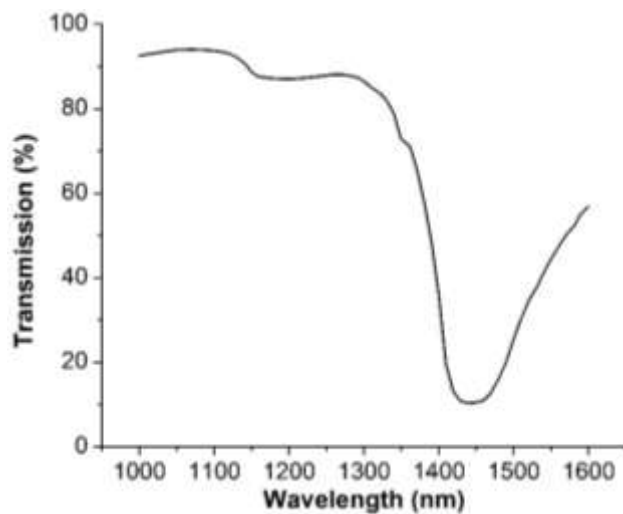
Supporting Figure 13.3.5: Transmission at 600 nm of 25 cm² metal-based dynamic windows with two (blue) and one (red) working electrodes during switching at -1 V for 60 s and +0.8 V for 60 s.



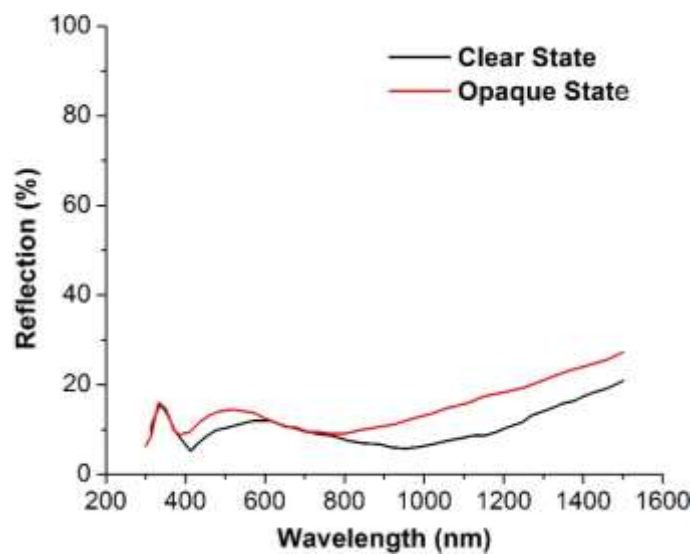
Supporting Figure 12.3.6: Transmission at 600 nm of 25 cm² metal-based dynamic windows with two (blue) and one (red) working electrodes during switching at -1.5 V for 60 s and +0.8 V for metal stripping.



Supporting Figure 12.3.7: Transmission at 600 nm of a 25 cm² metal-based dynamic window as a function of wavelength after 0 s (black) and 30 s (red) of window darkening.

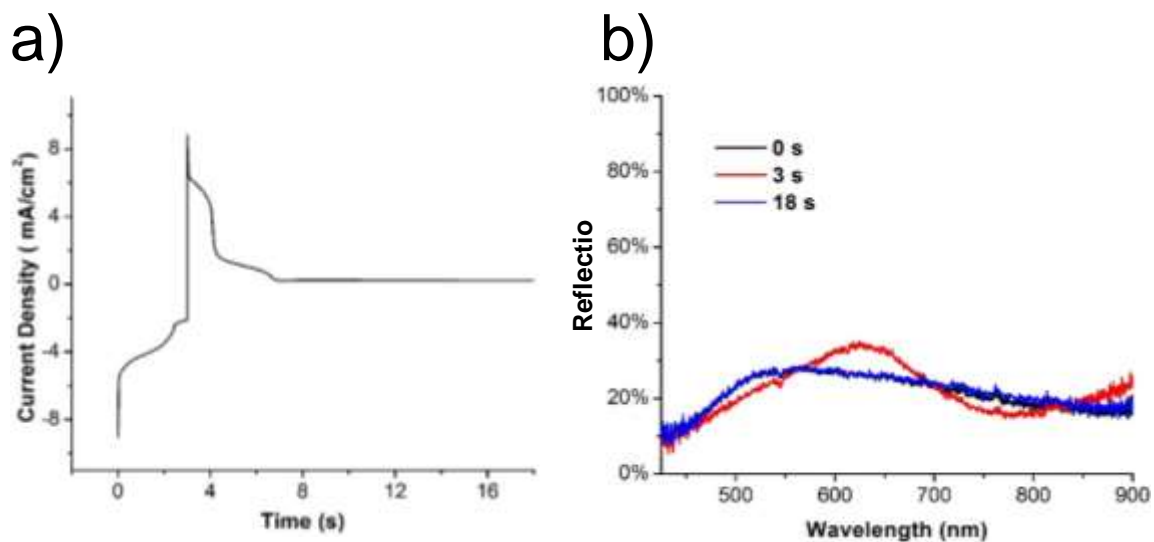


Supporting Figure 12.3.8: Near-infrared transmission of a 3 mm thick sample of the Bi-Cu electrolyte.

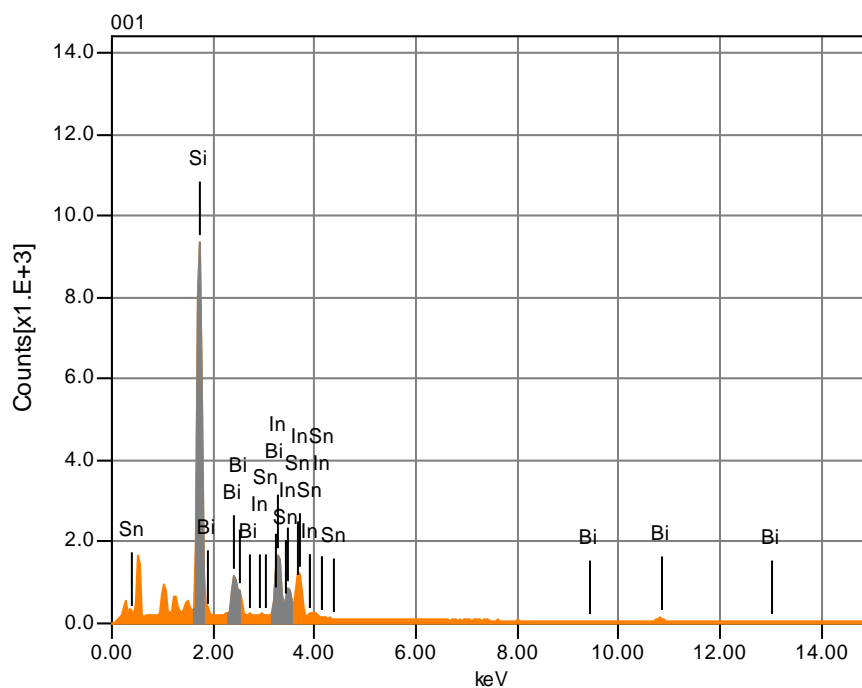


Supporting Figure 12.3.9: Reflection as a function of wavelength of a 25 cm² metal-based dynamic window with one working electrode before switching (black line) and after switching at -0.6 V for 60 s (red line).

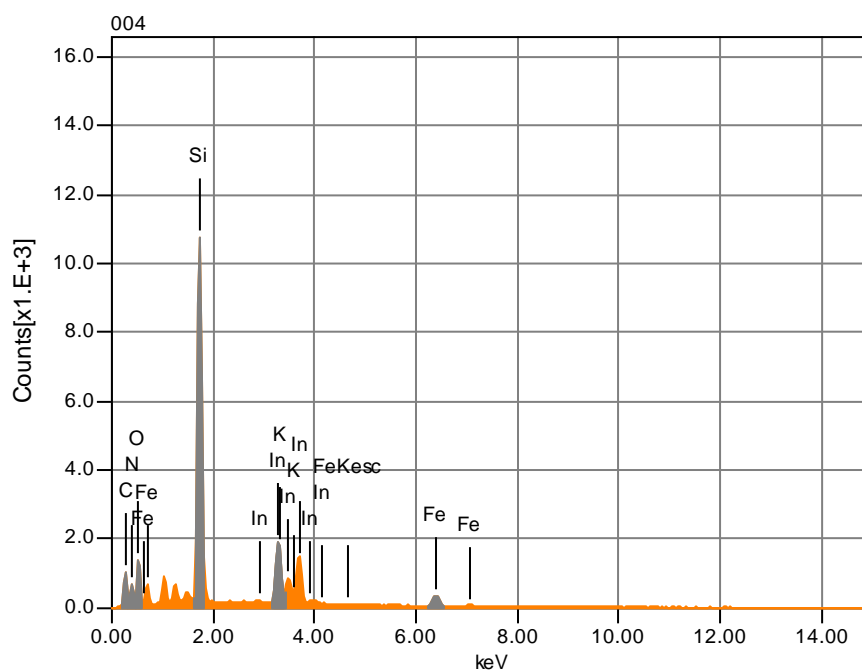
12.4. Supporting information for chapter 5: Dual Tinting Dynamic Windows using Reversible Metal Electrodeposition and Prussian Blue



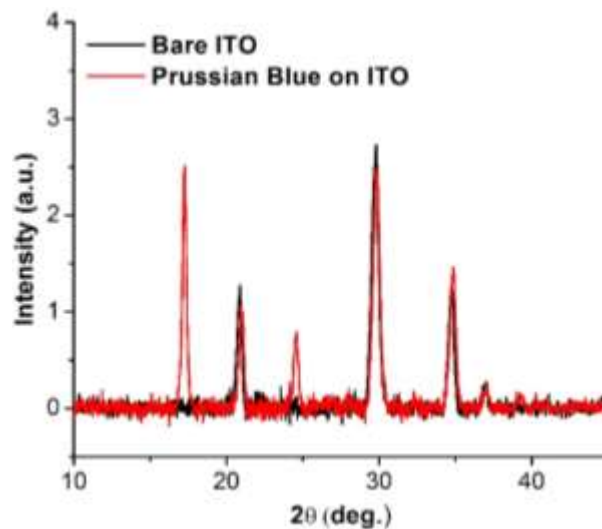
Supporting Figure 12.4.1. Chronoamperometry (a) and reflection (b) of a 25 cm² dynamic window with a Pt-modified ITO on glass working electrode, a Prussian blue on ITO on glass counter electrode formed using 6 minutes of electrodeposition, and a Bi gel electrolyte during 3 s of window tinting at -2 V and 15 s of window lightening at 1.5 V.



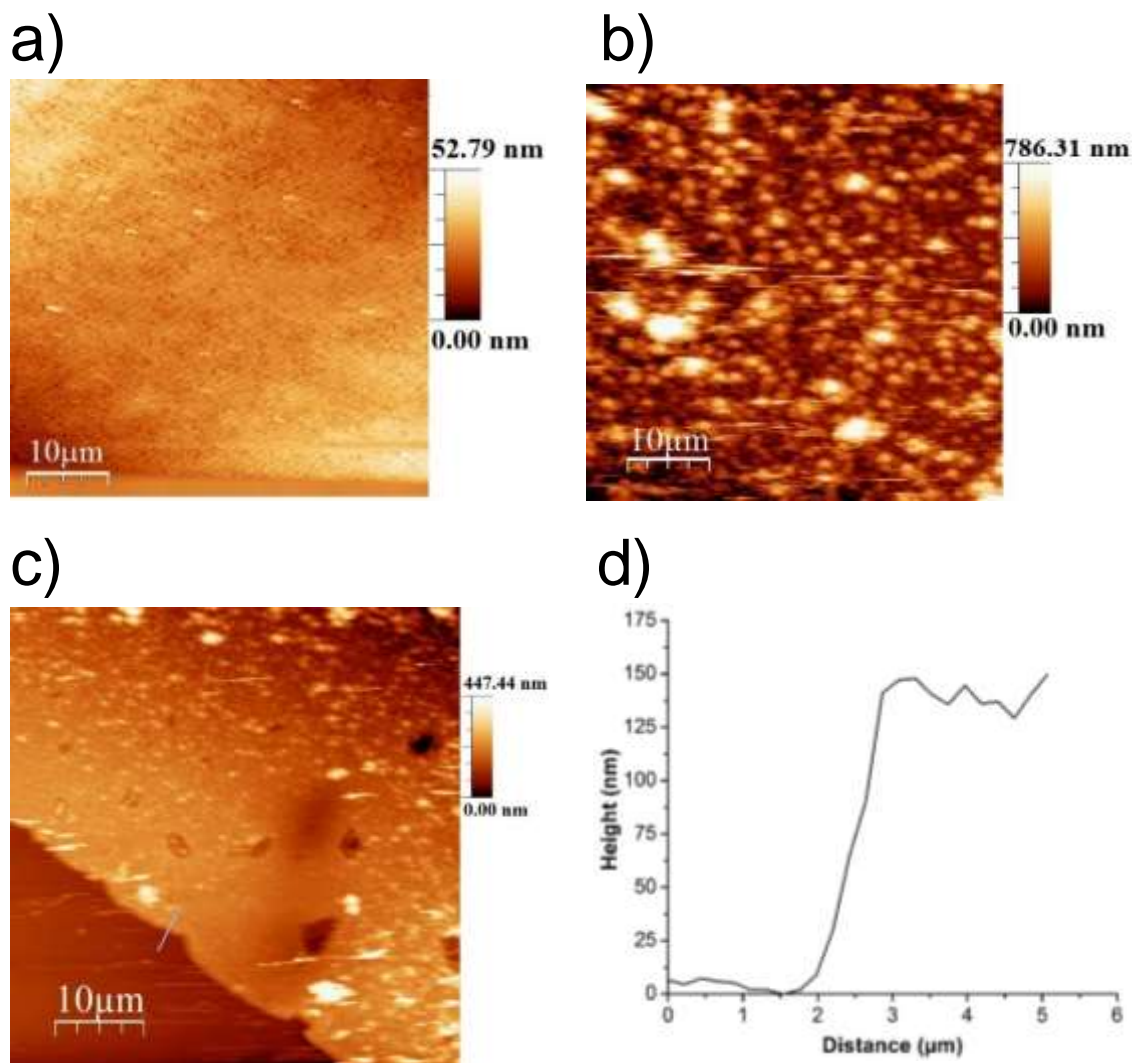
Supporting Figure 12.4.2a. Energy-dispersive X-ray spectrum of Bi electrodeposition on ITO on glass. The In and Sn peaks are from ITO, and the Si peaks from the glass.



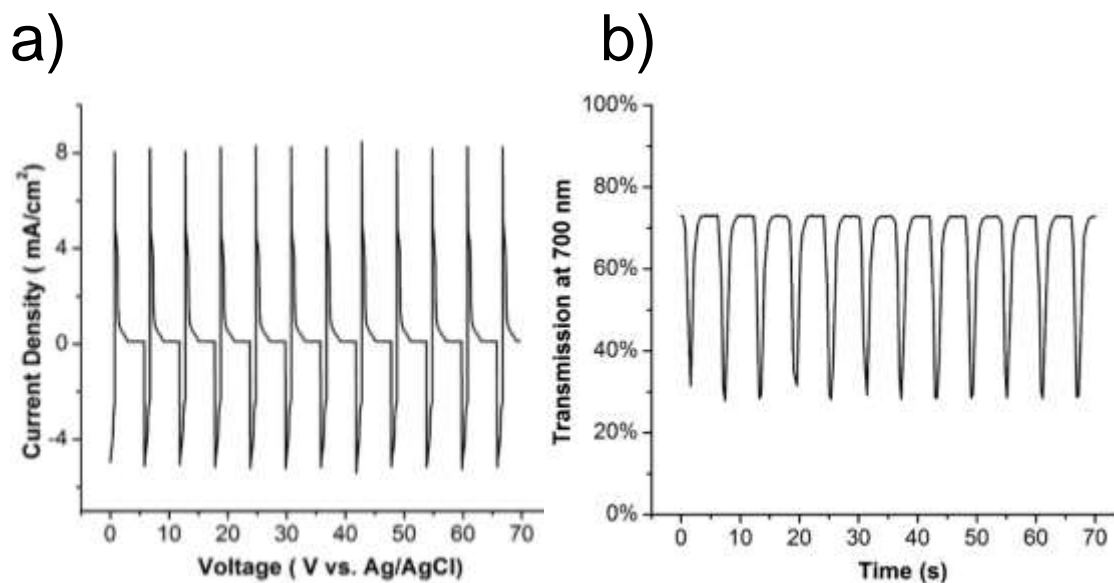
Supporting 12.4.2b. Energy-dispersive X-ray spectrum of the Prussian blue electrodeposited on ITO on glass for 6 minutes. The Fe, K, N, and C peaks are from the Prussian blue. The In and Sn peaks are from ITO, and the Si peaks from the glass.



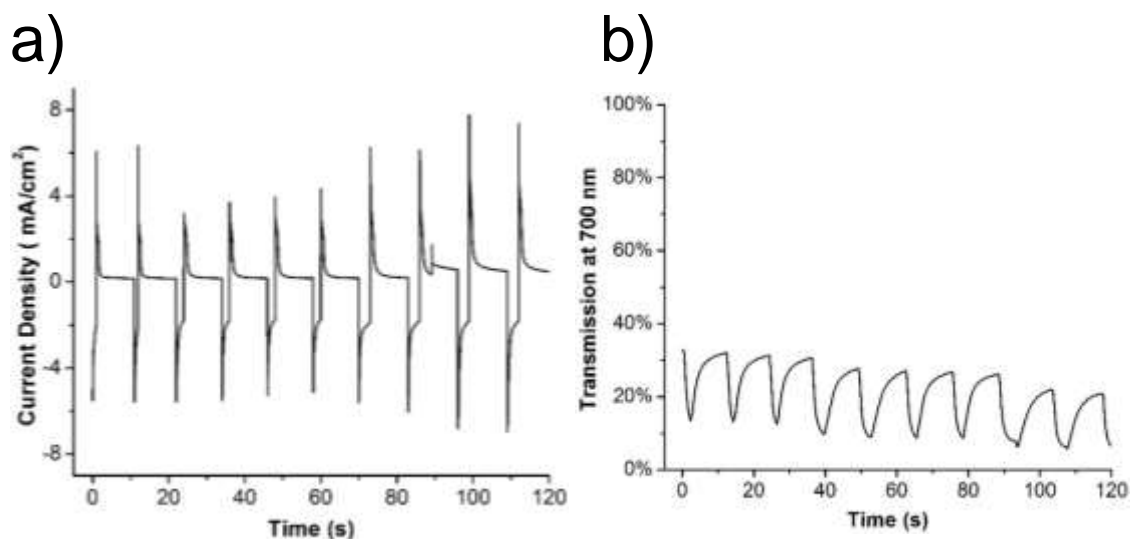
Supporting Figure 12.4.3. X-ray diffraction spectrum of the Prussian blue electrodeposited on ITO on glass for 6 minutes (red line) and of unmodified ITO (black line). The two peaks at 2θ values of 17.3° and 24.6° are not present in the unmodified ITO and are due to the (200) and (220) planes of Prussian blue, respectively, and match previous literature reports for Prussian blue thin films.[239]



Supporting Figure 12.4.4. Atomic force microscopy images of unmodified ITO on glass (a), Prussian blue electrodeposited for 6 minutes on ITO on glass electrodeposited (b), and the interface of Prussian blue and unmodified ITO (c). Panel d displays the height profile across the line drawn across the Prussian blue-ITO interface in panel c. The height profile indicates that Prussian blue thin film is ~150 nm thick.



Supporting Figure 12.4.5. Chronoamperometry (a) and transmission at 700 nm (b) of a 25 cm² dynamic window with a Pt-modified ITO on glass working electrode, a Prussian blue on ITO on glass counter electrode formed using 1 minute of electrodeposition, and a Bi gel electrolyte during 3 s of window tinting at -2 V and 3 s of window lightening at 1.5 V.

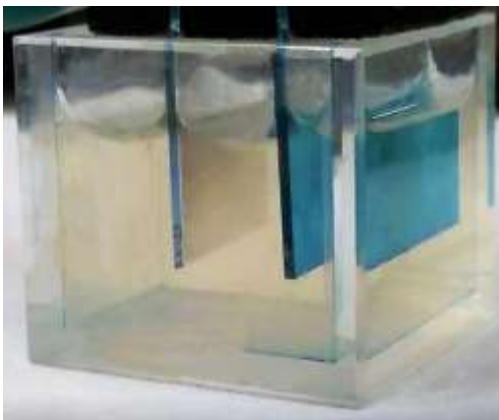


Supporting Figure 12.4.6. Chronoamperometry (a) and transmission at 700 nm (b) of a 25 cm² dynamic window with a Pt-modified ITO on glass working electrode, a Prussian blue on ITO on glass counter electrode formed using 10 minutes of electrodeposition, and a Bi gel electrolyte during 3 s of window tinting at -2 V and 9 s of window lightening at 1.5 V.

a)

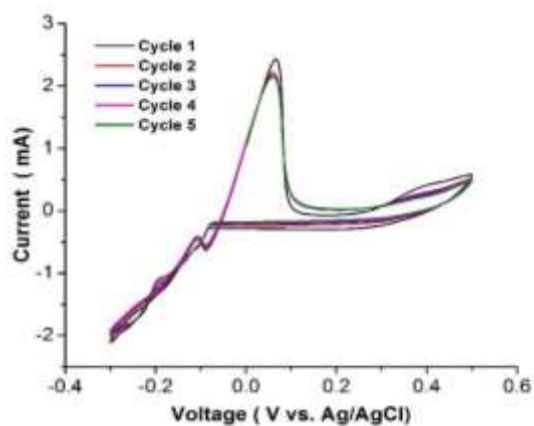


b)

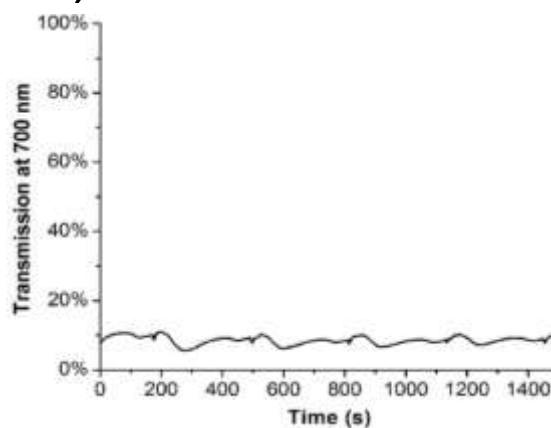


Supporting Figure 12.4.7. Photographs of a 2 cm² with a Pt-modified ITO on glass working electrode, a Prussian blue on ITO on glass counter electrode formed using 6 minutes of electrodeposition switching at -2 V for 0 s (a) and 3 s (b) in a liquid Bi electrolyte.

a)

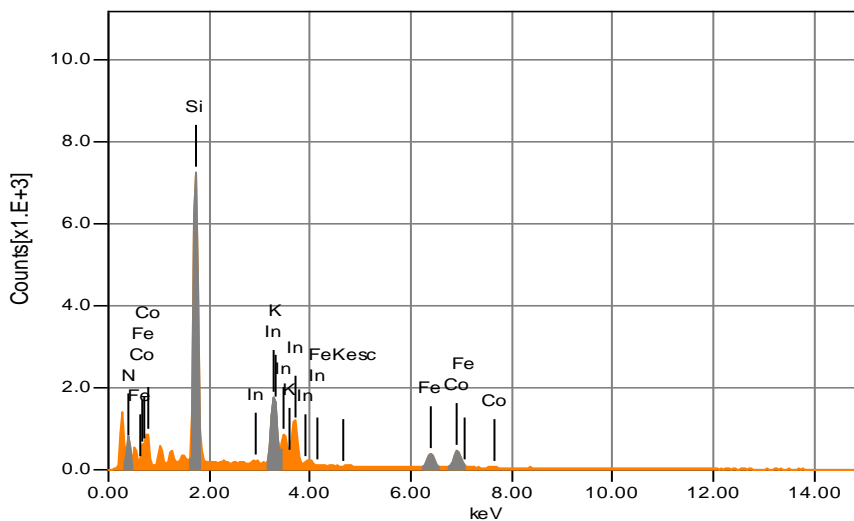


b)

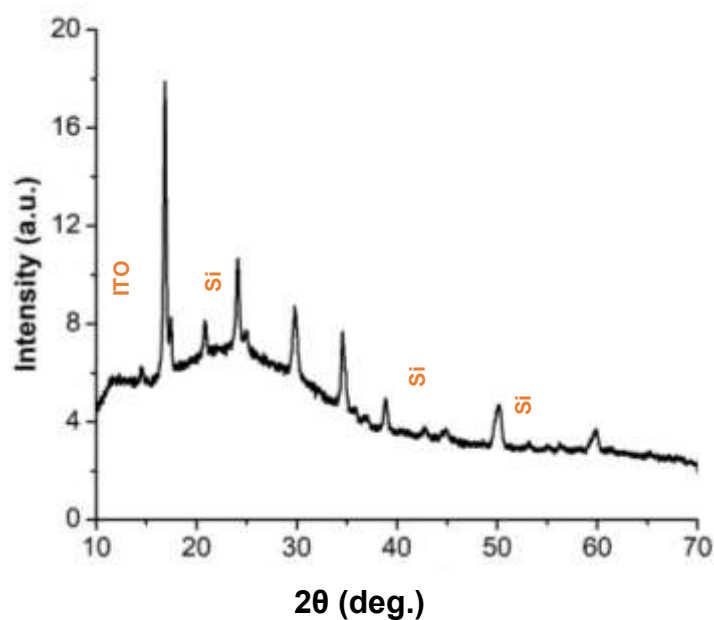


Supporting Figure 12.4.8. Cyclic voltammograms (a) and corresponding transmission at 700 nm (b) of Prussian blue on ITO on glass working electrode in the Bi-Cu electrolyte in a three-electrode cell at a scan rate of 5 mV/s.

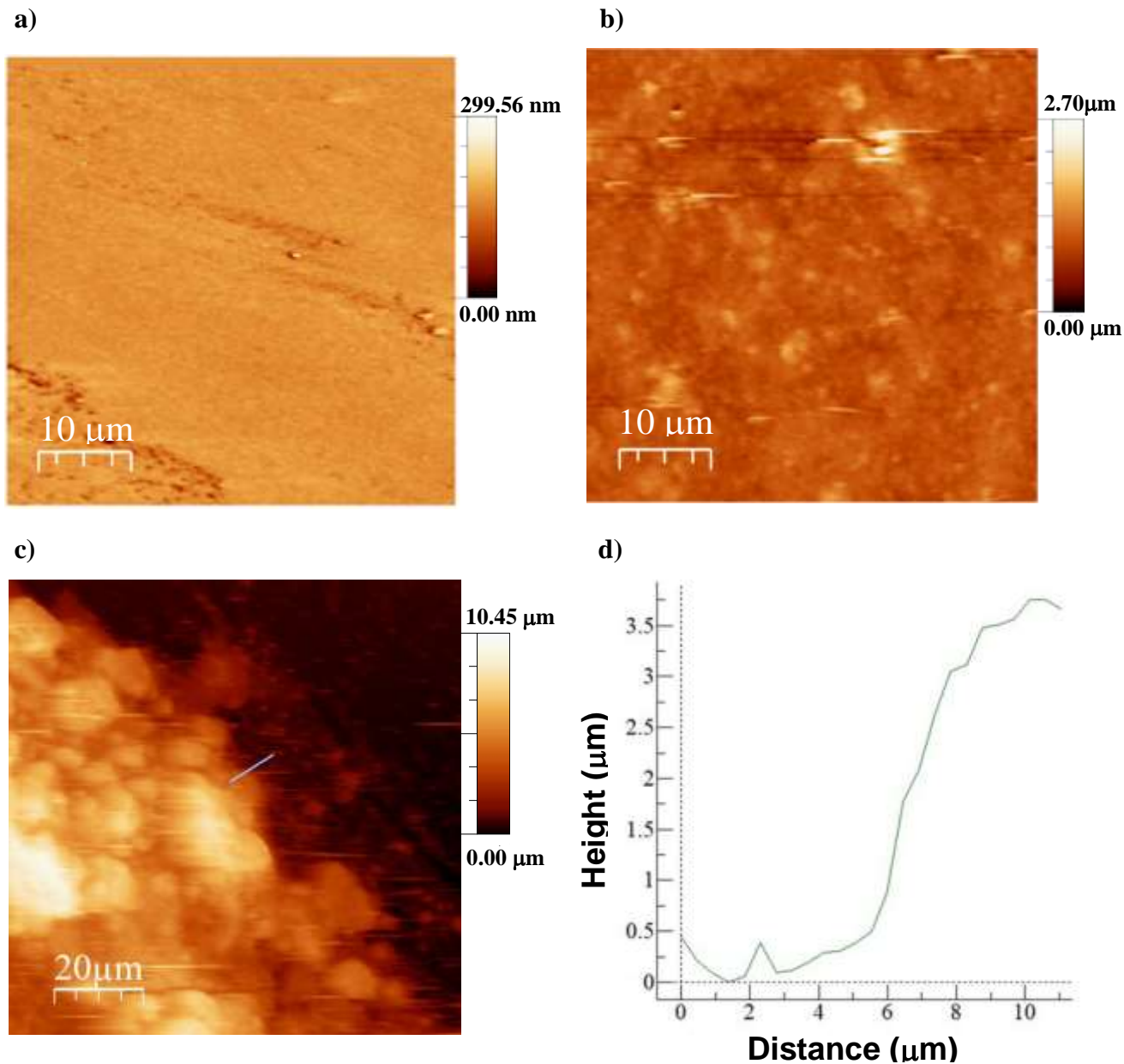
12. 5. Supporting Information for Chapter 7: Hybrid Dynamic Windows with Color Neutral and Fast Switching using Reversible Metal Electrodeposition and Cobalt Hexacyanoferrate Electrochromism



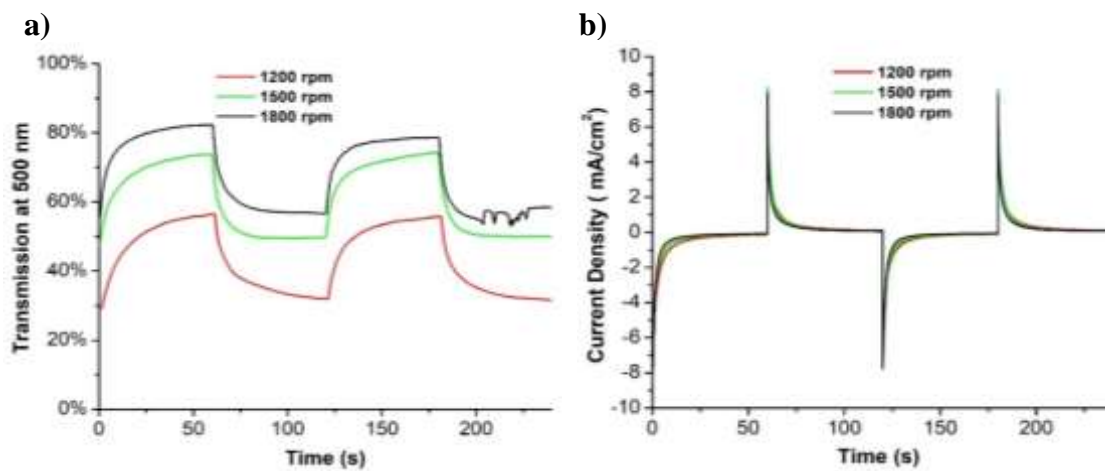
Supporting Figure 12.5.1: Energy-dispersive X-ray spectrum of a CoHCF on ITO on glass. The In peaks are from ITO, and the Si peaks are from the glass.



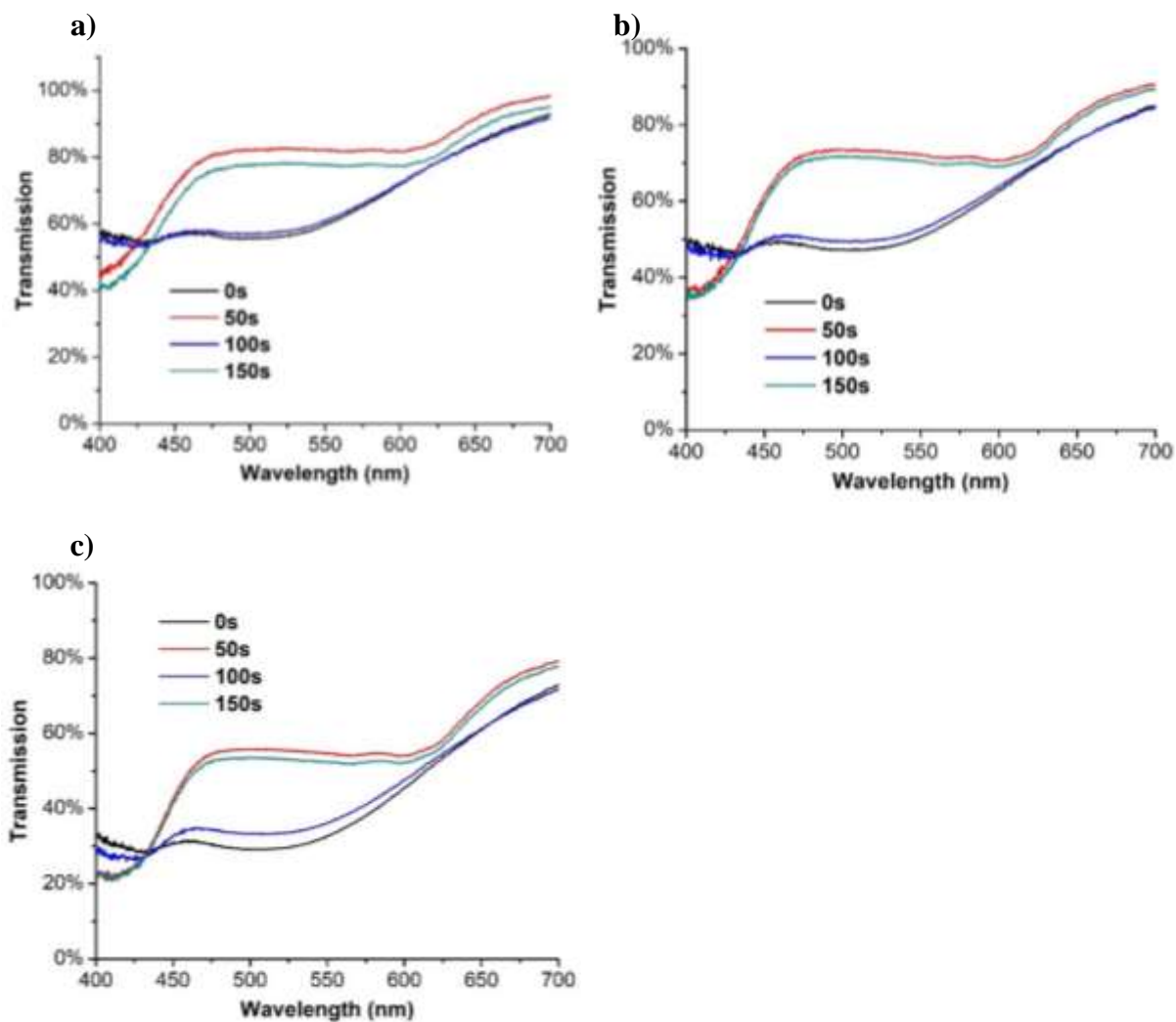
Supporting Figure 12.5.2. X-ray diffraction spectrum of the CoHCF on ITO on glass. The four peaks at 2θ values of 17.4° , 24.6° , 35.1° , and 39.3° are due to the (200), (022), (004), and (042) planes of CoHCF respectively, which match previous literature reports for CoHCF thin films. [110]



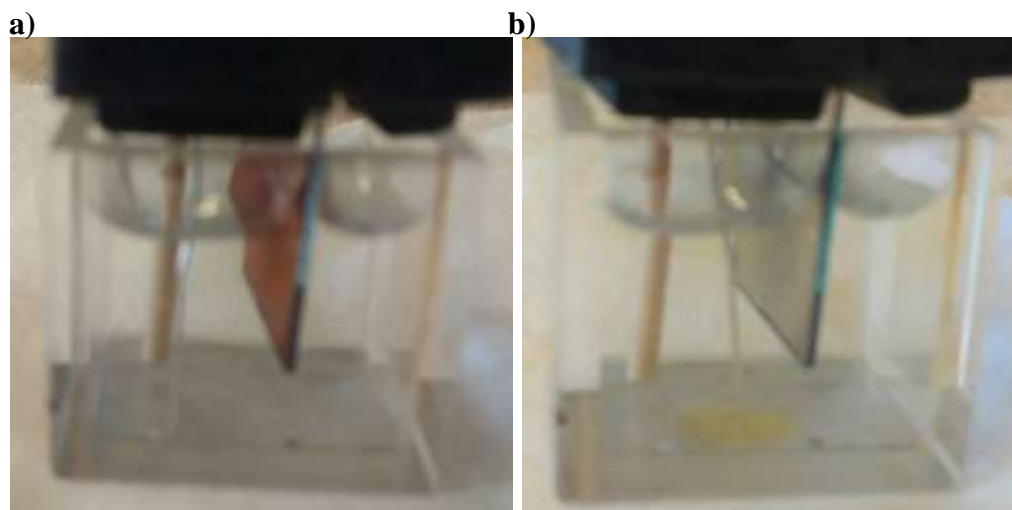
Supporting Figure 12.5.3: Atomic force microscopy images of unmodified ITO on glass (a), CoHCF on ITO spin-coated at 1500 rpm (b), and the interface of CoHCF and unmodified ITO (c). Panel (d) displays the height profile across the line drawn on the CoHCF-ITO interface in panel (c). The height profile indicates that CoHCF film is ~ 3.5 μm thick.



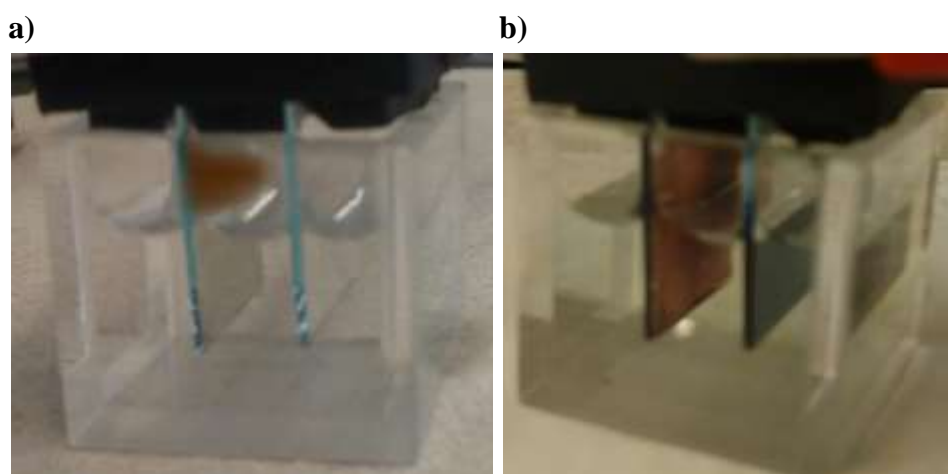
Supporting Figure 12.5.4: Transmission at 500 nm (a) and chronoamperometry (b) of 3 cm² dynamic windows with Pt-modified ITO on glass working electrode, a CoHCF on ITO on glass counter electrode formed using Bi-Cu-NaBr liquid electrolytes during 60 s of window clearing at 0 V and 60 s of window tinting at 1.0 V.



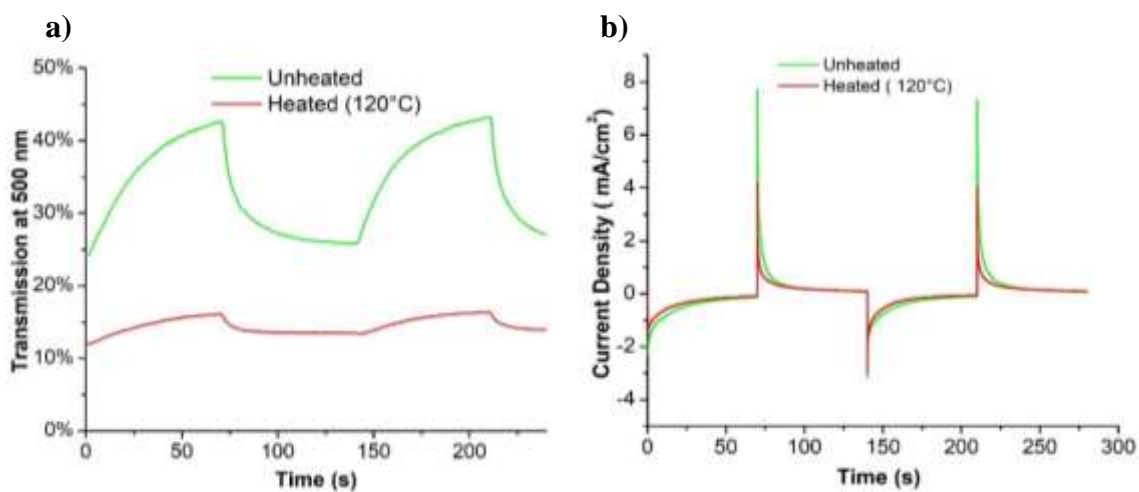
Supporting Figure 12.5.5: Transmission of 3 cm² dynamic windows with Pt-modified ITO on glass working electrode, a CoHCF on ITO on glass counter electrode at 1200 rpm (a), 1500 rpm (b), and 1800 rpm (c) formed using Bi-Cu-NaBr liquid electrolytes during 50 s of window clearing at 0 V and 50 s of window tinting at 1.0 V.



Supporting Figure 12.5.6: Photographs of a 3 cm² CoHCF on ITO on glass working electrode, Pt-wire counter electrode, and a Ag/AgCl reference electrode switching at -0.75 V for 0 s (a) and 30 s (b) in a liquid 1M NaBr electrolyte.



Supporting Figure 12.5.7: Photographs of a 3 cm² dynamic window with a Pt-modified ITO on glass working electrode, a Na-ion intercalated CoHCF on ITO on glass counter electrode switching at -2.5 V for 0 s (a) and 10 s (b) in a liquid Bi-Cu-NaBr electrolyte.



Supporting Figure 12.5.8: Transmission at 500 nm (a) and chronoamperometry (b) of 3 cm² dynamic windows with Pt-modified ITO on glass working electrode, a CoHCF on ITO on glass counter electrode formed using Bi-Cu-NaBr liquid electrolytes during 70 s of window clearing at 0 V and 70 s of window tinting at 1.0 V.

12.6: Supporting Information for chapter 8: Aqueous Alkaline Electrolytes for Dynamic Windows based on Reversible Metal Electrodeposition with Improved Durability

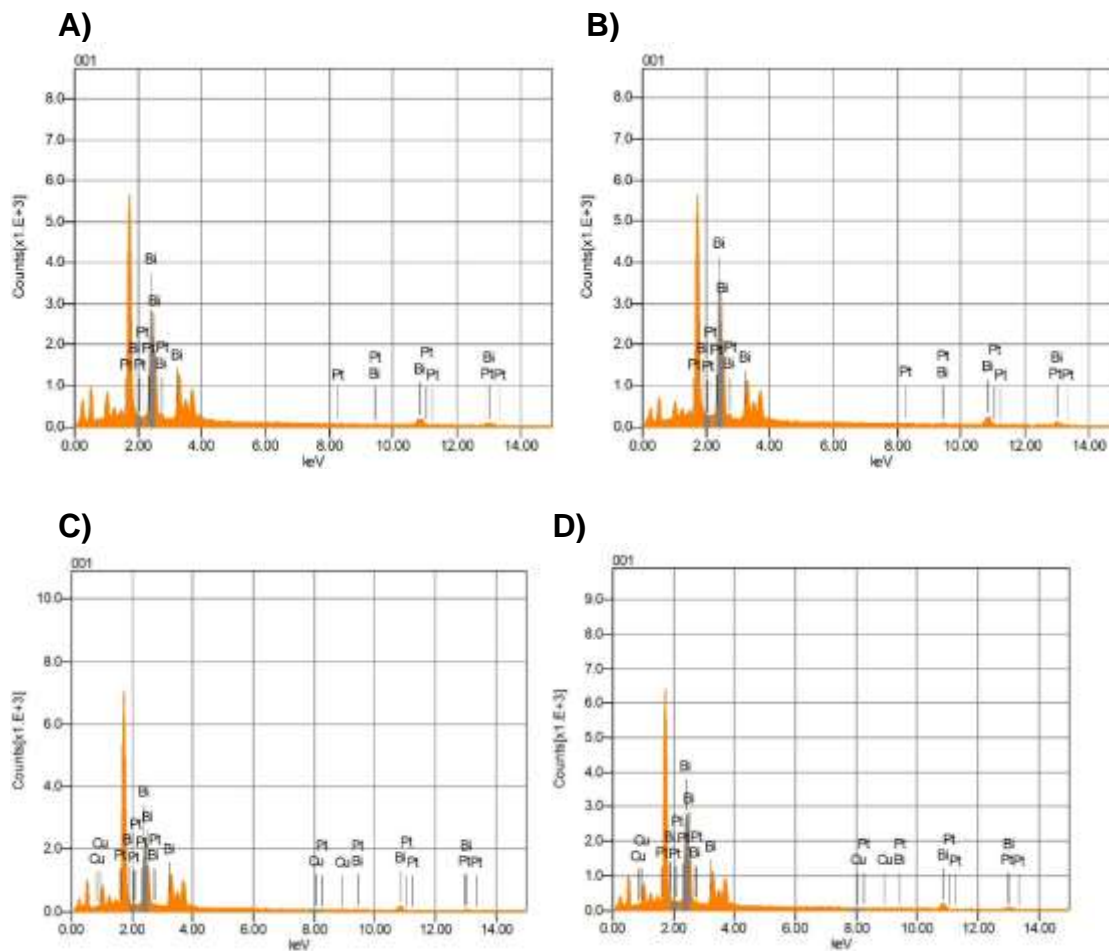


Figure 12.6.1: Energy-dispersive X-ray spectra of metal electrodeposits on Pt-modified ITO on glass working electrodes electrodeposited from an electrolyte containing 120 mM $\text{Bi}(\text{NO}_3)_2$, 1.5 M EDTA, and 2.0 M NaI adjusted to pH 8.5 with HCl without (A, B, Solution I) and with 5 mM CuCl_2 (C, D, Solution F). Electrodeposition was performed at -0.9 V for 30 s (A, C) or 60 s (B, D). The corresponding scanning electron microscopy images are displayed in Figure 7 in the main text.

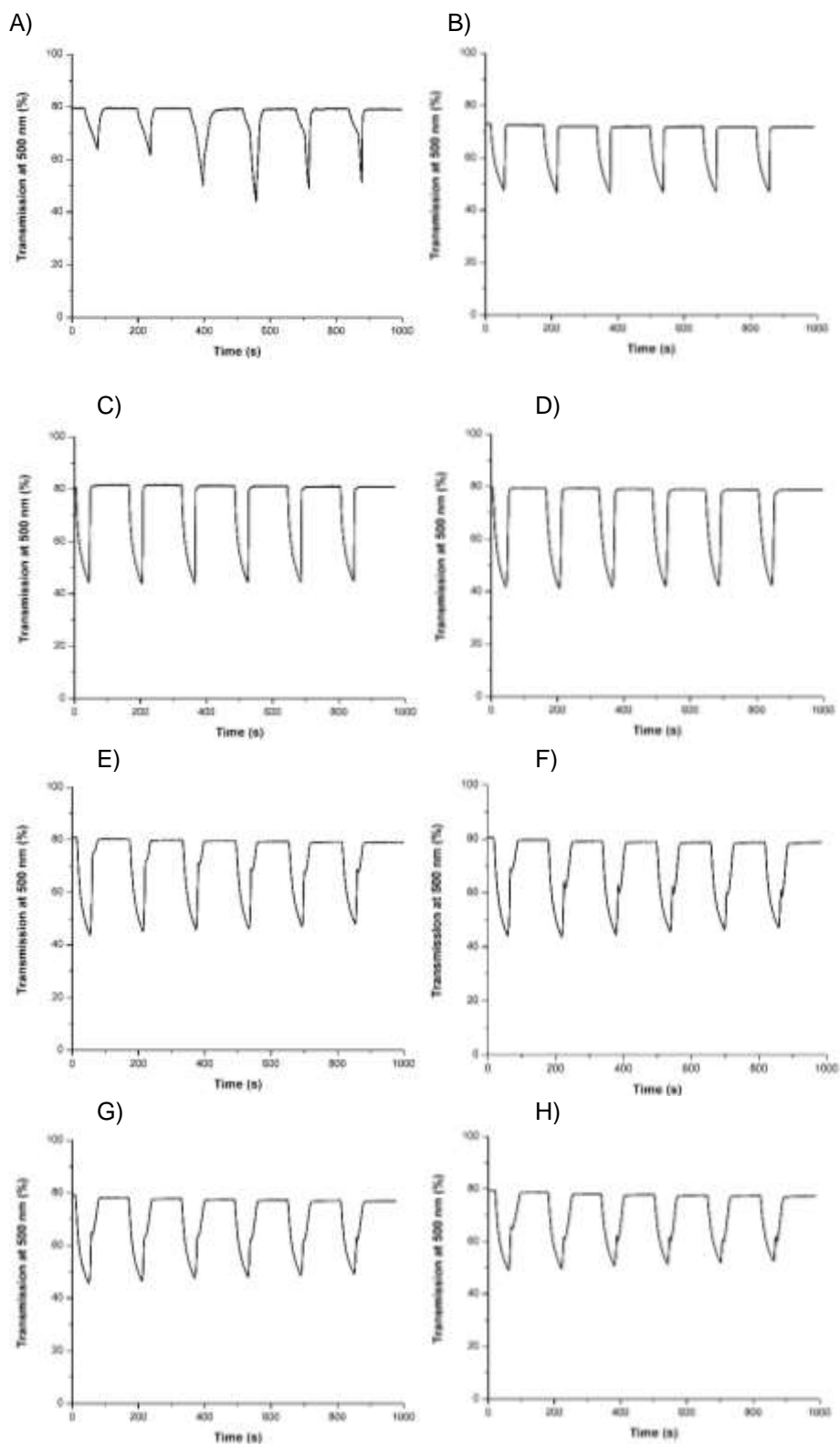
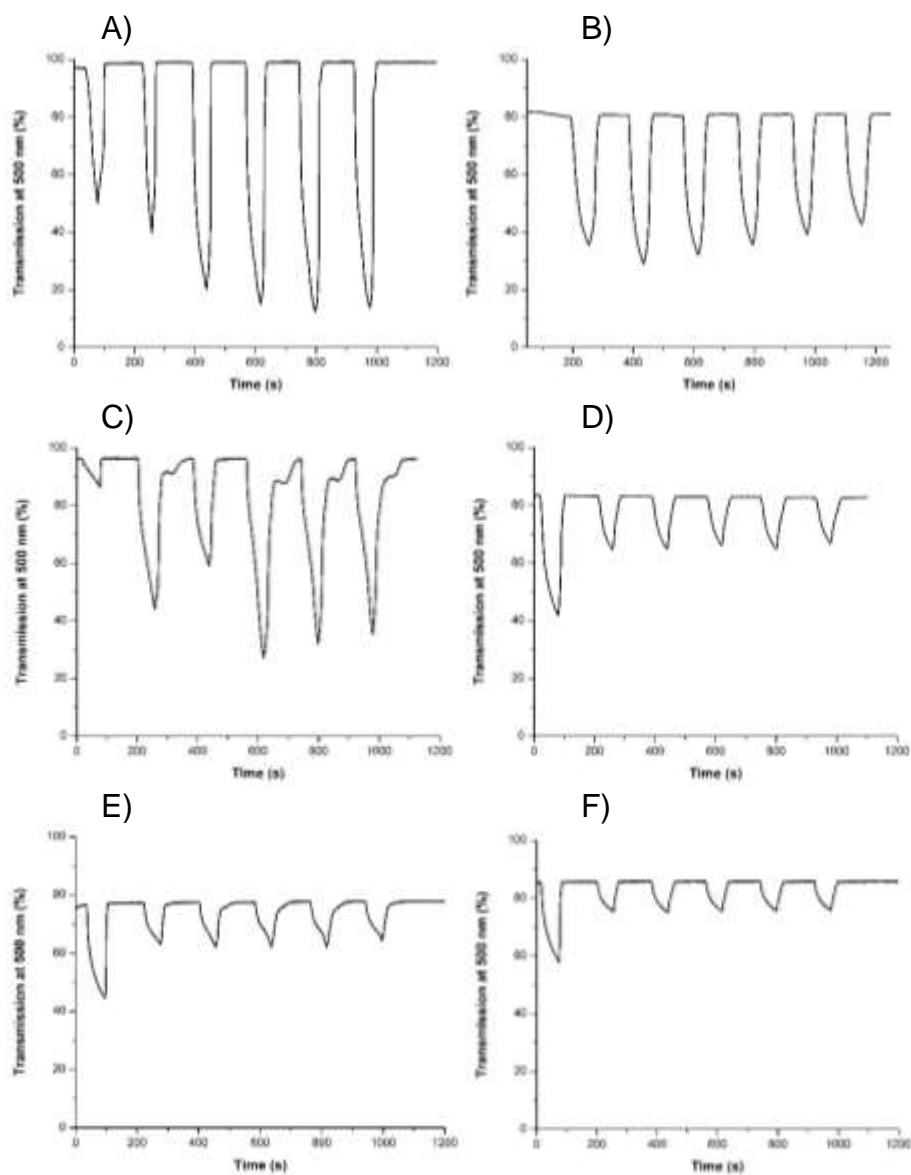


Figure 12.6.2: Transmission at 500 nm of a 25 cm² dynamic window using the EDTA Bi-Cu electrolyte (Solution F) during six cycles of chronoamperometry at -0.9 V for 40 s

followed by +0.8 V for 120 s after resting at open circuit potential for 0 (A), 1 (B), 2 (C), 3 (D), 4 (E), 5 (F), 6 (G), and 7 (H) days. The data points in Figure 10 in the main text are derived by taking the average contrast ratios across each six cycles for each day.



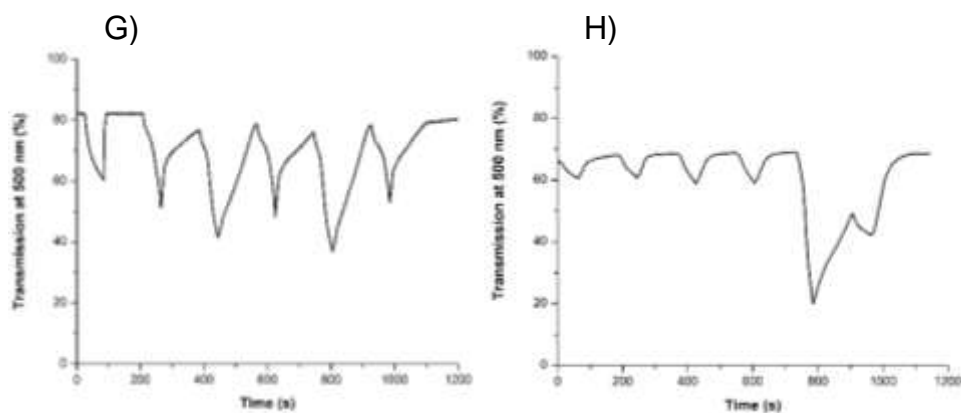


Figure 12.6.3: Transmission at 500 nm of a 25 cm² dynamic window using the acidic Bi-Cu electrolyte during six cycles of chronoamperometry at -0.6 V for 60 s followed by +0.8 V for 120 s after resting at open circuit potential for 0 (A), 1 (B), 2 (C), 3 (D), 4 (E), 5 (F), 6 (G), and 7 (H) days. The data points in Figure 10 in the main text are derived by taking the average contrast ratios across each six cycles after 0-5 days of rest. Because the transmission of the window on after six days of rest was irreversible after the first cycle, the contrast ratio plotted in Figure 10 (red point) for the sixth day is equal to the contrast during the first cycle.

12.7. Supporting Information for Chapter 9: Dynamic Windows using Reversible Zn Electrodeposition in Neutral Electrolytes with High Opacity and Excellent Resting Stability





Deposition Time (s)	Lightness (L*)	Green-red coordinate (a*)	Blue-yellow coordinate (b*)	Color neutrality (C*)	Best RGB representation
0	78	0.6	0.8	1.0	
10	40	4	8	9	
15	11	3	9	9	
30	0.02	1.0	3	3	

Figure 12.7.1: $L^*a^*b^*C^*$ values along with the best RGB color representations of the transmission of a 25 cm² dynamic window with an ITO on glass working electrode, a Zn mesh counter electrode, and a Zn acetate gel electrode during window darkening.

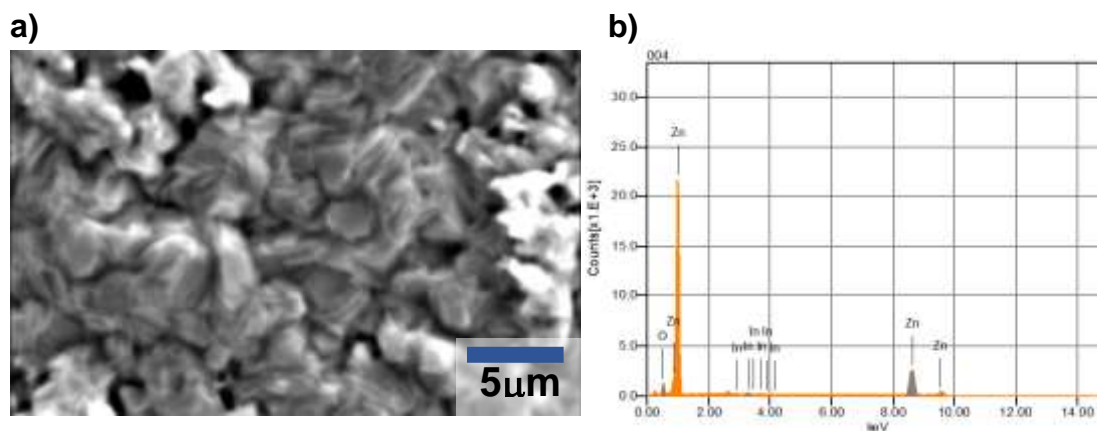


Figure 12.7.2: SEM image (a) and corresponding EDX spectrum (b) of an ITO working electrode after the application of -1V in a dynamic window. Peaks for In are due to the presence of ITO.

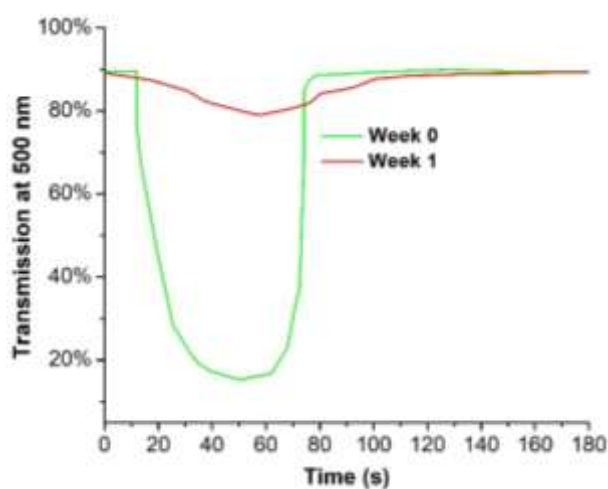


Figure 12.7.3: Transmission of a 25 cm² dynamic window with an ITO on glass working electrode, a Cu counter electrode, and an acidic Bi-Cu gel electrolyte during switching. The device was switched at week 0 and week 1. The window was darkened at -0.6 V for 60 s and lightened at +0.8 V for 120 s.

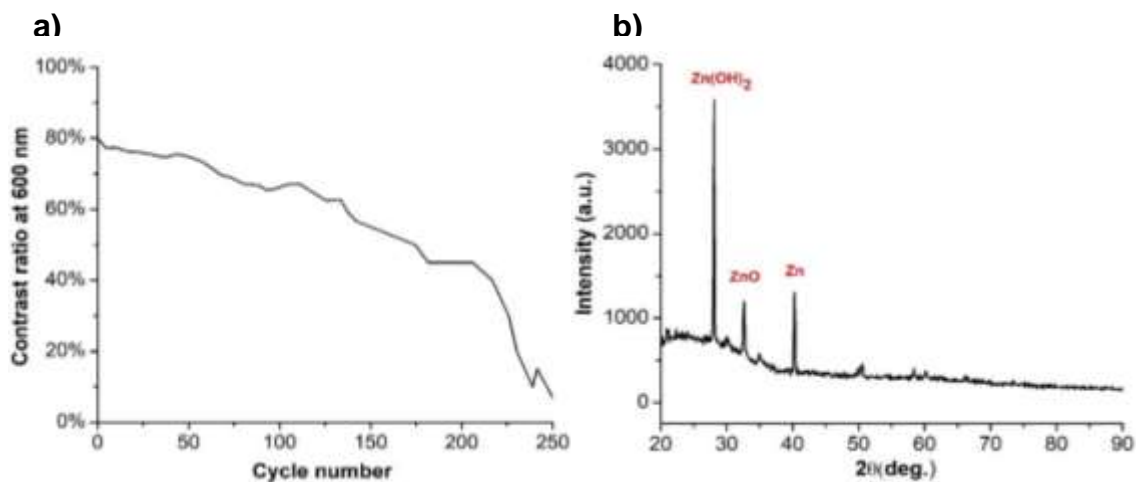


Figure 12.7.4: (a) Contrast ratio at 600 nm of a 25 cm² dynamic window with an ITO on glass working electrode, a Zn counter electrode, and a Zn acetate gel electrolyte during cycling over the course of 250 cycles. (b) XRD spectrum of the ITO working electrode after 250 cycles showing the accumulation of ZnO and Zn(OH)₂.

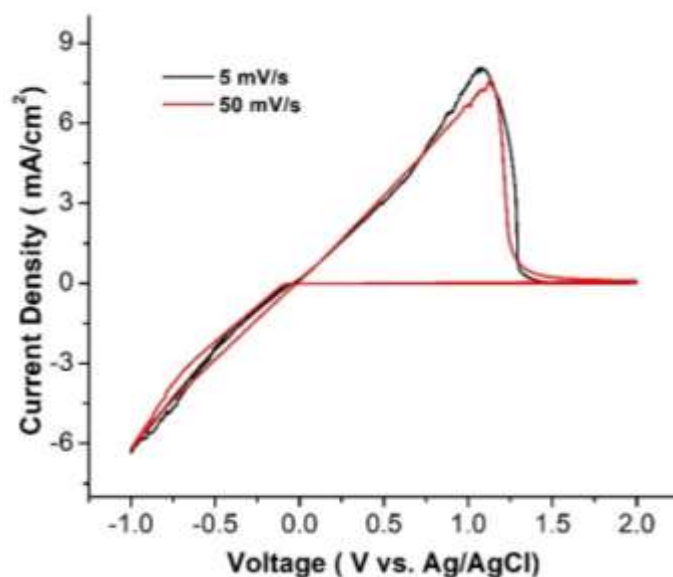


Figure 12.7.5: Cyclic voltammograms at a scan rate of 5 mV/s (black) and 50 mV/s (red) of a 25 cm² dynamic window with an ITO on glass working electrode and a Zn metal frame as the counter and reference electrodes with a 0.5 M Zn acetate gel electrolyte.

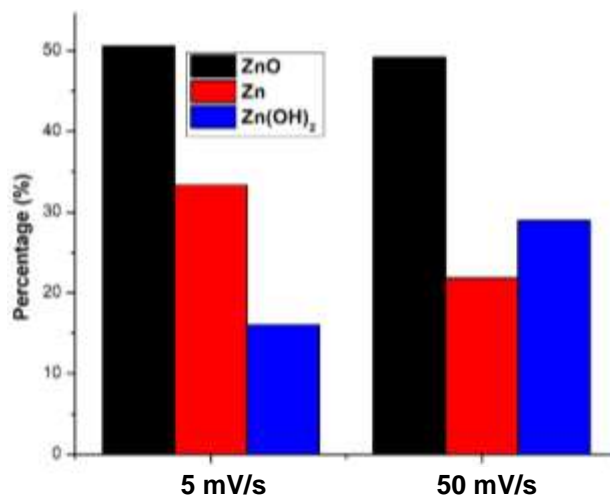


Figure 12.7.6: Compositional analysis obtained from XRD measurements of dynamic windows with an ITO on glass working electrode and a Zn frame as the counter and reference electrodes with a 0.5 M Zn acetate gel electrolyte. XRD data were obtained after performing LSVs at 5 mV/s or 50 mV/s from 2 V to -1 V.

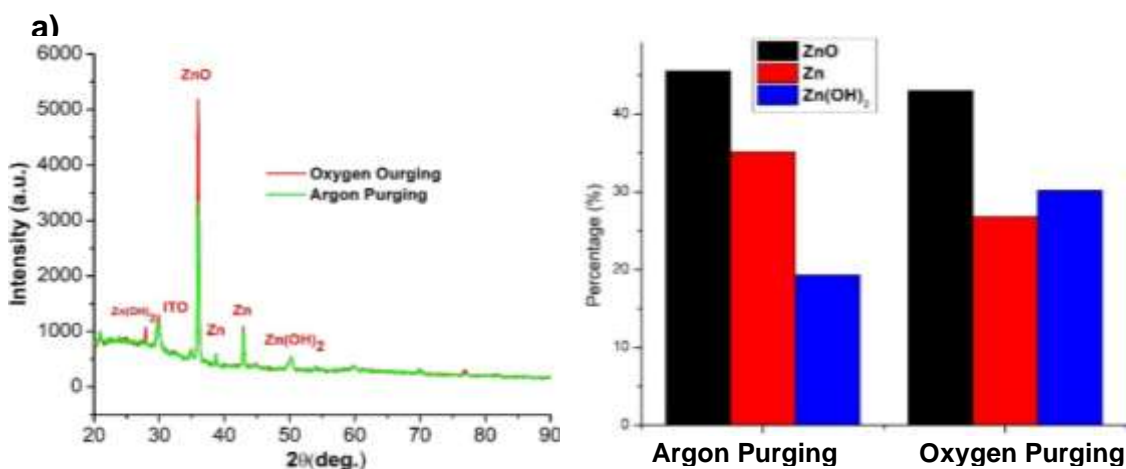


Figure 12.7.7: XRD spectrum of the working electrode of a dynamic window with an ITO on glass working electrode, a Zn metal counter/reference electrode, and 0.5 M Zn acetate gel electrolyte after linear sweep voltammetry at 25 mV/s from 2 V to -1 V (a). The electrolytes were bubbled with O₂ (red line) or Ar (green line) for 1 hr before performing the voltammetry. Compositional analysis from the XRD spectra (b).

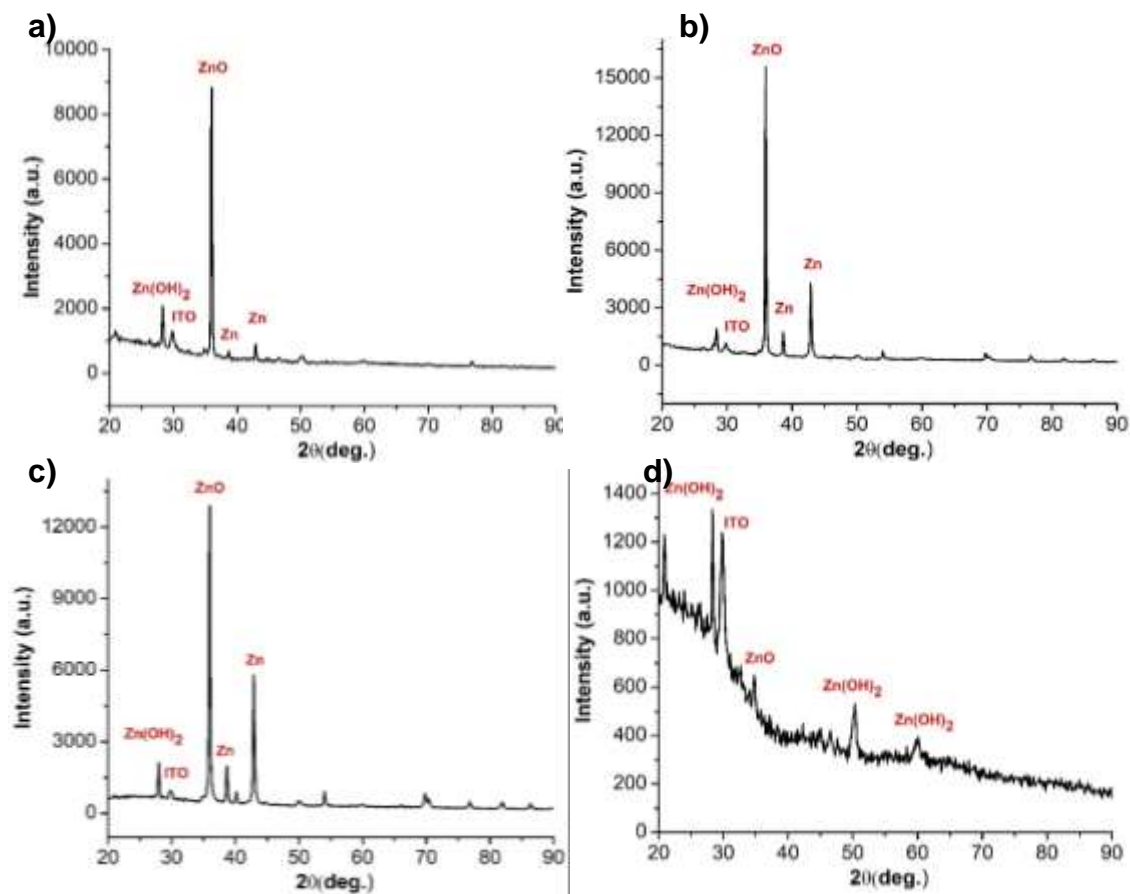


Figure 12.7.8: XRD spectra of a dynamic window with an ITO on glass working electrode, a Zn metal counter/reference electrode, and a 0.5 M Zn acetate gel electrolyte after voltammetry at 5 mV/s from (a) 2 V to -0.46 V (b) 2 V to -1 V (c) 2 V to -1 V to 0.5 V (d) 2 V to -1 V to 1.45 V.

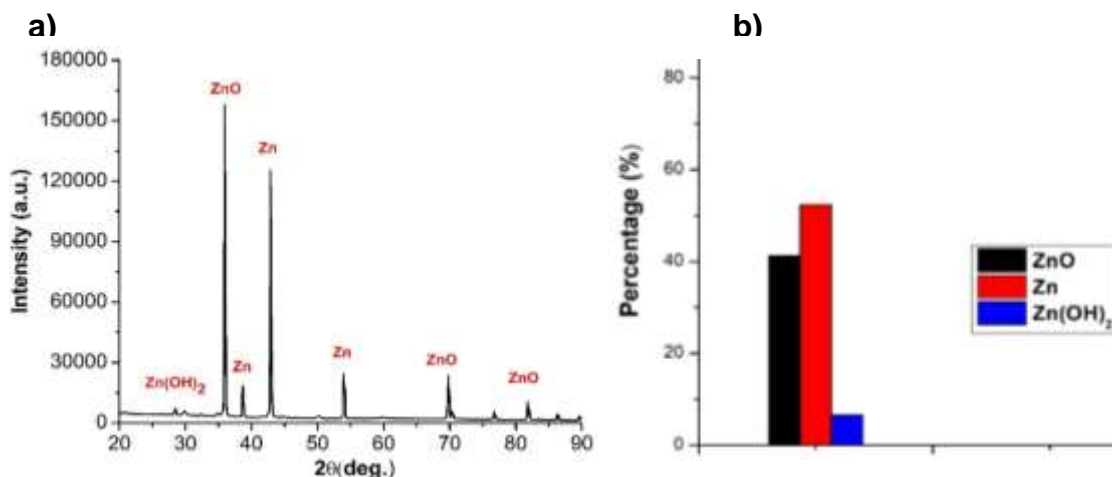


Figure 12.7.9: (a) XRD spectrum of the working electrode of a dynamic window with an ITO on glass working electrode, a Zn metal counter/reference electrode, and a 0.5 M Zn acetate gel electrolyte after chronoamperometry at -1 V for 15 s. (b) Percentage of Zn, ZnO, and Zn(OH)₂ during of the electrodeposits as determined from the XRD spectrum.

12.8. Supporting Information for Chapter 10: Electrolytes for Reversible Zinc Electrodeposition for Dynamic Windows

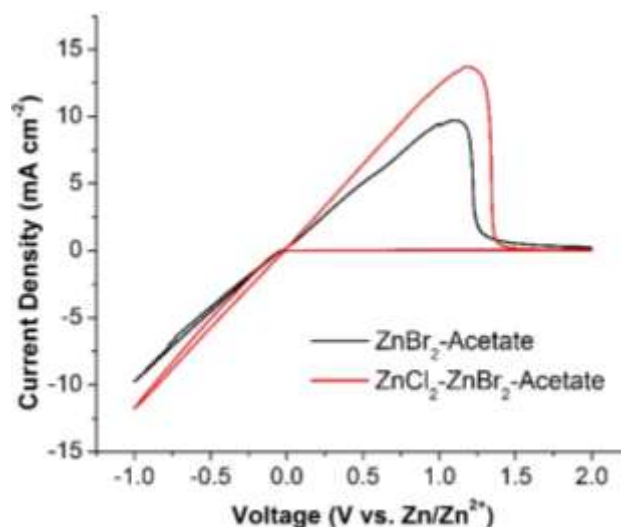


Figure 12.8.1: Cyclic voltammogram at a scan rate of 25 mV s⁻¹ of Pt-modified ITO working electrodes in electrolytes containing 0.5 M sodium acetate and 0.5 M ZnBr₂ (black line) or 0.25 M ZnCl₂ and 0.25 M ZnBr₂.

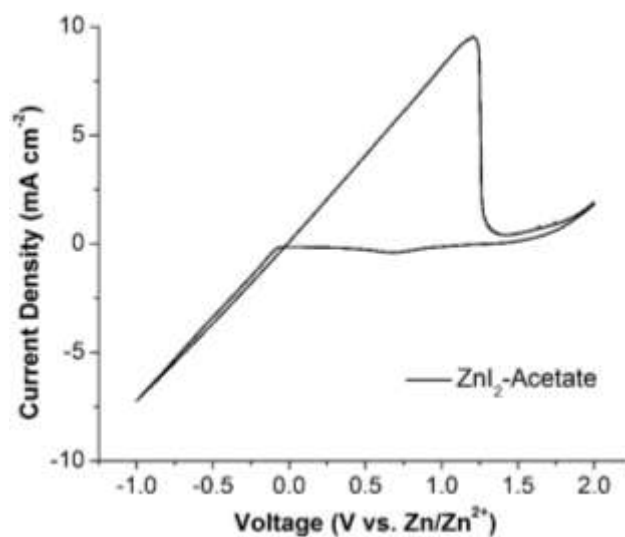


Figure 12.8.2: Cyclic voltammogram at a scan rate of 25 mV s^{-1} of a Pt-modified ITO working electrode in an electrolyte containing 0.5 M ZnI_2 and 0.5 M sodium acetate.

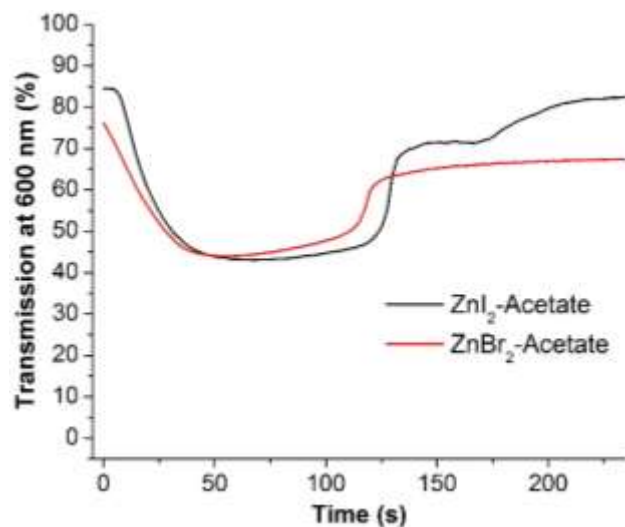


Figure 12.8.3: Transmission at 600 nm of the working electrode during the second cycle of CVs in an electrolyte containing 0.5 M sodium acetate and 0.5 M ZnI_2 (black line) or ZnBr_2 (red line). The corresponding CVs are displayed in Supporting Figure 12.8.1 and 12.8.2.

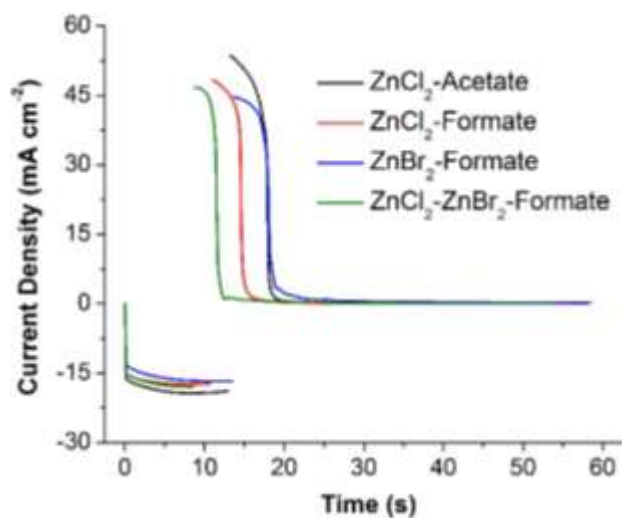


Figure 12.8.4: Chronoamperometry during Zn electrodeposition and stripping in electrolytes containing 0.5 M sodium acetate and 0.5 M ZnCl₂ (black line), or 0.5 M sodium formate and 0.5 M ZnCl₂ (red line), 0.5 M ZnBr₂ (blue line), or 0.25 M ZnCl₂ and 0.25 M ZnBr₂ (green line). To elicit Zn electrodeposition, chronoamperometry was conducted at -1.0 V until the transmission at 600 nm reached 1%. Next, Zn stripping was conducted at +2.5 V.

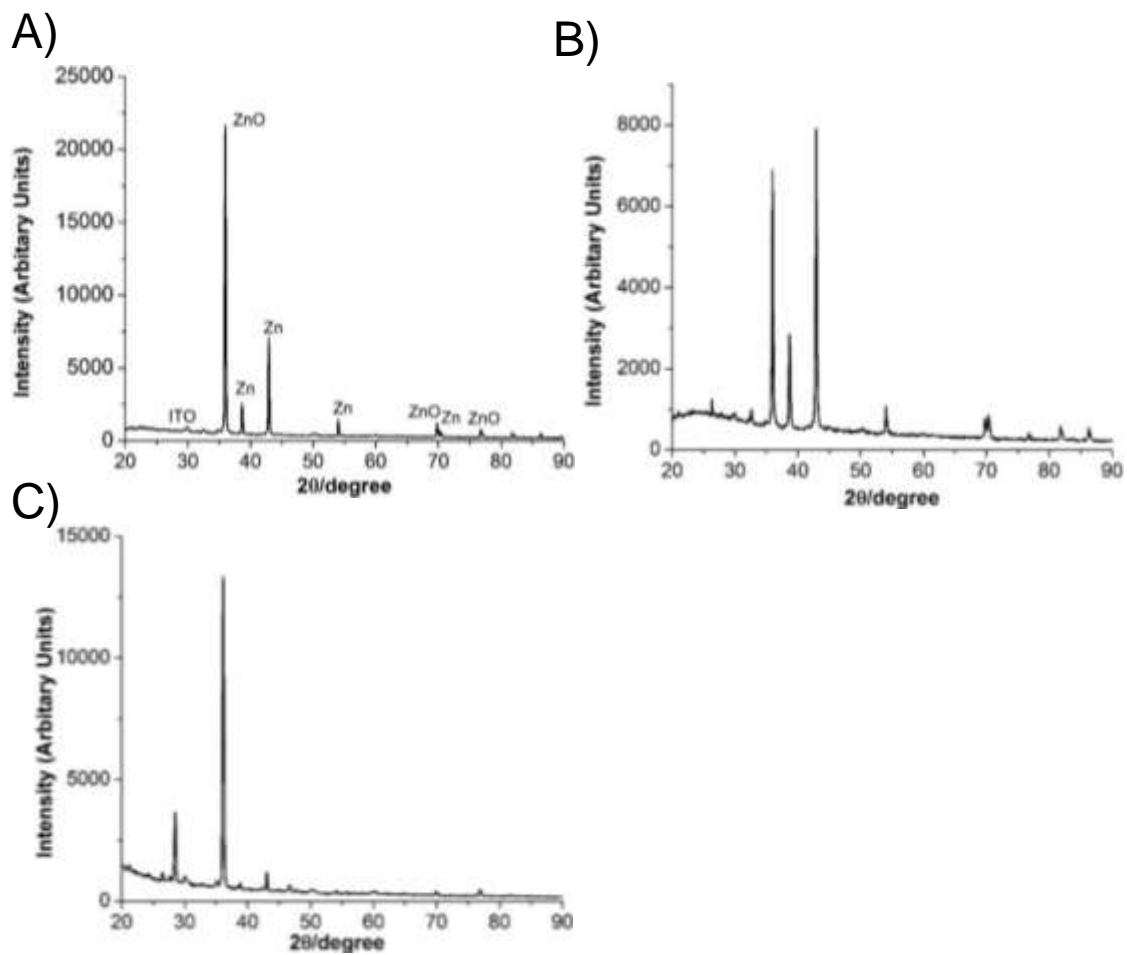


Figure 12.8.5: Representative X-ray diffraction spectra of Zn electrodeposits obtained after a linear sweep voltammogram from 0 V to -1 V at 5 mV s^{-1} in an electrolyte containing 0.5 M sodium formate and 0.5 M ZnCl_2 (A), 0.5 M ZnBr_2 (B), or 0.25 M ZnCl_2 and 0.25 M ZnBr_2 (C).

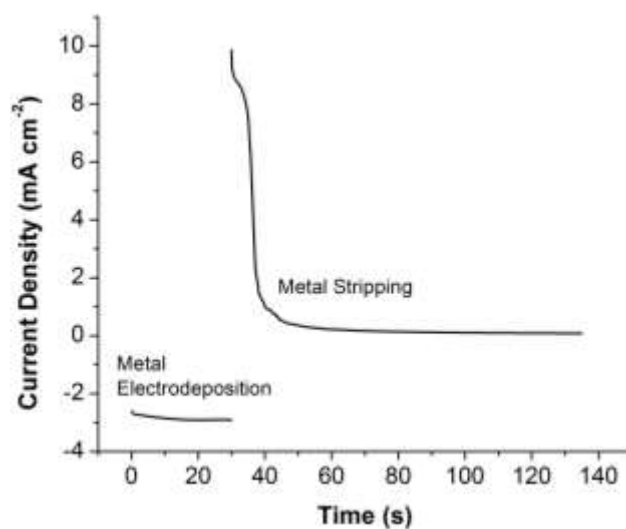


Figure 12.8.6: Chronoamperometry during switching of 25 cm² dynamic window based on reversible Zn electrodeposition. Metal electrodeposition on the working electrode was elicited by applying -0.8 V for 30 s before +2.3 V was applied to induce metal stripping.

12.9. Supplementary Information for Chapter 11: Nanographene Cathode Materials for Nonaqueous Zn-ion Batteries

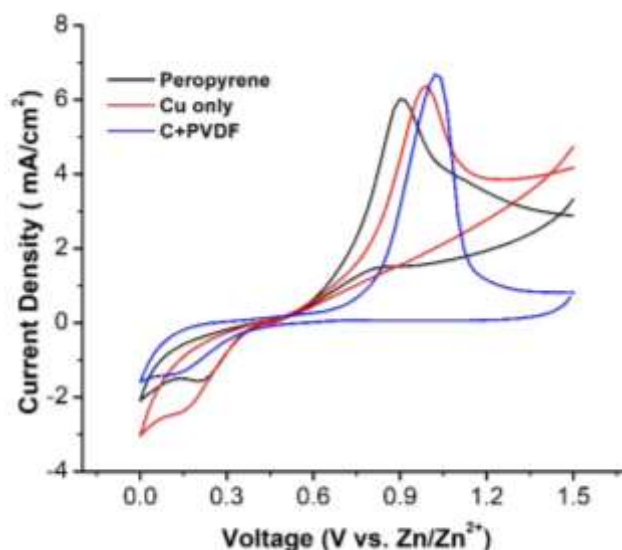


Figure 12.9.1: Cyclic voltammetry at 50 mV s^{-1} of the peropyrene cathode cast on Cu foil in an electrolyte containing $100 \text{ mM Zn}(\text{ClO}_4)_2$ in acetonitrile. The large anodic peaks for all of the electrodes tested is due to the oxidation of the Cu substrate in this electrolyte. On a bare Cu electrode, this same oxidative current is not seen with $100 \text{ mM Zn}(\text{CF}_3\text{SO}_3)_2$ under a wide range of scan rates. The reason why Cu stripping occurs in $\text{Zn}(\text{ClO}_4)_2$, but not $\text{Zn}(\text{CF}_3\text{SO}_3)_2$ is not entirely clear, but it could be due to the differing solvation properties of Zn^{2+} in these two electrolytes. As described in the main text, Zn^{2+} in $\text{Zn}(\text{CF}_3\text{SO}_3)_2$ in acetonitrile is known to be highly solvated compared to $\text{Zn}(\text{ClO}_4)_2$. We hypothesize that it is the Lewis acidity of Zn^{2+} , when less solvated in the form of $\text{Zn}(\text{ClO}_4)_2$, that catalyzes the anodic dissolution of Cu. Regardless of the origin of these differences, it is clear from Figure 2b that stainless steel is a more suitable substrate for the preparation of cathode materials to be evaluated in the $\text{Zn}(\text{ClO}_4)_2$ in acetonitrile electrolyte.

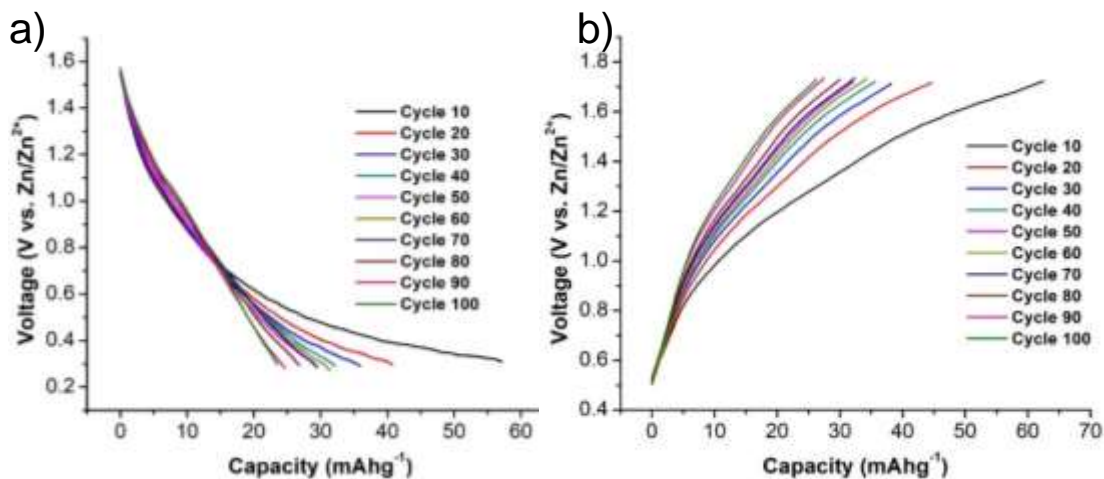


Figure 12.9.2: Discharge (a) and charge (b) curves of a Zn-ion battery with the peropyrene cathode, a Zn metal anode, and an electrolyte containing $\text{Zn}(\text{ClO}_4)_2$ in acetonitrile. Discharge and charge rates were 100 mA g^{-1} and 500 mA g^{-1} , respectively.

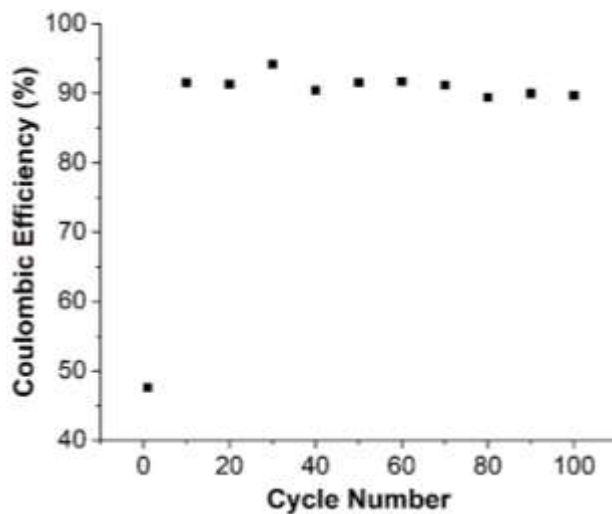


Figure 12.9.3: Coulombic efficiency, defined as the capacity during discharge divided by the capacity during charge, of a Zn-ion battery with the peropyrene cathode, a Zn metal anode, and an electrolyte containing $\text{Zn}(\text{ClO}_4)_2$ in acetonitrile during cycling.

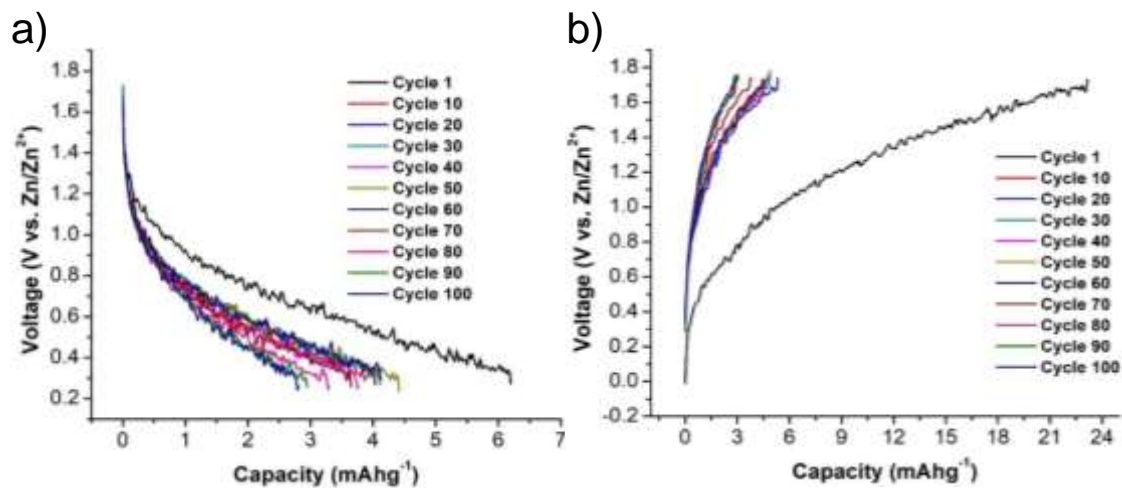


Figure 12.9.4: Discharge (a) and charge (b) curves of a Zn-ion battery using a cathode with Vulcan XC-72 and peropyrene without peropyrene, a Zn metal anode, and an electrolyte containing $\text{Zn}(\text{ClO}_4)_2$ in acetonitrile. Discharge and charge rates were 100 mA g^{-1} and 500 mA g^{-1} , respectively.

Chapter 13. References:

- [1] L. Pérez-Lombard, J. Ortiz, and C. Pout, "A review on buildings energy consumption information," *Energy and Buildings*, vol. 40, no. 3, pp. 394-398, 2008/01/01/ 2008, doi: 10.1016/j.enbuild.2007.03.007.
- [2] United States per capita energy use 1650-2010 [Online] Available: https://www.eia.gov/totalenergy/data/annual/pdf/sec16_1.pdf
- [3] U.S. energy facts explained [Online] Available: <https://www.eia.gov/energyexplained/us-energy-facts/>
- [4] Inventory of U.S. Greenhouse Gas Emissions and Sinks [Online] Available: <https://www.epa.gov/ghgemissions/inventory-us-greenhouse-gas-emissions-and-sinks>
- [5] D. Lüthi *et al.*, "High-resolution carbon dioxide concentration record 650,000–800,000 years before present," *Nature*, vol. 453, no. 7193, pp. 379-382, 2008, doi: 10.1038/nature06949.
- [6] Carbon Dioxide, Latest Measurement [Online] Available: <https://climate.nasa.gov/vital-signs/carbon-dioxide/>
- [7] A. Froggatt, D. Quiggin, "China, EU and US cooperation on climate and energy, An ever-changing relationship" [Online] Available: <https://www.chathamhouse.org/sites/default/files/2021-03/2021-03-26-china-eu-us-cooperation-froggatt.pdf>
- [8] U.S. electricity generation from renewables surpassed coal in April [Online] Available: <https://www.eia.gov/todayinenergy/detail.php?id=42336>
- [9] N. Carey, C. Steitz, "EU proposes effective ban for new fossil-fuel cars from 2035," in *Reuters*, ed, 2021. [Online] Available: <https://www.reuters.com/business/retail-consumer/eu-proposes-effective-ban-new-fossil-fuel-car-sales-2035-2021-07-14/>
- [10] A. G. Boulanger, A. C. Chu, S. Maxx, and D. L. Waltz, "Vehicle Electrification: Status and Issues," *Proceedings of the IEEE*, vol. 99, no. 6, pp. 1116-1138, 2011, doi: 10.1109/JPROC.2011.2112750.
- [11] H. Naims, "Economics of carbon dioxide capture and utilization—a supply and demand perspective," *Environmental Science and Pollution Research*, vol. 23, no. 22, pp. 22226-22241, 2016/11/01 2016, doi: 10.1007/s11356-016-6810-2.

- [12] S. Garg *et al.*, "Advances and challenges in electrochemical CO₂ reduction processes: an engineering and design perspective looking beyond new catalyst materials," *Journal of Materials Chemistry A*, 10.1039/C9TA13298H vol. 8, no. 4, pp. 1511-1544, 2020, doi: 10.1039/C9TA13298H.
- [13] Y. Pei, H. Zhong, and F. Jin, "A brief review of electrocatalytic reduction of CO₂—Materials, reaction conditions, and devices," *Energy Science & Engineering*, <https://doi.org/10.1002/ese3.935> vol. 9, no. 7, pp. 1012-1032, 2021/07/01 2021, doi: 10.1002/ese3.935.
- [14] S. Nitopi *et al.*, "Progress and Perspectives of Electrochemical CO₂ Reduction on Copper in Aqueous Electrolyte," *Chemical Reviews*, vol. 119, no. 12, pp. 7610-7672, 2019/06/26 2019, doi: 10.1021/acs.chemrev.8b00705.
- [15] C. M. Friend and B. Xu, "Heterogeneous Catalysis: A Central Science for a Sustainable Future," *Accounts of Chemical Research*, vol. 50, no. 3, pp. 517-521, 2017/03/21 2017, doi: 10.1021/acs.accounts.6b00510.
- [16] Technology Roadmap - Energy and GHG Reductions in the Chemical Industry via Catalytic Processes, IEA, Paris. [Online] Available: <https://www.iea.org/reports/technology-roadmap-energy-and-ghg-reductions-in-the-chemical-industry-via-catalytic-processes>
- [17] Z. J. Schiffer, A. M. Limaye, and K. Manthiram, "Thermodynamic Discrimination between Energy Sources for Chemical Reactions," *Joule*, vol. 5, no. 1, pp. 135-148, 2021/01/20/ 2021, doi: /10.1016/j.joule.2020.12.014.
- [18] A. Ponrouch and M. R. Palacín, "Post-Li batteries: promises and challenges," *Philosophical Transactions of the Royal Society A: Mathematical, Physical and Engineering Sciences*, vol. 377, no. 2152, p. 20180297, 2019/08/26 2019, doi: 10.1098/rsta.2018.0297.
- [19] N. Nitta, F. Wu, J. T. Lee, and G. Yushin, "Li-ion battery materials: present and future," *Materials Today*, vol. 18, no. 5, pp. 252-264, 2015/06/01/ 2015, doi: 10.1016/j.mattod.2014.10.040.
- [20] D. Selvakumaran, A. Pan, S. Liang, and G. Cao, "A review on recent developments and challenges of cathode materials for rechargeable aqueous Zn-ion batteries," *Journal of Materials Chemistry A*, 10.1039/C9TA05053A vol. 7, no. 31, pp. 18209-18236, 2019, doi: 10.1039/C9TA05053A.
- [21] M. Jacoby, "It's time to get serious about recycling lithium-ion batteries," in *Chemical and Engineering News (C&EN)* vol. 97, ed, July 14, 2019.

- [22] M. Chen *et al.*, "Recycling End-of-Life Electric Vehicle Lithium-Ion Batteries," *Joule*, vol. 3, no. 11, pp. 2622-2646, 2019/11/20/ 2019, doi: 10.1016/j.joule.2019.09.014.
- [23] W. Gao *et al.*, "Selective recovery of valuable metals from spent lithium-ion batteries – Process development and kinetics evaluation," *Journal of Cleaner Production*, vol. 178, pp. 833-845, 2018/03/20/ 2018, doi: 10.1016/j.jclepro.2018.01.040.
- [24] T. Georgi-Maschler, B. Friedrich, R. Weyhe, H. Heegn, and M. Rutz, "Development of a recycling process for Li-ion batteries," *Journal of Power Sources*, vol. 207, pp. 173-182, 2012/06/01/ 2012, doi: 10.1016/j.jpowsour.2012.01.152.
- [25] H. Li, N. L. Okamoto, T. Hatakeyama, Y. Kumagai, F. Oba, and T. Ichitsubo, "Fast Diffusion of Multivalent Ions Facilitated by Concerted Interactions in Dual-Ion Battery Systems," *Advanced Energy Materials*, vol. 8, no. 27, p. 1801475, 2018/09/01 2018, doi: 10.1002/aenm.201801475.
- [26] M. S. Chae, J. W. Heo, H. H. Kwak, H. Lee, and S.-T. Hong, "Organic electrolyte-based rechargeable zinc-ion batteries using potassium nickel hexacyanoferrate as a cathode material," *Journal of Power Sources*, vol. 337, pp. 204-211, 2017/01/01/ 2017, doi: 10.1016/j.jpowsour.2016.10.083.
- [27] D. Kundu, S. Hosseini Vajargah, L. Wan, B. Adams, D. Prendergast, and L. F. Nazar, "Aqueous vs. nonaqueous Zn-ion batteries: consequences of the desolvation penalty at the interface," *Energy & Environmental Science*, vol. 11, no. 4, pp. 881-892, 2018, doi: 10.1039/C8EE00378E.
- [28] Y. Li *et al.*, "Batteries: Recent Advances in Flexible Zinc-Based Rechargeable Batteries (Adv. Energy Mater. 1/2019)," *Advanced Energy Materials*, vol. 9, no. 1, p. 1970001, 2019/01/01 2019, doi: 10.1002/aenm.201970001.
- [29] G. A. Elia, K. V. Kravchyk, M. V. Kovalenko, J. Chacón, A. Holland, and R. G. A. Wills, "An overview and prospective on Al and Al-ion battery technologies," *Journal of Power Sources*, vol. 481, p. 228870, 2021/01/01/ 2021, doi: 10.1016/j.jpowsour.2020.228870.
- [30] J. L. Sweeney, *Energy Efficiency: Building a Clean, Secure Economy*. (Hoover Institution Press, 2016) [Online] Available: <https://www.hoover.org/research/energy-efficiency-building-clean-secure-economy>
- [31] A. B. Jaffe and R. N. Stavins, "The energy-efficiency gap What does it mean?," *Energy Policy*, vol. 22, no. 10, pp. 804-810, 1994/10/01/ 1994, doi: 10.1016/0301-4215(94)90138-4.

- [32] E. Lee, M. Yazdanian, and S. Selkowitz, "The energy-savings potential of electrochromic windows in the US commercial buildings sector," *Lawrence Berkeley National Laboratory*, 2004.
- [33] Windows and Building Envelope Research and Development: Roadmap for Emerging Technologies, February 2014 [Online] Available: https://www.energy.gov/sites/prod/files/2014/02/f8/BTO_windows_and_envelope_report_3.pdf
- [34] Monthly Energy Review [Online] Available: <https://www.eia.gov/totalenergy/data/monthly/archive/00352007.pdf>
- [35] H. N. Hersh, W. E. Kramer, and J. H. McGee, "Mechanism of electrochromism in WO₃," *Applied Physics Letters*, vol. 27, no. 12, pp. 646-648, 1975, doi: 10.1063/1.88346.
- [36] T. S. Hernandez, C. J. Barile, M. T. Strand, T. E. Dayrit, D. J. Slotcavage, and M. D. McGehee, "Bistable Black Electrochromic Windows Based on the Reversible Metal Electrodeposition of Bi and Cu," *ACS Energy Letters*, vol. 3, no. 1, pp. 104-111, 2018/01/12 2018, doi: 10.1021/acsenergylett.7b01072.
- [37] M. T. Strand *et al.*, "Factors that Determine the Length Scale for Uniform Tinting in Dynamic Windows Based on Reversible Metal Electrodeposition," *ACS Energy Letters*, vol. 3, no. 11, pp. 2823-2828, 2018/11/09 2018, doi: 10.1021/acsenergylett.8b01781.
- [38] S. M. Islam and C. J. Barile, "Dynamic Windows Using Reversible Zinc Electrodeposition in Neutral Electrolytes with High Opacity and Excellent Resting Stability," *Advanced Energy Materials*, vol. 11, no. 22, p. 2100417, 2021/06/01 2021, doi: 10.1002/aenm.202100417.
- [39] O. S. Heavens, *Optical properties of thin solid films*. New York: Academic Press, 1955, p. 261 pages.
- [40] C. J. Barile, D. J. Slotcavage, J. Hou, M. T. Strand, T. S. Hernandez, and M. D. McGehee, "Dynamic Windows with Neutral Color, High Contrast, and Excellent Durability Using Reversible Metal Electrodeposition," *Joule*, vol. 1, no. 1, pp. 133-145, 2017, doi: 10.1016/j.joule.2017.06.001.
- [41] T. S. Hernandez *et al.*, "Electrolyte for Improved Durability of Dynamic Windows Based on Reversible Metal Electrodeposition," *Joule*, vol. 4, no. 7, pp. 1501-1513, 2020, doi: 10.1016/j.joule.2020.05.008.

- [42] M. A. Jeffers, L. Chaney, and J. P. Rugh, "Climate Control Load Reduction Strategies for Electric Drive Vehicles in Warm Weather," 2015. [Online]. Available: doi: 10.4271/2015-01-0355.
- [43] R. J. Mortimer, A. L. Dyer, and J. R. Reynolds, "Electrochromic organic and polymeric materials for display applications," *Displays*, vol. 27, no. 1, pp. 2-18, 2006/01/01/ 2006, doi: 10.1016/j.displa.2005.03.003.
- [44] E. L. Runnerstrom, A. Llordés, S. D. Lounis, and D. J. Milliron, "Nanostructured electrochromic smart windows: traditional materials and NIR-selective plasmonic nanocrystals," *Chemical Communications*, 10.1039/C4CC03109A vol. 50, no. 73, pp. 10555-10572, 2014, doi: 10.1039/C4CC03109A.
- [45] G. A. Niklasson and C. G. Granqvist, "Electrochromics for smart windows: thin films of tungsten oxide and nickel oxide, and devices based on these," *Journal of Materials Chemistry*, 10.1039/B612174H vol. 17, no. 2, pp. 127-156, 2007, doi: 10.1039/B612174H.
- [46] W. H. Nguyen, C. J. Barile, and M. D. McGehee, "Small Molecule Anchored to Mesoporous ITO for High-Contrast Black Electrochromics," *The Journal of Physical Chemistry C*, vol. 120, no. 46, pp. 26336-26341, 2016/11/23 2016, doi: 10.1021/acs.jpcc.6b08820.
- [47] V. K. Thakur, G. Ding, J. Ma, P. S. Lee, and X. Lu, "Hybrid Materials and Polymer Electrolytes for Electrochromic Device Applications," *Advanced Materials*, vol. 24, no. 30, pp. 4071-4096, 2012/08/08 2012, doi: 10.1002/adma.201200213.
- [48] G. K. A. Alcaraz, J. S. Juarez-Rolon, N. A. Burpee, and C. J. Barile, "Thermally-stable dynamic windows based on reversible metal electrodeposition from aqueous electrolytes," *Journal of Materials Chemistry C*, 10.1039/C7TC05222G vol. 6, no. 8, pp. 2132-2138, 2018, doi: 10.1039/C7TC05222G.
- [49] C. J. Barile, D. J. Slotcavage, and M. D. McGehee, "Polymer–Nanoparticle Electrochromic Materials that Selectively Modulate Visible and Near-Infrared Light," *Chemistry of Materials*, vol. 28, no. 5, pp. 1439-1445, 2016/03/08 2016, doi: 10.1021/acs.chemmater.5b04811.
- [50] R.-T. Wen, G. A. Niklasson, and C. G. Granqvist, "Electrochromic nickel oxide films and their compatibility with potassium hydroxide and lithium perchlorate in propylene carbonate: Optical, electrochemical and stress-related properties," *Thin Solid Films*, vol. 565, pp. 128-135, 2014/08/28/ 2014, doi: 10.1016/j.tsf.2014.07.004.

- [51] Y. D. Gamburg and G. Zangari, *Theory and Practice of Metal Electrodeposition*, New York, NY, United States: Springer-Verlag New York Inc., 2011, pp. XVII, 378.
- [52] J. Jensen, M. V. Madsen, and F. C. Krebs, "Photochemical stability of electrochromic polymers and devices," *Journal of Materials Chemistry C*, vol. 1, no. 32, pp. 4826-4835, 2013, doi: 10.1039/C3TC30751D.
- [53] D. M. Tench and L. F. Warren, "Electrodeposition Cell with High Light Transmission," 2001. US Patent 5903382(1999).
- [54] Y.-R. Lu *et al.*, "Mechanism of Electrochemical Deposition and Coloration of Electrochromic V2O5 Nano Thin Films: an In Situ X-Ray Spectroscopy Study," *Nanoscale Research Letters*, vol. 10, no. 1, p. 387, 2015/10/05 2015, doi: 10.1186/s11671-015-1095-9.
- [55] N. N. Greenwood, A. Earnshaw, and Knovel (Firm), *Chemistry of the elements*, Second edition. ed. Oxford ; Boston: Butterworth-Heinemann., 1998, pp. xxii, 1341 pages.
- [56] The Energy Benefits of View Dynamic Glass [Online] Available: <https://view.com/assets/pdfs/workplace-demo-room.pdf>
- [57] D. Grujicic and B. Pesic, "Electrodeposition of copper: the nucleation mechanisms," *Electrochimica Acta*, vol. 47, no. 18, pp. 2901-2912, 2002/07/18/ 2002, doi10.1016/S0013-4686(02)00161-5.
- [58] J. J. Kelly, C. Tian, and A. C. West, "Leveling and Microstructural Effects of Additives for Copper Electrodeposition," *Journal of The Electrochemical Society*, vol. 146, no. 7, pp. 2540-2545, 1999/07/01 1999, doi: 10.1149/1.1391968.
- [59] T. Y. B. Leung, M. Kang, B. F. Corry, and A. A. Gewirth, "Benzotriazole as an Additive for Copper Electrodeposition Influence of Triazole Ring Substitution," *Journal of The Electrochemical Society*, vol. 147, no. 9, p. 3326, 2000, doi: 10.1149/1.1393902.
- [60] S. Araki, K. Nakamura, K. Kobayashi, A. Tsuboi, and N. Kobayashi, "Electrochemical Optical-Modulation Device with Reversible Transformation Between Transparent, Mirror, and Black," *Advanced Materials*, vol. 24, no. 23, pp. OP122-OP126, 2012/06/19 2012, doi: 10.1002/adma.201200060.
- [61] S. Passerini, B. Scrosati, and A. Gorenstein, "The Intercalation of Lithium in Nickel Oxide and Its Electrochromic Properties," *Journal of The Electrochemical Society*, vol. 137, no. 10, pp. 3297-3300, 1990, doi: 10.1149/1.2086202.

- [62] Q. Liu, G. Dong, Y. Xiao, M.-P. Delplancke-Ogletree, F. Reniers, and X. Diao, *Electrolytes-relevant cyclic durability of nickel oxide thin films as an ion-storage layer in an all-solid-state complementary electrochromic device*. 2016, pp. 844-852.
- [63] M. Mihelčič *et al.*, *Comparison of electrochromic properties of Ni_{1-x}O in lithium and lithium-free aprotic electrolytes: From Ni_{1-x}O pigment coatings to flexible electrochromic devices*. 2014, pp. 116-130.
- [64] J. Guo *et al.*, "Mechanistic Insights into the Coloration, Evolution, and Degradation of NiO_x Electrochromic Anodes," *Inorganic Chemistry*, vol. 57, no. 15, pp. 8874-8880, 2018/08/06 2018, doi: 10.1021/acs.inorgchem.8b00793.
- [65] B. Xin *et al.*, "Bioleaching mechanism of Co and Li from spent lithium-ion battery by the mixed culture of acidophilic sulfur-oxidizing and iron-oxidizing bacteria," *Bioresource Technology*, vol. 100, no. 24, pp. 6163-6169, 2009/12/01/ 2009, doi: 10.1016/j.biortech.2009.06.086.
- [66] C.-G. Granqvist, "Out of a niche," *Nature Materials*, vol. 5, no. 2, pp. 89-90, 2006/02/01 2006, doi: 10.1038/nmat1577.
- [67] H. S. Bergh *et al.*, "Electrochromic multi-layer devices with spatially coordinated switching," US patent US2016/0011481A1, 2016.
- [68] Y. Li, E. C. M. Tse, C. J. Barile, A. A. Gewirth, and S. C. Zimmerman, "Photoresponsive Molecular Switch for Regulating Transmembrane Proton-Transfer Kinetics," *Journal of the American Chemical Society*, vol. 137, no. 44, pp. 14059-14062, 2015/11/11 2015, doi: 10.1021/jacs.5b10016.
- [69] V. V. Kondalkar, P. B. Patil, R. M. Mane, P. S. Patil, S. Choudhury, and P. N. Bhosal, "Electrochromic Performance of Nickel Oxide Thin Film: Synthesis via Electrodeposition Technique," *Macromolecular Symposia*, vol. 361, no. 1, pp. 47-50, 2016/03/01 2016, doi: 10.1002/masy.201400253.
- [70] X. H. Xia, J. P. Tu, J. Zhang, X. L. Wang, W. K. Zhang, and H. Huang, "Electrochromic properties of porous NiO thin films prepared by a chemical bath deposition," *Solar Energy Materials and Solar Cells*, vol. 92, no. 6, pp. 628-633, 2008/06/01/ 2008, doi: 10.1016/j.solmat.2008.01.009.
- [71] N. Özer, "Optical properties and electrochromic characterization of sol-gel deposited ceria films," *Solar Energy Materials and Solar Cells*, vol. 68, no. 3, pp. 391-400, 2001/06/01/ 2001, doi: 10.1016/S0927-0248(00)00371-8.
- [72] G. Marbán and T. Valdés-Solís, "Towards the hydrogen economy?," *International Journal of Hydrogen Energy*, vol. 32, no. 12, pp. 1625-1637, 2007/08/01/ 2007, doi: 10.1016/j.ijhydene.2006.12.017.

- [73] M. Carmo, D. L. Fritz, J. Mergel, and D. Stolten, "A comprehensive review on PEM water electrolysis," *International Journal of Hydrogen Energy*, vol. 38, no. 12, pp. 4901-4934, 2013/04/22/ 2013, doi: 10.1016/j.ijhydene.2013.01.151.
- [74] M. Tahir *et al.*, "Electrocatalytic oxygen evolution reaction for energy conversion and storage: A comprehensive review," *Nano Energy*, vol. 37, pp. 136-157, 2017/07/01/ 2017, doi: 10.1016/j.nanoen.2017.05.022.
- [75] Y. Li and J. Lu, "Metal–Air Batteries: Will They Be the Future Electrochemical Energy Storage Device of Choice?," *ACS Energy Letters*, vol. 2, no. 6, pp. 1370-1377, 2017/06/09 2017, doi: 10.1021/acsenergylett.7b00119.
- [76] W. Weng *et al.*, "Polymer supported organic catalysts for O₂ reduction in Li-O₂ batteries," *Electrochimica Acta*, vol. 119, pp. 138-143, 2014/02/10/ 2014, doi: 10.1016/j.electacta.2013.12.027.
- [77] C. C. L. McCrory, S. Jung, J. C. Peters, and T. F. Jaramillo, "Benchmarking Heterogeneous Electrocatalysts for the Oxygen Evolution Reaction," *Journal of the American Chemical Society*, vol. 135, no. 45, pp. 16977-16987, 2013/11/13 2013, doi: 10.1021/ja407115p.
- [78] T. Reier, M. Oezaslan, and P. Strasser, "Electrocatalytic Oxygen Evolution Reaction (OER) on Ru, Ir, and Pt Catalysts: A Comparative Study of Nanoparticles and Bulk Materials," *ACS Catalysis*, vol. 2, no. 8, pp. 1765-1772, 2012/08/03 2012, doi: 10.1021/cs3003098.
- [79] F. M. Sapountzi, J. M. Gracia, C. J. Weststrate, H. O. A. Fredriksson, and J. W. Niemantsverdriet, "Electrocatalysts for the generation of hydrogen, oxygen and synthesis gas," *Progress in Energy and Combustion Science*, vol. 58, pp. 1-35, 2017/01/01/ 2017, doi: 10.1016/j.pecs.2016.09.001.
- [80] F. Song and X. Hu, "Exfoliation of layered double hydroxides for enhanced oxygen evolution catalysis," *Nature Communications*, vol. 5, no. 1, p. 4477, 2014/07/17 2014, doi: 10.1038/ncomms5477.
- [81] S. Hirai, S. Yagi, A. Seno, M. Fujioka, T. Ohno, and T. Matsuda, "Enhancement of the oxygen evolution reaction in Mn³⁺-based electrocatalysts: correlation between Jahn–Teller distortion and catalytic activity," *RSC Advances*, vol. 6, no. 3, pp. 2019-2023, 2016, doi: 10.1039/C5RA22873E.
- [82] Y. Zhang, B. Cui, C. Zhao, H. Lin, and J. Li, "Co–Ni layered double hydroxides for water oxidation in neutral electrolyte," *Physical Chemistry Chemical Physics*, vol. 15, no. 19, pp. 7363-7369, 2013, doi: 10.1039/C3CP50202C.

- [83] Z. Lu, L. Qian, Y. Tian, Y. Li, X. Sun, and X. Duan, "Ternary NiFeMn layered double hydroxides as highly-efficient oxygen evolution catalysts," *Chemical Communications*, vol. 52, no. 5, pp. 908-911, 2016, doi: 10.1039/C5CC08845C.
- [84] Y. Qiu, L. Xin, and W. Li, "Electrocatalytic Oxygen Evolution over Supported Small Amorphous Ni-Fe Nanoparticles in Alkaline Electrolyte," *Langmuir*, vol. 30, no. 26, pp. 7893-7901, 2014/07/08 2014, doi: 10.1021/la501246e.
- [85] M. Favaro *et al.*, "An Operando Investigation of (Ni-Fe-Co-Ce)Ox System as Highly Efficient Electrocatalyst for Oxygen Evolution Reaction," *ACS Catalysis*, vol. 7, no. 2, pp. 1248-1258, 2017/02/03 2017, doi: 10.1021/acscatal.6b03126.
- [86] J. A. Haber, D. Guevarra, S. Jung, J. Jin, and J. M. Gregoire, "Discovery of New Oxygen Evolution Reaction Electrocatalysts by Combinatorial Investigation of the Ni-La-Co-Ce Oxide Composition Space . United States," *ChemElectroChem*, 2014. doi: 10.1002/celc.201
- [87] Z. Xi *et al.*, "Ni_xWO_{2.72} nanorods as an efficient electrocatalyst for oxygen evolution reaction," *Green Energy & Environment*, vol. 2, no. 2, pp. 119-123, 2017/04/01/ 2017, doi: 10.1016/j.gee.2017.01.001.
- [88] J. M. V. Nsanzimana *et al.*, "An Earth-Abundant Tungsten-Nickel Alloy Electrocatalyst for Superior Hydrogen Evolution," *ACS Applied Nano Materials*, vol. 1, no. 3, pp. 1228-1235, 2018/03/23 2018, doi: 10.1021/acsanm.7b00383.
- [89] W. Seh Zhi, J. Kibsgaard, F. Dickens Colin, I. Chorkendorff, K. Nørskov Jens, and F. Jaramillo Thomas, "Combining theory and experiment in electrocatalysis: Insights into materials design," *Science*, vol. 355, no. 6321, p. eaad4998, 2017/01/13 2017, doi: 10.1126/science.aad4998.
- [90] I. C. Man *et al.*, "Universality in Oxygen Evolution Electrocatalysis on Oxide Surfaces," *ChemCatChem*, <https://doi.org/10.1002/cctc.201000397> vol. 3, no. 7, pp. 1159-1165, 2011/07/11 2011, doi: 10.1002/cctc.201000397.
- [91] T. D. Golden, M. G. Shumsky, Y. Zhou, R. A. VanderWerf, R. A. Van Leeuwen, and J. A. Switzer, "Electrochemical Deposition of Copper(I) Oxide Films," *Chemistry of Materials*, vol. 8, no. 10, pp. 2499-2504, 1996/01/01 1996, doi: 10.1021/cm9602095.
- [92] D. van der Vliet, D. S. Strmcnik, C. Wang, V. R. Stamenkovic, N. M. Markovic, and M. T. M. Koper, "On the importance of correcting for the uncompensated Ohmic resistance in model experiments of the Oxygen Reduction Reaction," *Journal of Electroanalytical Chemistry*, vol. 647, no. 1, pp. 29-34, 2010/08/15/ 2010, doi: 10.1016/j.jelechem.2010.05.016.

- [93] L.-X. Du *et al.*, "Control of morphologies and properties of zinc oxide nanorod arrays by slightly adjusting their seed layers," *Nanomaterials and Nanotechnology*, vol. 6, p. 1847980416663674, 2016/01/01 2016, doi: 10.1177/1847980416663674.
- [94] H. S. Yaddanapudi, K. Tian, S. Teng, and A. Tiwari, "Facile preparation of nickel/carbonized wood nanocomposite for environmentally friendly supercapacitor electrodes," *Scientific Reports*, vol. 6, no. 1, p. 33659, 2016/09/21 2016, doi: 10.1038/srep33659.
- [95] K. DeHority, N. Budin, S. S. Hilston, Y. Zhang, and A. Fillinger, "Deposition of Nickel on Electrodeposited Cu₂O Films at Potentials More Positive than the Nernst Potential of Ni²⁺/Ni⁰," *Journal of The Electrochemical Society*, vol. 164, no. 9, pp. H615-H620, 2017, doi: 10.1149/2.0751709jes.
- [96] J. S. Kim, B. Kim, H. Kim, and K. Kang, "Recent Progress on Multimetal Oxide Catalysts for the Oxygen Evolution Reaction," *Advanced Energy Materials*, <https://doi.org/10.1002/aenm.201702774> vol. 8, no. 11, p. 1702774, 2018/04/01 2018, doi: 10.1002/aenm.201702774.
- [97] H. Xiao, H. Shin, and W. A. Goddard, "Synergy between Fe and Ni in the optimal performance of (Ni,Fe)OOH catalysts for the oxygen evolution reaction," *Proceedings of the National Academy of Sciences*, vol. 115, no. 23, p. 5872, 2018, doi: 10.1073/pnas.1722034115.
- [98] B. Beverskog and I. Puigdomenech, "Revised Pourbaix diagrams for nickel at 25–300 °C," *Corrosion Science*, vol. 39, no. 5, pp. 969-980, 1997/05/01/ 1997, doi: 10.1016/S0010-938X(97)00002-4.
- [99] C. M. Amb, A. L. Dyer, and J. R. Reynolds, "Navigating the Color Palette of Solution-Processable Electrochromic Polymers," *Chemistry of Materials*, vol. 23, no. 3, pp. 397-415, 2011/02/08 2011, doi: 10.1021/cm1021245.
- [100] L. Bouteiller and P. L. Barny, "Polymer-dispersed liquid crystals: Preparation, operation and application," *Liquid Crystals*, vol. 21, no. 2, pp. 157-174, 1996/08/01 1996, doi: 10.1080/02678299608032820.
- [101] J. Murray, D. Ma, and J. N. Munday, "Electrically Controllable Light Trapping for Self-Powered Switchable Solar Windows," *ACS Photonics*, vol. 4, no. 1, pp. 1-7, 2017/01/18 2017, doi: 10.1021/acsphotonics.6b00518.
- [102] M. Kamalifarvestani, R. Saidur, S. Mekhilef, and F. S. Javadi, "Performance, materials and coating technologies of thermochromic thin films on smart windows," *Renewable and Sustainable Energy Reviews*, vol. 26, pp. 353-364, 2013/10/01/ 2013, doi: 10.1016/j.rser.2013.05.038.

- [103] H. Kim *et al.*, "Flexible Thermo-chromic Window Based on Hybridized VO₂/Graphene," *ACS Nano*, vol. 7, no. 7, pp. 5769-5776, 2013/07/23 2013, doi: 10.1021/nn400358x.
- [104] J. P. Ziegler and B. M. Howard, "Applications of reversible electrodeposition electrochromic devices," *Solar Energy Materials and Solar Cells*, vol. 39, no. 2, pp. 317-331, 1995/12/01/ 1995, doi: 10.1016/0927-0248(95)00067-4.
- [105] J. P. Ziegler, "Status of reversible electrodeposition electrochromic devices," *Solar Energy Materials and Solar Cells*, vol. 56, no. 3, pp. 477-493, 1999/01/30/ 1999, doi: 10.1016/S0927-0248(98)00192-5.
- [106] C. J. Barile, "Electrolyte dynamics in reversible metal electrodeposition for dynamic windows," *Journal of Applied Electrochemistry*, vol. 48, no. 4, pp. 443-449, 2018/04/01 2018, doi: 10.1007/s10800-018-1167-5.
- [107] T. Osaka, T. Momma, D. Mukoyama, and H. Nara, "Proposal of novel equivalent circuit for electrochemical impedance analysis of commercially available lithium ion battery," *Journal of Power Sources*, vol. 205, pp. 483-486, 2012/05/01/ 2012, doi: 10.1016/j.jpowsour.2012.01.070.
- [108] C. A. Tippets *et al.*, "Dynamic Optical Gratings Accessed by Reversible Shape Memory," *ACS Applied Materials & Interfaces*, vol. 7, no. 26, pp. 14288-14293, 2015/07/08 2015, doi: 10.1021/acsami.5b02688.
- [109] S. M. Islam, T. S. Hernandez, M. D. McGehee, and C. J. Barile, "Hybrid dynamic windows using reversible metal electrodeposition and ion insertion," *Nature Energy*, vol. 4, no. 3, pp. 223-229, 2019/03/01 2019, doi: 10.1038/s41560-019-0332-3.
- [110] E. Kholoud *et al.*, "Cobalt hexacyanoferrate nanoparticles for wet-processed brown-bleached electrochromic devices with hybridization of high-spin/low-spin phases," *Journal of Materials Chemistry C*, 10.1039/C7TC02576A vol. 5, no. 35, pp. 8921-8926, 2017, doi: 10.1039/C7TC02576A.
- [111] S. Pahal, M. Deepa, S. Bhandari, K. N. Sood, and A. K. Srivastava, "Electrochromism and redox switching of cobalt hexacyanoferrate-polyaniline hybrid films in a hydrophobic ionic liquid," *Solar Energy Materials and Solar Cells*, vol. 94, no. 6, pp. 1064-1075, 2010/06/01/ 2010, doi: 10.1016/j.solmat.2010.02.027.
- [112] T.-C. Liao, W.-H. Chen, H.-Y. Liao, and L.-C. Chen, "Multicolor electrochromic thin films and devices based on the Prussian blue family nanoparticles," *Solar Energy Materials and Solar Cells*, vol. 145, pp. 26-34, 2016/02/01/ 2016, doi: 10.1016/j.solmat.2015.08.004.

- [113] S. M. Islam, C. N. Fini, and C. J. Barile, "Dynamic Windows Based on Reversible Metal Electrodeposition with Enhanced Functionality," *Journal of The Electrochemical Society*, vol. 166, no. 8, pp. D333-D338, 2019, doi: 10.1149/2.0961908jes.
- [114] Z. Li, Y. Tang, K. Zhou, H. Wang, and H. Yan, "Improving Electrochromic Cycle Life of Prussian Blue by Acid Addition to the Electrolyte," *Materials*, vol. 12, no. 1, 2019, doi: 10.3390/ma12010028.
- [115] A. J. Bard and L. R. Faulkner, *Electrochemical methods : fundamentals and applications*, Second edition. ed. New York: Wiley, 2001, pp. xxi, 833 pages.
- [116] A. L. Eckermann, D. J. Feld, J. A. Shaw, and T. J. Meade, "Electrochemistry of redox-active self-assembled monolayers," (in eng), *Coordination chemistry reviews*, vol. 254, no. 15-16, pp. 1769-1802, 2010, doi: 10.1016/j.ccr.2009.12.023.
- [117] S. Phadke, R. Mysyk, and M. Anouti, "Effect of cation (Li+, Na+, K+, Rb+, Cs+) in aqueous electrolyte on the electrochemical redox of Prussian blue analogue (PBA) cathodes," *Journal of Energy Chemistry*, vol. 40, pp. 31-38, 2020/01/01/2020, doi: 10.1016/j.jechem.2019.01.025.
- [118] D. Ojwang *et al.*, *Structure Characterization and Properties of K-Containing Copper Hexacyanoferrate*. vol. 55, no. 12, pp 5924-5934, 2016/02/08, 2016, doi: 10.1021/acs.inorgchem.6b00227
- [119] K. Lei *et al.*, "A Porous Network of Bismuth Used as the Anode Material for High-Energy-Density Potassium-Ion Batteries," *Angewandte Chemie International Edition*, vol. 57, no. 17, pp. 4687-4691, 2018/04/16 2018, doi: 10.1002/anie.201801389.
- [120] R. J. Mortimer and J. R. Reynolds, "In situ colorimetric and composite coloration efficiency measurements for electrochromic Prussian blue," *Journal of Materials Chemistry*, 10.1039/B418771G vol. 15, no. 22, pp. 2226-2233, 2005, doi: 10.1039/B418771G.
- [121] C. G. Granqvist, *Handbook of Inorganic Electrochromic materials*. New York: Elsevier, 1995.
- [122] G. Assanto, G. Stegeman, M. Sheik-Bahae, and E. Van Stryland, "All-optical switching devices based on large nonlinear phase shifts from second harmonic generation," *Applied Physics Letters*, vol. 62, no. 12, pp. 1323-1325, 1993/03/22 1993, doi: 10.1063/1.109611.

- [123] C. G. Granqvist, "Electrochromic tungsten oxide films: Review of progress 1993–1998," *Solar Energy Materials and Solar Cells*, vol. 60, no. 3, pp. 201-262, 2000/01/31/ 2000, doi: [https://doi.org/10.1016/S0927-0248\(99\)00088-4](https://doi.org/10.1016/S0927-0248(99)00088-4).
- [124] R. H. Bulloch, J. A. Kerszulis, A. L. Dyer, and J. R. Reynolds, "An Electrochromic Painter's Palette: Color Mixing via Solution Co-Processing," *ACS Applied Materials & Interfaces*, vol. 7, no. 3, pp. 1406-1412, 2015/01/28 2015, doi: 10.1021/am507514z.
- [125] P. Shi *et al.*, "Broadly Absorbing Black to Transmissive Switching Electrochromic Polymers," *Advanced Materials*, vol. 22, no. 44, pp. 4949-4953, 2010/11/24 2010, doi: 10.1002/adma.201002234.
- [126] N. R. Armstrong, P. A. Veneman, E. Ratcliff, D. Placencia, and M. Brumbach, "Oxide Contacts in Organic Photovoltaics: Characterization and Control of Near-Surface Composition in Indium–Tin Oxide (ITO) Electrodes," *Accounts of Chemical Research*, vol. 42, no. 11, pp. 1748-1757, 2009/11/17 2009, doi: 10.1021/ar900096f.
- [127] K. Kondo, H. Kouta, M. Yokoi, N. Okamoto, T. Saito, and T. Hayashi, "Cuprous Ion As An Accelerant of Copper Damascene Electrodeposition," *ECS Transactions*, vol. 58, no. 17, pp. 89-96, 2014/02/27 2014, doi: 10.1149/05817.0089ecst.
- [128] P. B. Johnson and R. W. Christy, "Optical Constants of the Noble Metals," *Physical Review B*, vol. 6, no. 12, pp. 4370-4379, 12/15/ 1972, doi: 10.1103/PhysRevB.6.4370.
- [129] Schlesinger, M., Paunovic, and M., *Modern Electroplating*. John Wiley: Hoboken, NJ, 2010.
- [130] L. Chen, L. K. Thompson, and J. N. Bridson, "In situ oxidation of a copper (I) complex to produce a hydroxy-bridged dinuclear copper (II) complex. Structural, magnetic and electrochemical properties," *Inorganica Chimica Acta*, vol. 244, no. 1, pp. 87-93, 1996/03/01/ 1996, doi: 10.1016/0020-1693(95)04749-2.
- [131] H. Zhao, J. Chang, A. Boika, and A. J. Bard, "Electrochemistry of High Concentration Copper Chloride Complexes," *Analytical Chemistry*, vol. 85, no. 16, pp. 7696-7703, 2013/08/20 2013, doi: 10.1021/ac4016769.
- [132] G. Weng, X. Dong, J. Li, and J. Zhao, "Halide ions can trigger the oxidative etching of gold nanorods with the iodide ions being the most efficient," *Journal of Materials Science*, vol. 51, no. 16, pp. 7678-7690, 2016/08/01 2016, doi: 10.1007/s10853-016-0050-1.

- [133] R. R. Lunt and V. Bulovic, "Transparent, near-infrared organic photovoltaic solar cells for window and energy-scavenging applications," *Applied Physics Letters*, vol. 98, no. 11, p. 113305, 2011, doi: 10.1063/1.3567516.
- [134] Y. Zhao and R. R. Lunt, "Transparent Luminescent Solar Concentrators for Large-Area Solar Windows Enabled by Massive Stokes-Shift Nanocluster Phosphors," *Advanced Energy Materials*, vol. 3, no. 9, pp. 1143-1148, 2013, doi: 10.1002/aenm.201300173.
- [135] R. J. Mortimer, "Electrochromic materials," *Chemical Society Reviews*, 10.1039/CS9972600147 vol. 26, no. 3, pp. 147-156, 1997, doi: 10.1039/CS9972600147.
- [136] C. Lemire, D. B. B. Lollman, A. Al Mohammad, E. Gillet, and K. Aguir, "Reactive R.F. magnetron sputtering deposition of WO₃ thin films," *Sensors and Actuators B: Chemical*, vol. 84, no. 1, pp. 43-48, 2002/04/30/ 2002, doi: 10.1016/S0925-4005(02)00009-6.
- [137] S. M. Islam and C. J. Barile, "Dual Tinting Dynamic Windows Using Reversible Metal Electrodeposition and Prussian Blue," *ACS Applied Materials & Interfaces*, vol. 11, no. 43, pp. 40043-40049, 2019/10/30 2019, doi: 10.1021/acsami.9b13942.
- [138] J. Scarminio, "H Insertion and Electrochromism in NiO[sub x] Thin Films," *Journal of The Electrochemical Society*, vol. 139, no. 5, p. 1236, 1992, doi: 10.1149/1.2069389.
- [139] C. L. DeFoor, J. F. Jeanetta, and C. J. Barile, "Controlling the Optical Properties of Dynamic Windows Based on Reversible Metal Electrodeposition," *ACS Applied Electronic Materials*, vol. 2, no. 1, pp. 290-300, 2020/01/28 2020, doi: 10.1021/acsaelm.9b00780.
- [140] Fairchild and M. D., *Color and Image Appearance Models*. New York: John Wiley & Sons, Inc., 2005.
- [141] J. Schanda, *Colorimetry: Understanding the CIE system*. New York: John Wiley & Sons, Inc., 2007.
- [142] M. Ciabocco, M. Berrettoni, S. Zamponi, and J. A. Cox, "Deposition and characterization of a CoHCF nanorod array in a templated ormosil film on an electrode and application to electrocatalysis," *Journal of Solid State Electrochemistry*, vol. 20, no. 5, pp. 1323-1329, 2016/05/01 2016, doi: 10.1007/s10008-016-3123-9.
- [143] A. Hamnett, S. Higgins, R. S. Mortimer, and D. R. Rosseinsky, "A study of the electrodeposition and subsequent potential cycling of Prussian Blue films using

- ellipsometry," *Journal of Electroanalytical Chemistry and Interfacial Electrochemistry*, vol. 255, no. 1, pp. 315-324, 1988/11/10/ 1988, doi: 10.1016/0022-0728(88)80024-X.
- [144] J. Joseph, H. Gomathi, and G. P. Rao, "Electrodes modified with cobalt hexacyanoferrate," *Journal of Electroanalytical Chemistry and Interfacial Electrochemistry*, vol. 304, no. 1, pp. 263-269, 1991/04/10/ 1991, doi: 10.1016/0022-0728(91)85509-N.
- [145] G. A. P. Zaldivar, Y. Gushikem, E. V. Benvenuti, S. C. de Castro, and A. Vasquez, "Structure and electrochemical property of the cobalt(II) hexacyanoferrate complex immobilized on Sn(IV) oxide coated on silica gel surface," *Electrochimica Acta*, vol. 39, no. 1, pp. 33-36, 1994/01/01/ 1994, doi: 10.1016/0013-4686(94)85007-0.
- [146] R. A. Robinson and R. H. Stokes, *Electrolyte Solutions*, 2nd ed. London: Butterworth, 1959, pp. 120-126.
- [147] F. A. Cotton and G. Wilkinson, *Advanced Inorganic Chemistry*, 4th ed. New York: Wiley, 1980.
- [148] P. J. Kulesza *et al.*, "Electrochemical Charging, Countercation Accommodation, and Spectrochemical Identity of Microcrystalline Solid Cobalt Hexacyanoferrate," *The Journal of Physical Chemistry B*, vol. 102, no. 11, pp. 1870-1876, 1998/03/01 1998, doi: 10.1021/jp9726495.
- [149] F. Herren, P. Fischer, A. Ludi, and W. Haelg, "Neutron diffraction study of Prussian Blue, $\text{Fe}_4[\text{Fe}(\text{CN})_6]_3 \cdot x\text{H}_2\text{O}$. Location of water molecules and long-range magnetic order," *Inorganic Chemistry*, vol. 19, no. 4, pp. 956-959, 1980/04/01 1980, doi: 10.1021/ic50206a032.
- [150] I. Horcas, R. Fernández, J. M. Gómez-Rodríguez, J. Colchero, J. Gómez-Herrero, and A. M. Baro, "WSXM: A software for scanning probe microscopy and a tool for nanotechnology," *Review of Scientific Instruments*, vol. 78, no. 1, p. 013705, 2007, doi: 10.1063/1.2432410.
- [151] C. Banks and R. Singh, "Composition and Stability of 5-Sulfosalicylate Complexes of Beryllium and Copper," *Journal of American Chemical Society*.
- [152] M. W. Thomsen, "Determination of the solubility product of copper(II) tartrate," *Journal of Chemical Education*, vol. 69, no. 4, p. 328, 1992/04/01 1992, doi: 10.1021/ed069p328.
- [153] A. Morsali and L. Hashemi, *Main Group Metal Coordination Polymers: Structures and Nanostructures*. Hoboken, NJ: John Wiley and Sons, Inc., 2017.

- [154] Y. Heo, G. Augenbroe, D. Graziano, R. T. Muehleisen, and L. Guzowski, "Scalable methodology for large scale building energy improvement: Relevance of calibration in model-based retrofit analysis," *Building and Environment*, vol. 87, pp. 342-350, 2015/05/01/ 2015, doi: 10.1016/j.buildenv.2014.12.016.
- [155] E. Lee, M. Yazdanian, and S. Selkowitz, *The energy-savings potential of electrochromic windows in the US commercial buildings sector*. 2004/04/30 2019.
- [156] H. Khandelwal, R. C. G. M. Loonen, J. L. M. Hensen, M. G. Debijs, and A. P. H. J. Schenning, "Electrically switchable polymer stabilised broadband infrared reflectors and their potential as smart windows for energy saving in buildings," *Scientific Reports*, vol. 5, no. 1, p. 11773, 2015/07/01 2015, doi: 10.1038/srep11773.
- [157] N. R. Lynam, "Smart Windows for Automobiles," 1990. [Online]. Available: 10.4271/900419.
- [158] C. Ma, M. Taya, and C. Xu, "Smart sunglasses based on electrochromic polymers," *Polymer Engineering & Science*, vol. 48, no. 11, pp. 2224-2228, 2008, doi: 10.1002/pen.21169.
- [159] T. J. Richardson, "New electrochromic mirror systems," *Solid State Ionics*, vol. 165, no. 1, pp. 305-308, 2003/12/01/ 2003, doi: 10.1016/j.ssi.2003.08.047.
- [160] G. W. Kim *et al.*, "Next generation smart window display using transparent organic display and light blocking screen," *Optics Express*, vol. 26, no. 7, pp. 8493-8502, 2018/04/02 2018, doi: 10.1364/OE.26.008493.
- [161] H. Li, W. Zhang, and A. Y. Elezzabi, "Transparent Zinc-Mesh Electrodes for Solar-Charging Electrochromic Windows," *Advanced Materials*, <https://doi.org/10.1002/adma.202003574> vol. 32, no. 43, p. 2003574, 2020/10/01 2020, doi: 10.1002/adma.202003574.
- [162] B. Wang *et al.*, "A Long-Life Battery-Type Electrochromic Window with Remarkable Energy Storage Ability," *Solar RRL*, vol. 4, no. 3, p. 1900425, 2020/03/01 2020, doi: 10.1002/solr.201900425.
- [163] H. Ji, D. Liu, H. Cheng, and C. Zhang, "Inkjet printing of vanadium dioxide nanoparticles for smart windows," *Journal of Materials Chemistry C*, vol. 6, no. 10, pp. 2424-2429, 2018, doi: 10.1039/C8TC00286J.
- [164] D. D. Miller, J. Y. Li, S. M. Islam, J. F. Jeanetta, and C. J. Barile, "Aqueous alkaline electrolytes for dynamic windows based on reversible metal electrodeposition with improved durability," *Journal of Materials Chemistry C*, vol. 8, no. 5, pp. 1826-1834, 2020, doi: 10.1039/C9TC05546K.

- [165] "Electrochemical Series," in *Corrosion: Materials*, vol. 13B, S. D. Cramer and B. S. Covino, Jr. Eds.: ASM International, 2005.
- [166] Y. Zhang *et al.*, "Deeply Rechargeable and Hydrogen-Evolution-Suppressing Zinc Anode in Alkaline Aqueous Electrolyte," *Nano Letters*, vol. 20, no. 6, pp. 4700-4707, 2020/06/10 2020, doi: 10.1021/acs.nanolett.0c01776.
- [167] P. Quaino, F. Juarez, E. Santos, and W. Schmickler, "Volcano plots in hydrogen electrocatalysis – uses and abuses," *Beilstein Journal of Nanotechnology*, vol. 5, pp. 846-854, 2014, doi: 10.3762/bjnano.5.96.
- [168] C. Wang, Z. Wang, Y. Ren, X. Hou, and F. Yan, "Flexible Electrochromic Zn Mirrors Based on Zn/Viologen Hybrid Batteries," *ACS Sustainable Chemistry & Engineering*, vol. 8, no. 13, pp. 5050-5055, 2020/04/06 2020, doi: 10.1021/acssuschemeng.9b06818.
- [169] R. A. Huggins, *Negative Electrodes in Aqueous Systems. In: Advanced Batteries*. Boston, M: Springer, 2009.
- [170] C. W. Lee, K. Sathiyarayanan, S. W. Eom, H. S. Kim, and M. S. Yun, "Novel electrochemical behavior of zinc anodes in zinc/air batteries in the presence of additives," *Journal of Power Sources*, vol. 159, no. 2, pp. 1474-1477, 2006/09/22/ 2006, doi: 10.1016/j.jpowsour.2005.11.074.
- [171] Z. Hou, X. Zhang, X. Li, Y. Zhu, J. Liang, and Y. Qian, "Surfactant widens the electrochemical window of an aqueous electrolyte for better rechargeable aqueous sodium/zinc battery," *Journal of Materials Chemistry A*, vol. 5, no. 2, pp. 730-738, 2017, doi: 10.1039/C6TA08736A.
- [172] Z. Liu, S. Z. El Abedin, and F. Endres, "Dissolution of zinc oxide in a protic ionic liquid with the 1-methylimidazolium cation and electrodeposition of zinc from ZnO/ionic liquid and ZnO/ionic liquid–water mixtures," *Electrochemistry Communications*, vol. 58, pp. 46-50, 2015/09/01/ 2015, doi: 10.1016/j.elecom.2015.06.004.
- [173] F. Wang *et al.*, "Highly reversible zinc metal anode for aqueous batteries," *Nature Materials*, vol. 17, no. 6, pp. 543-549, 2018/06/01 2018, doi: 10.1038/s41563-018-0063-z.
- [174] Z. M. Wang, *Toward Functional Nanomaterials*. New York, NY: Springer.
- [175] Solubility Product Constants near 25 °C [Online] Available: <https://www.chm.uri.edu/weuler/chm112/refmater/KspTable.html>

- [176] Solubility Products of Selected Compounds [Online] Available: <https://saltlakemetals.com/solubilityproducts/>
- [177] S. M. Islam, A. A. Palma, R. P. Gautam, and C. J. Barile, "Hybrid Dynamic Windows with Color Neutrality and Fast Switching Using Reversible Metal Electrodeposition and Cobalt Hexacyanoferrate Electrochromism," *ACS Applied Materials & Interfaces*, vol. 12, no. 40, pp. 44874-44882, 2020/10/07 2020, doi: 10.1021/acsami.0c14420.
- [178] F. Mansfeld and S. Gilman, "The Effect of Lead Ions on the Dissolution and Deposition Characteristics of a Zinc Single Crystal in 6N KOH," *Journal of The Electrochemical Society*, vol. 117, no. 5, p. 588, 1970, doi: 10.1149/1.2407584.
- [179] J. M. Wang, L. Zhang, C. Zhang, and J. Q. Zhang, "Effects of bismuth ion and tetrabutylammonium bromide on the dendritic growth of zinc in alkaline zincate solutions," *Journal of Power Sources*, vol. 102, no. 1, pp. 139-143, 2001/12/01/ 2001, doi: 10.1016/S0378-7753(01)00789-3.
- [180] N. Ahmed, A. Majid, M. A. Khan, M. Rashid, Z. A. Umar, and M. A. Baig, "Synthesis and characterization of Zn/ZnO microspheres on indented sites of silicon substrate," (in English), *Materials Science-Poland*, vol. 36, no. 3, pp. 501-508, 01 Sep. 2018 2018, doi: 10.2478/msp-2018-0058.
- [181] M. Wang, L. Jiang, E. J. Kim, and S. H. Hahn, "Electronic structure and optical properties of Zn(OH)₂: LDA+U calculations and intense yellow luminescence," *RSC Advances*, 10.1039/C5RA17024A vol. 5, no. 106, pp. 87496-87503, 2015, doi: 10.1039/C5RA17024A.
- [182] G. Garcia, R. Buonsanti, A. Llodes, E. L. Runnerstrom, A. Bergerud, and D. J. Milliron, "Near-Infrared Spectrally Selective Plasmonic Electrochromic Thin Films," *Advanced Optical Materials*, <https://doi.org/10.1002/adom.201200051> vol. 1, no. 3, pp. 215-220, 2013/03/01 2013, doi: 10.1002/adom.201200051.
- [183] D. Coates, "Polymer-dispersed liquid crystals," *Journal of Materials Chemistry*, 10.1039/JM9950502063 vol. 5, no. 12, pp. 2063-2072, 1995, doi: 10.1039/JM9950502063.
- [184] J. W. Doane, A. Golemme, J. L. West, J. B. Whitehead, and B. G. Wu, "Polymer Dispersed Liquid Crystals for Display Application," *Molecular Crystals and Liquid Crystals Incorporating Nonlinear Optics*, vol. 165, no. 1, pp. 511-532, 1988/12/01 1988, doi: 10.1080/00268948808082211.
- [185] Y. Cui *et al.*, "Thermochromic VO₂ for Energy-Efficient Smart Windows," *Joule*, vol. 2, no. 9, pp. 1707-1746, 2018/09/19/ 2018, doi: 10.1016/j.joule.2018.06.018.

- [186] M. Aburas *et al.*, "Smart windows – Transmittance tuned thermochromic coatings for dynamic control of building performance," *Energy and Buildings*, vol. 235, p. 110717, 2021/03/15/ 2021, doi: 10.1016/j.enbuild.2021.110717.
- [187] X. Tao, D. Liu, J. Yu, and H. Cheng, "Reversible Metal Electrodeposition Devices: An Emerging Approach to Effective Light Modulation and Thermal Management," *Advanced Optical Materials*, vol. 9, no. 8, p. 2001847, 2021/04/01 2021, doi: 10.1002/adom.202001847.
- [188] J. Y. Li, J. S. Juarez-Rolon, S. M. Islam, and C. J. Barile, "Electrolyte Effects in Reversible Metal Electrodeposition for Optically Switching Thin Films," *Journal of The Electrochemical Society*, vol. 166, no. 12, pp. D496-D504, 2019, doi: 10.1149/2.0651912jes.
- [189] Z. Pawelka and M. C. Haulait-Pirson, "Substituent effects on specific interactions of acetate ions and acetic acid molecules," *The Journal of Physical Chemistry*, vol. 85, no. 8, pp. 1052-1057, 1981/04/01 1981, doi: 10.1021/j150608a026.
- [190] D. Shriver, M. Weller, T. Overton, F. Armstrong, and J. Rourke, *Inorganic Chemistry*. New York, NY: W. H. Freeman and Company, 2014.
- [191] D. D. Perrin, B. Dempsey, and E. P. Serjeant, *pKa Prediction for Organic Acids and Bases*. New York, NY: Springer Publications, 1981.
- [192] Y. R. Luo, *Comprehensive Handbook of Chemical Bond Energies*. Boca Raton, FL: CRC Press, Taylor & Francis Group, 2007.
- [193] W. S. M. Werner, K. Glantschnig, and C. Ambrosch-Draxl, "Optical Constants and Inelastic Electron-Scattering Data for 17 Elemental Metals," *Journal of Physical and Chemical Reference Data*, vol. 38, no. 4, pp. 1013-1092, 2009/12/01 2009, doi: 10.1063/1.3243762.
- [194] H. Yoshikawa and S. Adachi, "Optical Constants of ZnO," *Japanese Journal of Applied Physics*, vol. 36, no. Part 1, No. 10, pp. 6237-6243, 1997/10/15 1997, doi: 10.1143/jjap.36.6237.
- [195] J. D. Benck, B. A. Pinaud, Y. Gorlin, and T. F. Jaramillo, "Substrate Selection for Fundamental Studies of Electrocatalysts and Photoelectrodes: Inert Potential Windows in Acidic, Neutral, and Basic Electrolyte," *PLOS ONE*, vol. 9, no. 10, p. e107942, 2014, doi: 10.1371/journal.pone.0107942.
- [196] J. B. Goodenough and K.-S. Park, "The Li-Ion Rechargeable Battery: A Perspective," *Journal of the American Chemical Society*, vol. 135, no. 4, pp. 1167-1176, 2013/01/30 2013, doi: 10.1021/ja3091438.

- [197] M. Walter, M. V. Kovalenko, and K. V. Kravchyk, "Challenges and benefits of post-lithium-ion batteries," *New Journal of Chemistry*, 10.1039/C9NJ05682C vol. 44, no. 5, pp. 1677-1683, 2020, doi: 10.1039/C9NJ05682C.
- [198] J. M. Tarascon and M. Armand, "Issues and challenges facing rechargeable lithium batteries," (in English), *Nature*, vol. 414, no. 6861, pp. 359-67, 2019-09-06, 2001, doi: <http://dx.doi.org/10.1038/35104644>.
- [199] H.-J. Liang *et al.*, "Tempura-like carbon/carbon composite as advanced anode materials for K-ion batteries," *Journal of Energy Chemistry*, vol. 59, pp. 589-598, 2021/08/01/ 2021, doi: 10.1016/j.jechem.2020.11.039.
- [200] R. Deivanayagam, B. J. Ingram, and R. Shahbazian-Yassar, "Progress in development of electrolytes for magnesium batteries," *Energy Storage Materials*, vol. 21, pp. 136-153, 2019/09/01/ 2019, doi: 10.1016/j.ensm.2019.05.028.
- [201] Y. Jie *et al.*, "Electrolyte Solvation Manipulation Enables Unprecedented Room-Temperature Calcium-Metal Batteries," *Angewandte Chemie International Edition*, vol. 59, no. 31, pp. 12689-12693, 2020/07/27 2020, doi: 10.1002/anie.202002274.
- [202] Z. Li, O. Fuhr, M. Fichtner, and Z. Zhao-Karger, "Towards stable and efficient electrolytes for room-temperature rechargeable calcium batteries," *Energy & Environmental Science*, vol. 12, no. 12, pp. 3496-3501, 2019, doi: 10.1039/C9EE01699F.
- [203] S. Huang, J. Zhu, J. Tian, and Z. Niu, "Recent Progress in the Electrolytes of Aqueous Zinc-Ion Batteries," *Chemistry – A European Journal*, vol. 25, no. 64, pp. 14480-14494, 2019/11/18 2019, doi: 10.1002/chem.201902660.
- [204] H. Tang *et al.*, "Vanadium-Based Cathode Materials for Rechargeable Multivalent Batteries: Challenges and Opportunities," *Electrochemical Energy Reviews*, vol. 1, no. 2, pp. 169-199, 2018/06/01 2018, doi: 10.1007/s41918-018-0007-y.
- [205] A. Parija, Y. Liang, J. L. Andrews, L. R. De Jesus, D. Prendergast, and S. Banerjee, "Topochemically De-Intercalated Phases of V₂O₅ as Cathode Materials for Multivalent Intercalation Batteries: A First-Principles Evaluation," *Chemistry of Materials*, vol. 28, no. 16, pp. 5611-5620, 2016/08/23 2016, doi: 10.1021/acs.chemmater.6b01006.
- [206] R. Yazami and P. Touzain, "A reversible graphite-lithium negative electrode for electrochemical generators," *Journal of Power Sources*, vol. 9, no. 3, pp. 365-371, 1983/01/01/ 1983, doi: 10.1016/0378-7753(83)87040-2.

- [207] Y. Li, Y. Lu, P. Adelhelm, M.-M. Titirici, and Y.-S. Hu, "Intercalation chemistry of graphite: alkali metal ions and beyond," *Chemical Society Reviews*, vol. 48, no. 17, pp. 4655-4687, 2019, doi: 10.1039/C9CS00162J.
- [208] C. God *et al.*, "Intercalation behaviour of magnesium into natural graphite using organic electrolyte systems," *RSC Advances*, vol. 7, no. 23, pp. 14168-14175, 2017, doi: 10.1039/C6RA28300D.
- [209] D.-M. Kim *et al.*, "Cointercalation of Mg²⁺ Ions into Graphite for Magnesium-Ion Batteries," *Chemistry of Materials*, vol. 30, no. 10, pp. 3199-3203, 2018/05/22 2018, doi: 10.1021/acs.chemmater.8b00288.
- [210] J. Park, Z.-L. Xu, and K. Kang, "Solvated Ion Intercalation in Graphite: Sodium and Beyond," (in English), *Frontiers in Chemistry*, Review vol. 8, no. 432, 2020/5/21 2020, doi: 10.3389/fchem.2020.00432.
- [211] K. W. Nam, H. Kim, Y. Beldjoudi, T.-w. Kwon, D. J. Kim, and J. F. Stoddart, "Redox-Active Phenanthrenequinone Triangles in Aqueous Rechargeable Zinc Batteries," *Journal of the American Chemical Society*, vol. 142, no. 5, pp. 2541-2548, 2020/02/05 2020, doi: 10.1021/jacs.9b12436.
- [212] A. D. Senese and W. A. Chalifoux, "Nanographene and Graphene Nanoribbon Synthesis via Alkyne Benzannulations," *Molecules*, vol. 24, no. 1, p. 118, 2019. doi: doi.org/10.3390/molecules24010118.
- [213] W. Yang, J. H. S. K. Monteiro, A. de Bettencourt-Dias, V. J. Catalano, and W. A. Chalifoux, "Pyrenes, Peropyrenes, and Teropyrenes: Synthesis, Structures, and Photophysical Properties," *Angewandte Chemie International Edition*, vol. 55, no. 35, pp. 10427-10430, 2016, doi: 10.1002/anie.201604741.
- [214] W. Yang *et al.*, "Chiral Peropyrene: Synthesis, Structure, and Properties," *Journal of the American Chemical Society*, vol. 139, no. 37, pp. 13102-13109, 2017/09/20 2017, doi: 10.1021/jacs.7b06848.
- [215] A. Yoshino, "The Birth of the Lithium-Ion Battery," *Angewandte Chemie International Edition*, vol. 51, no. 24, pp. 5798-5800, 2012/06/11 2012, doi: 10.1002/anie.201105006.
- [216] Y. P. Wu, C. Jiang, C. Wan, and R. Holze, "Modified natural graphite as anode material for lithium ion batteries," *Journal of Power Sources*, vol. 111, no. 2, pp. 329-334, 2002/09/23/ 2002, doi: 10.1016/S0378-7753(02)00349-X.
- [217] W. Yang, J. H. S. K. Monteiro, A. d. Bettencourt-Dias, and W. A. Chalifoux, "New thiophene-functionalized pyrene, peropyrene, and teropyrene via a two- or four-fold alkyne annulation and their photophysical properties," *Canadian*

- Journal of Chemistry*, vol. 95, no. 4, pp. 341-345, 2017, doi: 10.1139/cjc-2016-0466.
- [218] W. Yang, R. R. Kazemi, N. Karunathilake, V. J. Catalano, M. A. Alpuche-Aviles, and W. A. Chalifoux, "Expanding the scope of peropyrenes and teropyrenes through a facile InCl₃-catalyzed multifold alkyne benzannulation," *Organic Chemistry Frontiers*, vol. 5, no. 15, pp. 2288-2295, 2018, doi: 10.1039/C8QO00389K.
- [219] W. Yang, J. H. S. K. Monteiro, A. de Bettencourt-Dias, V. J. Catalano, and W. A. Chalifoux, "Synthesis, Structure, Photophysical Properties, and Photostability of Benzodipyrenes," *Chemistry – A European Journal*, vol. 25, no. 6, pp. 1441-1445, 2019, doi: <https://doi.org/10.1002/chem.201805248>.
- [220] S.-D. Han *et al.*, "Origin of Electrochemical, Structural, and Transport Properties in Nonaqueous Zinc Electrolytes," *ACS Applied Materials & Interfaces*, vol. 8, no. 5, pp. 3021-3031, 2016/02/10 2016, doi: 10.1021/acsami.5b10024.
- [221] D. M. Donaldson, J. M. Robertson, and J. White, "The crystal and molecular structure of perylene," *Proceedings of the Royal Society of London. Series A. Mathematical and Physical Sciences*, vol. 220, no. 1142, pp. 311-321, 1953/12/08 1953, doi: 10.1098/rspa.1953.0189.
- [222] J. M. Robertson and J. G. White, "The Crystal Structure of Pyrene. A Quantitative X-Ray Investigation," *Journal of American Chemical Society*, no. 0, p. 607, 1945.
- [223] W. Xu and Y. Wang, "Recent Progress on Zinc-Ion Rechargeable Batteries," *Nano-Micro Letters*, vol. 11, no. 1, p. 90, 2019/10/17 2019, doi: 10.1007/s40820-019-0322-9.
- [224] R. Trócoli and F. La Mantia, "An Aqueous Zinc-Ion Battery Based on Copper Hexacyanoferrate," *ChemSusChem*, vol. 8, no. 3, pp. 481-485, 2015/02/01 2015, doi: 10.1002/cssc.201403143.
- [225] M. S. Chae, J. W. Heo, S.-C. Lim, and S.-T. Hong, "Electrochemical Zinc-Ion Intercalation Properties and Crystal Structures of ZnMo₆S₈ and Zn₂Mo₆S₈ Chevrel Phases in Aqueous Electrolytes," *Inorganic Chemistry*, vol. 55, no. 7, pp. 3294-3301, 2016/04/04 2016, doi: 10.1021/acs.inorgchem.5b02362.
- [226] R. Forgie, G. Bugosh, K. C. Neyerlin, Z. Liu, and P. Strasser, "Bimetallic Ru Electrocatalysts for the OER and Electrolytic Water Splitting in Acidic Media," *Electrochemical and Solid-State Letters*, vol. 13, no. 4, p. B36, 2010, doi: 10.1149/1.3290735.

- [227] C. Dong *et al.*, "Rational design of cobalt–chromium layered double hydroxide as a highly efficient electrocatalyst for water oxidation," *Journal of Materials Chemistry A*, vol. 4, no. 29, pp. 11292-11298, 2016, doi: 10.1039/C6TA04052G.
- [228] K. Liu *et al.*, "High-Performance Transition Metal Phosphide Alloy Catalyst for Oxygen Evolution Reaction," *ACS Nano*, vol. 12, no. 1, pp. 158-167, 2018/01/23 2018, doi: 10.1021/acsnano.7b04646.
- [229] J. A. Koza, Z. He, A. S. Miller, and J. A. Switzer, "Electrodeposition of Crystalline Co₃O₄—A Catalyst for the Oxygen Evolution Reaction," *Chemistry of Materials*, vol. 24, no. 18, pp. 3567-3573, 2012/09/25 2012, doi: 10.1021/cm3012205.
- [230] T. W. Kim, M. A. Woo, M. Regis, and K.-S. Choi, "Electrochemical Synthesis of Spinel Type ZnCo₂O₄ Electrodes for Use as Oxygen Evolution Reaction Catalysts," *The Journal of Physical Chemistry Letters*, vol. 5, no. 13, pp. 2370-2374, 2014/07/03 2014, doi: 10.1021/jz501077u.
- [231] R. Subbaraman *et al.*, "Trends in activity for the water electrolyser reactions on 3d M(Ni,Co,Fe,Mn) hydr(oxy)oxide catalysts," *Nature Materials*, vol. 11, no. 6, pp. 550-557, 2012/06/01 2012, doi: 10.1038/nmat3313.
- [232] Z. Lu *et al.*, "Three-dimensional NiFe layered double hydroxide film for high-efficiency oxygen evolution reaction," *Chemical Communications*, vol. 50, no. 49, pp. 6479-6482, 2014, doi: 10.1039/C4CC01625D.
- [233] X. Zou, A. Goswami, and T. Asefa, "Efficient Noble Metal-Free (Electro)Catalysis of Water and Alcohol Oxidations by Zinc–Cobalt Layered Double Hydroxide," *Journal of the American Chemical Society*, vol. 135, no. 46, pp. 17242-17245, 2013/11/20 2013, doi: 10.1021/ja407174u.
- [234] F. Yang *et al.*, "Synergistic Effect of Cobalt and Iron in Layered Double Hydroxide Catalysts for the Oxygen Evolution Reaction," *ChemSusChem*, vol. 10, no. 1, pp. 156-165, 2017/01/10 2017, doi: 10.1002/cssc.201601272.
- [235] S. L. Candelaria *et al.*, "Multi-Component Fe–Ni Hydroxide Nanocatalyst for Oxygen Evolution and Methanol Oxidation Reactions under Alkaline Conditions," *ACS Catalysis*, vol. 7, no. 1, pp. 365-379, 2017/01/06 2017, doi: 10.1021/acscatal.6b02552.
- [236] M. Gong *et al.*, "An Advanced Ni–Fe Layered Double Hydroxide Electrocatalyst for Water Oxidation," *Journal of the American Chemical Society*, vol. 135, no. 23, pp. 8452-8455, 2013/06/12 2013, doi: 10.1021/ja4027715.

- [237] Y. Cheng, C. Liu, H.-M. Cheng, and S. P. Jiang, "One-Pot Synthesis of Metal–Carbon Nanotubes Network Hybrids as Highly Efficient Catalysts for Oxygen Evolution Reaction of Water Splitting," *ACS Applied Materials & Interfaces*, vol. 6, no. 13, pp. 10089-10098, 2014/07/09 2014, doi: 10.1021/am500988p.
- [238] Y. Liu *et al.*, "Electrochemical tuning of olivine-type lithium transition-metal phosphates as efficient water oxidation catalysts," *Energy & Environmental Science*, vol. 8, no. 6, pp. 1719-1724, 2015, doi: 10.1039/C5EE01290B.
- [239] L. Chang *et al.*, "Facile one-pot synthesis of magnetic Prussian blue core/shell nanoparticles for radioactive cesium removal," *RSC Advances*, vol. 6, no. 98, pp. 96223-96228, 2016, doi: 10.1039/C6RA17525B.